Atom Probe Analysis of Crystallographic Defects in Silicon



David Tweddle

Lincoln College

University of Oxford

Thesis submitted for the degree of

Doctor of Philosophy

Trinity 2019

Supervisors: Professor Michael Moody, Professor Peter Wilshaw, Dr Phillip Hamer

Abstract

High performance multicrystalline silicon (HPMC-Si) is the dominant material used in photovoltaic (PV) devices. This material however contains a large number of defects, such as grain boundaries and dislocations. The decoration of such defects by transition metals and other impurities causes deep levels in the band gap, significantly affecting the performance and efficiency of PV devices. In the photovoltaic industry, processing techniques, such as hydrogen passivation and gettering, are used to increase the minority carrier lifetime, reducing the recombination activity of crystallographic defects. However, these techniques are not always effective and the reasons for this are currently not always well understood.

In this thesis, a correlative microscopy approach is developed, incorporating electron beam induced current (EBIC), electron back scatter diffraction (EBSD) and atom probe tomography (APT). This approach combines the characterisation of recombination activity, crystallographic information, and chemical composition of individual defects after various stages of processing. These methods were employed to determine the cause of contamination from room temperature colloidal silica polishing and also investigate the evolution of grain boundaries at various stages of gettering and hydrogenation. In addition, this approach was also applied to alternative PV materials of Red Zone HPMC-Si and n-type HMPC-Si, demonstrating wide-scale applicability.

Nitrogen was observed to correlate with an increase in recombination activity at certain grain boundaries. In addition, the light elements carbon and oxygen were also

observed to decorate grain boundaries. No transition metals, except copper, were detected. This may be due to the detection limit of APT, which was calculated to be as high as 10^{15} cm^{-3} for Fe.

Furthermore, applying this new multiscale correlative microscopical approach to the analysis of deuterium (^{2}H) passivated wafers, hydrogen has been directly observed to decorate crystallographic defects in silicon and the extent of segregation quantified. These new insights have the potential to directly address the question as to why some grain boundaries respond positively to hydrogenation, whereas others do not.

Preface

This thesis comprises the work carried out by the author in the Department of Materials, University of Oxford, under the supervision of Professor Michael Moody, Professor Peter Wilshaw and Dr Phillip Hamer.

No part of this thesis has previously been submitted for a degree at this or any other university. The work of other authors used in this thesis is acknowledged accordingly; a list of references is provided at the end of the text.

Some of the work presented in this thesis has already been published by the author or presented at conferences.

Acknowledgements

First and foremost, I would like to thank my supervisors Professor Michael Moody, Professor Peter Wilshaw and Dr. Phillip Hamer. Your unrelenting support and advice has been invaluable and I have benefited greatly from your experiences. I hope to see you all in many conferences to come.

Secondly, I would like to thank my colleagues in the Atom Probe and Semiconductor Groups. In particular, my office mates Megan, Ben, Charlie, Zhao and Tom have made my time at Oxford so much fun. I would also like to thank James and Tomas for training me on the FIB and atom probe.

Thirdly, my trip to Australia was perhaps the most memorable aspect of the DPhil experience. I would like to thank the group at UNSW for their expertise and for making me feel so welcome during my time in Sydney. Above all, I would like to express my gratitude to Dan, Moonyong, Ran, Ali and Zhuangyi.

Finally, my time at Oxford was truly the most rewarding and entertaining time of my life. I would like to give a big thanks to my friends at Lincoln College; Michael, Ineke, Jasha, George, James, Rob, Pablo, Lewis and others. Next step is the University of Alabama with the most amazing girl I have ever met. Roll Tide!

Journal and Conference Publications

Tweddle, D., P. Hamer, Z. Shen, V. Markevich, M.P. Moody, and P.R. Wilshaw, 'Direct Observation of Hydrogen at Defects in Multicrystalline Silicon', *Progress in Photovoltaics*, vol. Special Issue, 1-7, 2019.

Tweddle, D., P. Hamer, Z. Shen, M.P. Moody, and P.R. Wilshaw, 'Identification of Colloidal Silica Polishing Induced Contamination in Silicon', *Materials Characterization*, 152 (2019), 239–44.

Tweddle, D., E. C. Shaw, J. O. Douglas, R. S. Bonilla, M. P. Moody, P. Hamer, and P. R. Wilshaw, 'Atom Probe Tomography of Fast-Diffusing Impurities and the Effect of Gettering in Multicrystalline Silicon', in *AIP Conference Proceedings*, 2018, 1999.

Z. Shen, K. Chen, **D. Tweddle**, G. He, K. Arioka, and S. Lozano-Perez, "Characterization of the crack initiation and propagation in Alloy 600 with a cold-worked surface," Corrosion Science, vol. 152, pp. 82–92, 2019.

Bourret-Sicotte, G., P. Hamer, **D. Tweddle**, R. S. Bonilla, and P. R. Wilshaw, 'Hydrogen Related Defects in Float Zone Silicon Investigated Using a Shielded Hydrogen Plasma', in *2018 IEEE 7th World Conference on Photovoltaic Energy Conversion (WCPEC) (A Joint Conference of 45th IEEE PVSC, 28th PVSEC & 34th EU PVSEC)* (IEEE, 2018), pp. 0298–0302.

C. Lotharukpong, **D. Tweddle**, T. L. Martin, M. Wu, C. R. M. Grovenor, M. P. Moody, and P. R. R. Wilshaw, "Specimen preparation methods for elemental characterisation of grain boundaries and isolated dislocations in multicrystalline silicon using atom probe tomography," Materials Characterization, vol. 131, pp. 472–479, 2017.

Conferences

Microscopy of Semiconducting Materials, *Cambridge, UK – Oral Presentation*, April 2019

International Microscopy Congress, *Sydney, Australia – Oral Presentation*, September 2018

Silicon PV, *Lausanne, Switzerland – Oral Presentation*, April 2018

European Atom Probe Workshop, *Gothenburg, Sweden – Oral Presentation*, September 2017

Microscopy of Semiconducting Materials, *Oxford, UK – Oral Presentation*, April 2017

Funding

This project was funded by the UK government through the EPSRC (Supersilicon grant, EP/M024911/ 1). Further funding was received in the form of travel grants from Lincoln College, Oxford, the Royal Microscopical Society and the Oxford Materials Department travel grant.

Table of Contents

1 Introduction 1

1.1 Electrical Contacts and Junctions 2

1.1.1 Ohmic Contact 2

1.1.2 Schottky Junction 3

1.1.3 p-n Junction 3

1.2 Solar Power Fundamentals 5

1.3 Recombination 7

1.3.1 Radiative Recombination 8

1.3.2 Auger Recombination 9

1.3.3 Shockley Read Hall Recombination 11

1.3.4 Trapping 13
1.4 Concluding Remarks 14
2 Literature Review 15
2.1 Defects in Multicrystalline Silicon 15
2.1.1 Intrinsic Defects 15
2.1.2 Extrinsic Defects 18
2.2 Dislocations 25
2.2.1 Dislocations as Recombination Centres 28
2.2.2 Impurity Segregation 31
2.2.3 Precipitation at Dislocations 32
2.3 Grain Boundaries 33
2.3.1 Grain Boundaries as Recombination Centres 35
2.4 Gettering 37
2.4.1 Internal Gettering 38
2.4.2 External Gettering 40
2.5 Hydrogen Passivation 48
2.5.1 Principles and Mechanism 48
2.5.2 Hydrogen Passivation of Crystallographic Defects 50
2.6 Electron Beam Induced Current 52
2.6.1 EBIC of Crystallographic Defects 52
2.7 Atom Probe Tomography 54

2.7.1 Atom Probe Tomography of Silicon 54
2.8 Concluding Remarks 58
3 Experimental Techniques and Methods 60
3.1 Introduction 60
3.2 Experimental Procedure 60
3.3 Materials 61
3.4 Processing Techniques 62
3.4.1 Phosphorus Diffusion Gettering 62
3.4.2 Saw Damage Gettering 62
3.4.3 Hydrogen Passivation via Dielectric Layers 63
3.4.4 Hydrogen Passivation via Remote Plasma 63
3.4.5 Boron Diffusion Gettering 64
3.5 Polishing and Chemical Etching 64
3.5.1 Mechanical Polishing 64
3.5.2 HNA Etching 65
3.5.3 Selective Etching – Secco 66
3.6 Electron Beam Induced Current 66
3.6.1 EBIC Operating Principles 66
3.6.2 EBIC Sample Preparation 69
3.6.3 EBIC Imaging and Processing 70
3.7 Electron Backscatter Diffraction 72

3.7.1 Operating Principles 72

3.7.2 EBSD Imaging and Processing 73

3.8 Transmission Kikuchi Diffraction 74

3.8.1 Operating Principles 74

3.8.2 TKD Imaging and Processing 75

3.9 Dual Beam Scanning Electron Microscope and Focussed Ion Beam 75

3.10 APT Specimen Preparation 76

3.10.1 Sample Marking 76

3.10.2 Cantilever Production 77

3.10.3 Liftout 78

3.10.4 Needle Milling 79

3.11 Transmission Electron Microscopy 80

3.12 Atom Probe Tomography 82

3.12.1 Principles 82

3.12.2 APT Limitations 85

3.12.3 APT Instrumentation and Calibration 87

3.12.4 Three-Dimensional APT Reconstruction 89

3.12.5 Gibbsian Excess 90

3.12.6 APT Mass Spectra 92

3.13 Photoluminescence 94

3.14 Lifetime Testing 96

3.15 Concluding Remarks 96

4 Room Temperature Contamination of Transition Metals in Multicrystalline Silicon 97

4.1 Introduction 97

4.2 Results and Analysis 100

4.2.1 Electron Beam Induced Current 100

4.2.2 Electron Backscatter Diffraction 102

4.2.3 Atom Probe Tomography 104

4.3 Discussion 110

4.4 Conclusions 114

5 The Effect of Gettering and Conventional Hydrogen Passivation on High Performance Multicrystalline Silicon 116

5.1 Introduction 116

5.2 Photoluminescence 117

5.3 PL Region A 118

5.3.1 Electron Backscatter Diffraction 119

5.3.2 Electron Beam Induced Current 120

5.3.3 Transmission Electron Microscopy 123

5.3.4 Atom Probe Tomography 125

5.4 PL Region B 129

5.5 PL Region C 133

5.5.1 Electron Backscatter Diffraction 133

5.5.2 Electron Beam Induced Current Mapping 134

5.5.3 Atom Probe Tomography 136

5.6 Discussion 141

5.6.1 APT Sensitivity 151

5.7 Conclusions 155

6 Direct Observation of Hydrogen at Defects in Passivated Multicrystalline Silicon 157

6.1 Introduction 157

6.2 Results 160

6.3 Discussion and Analysis 166

6.4 Conclusions 169

7 Alternative Solar Cell Materials: Wide-scale Application of Atom Probe Tomography 171

7.1 Introduction 171

7.2 Saw Damage Gettering of Red Zone Multicrystalline Silicon 172

7.2.1 Macroscale Analysis 173

7.2.2 Nanoscale Analysis 174

7.2.3 Discussion 179

7.3 Boron Diffusion of n-type High Performance Multicrystalline Silicon 181

7.3.1 Photoluminescence 182

7.3.2 Grain Boundary 1 184

7.3.3 Grain Boundary 2 192

7.3.4 Grain Boundary 3 197

7.3.5 Discussion 199

7.4 Conclusions 205

8 Summary and Conclusions 207

9 Future Work 211

10 References 214

1 Introduction

Humans are now using more energy than ever before, leading increasingly energy intensive lives. Energy is essential for economic growth, with rapidly developing and highly populated nations facing a huge expansion in energy usage [1]. The most obvious example is the massive increase in China's GDP in the last 25 years. This has coincided with a huge growth in coal usage, with the consumption increasing from 679 million ton of oil equivalent (in 2000) to 1920 Mtoe (in 2015) [2]. The reliance of such economies on coal and other fossil fuels is unsustainable. Fossil fuels are being depleted 100,000 times faster than being formed, with current estimations only predicting 170 years of supply left [3]. The use of fossil fuels is also causing irrevocable damage to the environment, with the mass emission of the greenhouse gas CO_2 and other harmful gases such as SO_2 [4].

Solar energy might be the only source of energy that can be considered 'infinite'. In contrast to other renewable energies, solar power does not face the issues of radiation safety, or the wind turbine requirement of rare-earth elements. The total radiative energy delivered to the earth's surface vastly exceeds the current and projected future demands [3]. Furthermore, the vast majority of rapidly developing nations are exposed to relatively high levels of solar energy.

Although the growth of high efficiency multicrystalline silicon solar cells has been booming in recent years [5], the lifetime limiting mechanisms are not well known. This project intends to provide a greater insight into the nanoscale defects found in

these cells, in an atom-by-atom characterisation approach, in order to support the continuing growth in the industry.

1.1 Electrical Contacts and Junctions

In order to comprehend how solar energy is captured and converted to electricity in a solar cell, one must first understand what an electrical junction is. All solar cells require an electrical junction of some sort. A junction is formed when electrically dissimilar materials are placed in electrical contact. These junctions can consist of two completely different materials (heterojunction) or of the same material, electrically doped differently across the junction (homojunction).

1.1.1 Ohmic Contact

An Ohmic contact is formed when a metal is placed in electrical contact with a semiconductor (Figure 1.1b). Ohmic contacts allow the flow of majority carriers (electrons in n-type and holes in p-type semiconductors) and exist when the work function of the metal is less than the Fermi level in an n-type semiconductor (greater in a p-type semiconductor). When the materials are placed in contact (n-type semiconductor), electrons from the metal enter the conduction band, causing a band bending effect. Ohmic contacts can also be formed by damaging and heavily doping the surface of the semiconductor, allowing for quantum tunnelling [6]. Ohmic contacts are widely used in the photovoltaic industry, since current flow is required at electrical contacts.

1.1.2 Schottky Junction

Schottky junctions also consist of a semiconductor and metal placed in electrical contact (Figure 1.1c). In contrast to Ohmic contacts, Schottky junctions oppose the flow of majority carriers and are formed when the work function of the metal is greater than the Fermi level of an n-type semiconductor (lower in a p-type semiconductor). When the two materials are in contact (for an n-type semiconductor), electrons can lower their energies by flowing from the semiconductor to the metal, causing an opposing band distortion. Schottky junctions are used extensively in materials characterisation as collecting junctions, for example in electron beam induced current and capacitance voltage measurements.

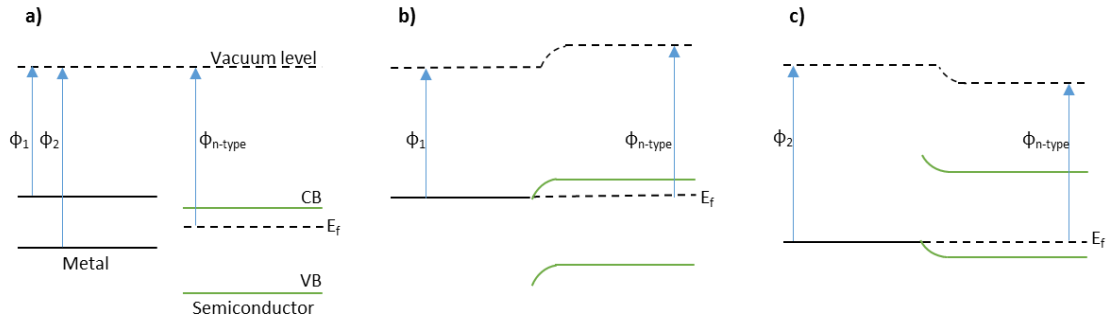


Figure 1.1. Metal, n-type semiconductor junctions. a) Pre-contact arrangement of two metals of work functions φ_1 and φ_2 and an n-type semiconductor. E_f denotes the Fermi level, VB is the valence band and CB is the conduction band. b) Ohmic junction between n-type semiconductor and metal 1. c) Schottky contact between n-type semiconductor and metal 2.

1.1.3 p-n Junction

The vast majority of solar cells utilise a p-n junction to generate electricity from light. A p-n junction is formed when a p-type semiconductor and an n-type semiconductor are placed in electrical contact. An alignment of the Fermi levels occurs, with majority

carriers from the p and n-type materials recombining; forming a depletion region consisting of positively charged ions at the n-type interface and negatively charged ions at the p-type interface, with no free charge carriers present. Ions at the interface create an electric field, which opposes the flow of majority carriers.

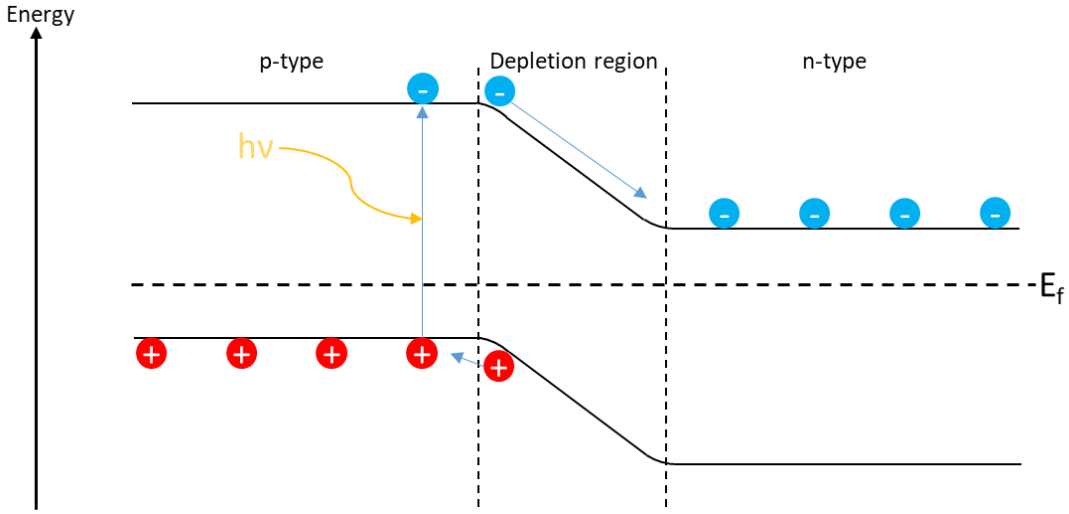


Figure 1.2. Schematic of a p-n junction, with a photon with a frequency υ causing the excitation of an electron from the valence band to the conduction band. E_f denotes the Fermi level.

The design of many photovoltaic devices, including silicon solar cells, make use of a p-n junction. In order to produce useful electrical energy, photons excite electrons from the valence band to the conduction band. The minority carrier must then diffuse to the depletion region and be swept across, as seen in Figure 1.2. The electrons/holes can then migrate to their respective contacts, resulting in a useful current output.

1.2 Solar Power Fundamentals

Solar cells utilise the absorbance of light to generate electron hole pairs, which in the presence of a p-n junction diffuse to their respective contacts creating a current. For an ideal solar cell under illumination, the current is described by the Shockley solar cell equation:

$$I = I_{ph} - I_0\left(e^{\frac{qV}{k_BT}} - 1\right) \qquad (1.1)$$

where the current I is equal to the photogenerated current (I_{ph}) minus the saturation current I_0 multiplied by an exponential term; where q is the charge on an electron, V is the applied voltage/bias at the junction, k_B is the Boltzmann constant and T is the absolute temperature.

The maximum power output of a solar cell is strongly related to the open-circuit voltage V_{OC} and the short-circuit current I_{SC}. These are defined as the voltage that develops when the cell is illuminated but no contacts are connected and the current that flows when the electrodes are connected but no potential difference is applied.

$$V_{OC} = \frac{k_BT}{q} ln\left(\frac{I_{ph}}{I_0}\right) \qquad (1.2)$$

Equation (1.2) describes the open-circuit voltage (V_{OC}), in terms of the photogenerated current (I_{ph}), in the ideal case in which the photogenerated current equals the short circuit current (I_{ph}=I_{SC}).

The maximum power P_{max} is produced at a voltage V_m and a current I_m, where P_{max} is the multiplication of these two values. The fill factor measures the closeness of the IV curve to the ideal, also termed the 'squareness' of the curve, as shown in Figure 1.3.

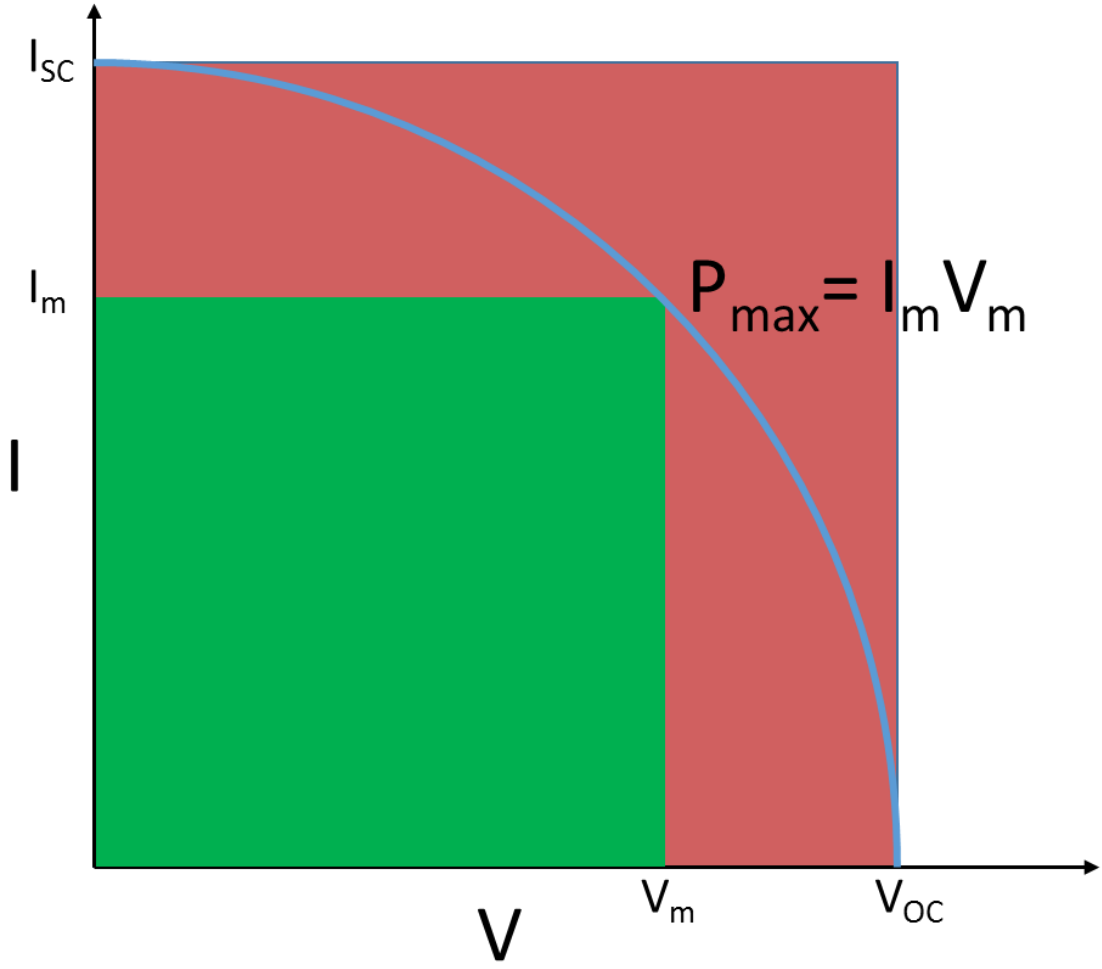


Figure 1.3. Plot of IV curve (blue line), between the short-circuit current I_{SC} and the open-circuit voltage V_{OC}. The P_{max} is defined as the area encompassed by the green square at V_m and I_m, while the fill factor FF is the area ratio of the green and red squares.

The fill factor (FF) can be expressed as:

$$FF = \frac{I_m V_m}{I_{SC} V_{OC}} = \frac{P_{max}}{I_{SC} V_{OC}} \qquad (1.3)$$

where P_{max} is the maximum power at I_m and V_m, and I_{SC} and V_{OC} are the short circuit current open circuit voltage respectively.

Since I_{SC} is proportional to the cell area exposed to light, which governs the number of electron-hole pairs generated by incident solar energy, the short-circuit current density J_{SC} is often preferred (where J_m is the maximum current density). Using the relationship between P_{max} and fill factor, a figure of merit for a solar cell can be created, termed the power conversion efficiency (PCE) which relates the power output to the input power P_{light}:

$$PCE = \frac{J_m V_m}{P_{light}} = \frac{J_{SC} V_{OC} FF}{P_{light}} \qquad (1.4)$$

1.3 Recombination

Photovoltaic cells suffer from a large number of potential losses, which result in a decreased efficiency, as shown in Figure 1.4. With the development of the back surface field and enhanced passivation of surfaces [7], bulk recombination has become an increasingly large concern for solar cell manufacturers. Recombination involves the elimination of free charge carriers, via the recombination of electrons in the conduction band and holes in the valence band. Bulk recombination occurs via three main mechanisms: radiative, Auger and Shockley Read Hall.

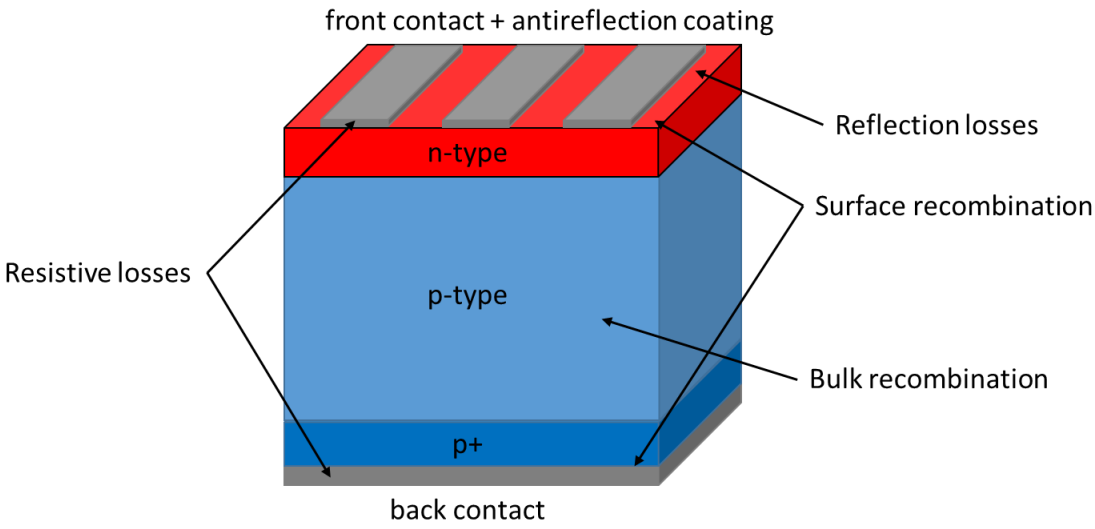


Figure 1.4. Schematic of a silicon solar cell, consisting of an n-type region, p-type region and heavily doped p+ region, providing a back surface field. The areas of recombination and other losses found in the photovoltaic cell are labelled.

1.3.1 Radiative Recombination

Radiative recombination, often called band-to-band recombination, is the direct opposite of photoexcitation. The electron in the conduction band drops back down to the valence band to recombine with a hole, with the excess energy released as a photon (Figure 1.5). The most obvious example of this phenomenon is in a light emitting diode (LED). Radiative recombination is more dominant in direct band gap semiconductors like GaAs, compared to indirect band gap semiconductors such as Si where a change in momentum of minority carriers is required.

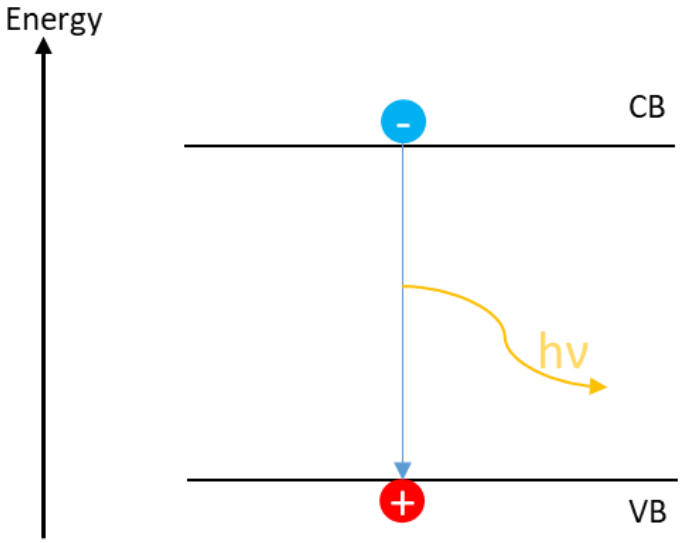


Figure 1.5. Schematic of radiative (band-to-band) recombination, in which an electron in the conduction band (CB) recombines with a hole in the valence band (VB), resulting in the release of a photon with a frequency υ.

The nett recombination rate away from thermal equilibrium via radiative recombination U_R is given by:

$$U_R = B(np - n_i^2) \qquad (1.5)$$

where B, the radiative recombination coefficient, is given by the total radiative recombination rate U_R divided by the square of the intrinsic carrier concentration n_i. In which, n and p are the densities of electrons and holes in the conduction band and valence band respectively.

1.3.2 Auger Recombination

Unlike radiative, Auger recombination involves three charge carriers. An electron in the conduction band drops down to the valence band to recombine with a hole, with

the excess energy given to the third charge carrier (e.g. an electron). This electron then falls back to the edge of the conduction band by the emission of phonons to the lattice. Auger recombination is significant in highly doped regions in Si, due to the requirement of three charge carriers being in close proximity at the same time [8], [9].

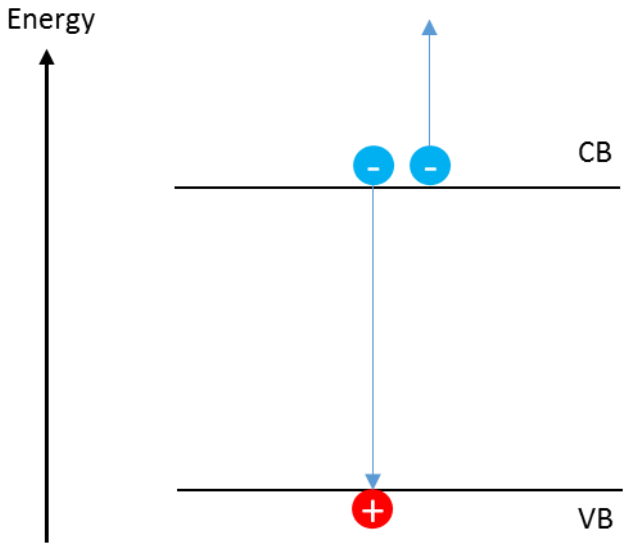


Figure 1.6. Schematic of Auger recombination, in which an electron in the conduction band (CB) recombines with a hole in the valence band (VB). The resulting energy is given to a third charge carrier, in this case an electron in the CB, which over time retreats to the edge of the CB by the emission of phonons into the lattice.

The nett recombination rate via Auger recombination U_A is given by [10]:

$$U_A = \left(C_{po}p + C_{no}n\right)(np - n_i^2) \qquad (1.6)$$

in which C_{po} and C_{no} denote the Auger coefficients for holes and electrons respectively, while n and p are the densities of electrons and holes respectively. It is worth noting that other formulations of the Auger recombination equation exist [11].

1.3.3 Shockley Read Hall Recombination

The dominant recombination mechanism in virtually all silicon devices is recombination through defect levels (as shown in Figure 1.7), termed Shockley Read Hall (SRH) recombination (discussed in detail in [12], [13]). The recombination rate U through an isolated defect level is given in Equation 1.7 [10]:

$$U = (np - n_1 p_1)/[\tau_{po}(n + n_1) + \tau_{no}(p + p_1)] \quad (1.7)$$

where,

$$n_1 = n_i exp\left(\frac{E_t - E_i}{k_B T}\right), p_1 = n_i exp\left(\frac{E_i - E_t}{k_B T}\right) \quad (1.8)$$

where n and p are the densities of mobile electrons and holes in the conduction band and valence band respectively, τ_{po} and τ_{no} the capture time constants for holes and electrons and depend inversely upon the product of the carrier thermal velocity, capture cross-section and the density of the defects involved. n_1 and p_1 are dependent on the energy of the defect level within the band gap, as shown in Equation 1.8 (where $n_1 p_1 = n_i^2$). E_t and E_i are the trap energy level and intrinsic Fermi level respectively, while k_B is the Boltzmann constant, n_i is the intrinsic carrier concentration and T is the absolute temperature [14].

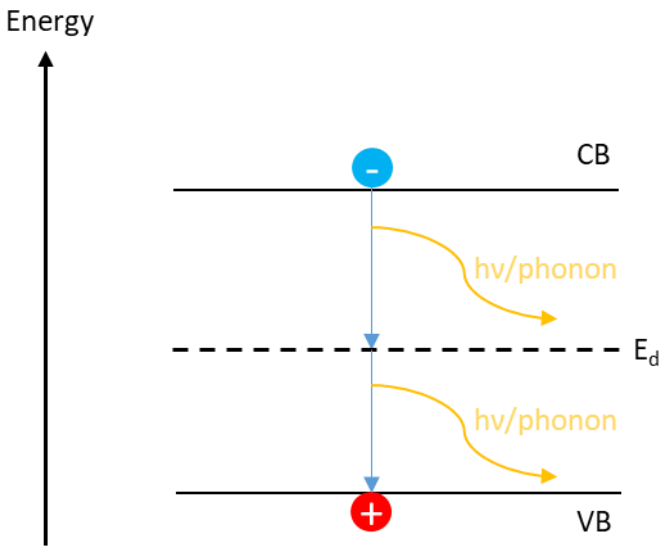


Figure 1.7. Schematic of Shockley Read Hall recombination, where E_d is the defect energy level. In this example, an electron in the conduction band (CB) is trapped by a defect level and then recombines with a hole in the valence band (VB). The energy is released by the emission of a photon with a frequency υ or by the emission of phonons.

These trap levels are caused by defects and may be either acceptor or donor states. In the case of an acceptor defect, a neutrally charged trap can accept an electron from the conduction band and become negatively charged. In p-type semiconductors, with an abundant number of holes in the valence band, a hole is electrically attracted to the level, resulting in recombination with the emission of phonons into the lattice. The effectiveness of SRH recombination is dependent on the location of the trap in the band gap [15]. As can be seen in Equation 1.7, providing τ_{po} and τ_{no} are similar, the recombination rate is maximised when $n_1 \approx p_1$. This occurs when the defect level lies in the centre of the band gap [11].

1.3.4 Trapping

Although technically not a form of recombination, trapping is a similar process to SRH recombination. Minority carriers can be captured or trapped by relatively shallow levels, but do not contribute directly to recombination [16]. The result of trapping is a large increase in the concentration of majority carriers, as a result of the requirement of maintaining charge neutrality [17], [18]. This can be seen by a large increase in the photoconductance, in addition to an apparent enhanced lifetime as the excess carrier density decreases [16].

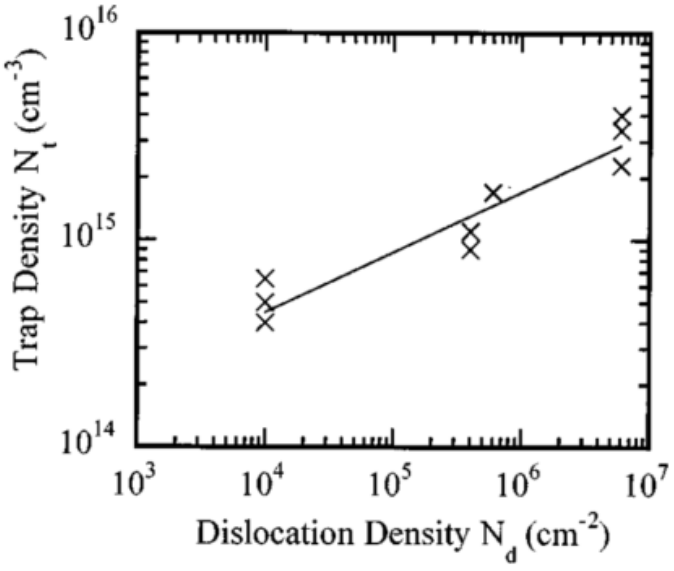


Figure 1.8. Graph showing correlation between dislocation density and trap density [16].

The source of minority traps has been subject to a large amount of investigation in the literature [16], [18], [19]. MacDonald and Cuevas has shown a strong correlation between the trap density and the dislocation density (Figure 1.8), indicating that dislocations play a role as defect states which trap charge carriers [16]. Kvande et al. [20] also indicated that Fe content significantly effects the trap density, with greater amounts of trapping at the top and bottom of a multicrystalline ingot, where Fe levels

are greater. It is likely that Fe and other impurities sit at such dislocation sites and contribute to increased trapping. This will be discussed in later in Section 2.2.

1.4 Concluding Remarks

In this section, key fundamental concepts regarding solar cells are presented. The importance of electrical contacts for solar cell operation and also electrical characterisation is discussed. Additionally, equations regarding key characteristics of solar cells, such as I_{SC}, V_{OC} and FF, are given. Finally, the importance of recombination, a key area of study in this thesis, is outlined in relation to solar cell efficiency.

2 Literature Review

2.1 Defects in Multicrystalline Silicon

Thermodynamics implies that defects are present within all crystals, with a large gain in entropy achieved from even a small number of defects. Defects are usually characterised as either intrinsic or extrinsic. Intrinsic defects are imperfections that arise relating to the crystal itself. In contrast, extrinsic defects relate to impurities or dopants added intentionally or unintentionally to the crystal lattice (Figure 2.1).

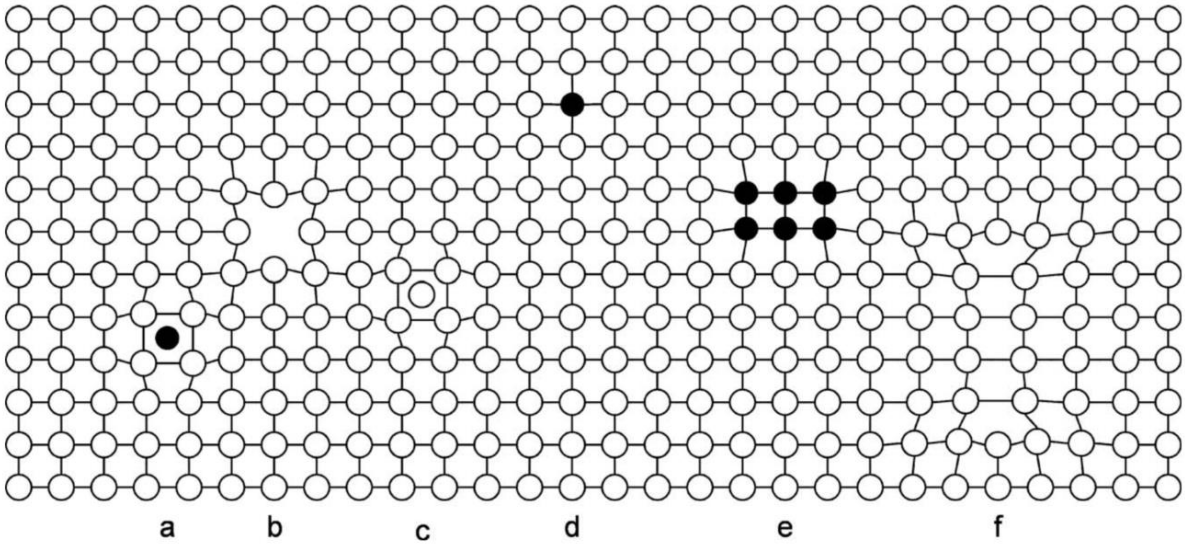


Figure 2.1. Examples of common defects in single crystal silicon: (a) interstitial impurity atom, (b) vacancy, (c) self-interstitial atom, (d) substitutional impurity atom (dopant), (e) precipitate of impurity atoms (cluster), (f) vacancy cluster [21].

2.1.1 Intrinsic Defects

Multicrystalline silicon contains a large amount of intrinsic defects, some of which are shown in Figure 2.1. Defects are often classed by their dimensionality. Point defects or zero-dimensional defects include vacancies and self-interstitials, which in

combination is termed a Frenkel defect. One-dimensional defects include dislocations and stacking faults. Higher dimensional defects include 2D grain boundaries and 3D precipitates or pores.

Self-interstitials and vacancies play important roles in silicon defect engineering, in addition to their presence allowing the diffusion of substitutional impurities [22]. The injection of silicon self-interstitials (Si_i) during phosphorus diffusion gettering, is an essential mechanism to enhancing the diffusion of substitutional metals towards the gettered layer [23]. Vacancy engineering is an additional innovative technique, investigated by Raineri et al. [24], which uses high energy $^{29}Si^{+}$ irradiation to induce large concentrations of vacancies. The vacancies generated annihilate self-interstitials at the surface, hindering the unwanted diffusion of boron present at the surface.

The primary defects inherent to multicrystalline silicon, not seen in single crystal silicon, are grain boundaries. Grain boundaries are known regions of recombination, as a result of impurity segregation, with Kurobe et al. finding a 10x increase in the Fe concentration at the grain boundary compared to the bulk [25]. The likelihood of contamination is related to the grain boundary type, with different grain boundaries having differing recombination activities (as shown in Figure 2.2) [26]. Large angle and random grain boundaries, have a large density of precipitation sites for impurities [27] and a high dislocation density [28]. In contrast, high coincidence twin Σ3 {111} planes have the lowest number of precipitation sites and hence, the lowest recombination activity [29]. This leads to their ineffectiveness as internal gettering sites as found by Ohno [30].

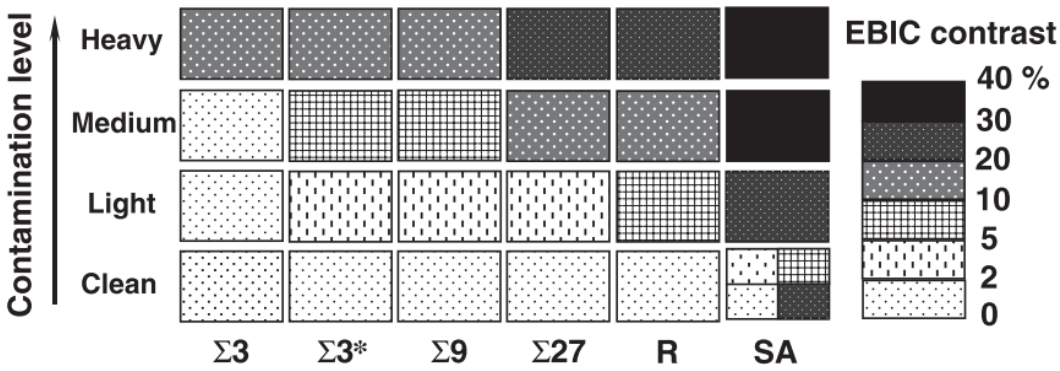


Figure 2.2. EBIC contrast of grain boundaries at 300 K with respect to the Σ value (where Σ3 is not orientated on the {111} plane, R is random angled grain boundary and SA is a small angle grain boundary) and contamination level [31]. Copyright © 2007, The Japan Society of Applied Physics.*

The control of grain boundary growth has been widely studied in recent years, especially with the emergence of high performance multicrystalline silicon (HPMC-Si) [32]. The main characteristics of HPMC-Si are small grain size, a high proportion of random angle grain boundaries and a low density of dislocation clusters [33]. These random angle grain boundaries act as free surfaces for the termination of dislocation clusters, in addition to reducing the global stress of the system hindering dislocation multiplication [34]. Although authors [33], [35] have found that random angle grain boundaries become electrically activated under gettering, they can often be efficiently passivated by hydrogen, while more harmful dislocation clusters and other grain boundary types remain recombination active.

2.1.2 Extrinsic Defects

Extrinsic defects are caused by the presence of impurities or dopant atoms, which reside interstitially, substitutionally or as a precipitate.

2.1.2.1 Native Impurities

Oxygen has a fundamental affinity with silicon, with a passivating SiO_2 surface layer forming when silicon is exposed to the atmosphere. During production, oxygen incorporated within the crystal during solidification from the silica crucible, with multicrystalline silicon typically containing approximately 10^{16} atoms cm^{-3} of interstitial oxygen [26]. Under cooling, the high concentration of oxygen becomes supersaturated and forms SiO_2 precipitates. These oxide precipitates have been found by Haunschild et al. [36] to decrease the absolute cell efficiency up to 4% in 'high quality' Cz-Si, although the exact chemistry of the precipitates found was not characterised. The recombination activity has been partially ascribed to the decorated dislocations and stacking faults formed in the vicinity of the oxide precipitates, causing deep levels in the band gap [37]. In addition, recombination has also been related to dangling bonds associated with oxygen precipitation [38].

Carbon is also termed a native impurity in multicrystalline silicon, with the concentration of substitutional carbon approximately 10^{17} atoms cm^{-3} [26]. Carbon is found as an impurity in the feedstock materials and usually forms SiC precipitates [39]. Carbon has also been found to segregate to grain boundaries [40] and dislocations [41], resulting in an increase in the defect recombination activities due to enhanced trapping of recombination active impurities [39], [42]. Carbon concentration has also

been found to correlate with an increase in the dislocation density, implying that carbon has the ability to induce conditions for dislocation multiplication [42]. This is in contrast to oxygen, which has been found to decrease the dislocation density in as-grown multicrystalline silicon [43].

Nitrogen is the third so-called ‘light’ or ‘native’ impurity found in silicon. It is found in large quantities in multicrystalline silicon cast in silicon nitride, via the in diffusion of nitrogen from the crucible to the ingot [33]. Similarly to carbon and oxygen, nitrogen in silicon is usually present as a precipitate (Si_3N_4) [44] or found to segregate to grain boundaries and other crystallographic defects, resulting in nitrogen depleted regions forming around grain boundaries [45]. Nitrogen interacts strongly with dislocations in silicon, hindering their motion [46], while also resulting in the formation of vacancies which stimulate the annihilation of dislocations [47]. Nitrogen also has a known affinity to oxygen, often forming nitrogen-oxygen complexes or precipitates [48]. Although these precipitates are often electrically inactive in silicon, some have been reported to introduce deep levels in the bandgap resulting in significant amounts of recombination [46].

2.1.2.2 Transition Metals

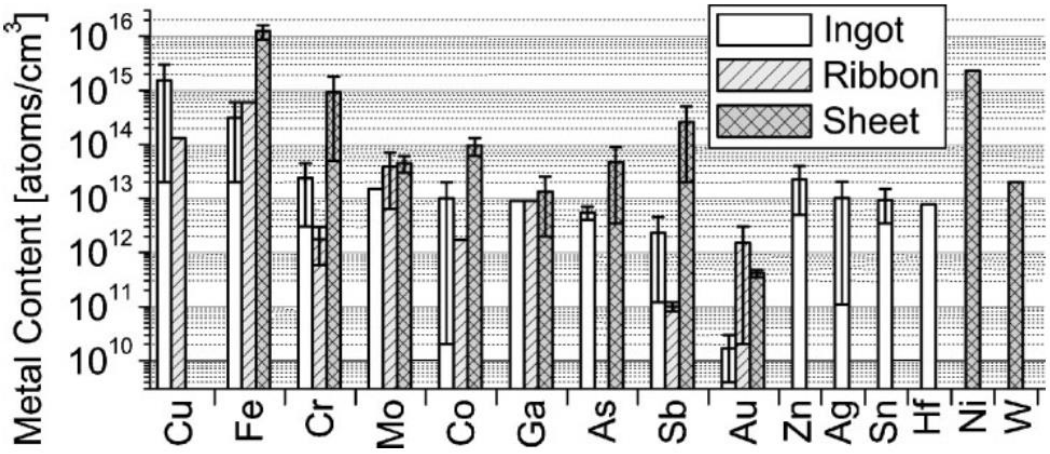


Figure 2.3. Neutron activation analysis data of the individual metal contents in ingot, ribbon and sheet mc-Si. Error bars give the discrepancy between different runs, due to the differences in feedstock quality [27]. *NB: For data please read referenced paper.*

Commercial multicrystalline silicon is known to contain metals in concentrations as high as 10^{14} – 10^{16} cm^{-3} (Figure 2.3). These impurities, primarily transition metals, are highly recombination active in silicon, directly decreasing the solar cell efficiency by introducing deep levels in the band gap [49]. Perhaps the most studied transition metal, known to cause a significant decrease in silicon solar cell efficiency, is iron.

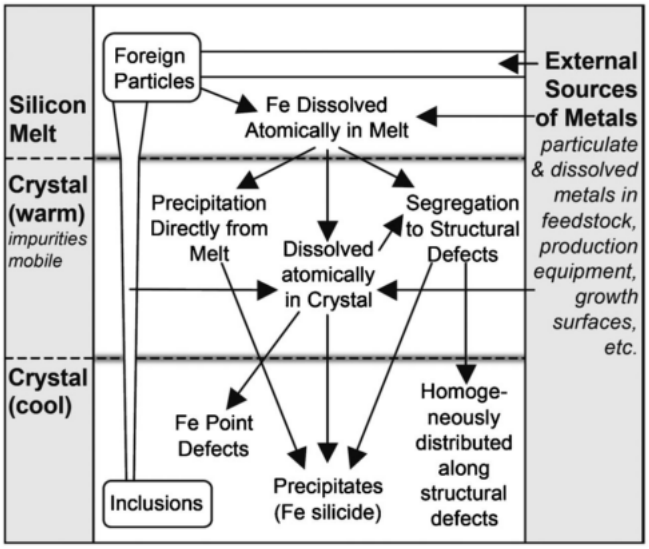


Figure 2.4. Graphical representation of the origins of Fe contamination in multicrystalline silicon. Three stages of production are shown; representing the silicon melt, the hot solidified crystal and the crystal cooled to room temperature [50].

The sources of Fe in multicrystalline silicon are shown graphically in Figure 2.4 with Fe found dissolved in the feedstock and the presence of large, undesirable foreign particles added with the feedstock. Iron and other metals are also introduced through diffusion from the walls of the crucible during solidification [50]. This results in a 'red zone' around the ingot, where the Fe concentration is too high for adequate minority lifetimes [51]. Large Fe concentrations are also observed at the top of the ingot (last to solidify), as a result of reduced Fe solubility under cooling [49]. This causes the segregation of Fe to the top of the ingot. This behaviour is common to most metals, which generally have low solubilities in silicon. In addition, segregation of Fe to structural defects also occurs, since they can provide heterogeneous sites for precipitation [52].

Iron in silicon is present either interstitially (Fe_i) or as precipitates, usually $FeSi_2$. The vast majority of Fe atoms are found in precipitates, with only approximately 1 in 200 Fe atoms occurring interstitially [53]. Per atom, precipitated Fe has a much lower recombination activity than interstitial Fe [50]. In addition, precipitate size also effects the electrical activity, with a low density of large precipitates favoured over a high density of small precipitates [54]. Indeed, 'bad grains' or grains with a low minority carrier diffusion length, have been found to possess a much higher density of precipitation sites for metals [55].

Despite the fact that Fe_i is found in low concentrations, its presence can dramatically decrease the minority carrier lifetime [18]. The concentration of Fe_i can be easily determined via the Zoth and Bergholz method [56], which involves the use of temperature or light to switch between FeB pairs and Fe_i. Since FeB and Fe_i introduce different deep levels in the band gap, they can be measured using deep level transient spectroscopy (DLTS) or more effectively surface photovoltage (SPV) due to the difference in minority carrier diffusion lengths. Additionally, photoconductance decay lifetime measurements can also be used to determine interstitial iron concentrations [57]. Although Fe_i can be extremely detrimental to solar cell efficiency, significant reductions of [Fe_i] can be achieved via phosphorus diffusion gettering (see Section 2.4.2.1) [58].

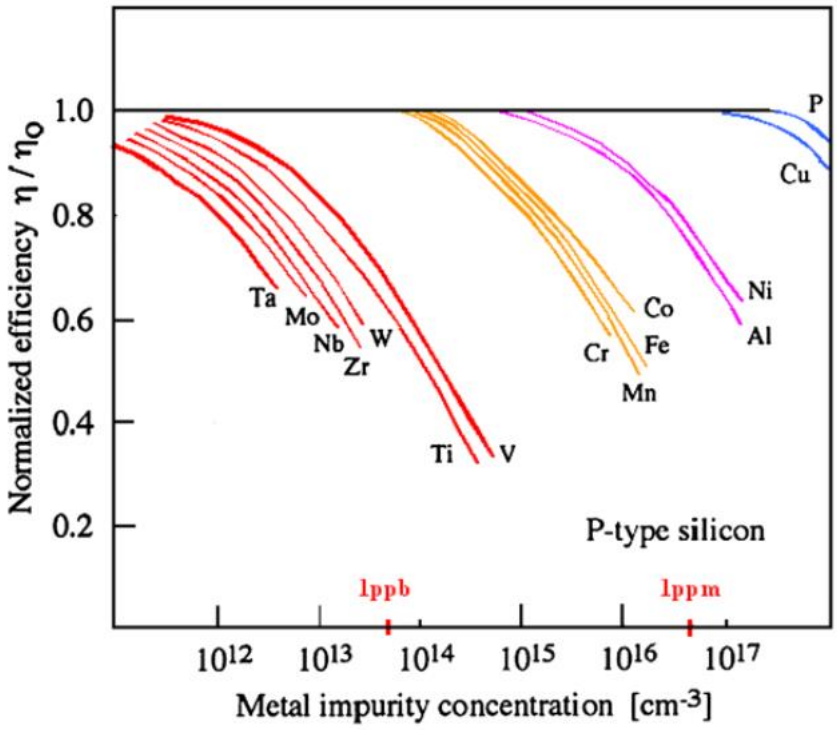


Figure 2.5. The effect of metallic impurity content in p-type single crystal silicon on the normalised solar cell efficiency (data from J.R. Davis, R.H. Hopkins, A. Rohatgi [59]*, cited by Pizzini* [43]*).*

Although Fe in mc-Si is widely studied, partially as a result of the ease of detection, other metals are present (Figure 2.3) and can cause significant reductions in minority carrier lifetime [51]. As shown in Figure 2.5, the efficiency of p-type single crystal silicon may be severely decreased by the presence of impurities at sub-ppm levels. These metallic impurities either reside interstitially (e.g. Cu, Fe, Ni) or substitutionally (e.g. Au, Sb, Ti, Mo), or for higher concentrations found as precipitates. These precipitates are usually silicides, in the form MSi_2, aside from Cu which is found as Cu_3Si [60]. Large nano-precipitate clusters form in metal rich areas, which are found to be regions of high recombination activity [27].

Co-precipitation of different metal silicides has been observed by Rudolf [61], who found a solid solution of Cu_3Si containing Ni and $NiSi_2$ precipitates containing small levels of Cu. The co-precipitation of Fe and Cu has also been postulated by Fenning et al. [62], who argued that the greater levels of precipitation in a Fe+Cu implanted sample, is as a result of a lowered energy for nucleation of Cu under co-precipitation as opposed to the formation of Cu_3Si. The implantation processes used in these studies however, allows for very high levels of impurities to be introduced, which may produce results which are not directly comparable to standard solar grade silicon, an issue which has been raised strongly by Istratov et al. [23].

Although the work published by Davis et al. [59] is still used as a reference in literature, a more recent study of impurities examining state of the art multicrystalline silicon solar cells, has been performed by Coletti et al. [7]. Interestingly, transition metals such as Ti and Cu are found to be much more hazardous to solar cell performance, as a percentage of feedstock impurity concentration, than the widely studied Fe. This is due to the ease of removing and passivating Fe, with only 0.11% electrically active in the final cell. This fact obviously brings in to question the large gap in the literature, surrounding other impurities found in silicon photovoltaic cells. In addition, since interstitial elements can be easily examined by lifetime spectroscopy [18], clusters and small precipitates often found at defects [63] have been comparatively neglected.

2.2 Dislocations

Multicrystalline silicon inherently contains dislocations, formed to compensate local internal stresses during casting. Dislocations are inhomogenously distributed, varying from virtually dislocation free regions up to dislocation densities of approximately 10^6 to 10^8 cm^{-2} [55], [60], [64]. The importance of dislocations in silicon have been known and studied for over 60 years, with work by Dash et al., finding preferential nucleation of copper precipitates along a dislocation in 1956 [65].

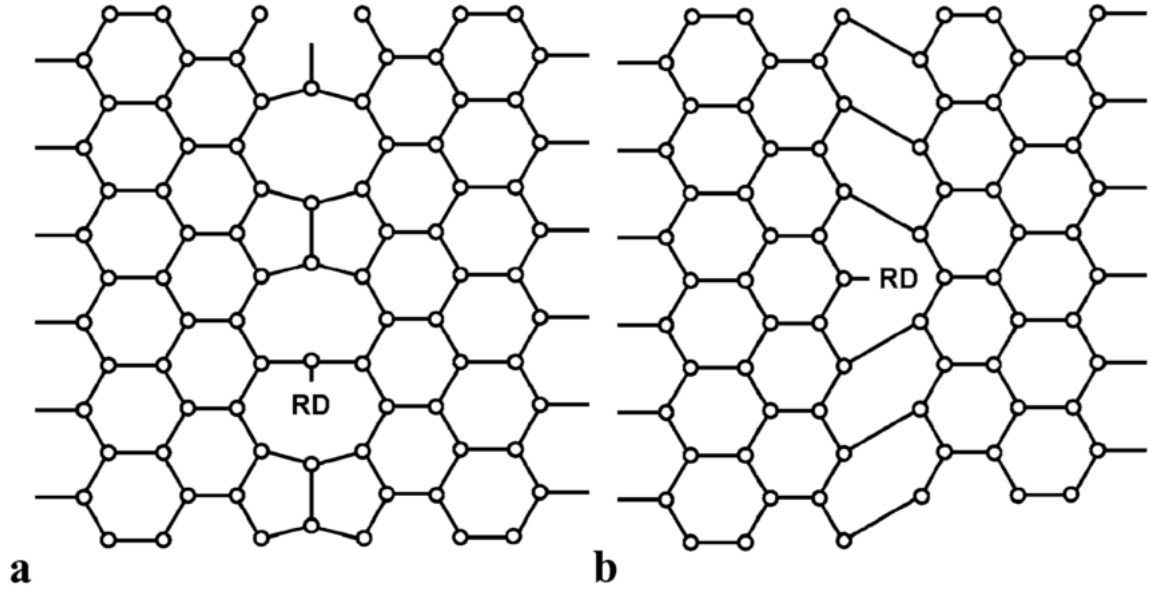


Figure 2.6. Schematic of reconstructed Shockley partials in the (111) glide plane view, where RD is a reconstruction defect which is mobile at high temperatures. (a) 30° partial, (b) 90° partial [60].

The vast majority of dislocations present in silicon are 60° dislocations of the glide set {111}, which dissociate into two partial segments (Shockley partials) 30° and 90° with a stacking fault between them (Figure 2.6), where $\vec{b} = \frac{\vec{a}}{2} < 110 > \rightarrow \frac{a}{6} < 112 > + \frac{a}{6} < 11\bar{2} >$ [66]. Screw dislocations have also been commonly observed in silicon

[67]. Lomer dislocations in mc-Si have been investigated intensively by Bauer [68], defined as edge dislocations lying along [011] and having a (100) slip plane ($\vec{b} = \frac{\vec{a}}{2} < 100 >$). These dislocations are considered immobile since they lie on a non-close packed glide plane.

Numerous authors have reported differences in the recombination activity with different dislocation types. Pasemann et al. found that the EBIC contrast (see Section 2.6) of screw dislocations are an order of magnitude lower than that of dissociated 60° dislocations [69]. It is worth noting however in that study, that only one screw dislocation was measured in comparison to thirteen 60° dislocations, and therefore no definitive conclusions could be drawn. A later study by Wilshaw [70] found that 60° and screw dislocations showed the same EBIC contrast at high minority carrier concentration. However, for low levels of injection and high temperatures, 60° dislocations show a small increase in contrast over screw dislocations.

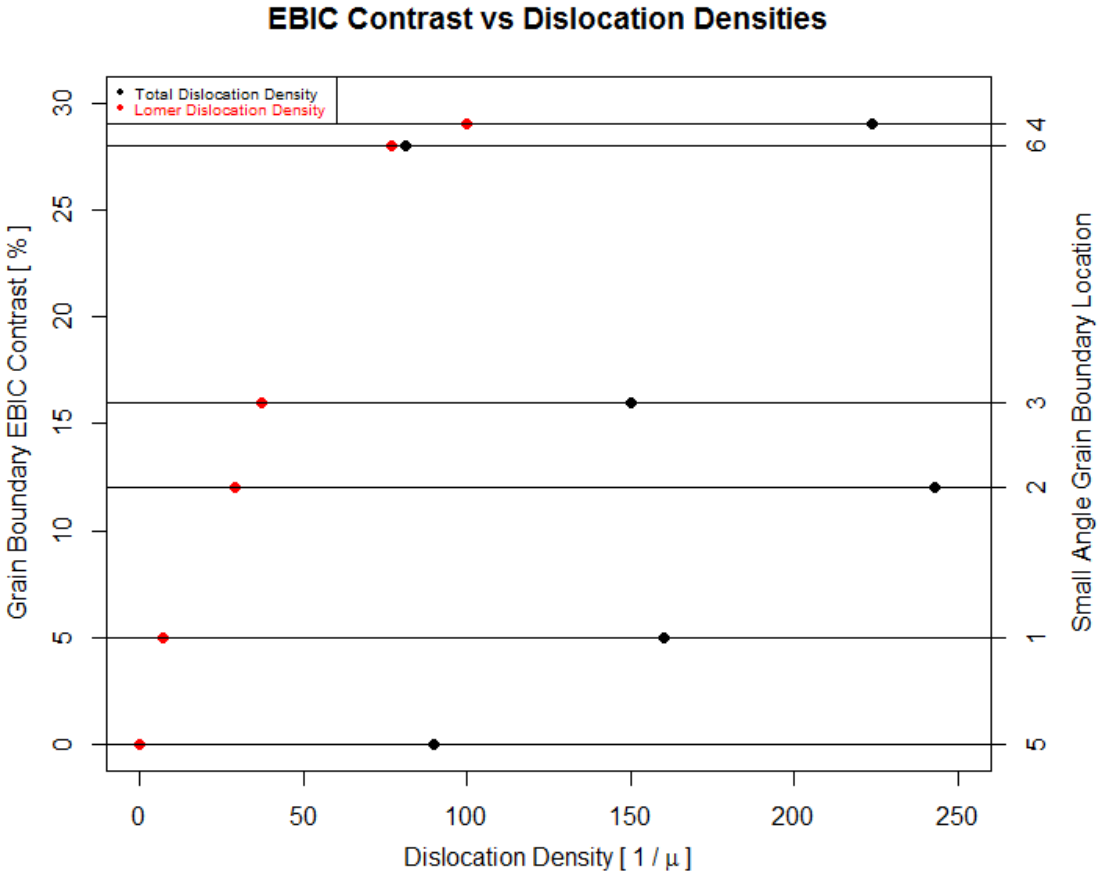


Figure 2.7. Average EBIC contrast at the small angle grain boundaries, with total dislocation density shown in black and only Lomer dislocation density shown in red. The dislocation density was determined by counting the number of dislocations in TEM. Small angle grain boundary position is labelled from 1 to 6. Data from Ref [68].

An extensive study of Lomer dislocations at small angle grain boundaries (SAGB) has been conducted by Bauer et al. [68]. Lomer dislocation density, as measured by TEM, was found to correlate closely with EBIC contrast. This is in contrast to the total dislocation density, which varied dramatically in contrast. SAGB position 2, Figure 2.7, has a relatively low EBIC contrast, but the greatest dislocation density. This led the author to postulate that "only Lomer dislocations contribute to the EBIC contrast

of SAGBs" [68]. It is thought that the immobile nature of Lomer dislocations enable them to act as effective sinks for transition metal impurities, introducing deep levels into the band gap.

Unlike Bauer et al., Seifert et al. found a strong correlation between dislocation density and EBIC contrast [71]. It is worth noting that the dislocation type was not characterised in this study and therefore the density of Lomer dislocations is not known. A large difference in average dislocation density was found for different grain boundary types. High coincidence grain boundaries, Σ3 and Σ9 were found to have much lower dislocation densities than general boundaries and therefore the lowest EBIC contrast.

2.2.1 Dislocations as Recombination Centres

The origin of the electrical activity at dislocations is a highly controversial topic, and has caused much debate in the silicon community [72]. The debate refers to whether recombination is caused by the dislocation structure itself (intrinsic) or impurities segregated to the dislocation core (extrinsic).

The theory indicating that the electrical activity is partially influenced by the dangling bonds and reconstruction defects is presented by Radzimski et al. [73]. The author postulated that 'clean' dislocations might indeed introduce shallow levels in the energy gap, which can be observed in EBIC at low temperatures. Low temperature EBIC contrasts at dislocations, with no recombination activity at room temperature, has also been seen by Kittler [72].

However work by Wilshaw and Fell [74] found that perfectly clean dislocations have no detectable electrical activity, with Si-Si bonds at 30° and 90° partial dislocations able to fully reconstruct, and hence cause no deep levels in the Si band gap [75]. An explanation for EBIC contrasts at low temperatures is given by Kittler and Seifert [76], who found that shallow centres caused by low levels of impurities become prominent recombination centres at low temperatures due to the increase in the Fermi level and subsequent charging of the defect levels (in n-type Si). In addition, lattice stresses caused by mechanically generated dislocations, once thought to produce a small concentration of deep defect states [75], [77] are now believed to be caused by impurities segregating to these regions, during the high temperature deformation process.

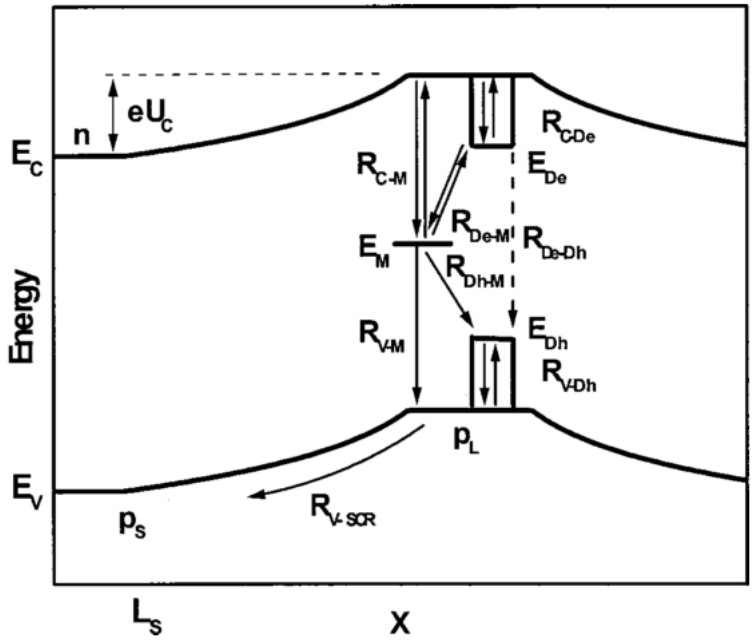


Figure 2.8. Charge carrier recombination at dislocations. For clean dislocations, recombination rate is determined by direct recombination of electrons and holes captured by 1D dislocation bands E_{De}, E_{Dh} (channel $R_{De\text{-}Dh}$). In the presence of impurities, which create deep centres in the band gap at E_M, recombination of captured carriers is governed by transitions $R_{De\text{-}M}$, $R_{Dh\text{-}M}$ via the deep levels at the dislocation core x [77].

The mechanism of recombination at dislocations was derived by Kveder and Kittler [77] expanding on the model developed by Wilshaw [70], as shown in Figure 2.8. Coulomb band bending eU_C is caused by the capture of majority carriers by the dislocation states, acceptor doping in n-type silicon. This electrostatic potential is attractive for minority carriers, increasing the likelihood of attraction and recombination at dislocations. The levels E_{De} and E_{Dh} are one dimensional energy bands, inherent to the dislocation. They are caused by intrinsic stresses or defects, as a result of vacancies and self-interstitials incorporated into the dislocation core. They

may also be caused by impurity atoms at the dislocation core, in the form of narrow clouds (≈1 nm) [60].

Not shown in Figure 2.8, impurities at dislocations actually introduce a narrow range of deep bands at E_M. This is thought to be caused by different transition metal impurities present at the dislocation, having slightly different energy levels in the Si band structure. Fell and Wilshaw [15] determined that the recombination activity at dislocations is affected only by the position of states E_M in the band gap. This is in contrast to the previously held belief that the concentration of defect states affects recombination activity. This statement is valid so long as precipitates do not form at the dislocation. If the energy level is too close to the edge of the band gap extensive recombination cannot occur. Instead carrier trapping ensues, evident by the clear correlation between dislocation density and trap density (Figure 1.8), seen by Macdonald [16].

2.2.2 Impurity Segregation

Dislocations are inherently regions of high strain, and hence form efficient gettering sites for interstitial impurities (usually transition metals) [78]. Transition metal interstitials often have high diffusivities in silicon and can therefore migrate to regions of high strain, where their free energy is reduced [60]. McHugo et al. [79], [80], using correlative light beam induced current (LBIC) and X-ray fluorescence mapping (XRF), found increased levels of Cr, Fe and Ni at regions of low minority carrier recombination. These are thought to be regions of high dislocation density. Light

elements, such as N and O, have also been found to decorate dislocations and have been studied extensively with respect to dislocation locking [81]–[83].

Using transmission electron microscopy (TEM), Ohno et al. [66] studied dislocations formed by applying a compressive stress, in heavily P doped n-type Cz-Si. P atoms were found to have diffused to dislocations, causing an increase in the separation of dissociated partials, as a result of the Patel effect [84]. This effect is caused by the negative charging of the defect by the P atoms, causing Columbic repulsion between dislocations [66].

2.2.3 Precipitation at Dislocations

In addition to the segregation of interstitial impurities, dislocations are thought to be the most efficient sites for metal silicide precipitate nucleation [85]. This is evident by the work of Bailey and Weber [55], who found that an increase in the dislocation density of polycrystalline silicon, is accompanied by a large increase in the iron precipitation rate. An artificially high oxygen concentration seemed to reduce the effectiveness of dislocations as nucleation sites, perhaps due to the homogeneous nucleation of metal oxides [55].

Dislocations or other secondary defects may also be caused by the act of precipitation. Copper precipitates less easily than other metals, due to the large mismatch between the Si lattice and Cu_3Si, requiring large quantities of silicon interstitial emission [86]. This mismatch causes the formation of metastable stacking faults and edge dislocations, in addition to punched out dislocations [60].

An in-depth study on copper and iron precipitation in silicon was performed by Shen et al. [67]. The dislocation type was found to significantly influence the precipitation behaviour, with Cu precipitate colonies preferentially forming on screw dislocations in the slow cooled specimen. This does however contrast with the work of Pasemann et al. who found that screw dislocations were less recombination active than edge dislocations [69]. For the fast cooled specimen, Cu is found to form very small precipitates on both screw dislocations and 60° dislocations, with differing morphologies. In the Fe doped sample, no precipitates were seen, although an increase in the dislocation EBIC contrast was observed [67]. This indicates that interstitial Fe is decorating the dislocations but the local concentration is not high enough to cause precipitation.

2.3 Grain Boundaries

Multicrystalline silicon, by its very definition, contains grain boundaries. A grain boundary can be fully described by 9 degrees of freedom. As described by L. Priester [87], there are 5 macroscopic degrees of freedom which are sufficient to describe the complete thermodynamic nature of the grain boundary:

- *"One for the rotation angle θ between the two crystals*
- *Two for the rotation axis [uvw] defined by its direction cosines*
- *Two for the orientation of the grain boundary plane defined by its normal* ***n****."*

And there are 4 microscopic degrees of freedom:

- *"Three for the translation of one crystal with respect to the other: the rigid body translation vector τ.*

- *One for the vector **d** normal to the grain boundary plane that indicates the position of the plane along its normal."*

Grain boundaries are also defined by the concept of the coincidence site lattice (CSL) value. This is determined by superimposing the two separate lattices on top of each other. For some orientations and specific rotation angles, a significant number of coincidence sites or direct overlap of atoms from each lattice are observed. The grain boundary is characterised by the proportion of the unit cell volumes of the CSL and the primitive unit cell:

$$\Sigma = \frac{Coincidence\ unit\ cell\ volume}{Crystal\ primitive\ unit\ cell\ volume} \qquad (2.1)$$

where the value of Σ is always an odd integer with a Σ1 boundary being a perfect crystal or no boundary at all. An example of two different CSL boundaries is shown in Figure 2.9. Overlapping coincident atoms are shown as unfilled circles.

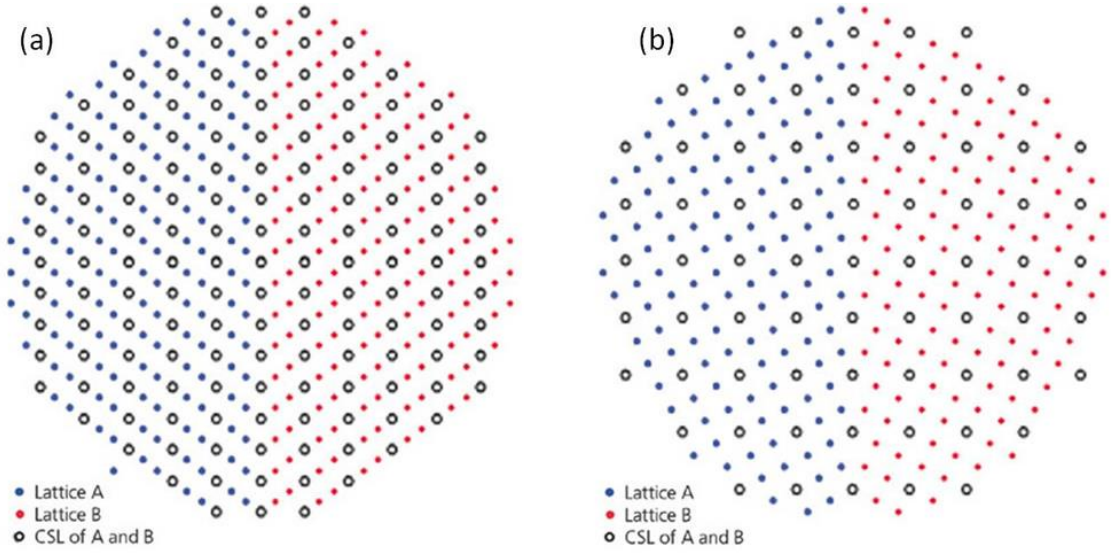


Figure 2.9. a) Σ3 grain boundary (twin boundary) with a 60° misorientation about the [111] direction. b) Σ5 grain boundary with a 36.9° misorientation about the [100] direction. Image courtesy of Oxford Instruments (www.ebsd.com/solving-problems-with-ebsd/grain-size-and-grain-boundary-characterisation-in-sem).

2.3.1 Grain Boundaries as Recombination Centres

As previously discussed in Section 2.1.1, grain boundaries are known centres of recombination due to the segregation of impurities. As shown in Figure 2.2, the type of grain boundary is known to affect the quantity of impurities segregated to the boundary, which ultimately affects the recombination activity. Coherent Σ3 {111} grain boundaries have the lowest EBIC contrast and have been found using APT to possess no measurable segregation of impurities [30]. In contrast random angle grain boundaries and small angle grain boundaries have a large concentration of available sites and hence greater recombination activity even under light levels of contamination.

Consistently, the most deleterious grain boundary type in multicrystalline silicon are small angle grain boundaries [31], [88]. Small angle grain boundaries can be described as a series of dislocations, which compensate for small misorientations between two grains (<15°). Work by Chen and Sekiguchi [31] and Sameshima et al. [89] found that for misorientations >1.5°, the EBIC contrast is significant, especially when exposed to contamination.

The grain boundary type and misorientation also influences their electrical response to solar cell processing, such as phosphorus diffusion gettering (PDG) and hydrogen passivation. Coherent Σ3 {111} grain boundaries remain inactive after PDG and H passivation, due to the low energy of the boundary and lack of sites for impurities to precipitate at [90]. In contrast, numerous authors have reported that random angle grain boundaries, previously inactive in the ungettered state, become recombination

active after PDG [32], [35], [90], [91]. This phenomenon is shown in Figure 2.10, in which random angle grain boundaries all become significantly more electrically active after gettering in a high performance multicrystalline silicon wafer. However, after hydrogen passivation the vast majority of these boundaries become electrically inactive, suggesting that hydrogen is effective at passivating such boundaries.

Unlike random angle grain boundaries, Figure 2.10 shows a number of grain boundaries that do not respond to hydrogen passivation. These boundaries are predominantly higher order CSL (e.g. Σ9 and Σ27) grain boundaries. Such CSL grain boundaries are of high energy and have been found to contain a number of facets [92] in silicon, which has been correlated to dislocation formation [93]. However, it is still unknown why these grain boundaries remain unaffected by hydrogen; an issue that could be addressed directly using APT (see Chapter 6).

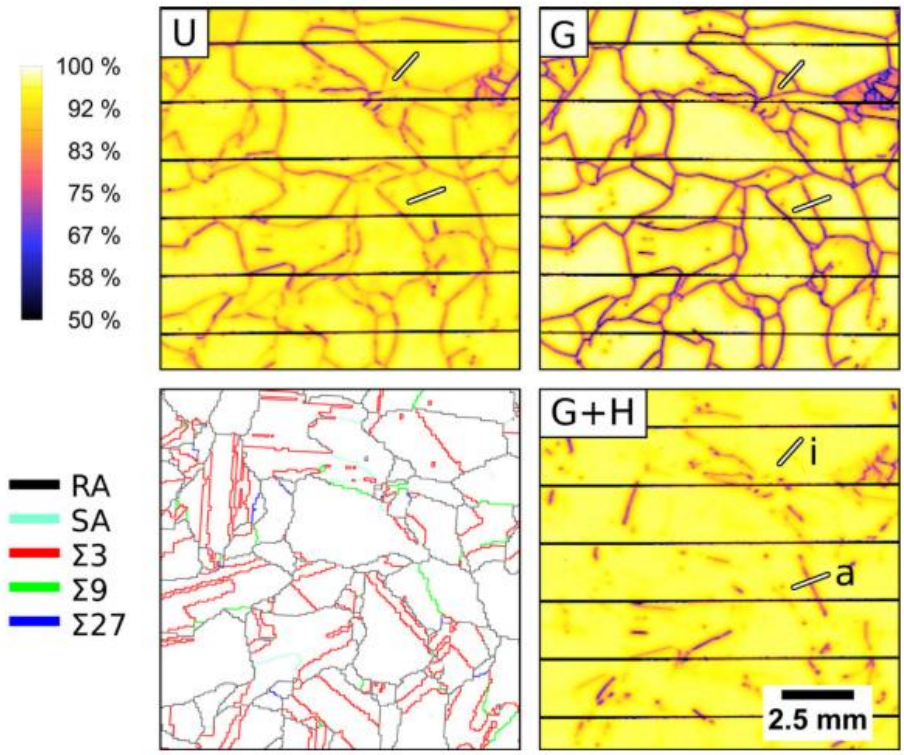


Figure 2.10. Internal quantum efficiency (laser beam induced current contrast) maps of high performance multicrystalline silicon after different processing steps. U) ungettered, G) Phosphorus diffusion gettered, G+H) Phosphorus diffusion gettered plus hydrogen passivation. The bottom left image shows an EBSD map of the region, where the grain boundary types are marked [91].

2.4 Gettering

In Section 2.1.2, a description of the strongly negative effects of impurities in mc-Si is given. To reduce the harmful effects of such impurities, industry uses a process called gettering. This involves the removal of metallic and other impurities from the active region of the device, by the formation of preferential sites either in the bulk (internal gettering) or at the wafer surface (external gettering). At elevated temperatures, impurities diffuse to these regions, where their electrical activity with

respect to solar cell performance is minimised. Gettering can be well characterised as a three step process of release, transport and capture [94]. Each of these stages can limit the efficiency of the gettering process.

2.4.1 Internal Gettering

Internal gettering utilises defects present in the material, as efficient gettering sites. These defects include grain boundaries, dislocations and oxide precipitates [95]. Krain et al. [96] successfully gettered mc-Si by annealing at relatively low temperatures, achieving a reduction in interstitial iron concentration of over an order of magnitude (Figure 2.11). This was accompanied by an increase in bulk photoluminescence lifetime, with Fe thought to be residing at grain boundaries and dislocations. This study did not investigate however, whether Fe was present as precipitates or interstitially. Additionally, this study did not use sister wafers and contrasts with the work of Al-Amin and Murphy [97] who in some samples initially observed an increase in $[Fe_i]$ under annealing, and did not measure the exponential decay of interstitial Fe as seen in Figure 2.11. Internal gettering by grain boundaries is seen significantly in HPMC-Si, due to the large concentration of random angle grain boundaries. These grain boundaries become recombination active after gettering due to the high quantity of favourable heterogeneous nucleation sites for impurities [32], [33].

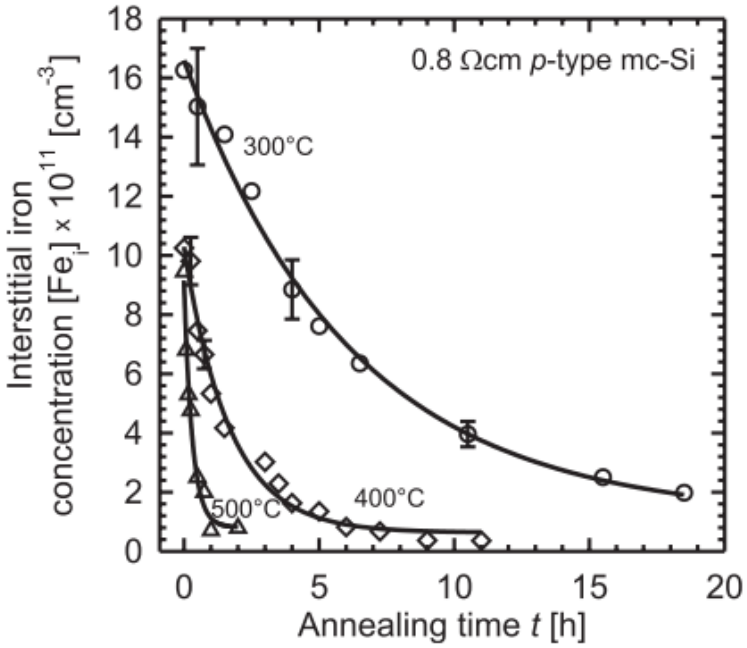


Figure 2.11. Evolution of the interstitial iron concentration at annealing temperatures of 300, 400 and 500 °C. The Zoth and Bergholz method was utilised to calculate the interstitial iron concentration. Exponential decay curves are shown for each temperature profile [96].

The use of internal gettering results in the formation of denuded zones around the defect sites, which are much cleaner and have greater lifetimes [98]. These denuded zones are also seen in the vicinity of Fe precipitates, which have been seen as potential internal gettering sites [99]. Under annealing, larger precipitates grow due to Ostwald ripening, confining the Fe to a small number of large precipitates. Although this technique may be accompanied with an increase in lifetime, silicon solar cells are whole-wafer devices, and therefore external gettering is preferred.

2.4.2 External Gettering

External gettering involves the creation of an impurity sink at the surface of the wafer, often achieved by the formation of a heavily doped surface layer. The most common examples of this process are phosphorus diffusion gettering (PGD), aluminium gettering (AG), and boron diffusion gettering (BDG). For information on the gettering techniques used in this thesis see Section 3.4. External gettering is divided into two types with separate mechanisms: relaxation and segregation. Relaxation gettering involves the formation of surface heterogeneous precipitation sites, which metals diffuse to when they become supersaturated. In contrast, segregation gettering comprises of a highly doped surface layer with a higher metal solubility to which impurities segregate under cooling [52].

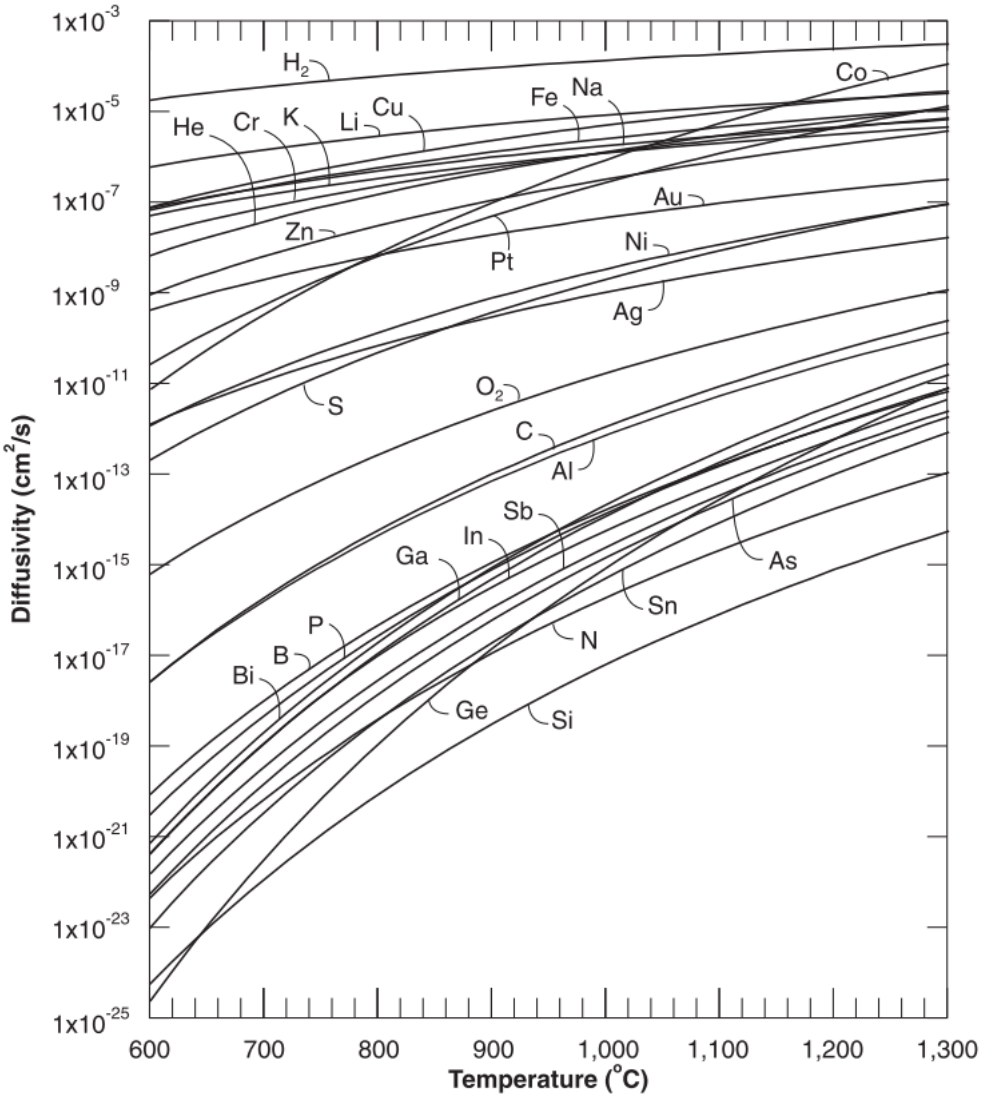


Figure 2.12. Diffusivities of selected impurities in single crystal silicon versus temperature [100].

All gettering processes rely on adequate diffusivity of impurity elements, necessary for the transport stage of the process. It is therefore common to use high temperatures to ensure the impurity diffusivity is large enough to prevent limitations in the gettering efficiency. Substitutional diffusers are found to have the lowest diffusivities (Figure 2.12), making elements such as As, Sb, Sn and Zn very hard to getter [101]. Lotfi and

Hatem [102] observed diffusion limited gettering below an optimum temperature of 900 °C, where the gettering time was not sufficient for efficient gettering.

2.4.2.1 Phosphorus Diffusion Gettering (PDG)

Phosphorus diffusion gettering (PDG) is the primary gettering technique used in commercial multicrystalline silicon production. In the bulk p-type silicon solar cell production process, PDG is a vital procedure required to form a phosphorus doped n-type emitter at the surface [103]. PDG can be performed by applying a phosphorus rich coating, either from a liquid deposition or gaseous exposure to $POCl_3$, and applying heat for a fixed duration to allow the diffusion of phosphorus into the surface [102].

The process of PDG has two rate limiting steps. If the process is performed above an optimum temperature the rate is governed by the segregation model [104], in which impurities segregate to the phosphorus rich surface layer with an enhanced solid solubility [105]. Below the optimum temperature, gettering is limited to the dissolution and diffusion of metal precipitates and impurities to the surface [78], [106]. The increased solubility of the phosphorus region has been ascribed to the formation of phosphorus-transition metal pairs [104], [105].

It has also been claimed that the change in Fermi energy in the highly P doped region also increases the solid solubility for transition metal impurities [23]. This claim has been widely criticised, with Kang et al. [78] finding a decrease in the minority carrier lifetime with As diffusion, which would provide the same increase in Fermi level. In

addition, the Fermi level shift in P diffusion is likely to increase the solubility of negatively charged ions, not the positively charged transition metal ions [105].

PDG has repeatedly been shown to have an increased effectiveness due to the large emission of silicon self-interstitials during the gettering process [107]. These self-interstitials cause the dissolution of metal precipitates, by reducing the critical radius for shrinkage [108]. Self-interstitials are also responsible for the 'kick out' of substitutional elements, generating interstitials. This causes a vast improvement in their diffusivities, as seen in the gettering of Au using corona discharge by Falster et al. [109]. However, this is contradicted by the work of Pietila and Masson [110] who, in an attempt to internally getter Au, produced a number of defects (e.g. oxide particles) which are known to produce a large amount of Si_i. In this study, Au was not gettered, with a homogenous distribution of Au precipitates found, indicating that oxide particles are not sufficient precipitation sites. This finding was used by Kang et al. [78] to conclude that 'silicon interstitials do not contribute to gettering or contribute only minimally' in silicon.

Unfortunately, PDG is not always completely effective and the reasons for this are not broadly understood. This is most evident in the work performed by Bentzen et al. [64], who found that regions with high dislocation densities did not improve after gettering. This phenomenon has also been seen by a number of other authors [17], [62], [111] and has been ascribed to defect pinning. No attempt to characterise the individual impurities in these regions has been made, although it has been postulated that the incomplete dissolution of Fe precipitates in these regions may be a limiting factor

[111]. Alternatively, the dissolution of the metallic precipitates may occur, with PDG limited by competitive gettering of impurities to dislocations and grain boundaries [91]. Indeed, Al-Amin and Murphy [97] show that a low temperature anneal following PDG is effective at improving material lifetime due to internal gettering by defects.

As previously stated, a major limiting factor to the efficiency of PDG is the dissolution and subsequent diffusion of metal precipitates. The obvious way to increase the dissolution rate of precipitates is to raise the temperature of diffusion. When applied, this method has given mixed results. Peters et al. [112] and MacDonald et al. [113] both encountered reductions in minority carrier lifetimes when the temperature exceeded 860 °C and 900 °C respectively. The source of the thermal degradation was examined by Macdonald et al. [113], who found an increase in the dislocation density after processing.

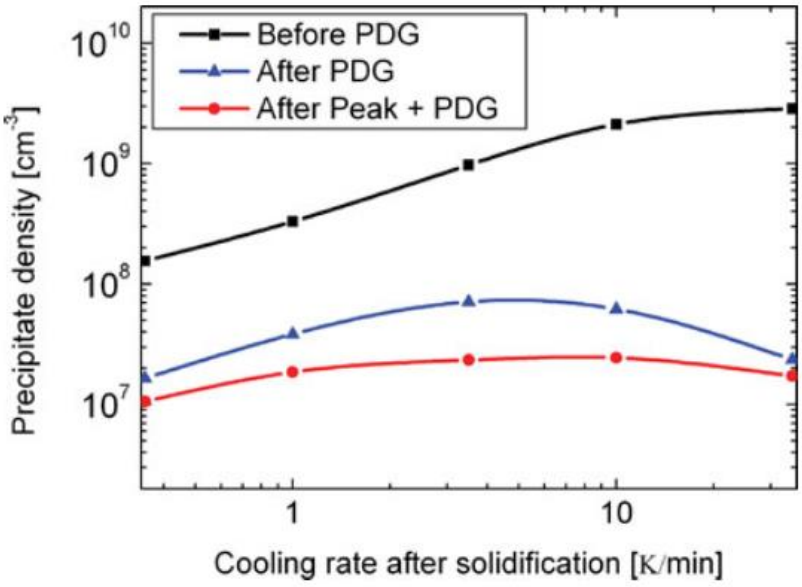


Figure 2.13. Overall density of Fe precipitates before and after phosphorus diffusion gettering at 900 °C, with or without a preceding temperature peak at 950 °C for 5 minutes [54].

To overcome the problem of high temperature degradation, Plekhanov et al. [114] proposed the use of a multi-step, variable temperature profile. This process would allow for a large reduction in the gettering time, while still preventing thermal degradation and inadequate segregation of impurities at the higher temperatures. Schön et al. [54], as shown in Figure 2.13, successfully applied the variable temperature approach, finding a significant decrease in Fe precipitate density following a 5 minute high temperature exposure.

Similar success using a N_2 pre-anneal was found by Fenning et al. [62], who found that the annealing step caused a homogenisation of the lifetime across the specimen. Although higher temperatures gave the greatest reduction in Fe precipitate size, the pre-anneal step prevented the need for further defect processing caused by the large concentration of Fe_i in the bulk at high temperatures.

More recently, industry has moved towards producing lightly doped emitters, with lower phosphorus dopant concentrations. This shift is used to increase the efficiency of the solar cells, by reducing the concentration of crystalline defects in the emitter region, minimising SRH recombination [115]. In addition, a lightly doped emitter can be more easily passivated, resulting in a reduced surface recombination velocity [116]. However, the use of a light phosphorus diffusion reduces the efficiency of the gettering process, leading to lower bulk lifetimes [117]. It is therefore imperative that the reasons behind incomplete gettering are investigated further.

2.4.2.2 Aluminium Gettering

Aluminium gettering (AlG) is an essential component in the manufacture of multicrystalline silicon solar cells, used to form a back surface field. The aluminium diffused p^+ region injects a high density of holes, forming a barrier to the movement of electrons to the back contact, causing an increase in the open-circuit voltage [118]. Fortunately, AlG also has the capability to getter impurities, allowing for significant increases in the minority carrier lifetimes, with efficiencies exceeding 20% [119].

Aluminium diffusion is performed by the annealing of an evaporated or liquid deposited Al surface layer at an elevated temperature [120]. Similar to PDG, the aluminium gettering mechanism is the segregation of impurities to the Al-Si layer [23]. The efficacy of AlG has also been related to the introduction of pitting/damage to the back surface, which increase the bulk diffusion length and provide efficient sinks for impurities [121].

AlG faces the similar limitations as PDG, in relation to diffusion-limited gettering [94]. Thompson et al. [122] managed to successfully getter a very large quantity of Cu through a silicon wafer, but detected no gettering of the slower diffusing elements Ag and Au to the Al layer. In addition, impurities present in the aluminium coating have been identified as potentially harmful to the silicon bulk. In a theoretical model created by Schubert et al. [123], the interstitial Fe concentration was predicted to increase after AlG at 900 °C due to the in-diffusion of contaminants from the Al layer. This model does however conflict with the 99.9% efficiency of [Fe_i] removal seen by Phang et al.

[94] at 650 °C. This indicates that the purity of the Al rich deposited layer is of great importance to the efficacy of the AlG process.

Commercially, the application of AlG is limited by the architectures used in multicrystalline silicon solar cells. With the shift from Al-BSF solar cells, which has the potential for gettering, PERC solar cells only have localised Al regions [124]. Additionally, the thermal budget of the firing process in these cells is much less than required for AlG [125] and there are concerns that extending this process may introduce contamination, as predicted by Schubert et al. [123].

2.4.2.3 Boron Diffusion Gettering

With the recent drive towards n-type HPMC-Si solar cells (examined in Chapter 7), the use of boron diffusion gettering (BDG) in solar cell processing has become the subject of substantial research [126]. In n-type silicon, boron diffusions are performed to produce the p-type emitter on the surface of the solar cell, required for operation. Boron diffusions are usually performed at high temperatures of approximately 900 °C, via gaseous exposure in a BBr_3 ambient followed by a drive in step under a N_2 environment [127]. Boron rich layers have also been formed by ion implantation at energies of 20 or 30 KeV, followed by a high temperature anneal at temperatures between 800 and 1000 °C [128].

Similar to PDG and AlG, BDG has been found to be effective at gettering impurities from the bulk. A direct comparison of these processes was conducted by Phang et al. [94], who found that the effectiveness of the gettering via BDG was much more

sensitive to the deposition conditions than PDG and AlG. Indeed, BDG was found to be completely ineffective at gettering at temperatures above 850 °C because of the reduced driving force for impurity segregation at these temperatures. Furthermore, work by Haarahiltunen et al. [129], predicted highly effective gettering of Fe by BDG, at an optimal temperature of 500 °C, achieved via a low temperature anneal. The efficacy of BDG is primarily limited by the low solubility of impurities, such as Fe, in the boron rich region. Therefore, in order to compensate for the reduced effectiveness of BDG, co-gettering of BDG and PDG has been used and shown to be extremely successful at reducing Fe concentrations, with the out-diffusion of impurities to both surfaces [130].

2.5 Hydrogen Passivation

2.5.1 Principles and Mechanism

Hydrogen passivation is an essential tool for reducing the recombination activity of defects in multicrystalline silicon. Unlike gettering, where impurities are diffused away to a suitable area, hydrogen passivation uses monoatomic hydrogen to passivate individual defects present in the wafer. Hydrogen passivation was first performed by Seager and Ginley [131], who found a significant increase in the solar cell performance after the application of a DC hydrogen plasma.

Although hydrogen passivation is a widely used industrial technique, the precise mechanism of passivation is not fully understood [132]. The main principle however, is the elimination of deep centres in the band gap [133], which are vital for SRH recombination (see Section 1.3.3). The reduction in the density of deep centres has

been linked to the annihilation of dangling bonds [134] and the formation of covalent bonds in H complexes [132].

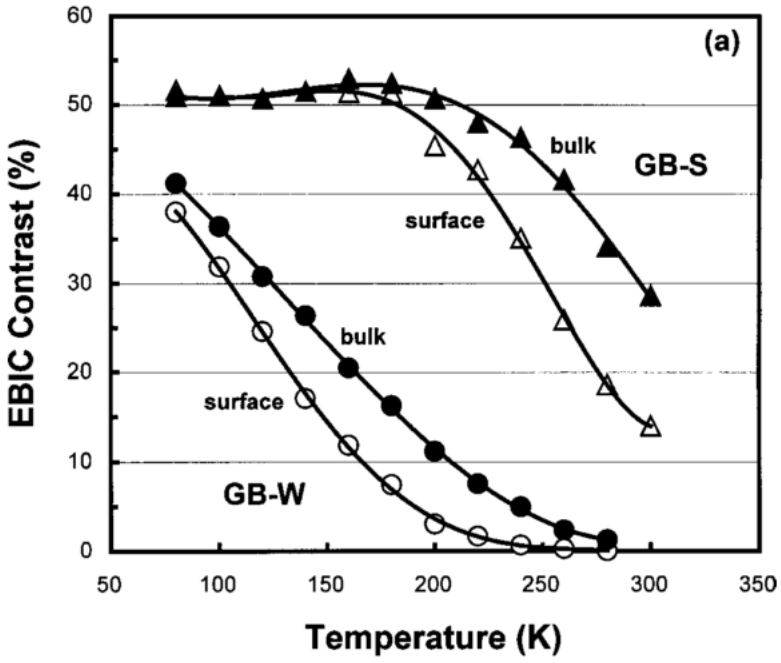


Figure 2.14. Temperature dependence of EBIC contrast for strongly recombining (GB-S) and weakly recombining (GB-W) grain boundaries. The bulk measurement is taken 150 µm from the surface (outside the hydrogen passivated region) and the surface measurement is taken 20 µm from the surface where the hydrogen is applied [135].

Hydrogen is much less effective at passivating shallow centres in the band gap. Using low temperature EBIC, Vyvenko et al. [135] found a large increase in the EBIC contrast at lower temperatures (Figure 2.14). This was significant for the highly inactive grain boundary, with no detectable EBIC contrast at room temperature. This indicates that a substantial proportion of shallow centres are still present after the hydrogen passivation process.

Hydrogen passivation has been cleverly implemented into solar cell production, during the plasma enhanced chemical vapour deposition (PECVD) of SiN_x, which is used as a surface antireflection coating [37]. A plasma of SiH_4 and NH_3, allows for a ready source of hydrogen, with the process typically performed at 400 °C [136]. Finally, the front contact is fired at approximately 850 °C, which allows the hydrogen to diffuse into the bulk of the silicon (See Section 3.4).

Other methods, such as using molecular H_2 gas, have been investigated as potential hydrogenation routes [137]. However, this method was deemed inefficient without the presence of surface damage and elevated temperatures, which are required to enable adequate hydrogen diffusion. More recently, in work by Saha et al. [138], large increases in lifetime have been achieved by the use of H_2S gas at 550 °C, in which sulphur assists with the passivation of defects.

2.5.2 Hydrogen Passivation of Crystallographic Defects

Hydrogen passivation of crystallographic defects is of great importance to achieving high efficiency multicrystalline solar cells and has been widely studied in the literature. For hydrogen to passivate dislocation and grain boundaries, it must first diffuse to the defect region and then interact with the impurities or precipitates found at the crystallographic defect.

The diffusion of hydrogen in the presence of dislocations is still a subject of discussion. Dislocations are known to trap hydrogen, as required for H passivation to occur. There are reports of this trapping effect by dislocations resulting in incomplete diffusion of

hydrogen through the bulk [132]. However, many authors have reported an increased diffusivity of hydrogen at highly dislocated regions [111], [139], with Dubé and Hanoka [140] finding H diffusion lengths five times greater through heavily dislocated regions compared to the bulk. Similar confusion regarding hydrogen diffusion in the presence of grain boundaries exists, with Jackson et al. [141] noting that H diffusion in polycrystalline silicon is significantly supressed compared to single crystal silicon. In contrast, Johnson et al. [142] using ^{2}H and secondary ion mass spectroscopy (SIMS) profiling, showed greatly enhanced diffusion along grain boundaries. To summarise, providing hydrogen does not become trapped or bound to impurities decorating dislocations and grain boundaries, its diffusion increases along these crystallographic defects.

Hydrogen passivation has been seen to successfully passivate dislocations and grain boundaries, with the transformation of deep levels into shallow levels [91], [143]. This results in a large decrease in the defect recombination activity at room temperature. Hydrogen is also known to increase the mobility of crystallographic defects, such as dislocations [144], although at the temperatures required for dislocation annihilation all of the hydrogen will have diffused from the silicon [47].

Hydrogen passivation effectiveness can however, be severely limited in the presence of highly dislocated regions [64]. The presence of dislocations at grain boundaries was correlated to the reduced effectiveness of hydrogen passivation, indicating the difficulty of passivating dislocations [145]. The passivation of impurities at

dislocations and grain boundaries are also limited by the formation of hydrides, e.g. Fe-H, which introduce deep levels in the band gap [134].

2.6 Electron Beam Induced Current

Electron beam induced current (EBIC) mapping is a technique, which is implemented into a scanning electron microscope, and allows for the high resolution spatial mapping of recombination activity. For a detailed description of this technique and how it is used in this thesis, please see Section 3.6.

2.6.1 EBIC of Crystallographic Defects

In regards to EBIC of crystallographic defects, investigations of multicrystalline silicon have largely focused on grain boundaries, examining the difference in recombination activity with contamination level, grain boundary type, and misorientation [88], [146]. Indeed, Palm [147] successfully managed to use a grain boundary as a collecting junction between two Ohmic contacts. As previously discussed (Section 2.3.1), small angle grain boundaries are usually considered the most deleterious grain boundaries in multicrystalline silicon (Figure 2.2). These can be described as a series of dislocations, which compensate for the misorientation.

Historically, significant work investigating the origin of EBIC contrast at dislocations was performed by Wilshaw and Booker [70], [148] and Kittler et al. [72]. Dislocations are classed, with respect to EBIC current, as either type-1 (deep levels with charged defects) or type-2 (shallow centres).

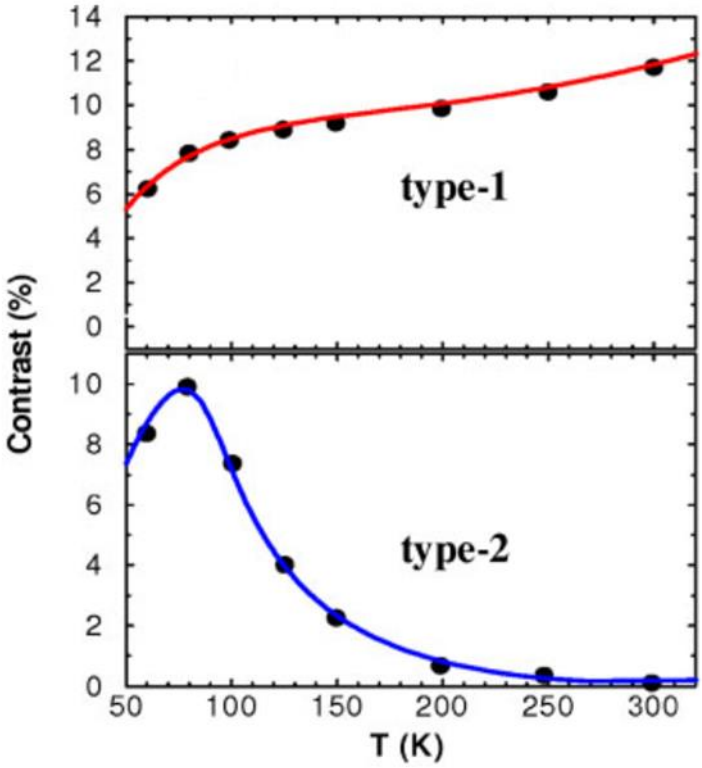


Figure 2.15. Temperature behaviour of EBIC contrast of dislocations in FZ-Si, before (type-1) and after (type-2) phosphorous diffusion gettering [149].

The two types of dislocations with relation to temperature are shown in Figure 2.15. A small increase in the impurity concentration from 1 ppb to 15 ppb of Cu can change the behaviour of the dislocation from type-1 to type-2 [150]. The sudden increase in the contrast of type-2 dislocations under cooling is caused by the increase of the Fermi level (n-type silicon), which enables the charging of the shallow levels, increasing the rate of SRH recombination. In contrast, the decrease in EBIC contrast with decreasing temperature for type-1 dislocations is thought to be due to kinetics. At lower temperatures, the diffusion rate for minority carriers is lower, and in order for SRH recombination to occur both charge carriers much be present [77].

When directly comparing quantitative EBIC contrasts, there are a number of caveats that must be stated. The EBIC contrast of a dislocation or grain boundary in silicon is dependent on a number of factors; the electron beam depth penetrated R_p, depth of the defect d, the diffusion length of minority charge carriers L and the recombination strength γ [151]. The EBIC contrast, can be written approximately as $C \propto \gamma^n$, where $n < 1$ and is dependent on depth (using data from Pasemann et al. [152]) [70]. The depth dependence of EBIC contrast has been successfully used by Phua and Ong [153] to estimate the depth of individual defects, using a range of accelerating voltages (assuming zero surface recombination velocity).

2.7 Atom Probe Tomography

Atom probe tomography (APT) is an extremely powerful technique, which allows for the three-dimensional characterisation of individual 'atoms', providing both chemical and spatial information of a needle shaped specimen. A detailed discussion of the technique is given in Section 3.12.

2.7.1 Atom Probe Tomography of Silicon

In relation to APT of silicon for solar applications, there have been calls in the literature for an atom probe study of the local chemistry of individual defects [40], [68]. Atom probe, with its unique combination of high chemical and 3D spatial resolution, may be able to provide direct evidence of the presence of impurities at defects of varying recombination activity.

APT of Fe doped PV polycrystalline silicon has been successfully applied by Gorman et al. [154]. Gettering of oxygen by Fe was suggested, due to the presence of FeO found in nanometre-sized clusters. In addition, the clusters were found to lie along a 2D plane, indicating that the precipitates are lying along a grain boundary. Unfortunately, the TEM performed prior to APT was inconclusive at determining the structural defects present.

Correlative TEM and APT was successfully performed by Ohno et al. [30], investigating the gettering ability of Σ3 {111} grain boundaries in Czochralski grown silicon. Although TEM confirmed the presence of a grain boundary in the specimen tip, impurities (oxygen and carbon) were homogeneously distributed through the specimen. Although this can be ascribed to the weak gettering ability of Σ3 grain boundaries, with the difficulty of detecting small levels of impurities in atom probe significant.

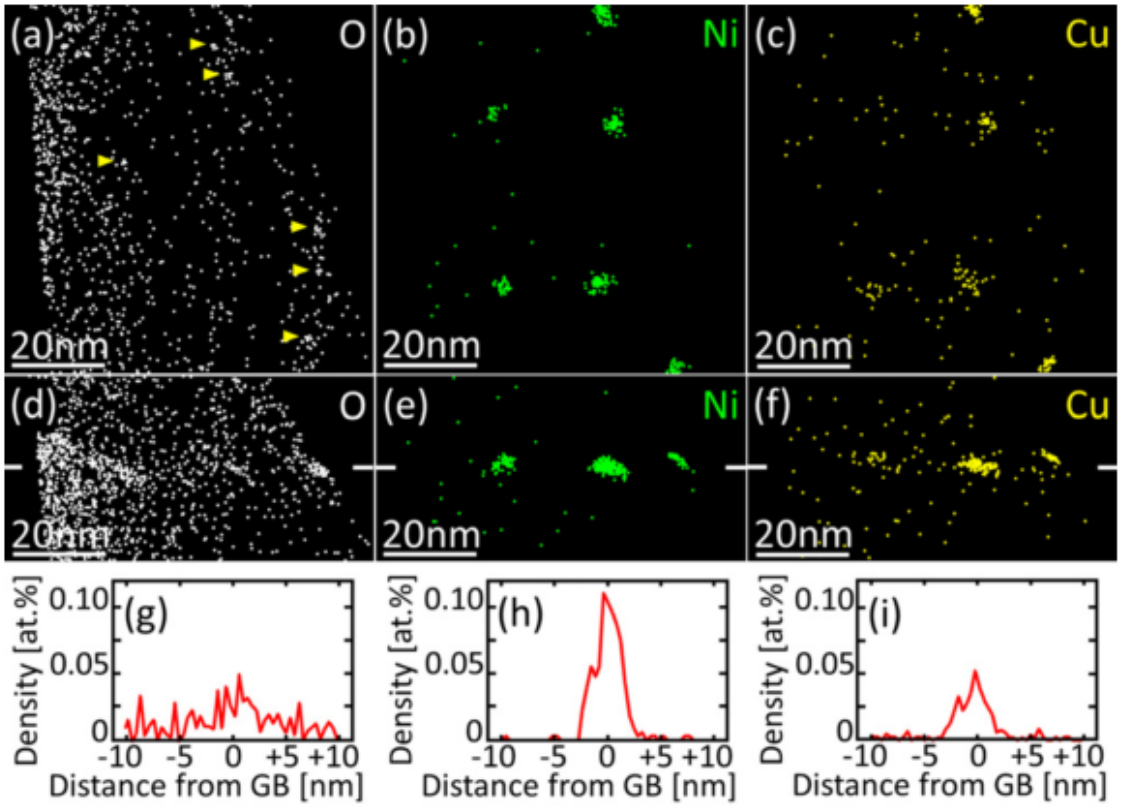


Figure 2.16. Atom probe analysis of a grain boundary with a photoluminescence contrast of 33%. (a), (b) and (c) show the distribution of oxygen, nickel and copper normal to the GB plane. (d), (e) and (f) are viewed along the GB dislocations, with the solid lines indicating the GB location. APT density profiles of oxygen, nickel and copper across the grain boundary are shown in (g), (h) and (i) [155].

Further grain boundary analysis in quasi-single crystalline silicon by Ohno et al. [155] observed nickel and copper silicide precipitates at dislocations along a grain boundary, as seen in Figure 2.16. In addition, smaller single nanometre size oxide clusters were seen along the grain boundary. The impurity concentration was correlated to the recombination activity, as measured by photoluminescence. At more recombination active grain boundaries, much greater concentrations of Ni and Cu clusters were found, whereas the concentration of SiO decreased with increasing recombination. This

indicates that the presence of Ni and Cu clusters are significantly more hazardous to the electrical properties of such defects than oxide precipitates.

Ohno et al. also observed oxygen segregation around dislocations at grain boundaries [156]. Oxygen is found interstitially in silicon and induces a significant compressive stress in the lattice. Using *ab-initio* calculations, Ohno et al. predicted that oxygen atoms agglomerate within the tensile region around a dislocation, under tensile stresses above 2 GPa. Although this study examined dislocations at a grain boundary, it is assumed that oxygen segregation should occur for isolated dislocations, providing the tensile stresses are great enough. The only individual isolated dislocation observed in Si by APT, was observed by Lotharukpong et al. [157] who found decoration by C and Ni.

A detailed study investigating local chemistry at defects in multicrystalline silicon has been performed by Stoffers et al. [158]. Highly recombining grain boundaries in intentionally Fe and Cu doped mc-Si were found to contain measurable amounts of Cu and C, which were not seen in grain boundaries with low recombination activity. No Fe was detected in the sample, which may be partially ascribed to the lower concentration of Fe compared to Cu and the peak overlap between $^{56}Fe^{2+}$ and $^{28}Si^{+}$ (Section 5.6.1)

More recently, Stoffers et al. utilised correlative electron backscatter diffraction (EBSD), EBIC, high resolution scanning TEM (HRSTEM) and APT to fully characterise grain boundaries in mc-Si [159]. Strongly recombining grain boundaries,

contained elevated levels of FeN^{2+}, in addition to greater levels of carbon and copper. Although no individual Fe ions were found, it is thought that overlap between Fe and Si limits the detection and therefore the quantities of FeN^{2+} are regarded as minimum concentrations.

2.8 Concluding Remarks

During the course of this review, the importance of crystallographic defects in multicrystalline silicon has been outlined. SRH recombination, a major limit to solar cell efficiency, occurs due to the segregation of transition metal impurities to these defect regions. It is therefore important to gain an understanding of the characteristics of recombination active crystallographic defects.

In an attempt to improve the efficiency of multicrystalline silicon, both hydrogen passivation and gettering are used. These techniques however, are not completely effective, especially in regions of high defect density. The precise reason for this is not known, with further investigation required.

Electron beam induced current is a widely used technique in the semiconductor industry. It allows for the recombination strength, given as EBIC contrast, of individual dislocations and grain boundaries to be measured. EBIC contrast however does not provide any information of the structure or chemistry of the defects and requires the use of further complementary techniques.

Atom probe tomography has become an increasingly relevant technique in recent times, especially with the large advances in laser technology. APT allows for an atom-by-atom characterisation of a sample, with 3D sub-nm resolution.

Correlative EBIC/TEM/APT should allow for a complete investigation of the recombination activity, crystal structure and chemistry of dislocations and grain boundaries. This approach should also allow for a greater understanding of what limits the effectiveness of hydrogen passivation and gettering.

3 Experimental Techniques and Methods

3.1 Introduction

This chapter describes the various materials, processing techniques and analytical methods employed to characterise crystallographic defects in this thesis.

3.2 Experimental Procedure

During the course of this project, a multi-stage characterisation procedure has been developed, entailing numerous processing stages and a variety of analytical techniques. Since a number of different materials were analysed, not all processing steps were applied on every occasion. Additionally in some cases, prior characterisation, using photoluminescence (PL and micro PL), was performed by external collaborators. In general, processing and analysis techniques were applied in the following order:

1. Saw damage removal and wafer polishing
2. Chemical polishing (HNA)
3. Preferential etching (Secco)
4. RCA cleaning
5. EBIC specimen preparation
6. EBIC imaging
7. Al contact removal
8. EBSD imaging
9. Selection of defect of interest
10. APT specimen preparation

11. TEM/TKD imaging of APT specimen
12. APT analysis of the APT specimen

3.3 Materials

The predominant material investigated in this thesis was p-type high performance multicrystalline silicon (HPMC-Si) of resistivity 1.3 Ωcm. This material was sourced from an industrial manufacturer and is of high relevance to the solar community due its wide-scale adoption as the industry's material of choice [160]. In order to investigate the effect of processing, sister wafers were used. These are wafers that are vertically adjacent in the ingot and therefore have a similar crystallographic defect distribution. The sectioning of the ingot into wafers was performed via diamond wire sawing, as described in [161].

In Chapter 7, two alternative solar cell materials have been analysed, red zone and high performance n-type silicon. The red zone material consisted of sister wafers taken from the bottom of a high performance p-type multicrystalline silicon ingot. The p-type wafers have a resistivity of 0.3 Ωcm and a corresponding boron doping concentration of 6 x 10^{16} cm^{-3}. The n-type high performance multicrystalline silicon was produced by Fraunhofer ISE, with a resistivity of 0.5-1.3 Ωcm and a corresponding P doping concentration of (7-8) x 10^{15} cm^{-3}.

All of the wafers examined in this study were received as-sawn, and sectioned from 15 cm x 15 cm wafers into 2 cm x 2 cm wafers by a laser scribe. The thickness of the wafers varied from 150 μm to 250 μm.

3.4 Processing Techniques

In this study, the effects of various processing techniques on the properties of crystallographic defects in solar cell materials were analysed. The two key industrial techniques studied were phosphorus diffusion gettering and hydrogen passivation. Hydrogen passivation was performed using two alternate methods, namely via the firing of surface nitrides, and via remote plasma hydrogenation. Additionally, in the case of n-type high performance multicrystalline silicon, the effect of a boron diffusion approach was also studied.

3.4.1 Phosphorus Diffusion Gettering

In this study, PDG was completed by collaborators in the photovoltaics group at the University of New South Wales. This was performed in an industrial size Tempress Diffusion Furnace, on 6 by 6 inch wafers. These wafers were annealed at a temperature of 795 °C for 25 mins, in an atmosphere of $POCl_3$, O_2 introduced at flow rates of 425 sccm (standard cubic centimeters per minute) and 600 sccm respectively. This was followed by a thermal drive in process at 880 °C with 7.5 L of N_2 for a period of 40 mins. The emitter was then removed using KOH alkaline etching, with approximately 10 μm removed from the surface.

3.4.2 Saw Damage Gettering

SDG was applied to a number of silicon carbide slurry wire sawn wafers, with initial start temperatures of 850 °C and 900 °C for 10 minutes followed by an exponential cool to 500 °C over 50 minutes in a tube furnace with a nitrogen ambient. This process and the subsequent cooling profile is described in Reference [7].

3.4.3 Hydrogen Passivation via Dielectric Layers

In this thesis, hydrogen passivation via the firing of dielectric layers was completed by collaborators in the photovoltaics group at the University of New South Wales. In order to imitate the hydrogen passivation performed in industry, a 75 nm silicon nitride SiN_x:H antireflection coating was deposited on the surface using a plasma-enhanced chemical vapour deposition Meyer Burger MAiA tool at 400 °C for 15 mins. Replicating the metallisation firing step, the nitride layers were fired at a peak temperature of 744 °C for a duration of 2 s, using a belt firing furnace. In this time, hydrogen released from the dielectric layers penetrated throughout the bulk.

3.4.4 Hydrogen Passivation via Remote Plasma

In Chapter 6, remote plasma hydrogenation using deuterium was completed by Dr Vladimir Markevich at the University of Manchester. A schematic of the remote plasma hydrogenation process is shown in Figure 3.1. Prior to remote plasma hydrogenation, samples were chemically etched using HNA (see Section 3.5.2) to remove the surface damage and also Secco etched (Section 3.5.3) in order to allow for the subsequent selection of defects in APT.

Samples were passivated using a ^2H remote plasma for a period of 60 minutes, under a plasma power of 30 W, with the sample held at a temperature of 200 °C. In the remote plasma process, the sample is not exposed to the plasma, which is known to produce harmful UV radiation, and therefore the surface damage is much lower [162]. In addition, the deuterium enters the sample atomically as ^2H, in order to more closely replicate how hydrogen is introduced by industrial processes (see Section 3.4.3).

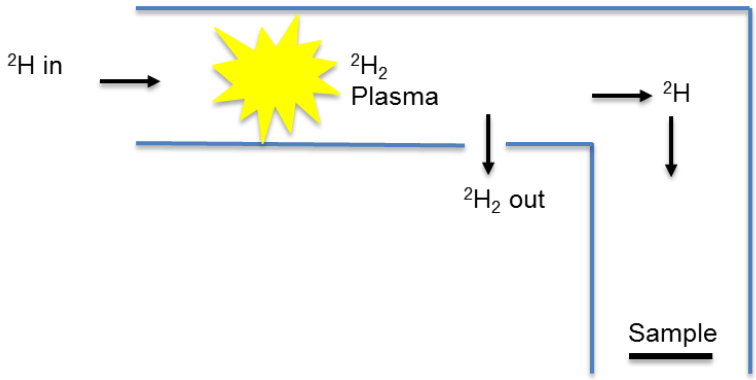


Figure 3.1. Simple schematic of a remote hydrogen passivation process, using pure ^{2}H gas to form a plasma, which is obscured from the sample. ^{2}H is then able to enter the sample atomically at an elevated temperature.

3.4.5 Boron Diffusion Gettering

Boron diffusion gettering (BDG) was performed at Fraunhofer ISE by F. Heinz and F. Schindler. In a similar manner to phosphorus diffusion when producing an emitter in p-type multicrystalline silicon, BDG is required in n-type silicon. The effectiveness of BDG have been found to be extremely dependent on the processing conditions and require a much larger thermal budget than phosphorus diffusions [94]. In this study, boron diffusion was performed at a temperature of 890 °C, in an atmosphere containing BBr_3, for a duration of 1 hour.

3.5 Polishing and Chemical Etching

3.5.1 Mechanical Polishing

Mechanical polishing was performed in order to produce a flat surface prior to microscopical analysis. Polishing was performed using an oil lubricated polishing pad in a diamond suspension, containing particles of 0.25 µm in diameter for

approximately 2 hours. This produced a near mirror finish, with subsurface damage then removed using a 2 minute second HNA etch (Section 3.5.2). Originally, chemomechanical polishing was performed using colloidal silica polishing. This was however, found to introduce significant quantities of impurities at room temperature and could therefore not be used (see Chapter 4).

3.5.2 HNA Etching

HNA etching, or the etching in a mixture of hydrofluoric acid, nitric acid and acetic acid is a planar etch used commonly in the photovoltaic community [163], [164]. It operates by the nitric acid induced oxidation of silicon surface and subsequent oxide dissolution due to the hydrofluoric acid. HNA was performed on samples after mechanical polishing for 2 minutes to remove surface damage from polishing. The precise mixture used in this study is given in Table 3.1.

Table 3.1. Volume of acids in planar HNA etching, used to remove saw and polishing damage.

	Volume	Concentration
Acetic Acid (CH_3COOH)	30 ml	100 $V/V\%$
Hydrofluoric Acid (HF)	50 ml	40 $V/V\%$
Nitric Acid (HNO_3)	220 ml	70 $V/V\%$

3.5.3 Selective Etching – Secco

The etchant chosen for the marking of crystallographic defects, such as dislocations and grain boundaries, was Secco as described in Table 3.2 [165]. Work conducted by Lotharukpong in his D.Phil thesis confirmed this type of etchant was the optimum for APT liftouts [166]. This etchant forms narrow, but deep etch pits on the surface, which can be filled with electron beam deposited tungsten prior to liftout. Etching was performed by submersion of the sample for 30 seconds.

Table 3.2. Volume of acids used for selective Secco etching, used to mark out individual grain boundaries and dislocations.

	Volume	Concentration
Potassium Dichromate ($K_2Cr_2O_7$)	20 ml	0.05 M
Hydrofluoric Acid (HF)	40 ml	40 $V/V\%$

3.6 Electron Beam Induced Current

3.6.1 EBIC Operating Principles

Electron beam induced current (EBIC) is an extremely effective and powerful tool, used extensively in the semiconductor industry. In scanning electron microscopy (SEM), a concentrated electron beam is scanned across the surface of the sample. The highly energetic electrons undergo inelastic scattering events with valence or core electrons in the sample, giving surface electrons sufficient energy to enter the conduction band, leaving behind a hole in the valence band.

In order to measure the resulting current caused by the electron beam, a Schottky or p-n junction was used as a collecting junction for minority carriers, as shown in Figure 3.2. For example, in p-type silicon, electrons diffuse to the depletion zone and are collected by the surface probe. At the same time, the generation of an electric field causes holes to flow in the opposite direction to maintain charge neutrality. This results in the formation of a current, which is measured.

The current measured is dependent on the number of minority carriers which reach the depletion zone. This relies on a large number of minority charge carriers reaching the contact before recombination occurs (discussed in Section 1.3). Although there are three types of bulk recombination, band-to-band recombination is usually prominent only in direct band gap semiconductors, and Auger recombination is typically only significant in highly doped samples [8]. Therefore, the differences in electron beam induced current across the surface is primarily dependent on the magnitude of SRH recombination.

As previously discussed in Section 1.3.3, SRH recombination is caused by the presence of deep levels at defects in the band gap. These defects can trap charge carriers and allow a carrier of the opposite type to make a transition to this level and cause recombination. EBIC is therefore used as an effective tool for measuring the recombination strength of defects in silicon. The recombination strength of such defects is expressed as a percentage EBIC contrast C [167]:

$$C = (I_{background} - I_{defect})/I_{background} \qquad (3.1)$$

where $I_{background}$ and I_{defect} are the currents collected at the background (intragranular regions free of apparent dislocations) and at the defects respectively.

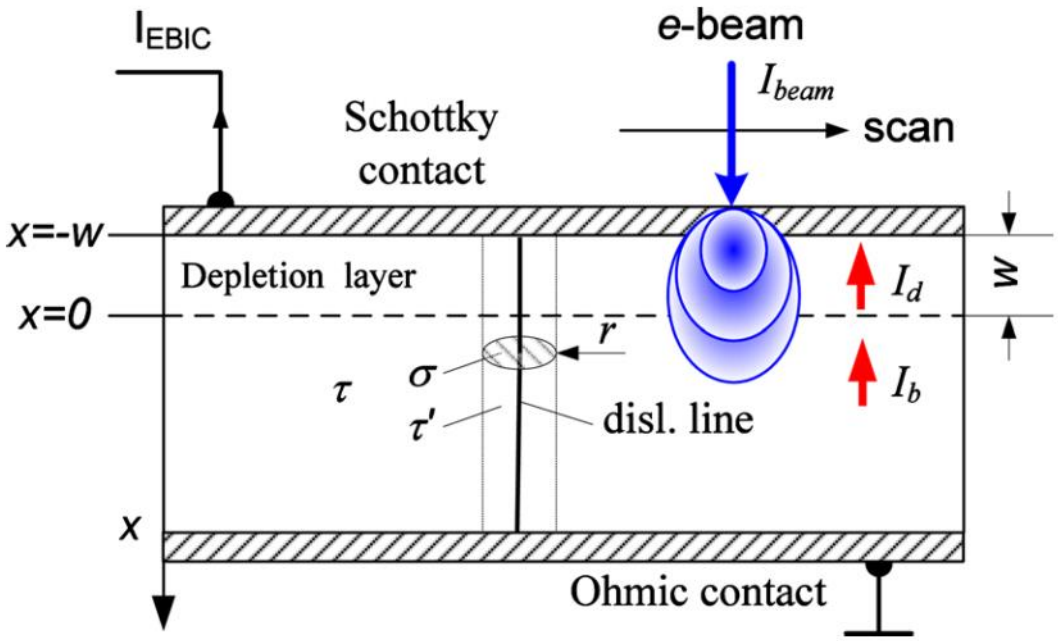


Figure 3.2. Schematic of the EBIC technique, in which a scanning electron beam interacts with the surface of a sample containing a front Schottky junction and a rear Ohmic contact, with the current measured using a probe placed on the surface. I_d and I_b are the current collected from the depletion and quasineutral regions respectively, τ is the minority carrier lifetime and σ is the capture cross section of the dislocation [168].

Lowering the applied beam energy causes an increase in the lateral resolution of EBIC, due to the reduced spreading of the beam [169]. However, the beam energy must be sufficient to allow for the generation of charge carriers outside the depletion region (Figure 3.2). This ensures that an accurate measure of the background can be determined, since recombination within the depletion region is highly unlikely.

Equation 3.2 shows the depth penetrated in µm, R_p, with respect to the accelerating voltage E_b (kV) and the density ρ (g/cm^3) of multicrystalline silicon. Pasemann [69], using the relationship of Everhart and Hoff [170], proposed that:

$$R_p = 3.98 \times 10^{-2} \left(\frac{E_b^{1.75}}{\rho} \right) \mu m \qquad (3.2)$$

this results in an approximate penetration depth $R_p \approx 1$ µm for 10 kV and 3.2 µm for 20 kV [146]. Using Equation 3.3 and work function values from Michaelson [171], it is possible to estimate a value for the depletion layer width:

$$W_D = \sqrt{\frac{2\varepsilon_s}{qN_D}\left(\psi_{bi} - V - \frac{k_B T}{q}\right)} \qquad (3.3)$$

Where the depletion width of a metal-silicon Schottky junction W_D, is expressed as the permittivity of silicon ε_s, the silicon doping concentration N_D, the built in potential at the junction ψ_{bi}, the applied voltage at the junction V, the Boltzmann constant k_B, the absolute temperature T and the charge on an electron q [172]. For a 10^{16} cm^{-3} B doped Si sample, the depletion layer width is approximately 0.3 µm.

3.6.2 EBIC Sample Preparation

As shown in the schematic in Figure 3.2, EBIC requires both a Schottky and Ohmic contact on the front (polished) and rear (unpolished) surfaces of the samples, respectively.

The Schottky contact operates as a collecting junction for minority carriers generated by the electron beam. The Schottky contacts in p-type silicon were formed by the deposition of a 13 nm thin film of aluminium, as measured using the predicted Al

evaporation rate of the instrument, through a 5 mm by 5 mm square mask. This was performed by thermal evaporation, using a 99.999% Al wire wrapped around a tungsten filament.

In order to measure the EBIC current, an Ohmic contact was required on the rear of the sample. It was formed by applying mechanical damage to the back surface, from coarse P80 grit sand-paper, followed by the application of InGa paste. The sample was then attached to an SEM stub via silver dag paste.

To remove the Al front contact for EBSD analysis, hydrochloric acid (37 V/V%) was applied to the surface via a cotton swab. The acid was deposited on the surface and left until the thin layer of Al had completely dissolved. The sample was then cleaned by submersion in distilled water.

3.6.3 EBIC Imaging and Processing

In this study, EBIC was performed in a Zeiss NVision SEM/FIB, using an accelerating voltage of 12.5 kV and a working distance of 5 mm. The images were acquired using an Omniprobe 200 surface probe, connected to a Point Electronik EBIC system. The gain, contrast and I-offset were adjusted to ensure the signal was neither saturated or below measured current values.

The selection of the accelerating voltage for EBIC was performed with reference to the Equations 3.2 and 3.3. It is essential that the recombination activity of the defect is measured outside the depletion region, in order to allow for quantitative EBIC

measurements to be made. Additionally, EBIC measurements taken at very low accelerating voltages are very susceptible to surface topography, such as etch pits which can be seen as white regions in Figure 3.3. In contrast, at much greater accelerating voltages, the ability to resolve individual dislocations and other intragrain defects becomes difficult, due to the large volumes sampled by the electron beam (Figure 3.3). In this study, an accelerating voltage of 12.5 kV was selected. At this voltage, the measurement was much less sensitive to surface roughness, while maintaining sufficient resolution for measuring individual electrically active defects.

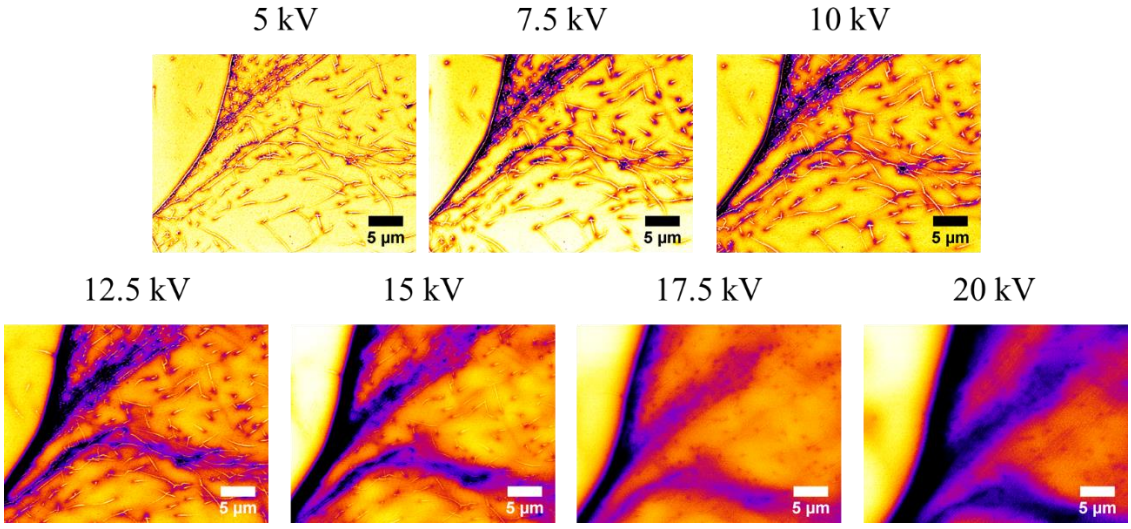


Figure 3.3. EBIC images showing grain boundaries and intra-granular dislocations, taken at various accelerating voltages. This sample has been prepared using a colloidal silica polishing process, which introduces contamination (See Chapter 4).

Image analysis was performed using the Point Electronik Digital Image Processing System 2.9 (DIPS). In order to determine defect contrast, a line scan was drawn intersecting the defect (Figure 3.4). From the EBIC current measured at the defect and

an average current measured at the background, a contrast value was determined for the individual defects.

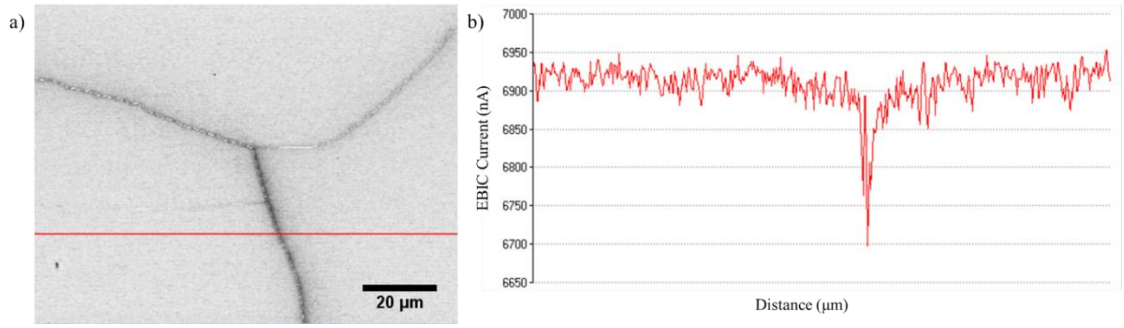


Figure 3.4. Example showing the contrast values for defects are determined using the DIPS software, where a) is an EBIC image and b) is the profile of the line scan from which the contrast is determined. Total distance across images a) and b) is 114.4 µm.

EBIC images were taken at various magnifications, with contrast comparisons between images only made at the same magnification. Scale bars were added using the image processing software ImageJ.

3.7 Electron Backscatter Diffraction

3.7.1 Operating Principles

Electron Backscatter Diffraction (EBSD) is an effective characterisation technique, able to distinguish both phases and grain orientations. In this study, EBSD was used extensively to determine grain boundary types and misorientation between grains. The crystallographic nature of the grain boundaries is known to significantly affect the recombination activity, with certain grain boundary types being particularly harmful to solar cell performance [31], [88].

The key principle of EBSD involves the focus of an electron beam onto the surface of the tilted sample. Some electrons are then diffracted from the sample, with minimal loss of energy [173]. A fraction of these electrons incident the crystallographic planes in the sample at angles that satisfy the Bragg equation:

$$n\lambda = 2dsin\theta \qquad (3.4)$$

where n is an integer, λ is the wavelength of the electrons, θ the angle of incidence of the electrons on the diffracting plane, and d is the spacing of the diffracting plane.

The diffraction of these electrons in the form of large angle cones, results in the formation of Kikuchi bands in the detected image, which can be directly associated to the diffracting crystallographic planes. The use of a phosphor screen allows for the capture of such patterns, which are then indexed to enable characterisation of relative grain orientations.

3.7.2 EBSD Imaging and Processing

EBSD was performed on a Zeiss Crossbeam 540 FEG-SEM equipped with an Oxford Instrument (OI) EBSD Nordlys Max 3 detector. Samples were pre-tilted to 70° and exposed to an electron beam accelerating voltage of 30 kV and beam current of 3 nA. An in-chamber image of this set-up is shown in Figure 3.5. The EBSD images were acquired at a working distance of 18 mm using the Oxford Instruments Aztec software. Further processing, including noise reduction and boundary type determination was performed in the Oxford Instruments Channel 5 software, using the HKL Tango add-on.

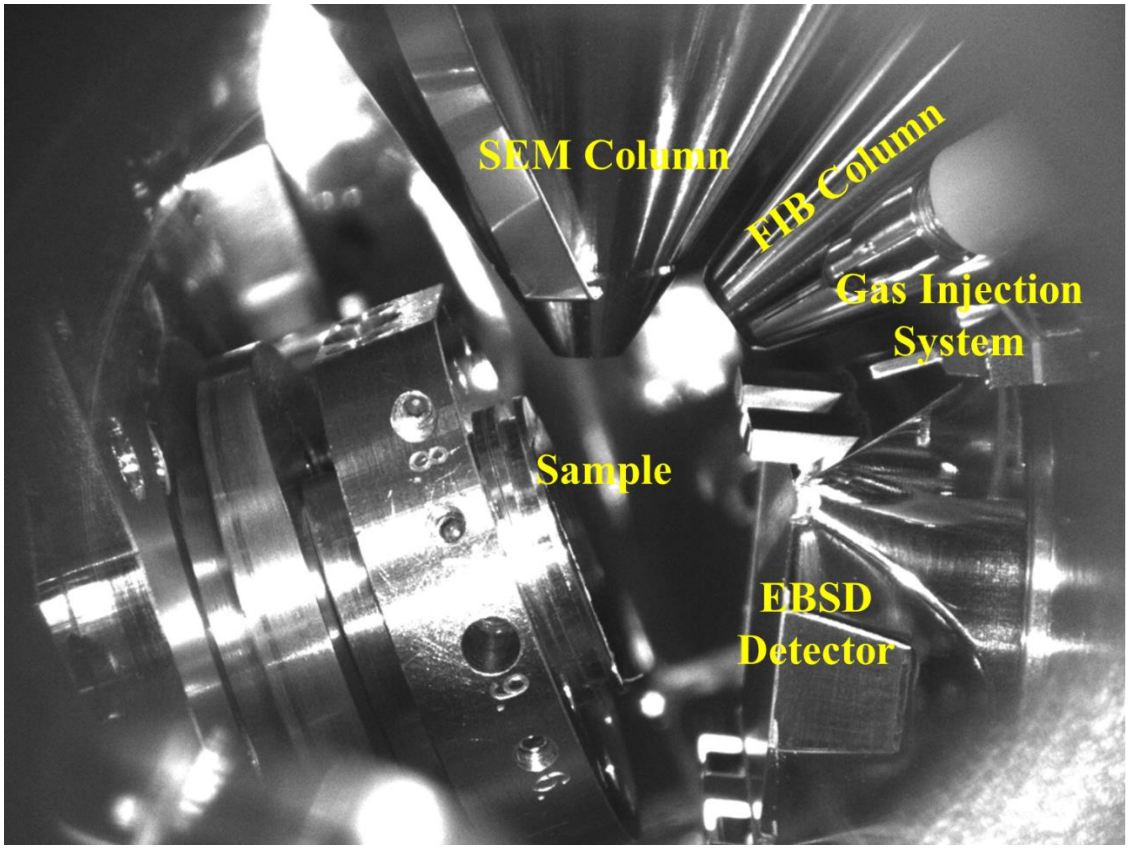


Figure 3.5. Experimental set-up for EBSD in the Zeiss Crossbeam 540 FEG-SEM. The sample is shown tilted at 70°, with the SEM column, FIB Column, gas injection system and EBSD detector labelled.

3.8 Transmission Kikuchi Diffraction

3.8.1 Operating Principles

The fundamental principles of transmission Kikuchi diffraction (TKD) are very similar to EBSD, involving the indexing of Kikuchi patterns of diffracted electrons. However, in the case of TKD, electrons penetrate through the sample and are diffracted by the rear crystal planes [174]. This allows much greater spatial resolution scans to be made, with nanometre scale resolution achievable [175].

A requirement of this technique is that the sample must be electron transparent, usually under 200 nm in thickness. Opportunely, APT specimens are also required to be under this thickness. TKD is therefore a powerful tool for the pre-screening of APT needles to confirm the presence of a grain boundary within the needle and confirm its type and misorientation [176].

3.8.2 TKD Imaging and Processing

As with EBSD, TKD was performed on a Zeiss Crossbeam 540 FEG-SEM equipped with an Oxford Instrument (OI) electron backscattered diffraction (EBSD) Nordlys Max 3 detector. Specimens were pre-tilted to 54°, allowing for real time correlative FIB milling and TKD imaging. Specimens were exposed to an electron beam accelerating voltage of 30 kV and beam current of 2 nA. The images were taken at a working distance of 5.2 mm using the Oxford Instruments Aztec software. Further processing, including noise reduction and boundary type determination was performed in the Oxford Instruments Channel 5 software, using the HKL Tango add-on.

3.9 Dual Beam Scanning Electron Microscope and Focussed Ion Beam

Two dual beam SEM/FIB were used in the course of this thesis, the NVision and the Crossbeam 540 FEG-SEM, both manufactured by Carl Zeiss Microscopy GmbH, Jena, Germany. Since the operating principles of both SEM [177], [178] and FIB [179], [180] are well established and widely known, they will not be discussed in this thesis.

3.10 APT Specimen Preparation

A significant part of this project involved the development and optimisation of a technique which reliably allowed for the analysis of large sections of specific grain boundaries. This technique was pioneered by C. Lotharukpong during his DPhil thesis, from which more information can be found in [157]. In order to consistently produce defect containing APT specimens, significant and substantial optimisation of this technique was performed in the course of this work. The following section describes the step-by-step process used to produce APT specimens. All deposition and milling was performed at the coincidence point of the microscope.

3.10.1 Sample Marking

In order to ensure a specific grain boundary of interest was targeted for APT analysis, grain boundary marking was required. Since grain boundaries were already marked via an etch pit from Secco etching (see Section 3.5.3) they were visible in the SEM. With the GIS inserted, a 15 µm by 200 nm region containing the length of the grain boundary was imaged in SEM in line averaging mode. The tungsten gas precursor was then released into the chamber, which was cracked by the electron beam resulting in the deposition of tungsten along the grain boundary. This was performed for a period of 5 minutes until the grain boundary etch pit was completely filled with tungsten.

Following tungsten deposition, the sample was tilted to 54°, normal to the FIB, and rotated by 3°. A carbon strip of 15 µm by 3 µm was then deposited using the FIB at a 30 kV accelerating voltage and 40 pA gallium ion beam current, with a pixel fill factor of 50%. The use of a low beam current limits the surface damage caused by the

incident gallium ions, while ensuring sufficient imaging quality. The stages of this defect marking process are shown in Figure 3.6.

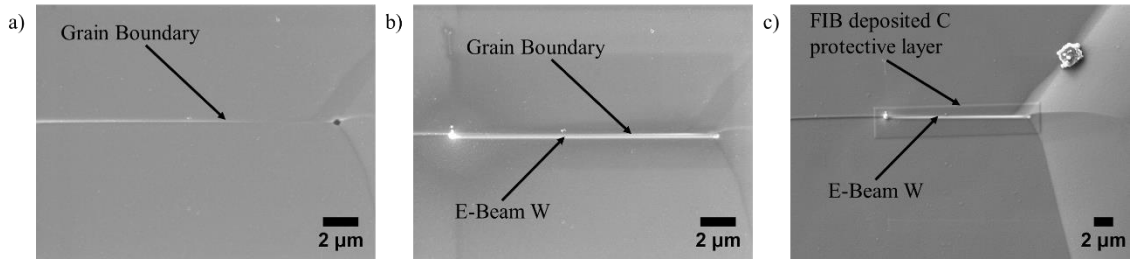


Figure 3.6. a) SEM image of a silicon wafer with a grain boundary marked via Secco preferential defect etching. b) SEM image of the grain boundary marked via the electron beam deposition of tungsten. c) SEM image of the tungsten marked grain boundary ready for cantilever production, with a FIB deposited carbon protective layer on the surface.

3.10.2 Cantilever Production

Following the marking of the grain boundary by tungsten and the deposition of a carbon protective layer, a cantilever ready for liftout was produced. This process entailed two steps, both performed at a tilt of 9°. This gave a FIB incident angle of 45° relative to the sample. First, two large trenches of depth 10 µm were made via FIB milling at an accelerating voltage of 30 kV and beam current of 3 nA. Secondly, the undercut and end cut were performed at the lower beam current of 1.5 nA. This resulted in a cantilever free to liftout, as shown in Figure 3.7.

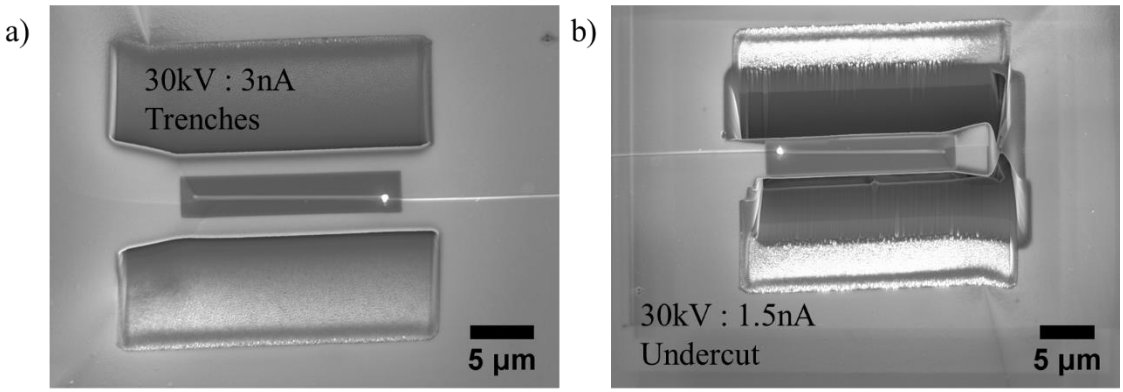


Figure 3.7. a) Scanning electron micrograph of grain boundary containing cantilever, with two 10 µm deep trenches produced via FIB milling at an accelerating voltage of 30 kV and beam current of 3 nA. b) SEM image of a cantilever ready for liftout, with undercuts and end cut made at a beam accelerating voltage of 30 kV and beam current of 1.5 nA.

3.10.3 Liftout

The liftout was performed onto a TEM half grid, using the method described in the co-authored paper [157]. In this method, the liftout bar is attached to the end of a TEM half grid, in an end-on configuration. FIB deposited tungsten attached the bar to the TEM post, with a beam current of 40 pA and accelerating voltage of 30 kV for a period of 9 minutes. Images of the end-on liftout method are shown in Figure 3.8

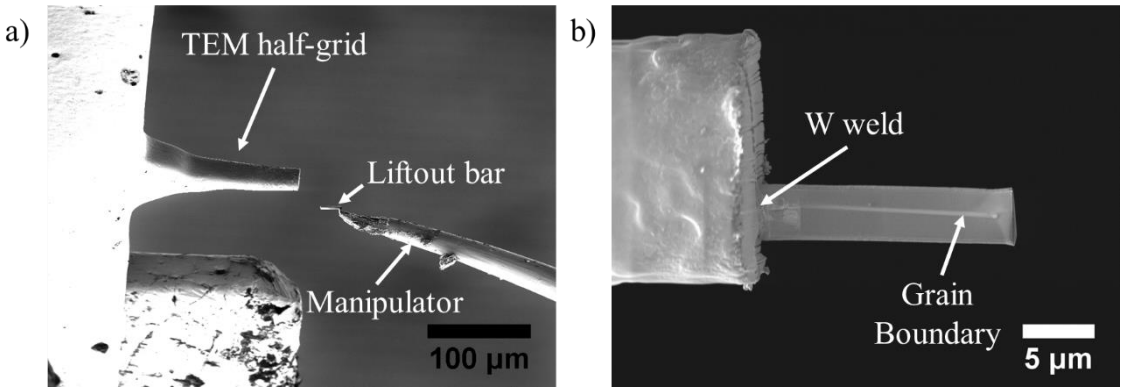


Figure 3.8. a) FIB image of the liftout bar prior to attachment to the TEM half grid post. b) SEM image of the liftout bar attached to the TEM post, with the grain boundary clearly visible running down the bar.

3.10.4 Needle Milling

Figure 3.9 displays the various stages of needle production, from the liftout bar to the finished specimen ready for TEM and APT analysis. Needles were made at a tilt of 54°, normal to the FIB beam, using a doughnut milling pattern. Initial milling occurred using an accelerating voltage of 30 kV and a beam current of 300 pA (Figure 3.9 a - b). Finer milling was performed at the lower beam current (80 pA), while ensuring the grain boundary was at the centre of the needle (Figure 3.9 c). When the needle had an apex radius of less than 100 nm, low accelerating voltage milling was used to minimise damage caused by gallium implantation. A lower voltage of 2 kV and beam current of 300 pA was used, removing approximately 300 nm of surface material (Figure 3.9 d)

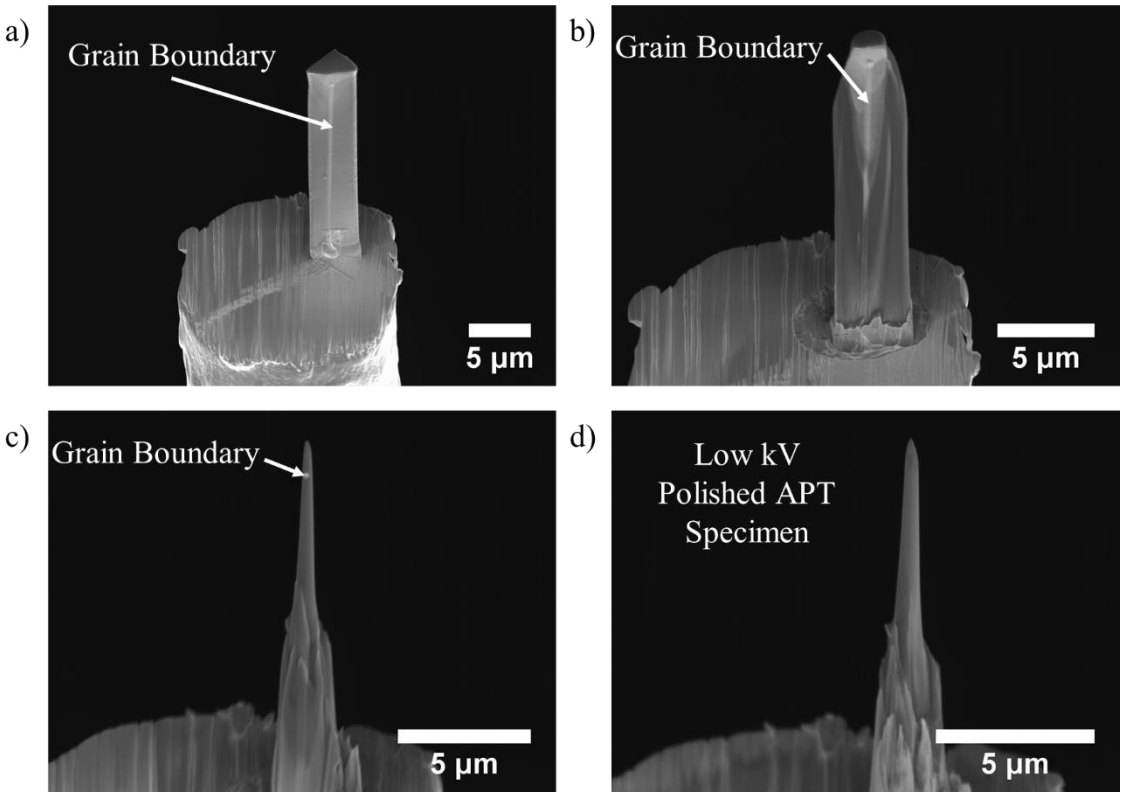


Figure 3.9. SEM micrographs of the various stages of needle production and sharpening. At every stage (a-c) the grain boundary is centred in the needle. d) The finished needle ready for TEM and APT analysis, following a low kV polish at 2kV and 300 pA.

3.11 Transmission Electron Microscopy

Transmission electron microscopy (TEM) operates via the use of high energy electrons, focussed onto an electron transparent sample. Electrons are transmitted through the sample and can be scattered by defects such as grain boundaries and dislocations. The use of additional apertures enable the filtering of weakly scattering and strongly scattering electrons, resulting in the formation of a bright field and dark field images respectively. A definitive and exhaustive description of TEM is found in the book by Williams and Carter [181].

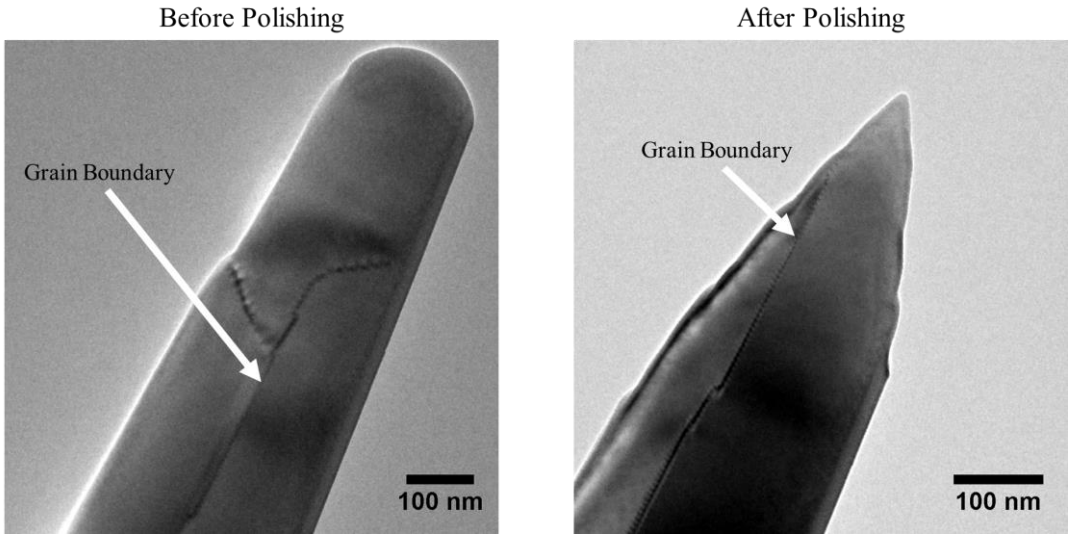


Figure 3.10. Bright field TEM images displaying an APT needle containing a grain boundary. When the needle was first made, the grain boundary was not in the top 150 nm (left image). Low kV polishing was then used to polish the needle until the grain boundary was at the apex (right image).

In this study, TEM was used to confirm and ensure the presence of the grain boundary of interest at the very apex of the APT needle. The TEM used was a JOEL 2100 TEM, at an accelerating voltage of 200 kV. An example of how TEM was used in this study is shown in Figure 3.10. Initially the grain boundary was not present at the apex of the needle. As previously described, the APT specimen was produced with the grain boundary running through the needle at an angle of 3°. The specimen could therefore be polished a fixed distance, as determined by TEM, to ensure the grain boundary is at the apex. This was then re-checked with TEM, prior to APT analysis. To limit gallium damage, polishing was performed using low kV FIB imaging at 2kV: 300pA.

3.12 Atom Probe Tomography

3.12.1 Principles

Atom probe tomography (APT) is unique materials characterisation technique, allowing for 3D characterisation of 'individual' atoms [182]. APT, a successor of field ion microscopy (FIM), utilises the application of high electric fields to ionise and evaporate surface atoms from the sample. If the field is sufficiently intense, surface atoms are pulled away from the surface while electrons are drained into the bulk [183]. At a critical distance, x_s (Figure 3.11), ionisation and evaporation occurs, where the activation energy for the process is $Q_n(\mathbf{E})$.

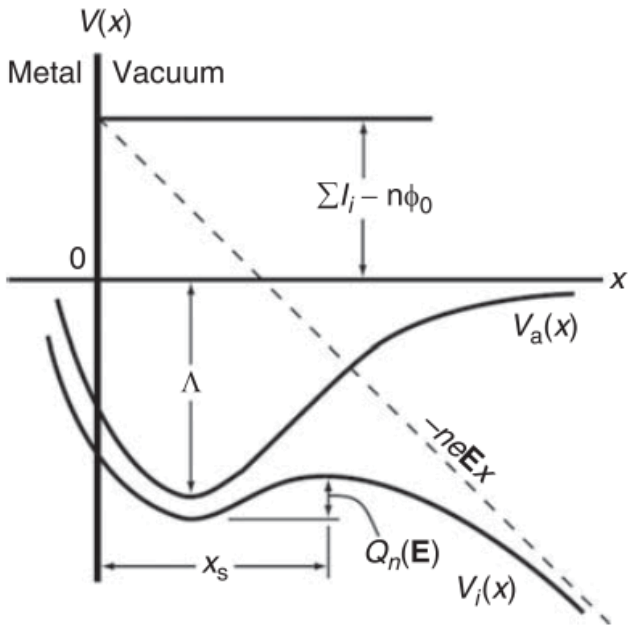


*Figure 3.11. Potential energy V(x) as a function of distance from the specimen surface (x=0). $V_a(x)$ is the potential energy of an atom in the absence of an electric field (**E**). $V_i(x)$ is the potential energy of an ion of the ith ionisation state, with I_i as the i^{th} ionisation state in the presence of **E**. Λ is the cohesive energy of a solid, with Φ_0 as the local work function, $Q_n(\mathbf{E})$ as the height of the Schottky hump or the energy barrier under an applied field* [184].

Field evaporation is a probabilistic and thermally assisted process, which can be modelled by the Maxwell-Boltzmann equation:

$$P_{evap} \propto e^{\left(\frac{Q(E)}{k_B T}\right)} \qquad (3.5)$$

where the probability of field evaporation P_{evap} is related to Q(E), the height of the energy barrier under an applied field, k_B is the Boltzmann constant and T is the absolute temperature.

To achieve the high fields required for field evaporation, a very sharp needle-shaped specimen is required. The electric field at the tip of the needle can be approximated using Equation 3.6,

$$F = \frac{V}{k_f R} \qquad (3.6)$$

where the electric field F at the surface of the needle, can be calculated using the voltage applied V, the field factor k_f and the radius of curvature R at the specimen apex.

Following evaporation, the electric field projects the ions onto a position sensitive microchannel plate delay-line detector assembly. Using a pulsed field to trigger evaporation enables the mass-to-charge-state ratio of the evaporated ions to be determined using time-of-flight (TOF) mass spectroscopy:

$$\frac{m}{n} = M \approx 2eV\left(\frac{t_{flight}}{L}\right)^2 \qquad (3.7)$$

where the mass-to-charge-state ratio (m/n), can be calculated from the time-of-flight t_{flight}, the applied voltage V and flight length (specimen to detector) L.

Historically, HV pulses were used to enable field evaporation of surface atoms from the sample. This however requires the sample to have high electrical conductivity ($>10^2$ Scm^{-1}), which limited the technique to metals and heavily doped semiconductors [185]. The advancement of using laser assisted APT, first developed by Kellogg and Tsong [186], enabled the analysis of materials regardless of their conductivity. Although the laser pulsing technique was initially expensive and unstable, the development of laser technology in the last 30 years has resulted in the widespread use and commercial production of laser assisted atom probes [185], [187].

A simplified schematic of the atom probe technique is shown in Figure 3.12a. The surface atoms of a needle shaped sample are ionised and desorbed from the surface under an electric field (and laser pulsing). A large field is generated by the voltage applied from the local electrode, which has an aperture allowing the evaporated ions to travel through the electrode and hit the position sensitive detector. In many cases, crystallographic information from the specimen can also be determined by examining the field desorption map, or 'hit map', which is a 2D histogram of detected events across the face of the detector. High or low intensity regions in these hit maps often correspond to the projection direction of certain crystallographic poles (illustrated by the detector image on the right hand side of Figure 3.12a).

Using a simplified model of specimen geometry of a hemispherical apex, the coordinates where each ion struck the detector and the sequence of ion detection, a 3D atom-by-atom image of the original specimen can be reconstructed using a straightforward backward projection algorithm [188]. An example of such a reconstruction is seen in Figure 3.12b, in which spheres represent individual atoms of silicon (grey) and carbon (green).

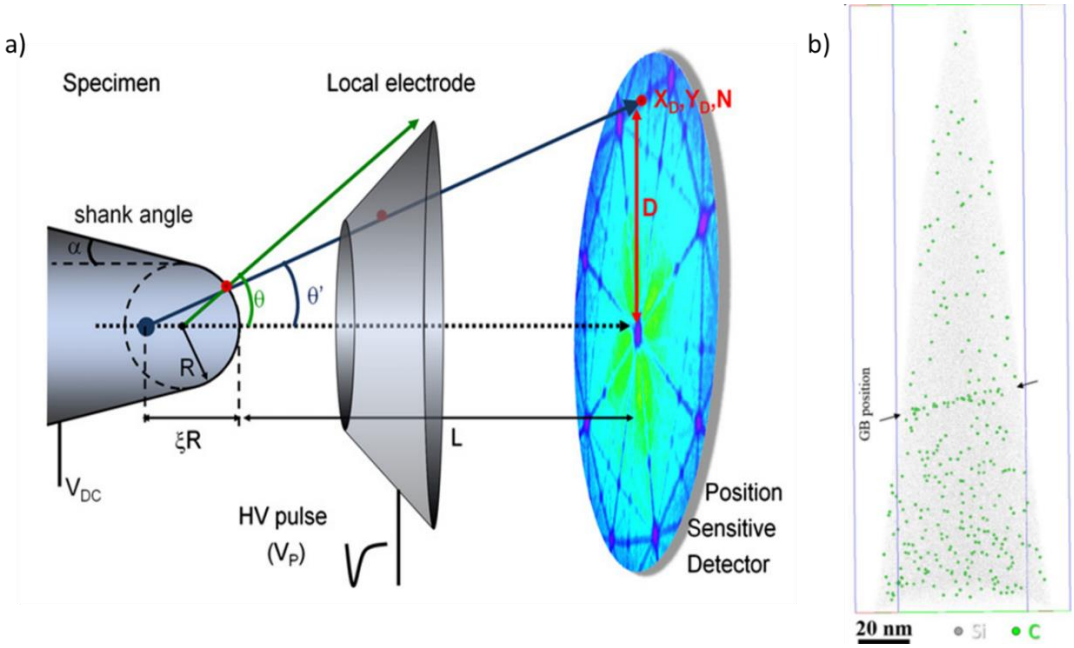


Figure 3.12. a) Schematic of atom probe tomography using a local electrode, with X_D, Y_D are the coordinates of the atoms hitting the detector respectively; N relates to the position of the atom within the sequence of detected atoms [189]. *b) Example of an atom probe reconstructive of a silicon dataset, where carbon segregation (green) is observed along a grain boundary* [159].

3.12.2 APT Limitations

Although APT has the potential to provide three-dimensional reconstructions of individual atoms, there are a number of limitations associated with the technique.

These limitations can originate from the technique itself or the sample preparation required prior the experiment.

The determination of the individual elements in atom probe is performed by TOF mass spectroscopy, using Equation 3.7 to give a mass-to-charge-state ratio for each detected ion. This mass-to-charge-state-ratio of a peak in the mass spectra is not always unique to single element or a particular molecular ion. This can make the deconvolution of respective contributions of different types of ions to the same peak very difficult; for example, determining the presence of small amounts of $^{58}Ni^{2+}$ at 28 Da in a silicon sample containing resulting in the detection of large quantities of $^{29}Si^{+}$ [190]. A detailed discussion regarding the sensitivity of APT is given in Section 5.6.1.

A further limitation of APT refers to issues associated with using FIB for sample preparation. It is well known that the application of FIB can result in the amorphisation of the sample surface and also gallium implantation, which can be observed in the APT experiment [191]. To reduce the damage to the surface caused by the gallium ion beam, a thin protective layer of Pt or W is often deposited onto the surface prior to milling [192].

Ion trajectory aberrations in APT can also cause significant issues. These occur when during experiment the evolution of the specimen deviates from the simplified geometric shape assumed by the reconstruction protocol, affecting the spatial resolution of the technique. Additional aberrations can be caused by the surface migration of atoms that require relatively larger electric fields for evaporation, which are retained for longer on the surface. These elements can undergo a directional walk

on the surface to regions of greater electric fields, resulting in misleading results [193]. Atomistic modelling of the APT process, may increase the resolution of the reconstruction, although the complexity of the effects make it difficult to achieve analytical solutions [194].

Finally, atom probe suffers from low yields of successful experiments, with many specimens often fracturing prematurely during the experiment. Fracture is often caused by a field-induced stress on the sample, under the high fields required for evaporation. A number of techniques can be used to reduce the required evaporation field and thus applied stress or to increase the strength and viability of the sample [195]. These include using laser mode rather than voltage pulsing and prior to analysis removing surface materials that are not of interest and have incompatible evaporation characteristics to the main sample, which can result in specimen fracture [195].

3.12.3 APT Instrumentation and Calibration

The atom probe used in this study was the Cameca LEAP 5000 XR, with a 355 nm UV laser and reflectron. The detection efficiency, i.e. the percentage of ions within the field of view actually detected, for this instrument is 52% and this must therefore be included in calculations regarding quantities of impurities at crystallographic defects.

The LEAP 5000 XR allows for the user control of four key experimental parameters, namely the specimen temperature, laser energy, pulse frequency and detection rate (percentage of pulses where one or more hits are detected). The specimen temperature,

laser energy and pulse frequency were set as 50 K, 50 pJ and 200 kHz respectively, with reference to previous optimisation work on silicon completed at Oxford [166].

However, the effect of detection rate was not studied previously. The detection rate has a significant impact on the time taken for APT analysis, the background levels in the mass spectra and the yield of successful samples. Since this study relies on the detection of ppm levels of impurities segregated to crystallographic defects, optimising this parameter was paramount.

Figure 3.13 shows the dependence of detection rate on the mass spectra background and the total number of counts in a number of silicon datasets. The background level is estimated by the total number of counts between 5 and 7 Da, a region with no peaks in the mass spectrum, normalised by the total number of counts. This value must be regarded as an estimation, since it does not account for the increase in background at greater evaporation voltages. As to be expected, the background was found to decrease with increasing detection rate [185]. This is due to the reduced time for the acquisition of data, reducing the effect of random noise on the detector, which is partially dependent on the duration of the analysis.

Also shown in Figure 3.13, is the effect of detection rate on the total number of counts to sample fracture or the yield of the specimens. Although it is often stated that higher detection rates increase the number of fractures caused by increased field acceleration [185], the scatter in this data shows no clear trend. According to this finding and the

lower backgrounds observed at higher detection rates, the detection rate chosen for the analysis of silicon specimens in this study was 1.5%.

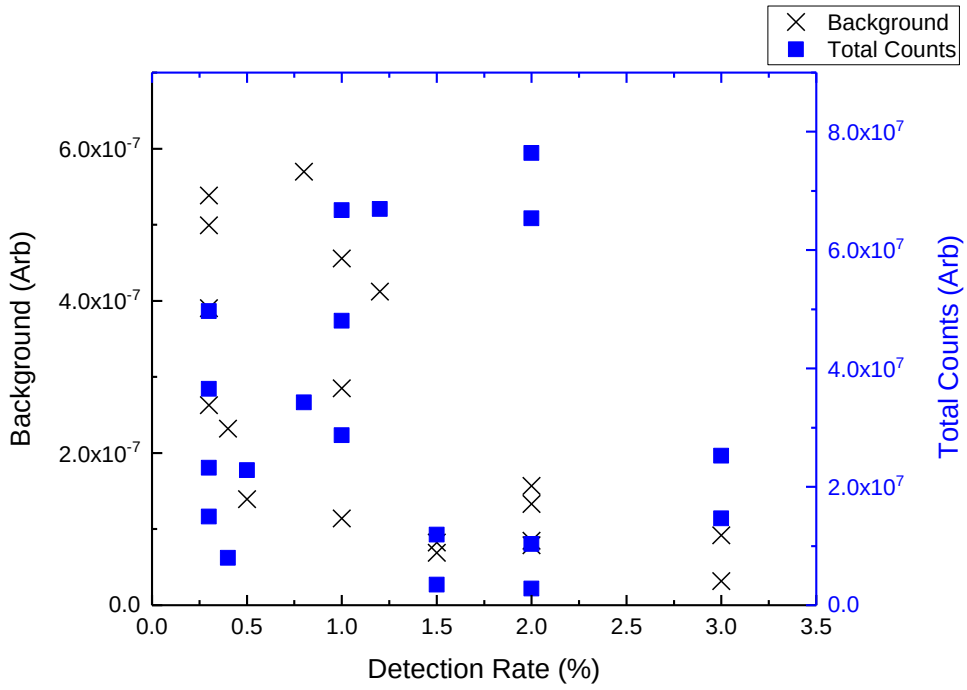


Figure 3.13. An estimation of background, using the total number of counts between 5 and 7 Da over the total number of counts, versus the detection rate for a number of p-type multicrystalline silicon APT datasets (black crosses). Also plotted, are the total number of counts in each dataset versus the detection rate (blue squares).

3.12.4 Three-Dimensional APT Reconstruction

As previously stated in Section 2.7, an important aspect of APT is the ability to accurately reconstruct an atom-by-atom 3D image of the original specimen. The reconstruction procedure uses ions within defined ranges of identified peaks in the mass spectrum and their positions on the detection, which provide the hit coordinates X_d and Y_d. Using an assumed simplified geometry tip geometry of a hemispherical tip on a cone, the original position of an ion on the sample surface in terms of x and y by:

$$x = \frac{X_d \beta r_i}{a} \quad (3.8)$$

$$y = \frac{Y_d \beta r_i}{a} \quad (3.9)$$

where β is the image compression factor, r_i is the instantaneous radius of curvature of the specimen tip at the time of evaporation of that ion, X_d and Y_d are the hit coordinates and a is the distance between the specimen surface and the detector. The depth coordinate of the i^{th} detected ion z_i is given by:

$$z_i = \Sigma \delta z + r_i \left(1 - \sqrt{\frac{X_d^2 + Y_d^2}{{r_i}^2}}\right) \quad (3.10)$$

where δz is the elemental depth increase. This equation determines the z coordinate from the sequence in which ions reach the detector, assuming that later hits are from deeper into the needle [188].

There are a number of ways by which APT 3D reconstructions can be calibrated. In this study, the voltage profile was used to estimate the tip radius throughout the APT experiments. This was deemed sufficient due to the purity of the silicon needles measured. This increases the accuracy of the estimation, since the tip radius calculated is based on the evaporation field of silicon, as shown in Equation 3.6.

3.12.5 Gibbsian Excess

An important aspect of APT is the quantitative comparisons of individual impurities, which can be drawn between different datasets. In the case of this study, Gibbsian interfacial excesses for different grain boundaries are determined [196]. This value

gives an approximation of the magnitude of segregation certain impurities have to the grain boundaries, relative to the background level. An expression for the interfacial excess Γ is given as:

$$\Gamma = \frac{N\left(c_i - c_{i(\alpha)}\right)}{\eta A} \qquad (3.11)$$

where N is the number of atoms in the volume of the grain boundary containing region of interest, c_i and $c_{i\alpha}$ are the concentrations of impurities at the grain boundary and bulk respectively, η is the detection efficiency (52% on the LEAP 5000 XR) and A is the cross sectional area of the grain boundary containing volume analysed. The concentrations of impurities at the bulk and grain boundaries were determined by the use of two regions of interest (ROIs) in the reconstructed APT data, created using the Cameca IVAS 3.8.2 software (Figure 3.14). All of the ranged ions within the ROIs were included in the calculation of the impurities concentrations. This method relies on the assumption of a constant atomic density throughout the dataset. In order to minimise this error, the Gibbs excess was calculated three times independently at different locations throughout the dataset.

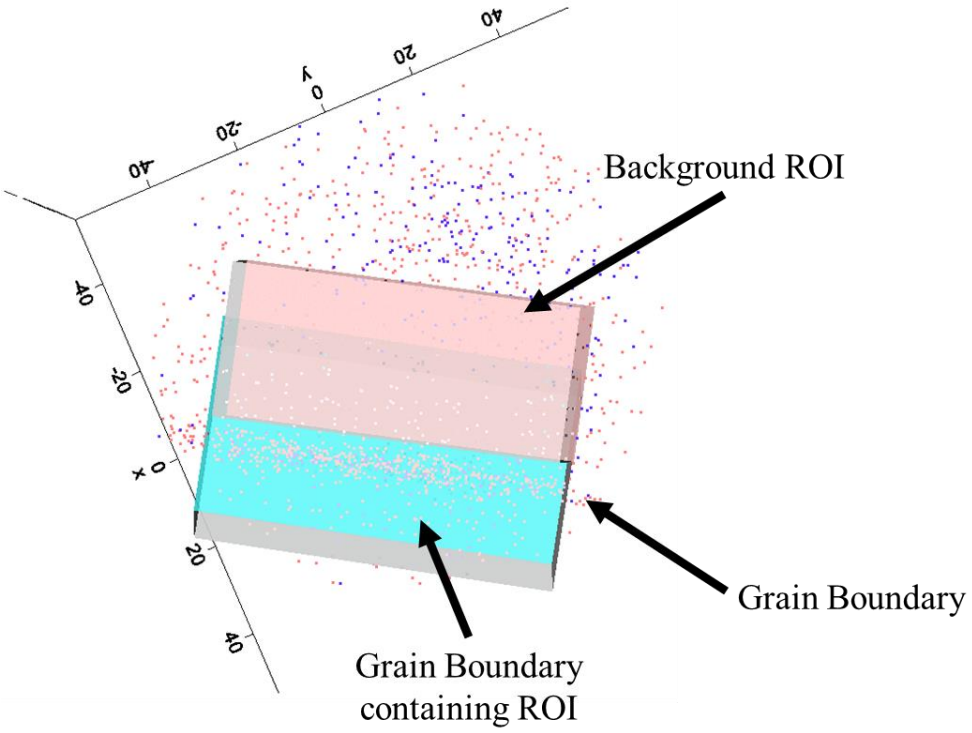


Figure 3.14. APT 3D reconstruction containing a grain boundary. Two regions of interest (ROIs) containing a sample of ions from which the impurity concentrations are calculated. The blue ROI contains the grain boundary and the red ROI was used to measure the background impurity level. Scale markers are given in nm.

3.12.6 APT Mass Spectra

As previously discussed, a primary output of APT is the mass spectrum. The peaks in the mass spectrum are ranged between background levels and assigned to the detection of specific elemental ions or molecular ions. An example mass spectrum for a silicon dataset analysed in this thesis is presented in Figure 3.15. Ranges and labelling for the peaks in the dataset are shown above the figure. A number of overlaps are present in the spectrum, and will be addressed in Section 5.6.1.

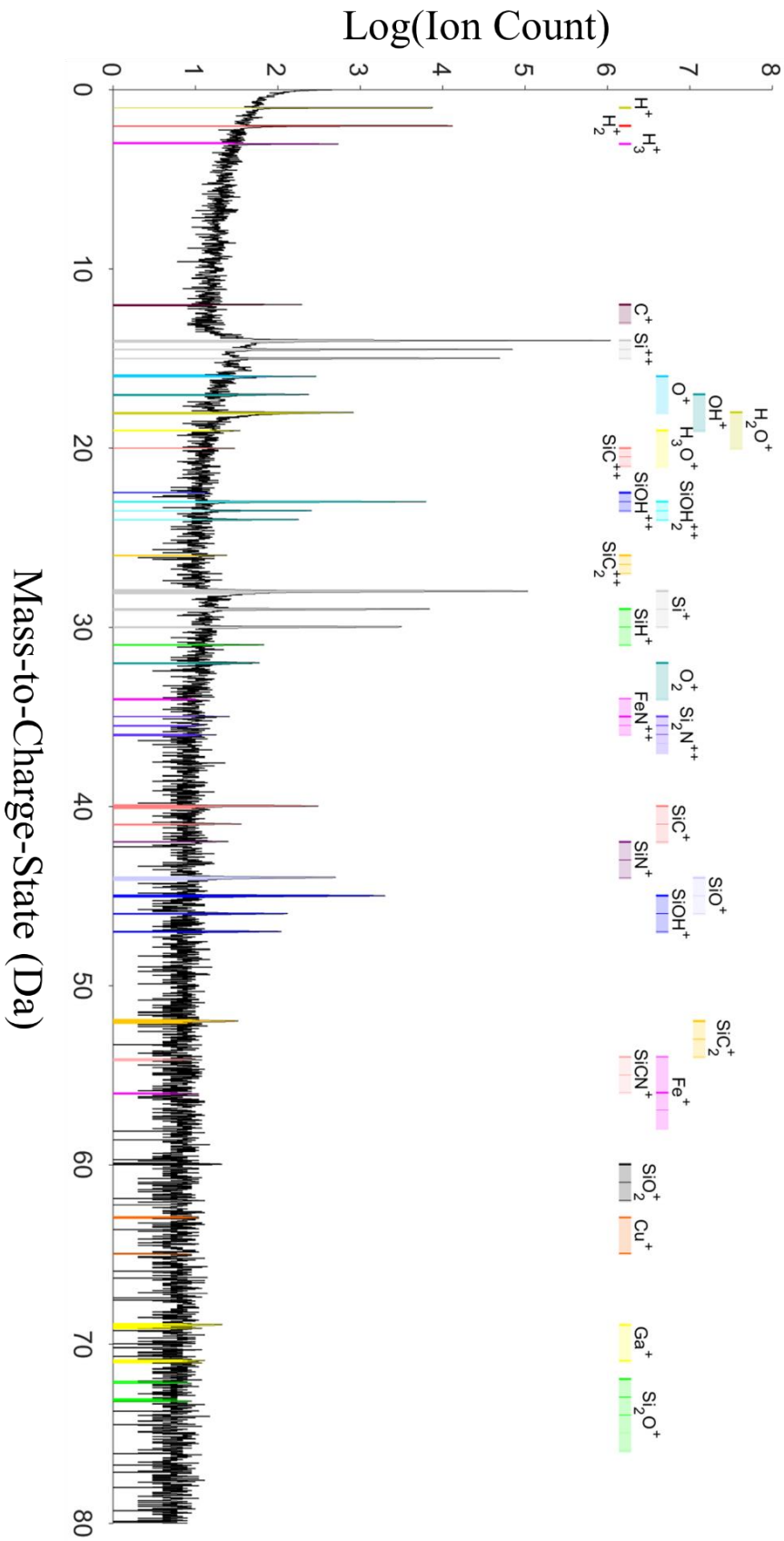


Figure 3.15. Mass spectrum of an example silicon dataset, with peaks labelled above.

3.13 Photoluminescence

Photoluminescence (PL) is a fast and commonly used technique, for the spatially resolved characterisation of electrical activity across silicon wafers. The key principle of photoluminescence is the measurement of radiative, band-to-band recombination from a silicon wafer. The radiative recombination is proportional to the excess carrier density across the material. Regions of high recombination will have lower carrier densities and therefore can be effectively mapped using PL [197]. This occurs by the continuous illumination of the sample surface by laser or LED array, to excite numerous electron hole pairs. Numerous types of cameras, usually a CCD camera, can then be used to measure the counts emitted from the bulk of the sample [198].

The number of counts measured by the detector can be further converted into the local effective minority carrier lifetime τ_{eff} using:

$$\tau_{eff} = \frac{\Delta n}{G} \qquad (3.12)$$

where the generation rate per unit volume G is calculated form the incident photon flux, the from surface reflectance, and the thickness of the wafer. The local excess carrier concentration Δn is determined from the counts per pixel measured, by comparison with the spatially averaged quasi steady state photoluminescence taken at the same light intensity [198].

The extremely high speeds of operation and reasonable spatial resolution of PL have opened up the technique for in-line quality inspection of silicon wafers [199].

Additionally, PL can be used as an effective tool to quantify the distribution of electrically active grain boundaries and dislocations across numerous samples [200], [201].

In order for effective PL, able to measure the internal localised band-to-band recombination of a silicon wafer, the effect of surface recombination should be minimised. There are a number of effective methods in which sufficient passivation can be achieved. One possible method is termed superacid passivation, involving the submersion in HF and a 'superacid' during PL measurements [202]. The standard method, as used in this study, involves the deposition of a passivating SiN_x film on the surface prior to measurement [198].

More recently, the development of spectrally resolved micro-photoluminescence (micro-PL) has enabled much greater resolution analysis and the possibility of impurity distribution analysis. In order to measure at much high resolutions, low wavelength and small spot size UV lasers are used, giving both high lateral resolution and smaller penetration depths [203]. The further integration of CCD cameras able to filter certain wavelengths of light, enables the possibility for the mapping of radiative recombination from various deep levels in the band gap [204].

A number of different institutions conducted the PL performed in this study. The University of New South Wales, Sydney conducted the PL on the HPMC-Si using a BTImaging LIS-R1 instrument. For Red Zone silicon, studied in Section 7.2, PL was

performed at the University of Warwick on a BT Imaging LIS-L1 instrument. Illumination intensities and exposure times are provided in the PL figure captions.

3.14 Lifetime Testing

Lifetime testing was by photoconductance measurements using a Sinton WCT-120 and analysed with the generalised method [205]. The author would like to thank E. Shaw for performing these measurements.

3.15 Concluding Remarks

In this chapter, the numerous techniques utilised throughout this thesis are discussed. Particular focus is given to EBIC and APT, two key techniques that provide defect electrical and chemical information respectively. A detailed analysis of how these techniques have been used in isolation and in correlation is given. Additional analysis techniques such as EBSD, TEM, PL and lifetime testing are also examined.

The large number of analytical techniques used in this thesis, has required the development of a detailed sample preparation method. Information regarding this approach is given, with a particular focus to the novel defect selection APT lift-out method used extensively in this thesis. This approach allows for the multi-microscopical analysis of individual defects.

4 Room Temperature Contamination of Transition Metals in Multicrystalline Silicon

4.1 Introduction

This thesis utilises a correlative electron beam induced current (EBIC), electron backscatter diffraction (EBSD), and atom probe tomography (APT) microscopical approach to analyse impurities present at electrically characterised crystallographic defects in multicrystalline silicon. In the first stages of specimen preparation, prior to the application of any of these experimental techniques, a sample with a flat surface of lower than 50 nm in roughness is preferred [206]. A conventional method for producing such a surface is chemomechanical polishing using colloidal silica, which has been used extensively in the preparation of samples for a number of material systems [207]–[209]. However, this technique has been historically linked with contamination in silicon [210]–[212], dependent upon the purity of the colloidal silica used. With the increased interest in advanced microscopy of silicon for photovoltaic applications [30], [159], it is imperative to ensure sample preparation does not introduce contamination prior to analysis.

As previously described in Section 2.1.2.2, transition metals are notorious impurities in multicrystalline silicon, known to significantly increase carrier recombination via the introduction of deep levels into the band gap [17]. These impurities have been found to segregate to crystallographic defects, such as grain boundaries and dislocations [213], in addition to forming large intragranular metallic precipitates [98]. Nickel and copper are both known to limit the performance of multicrystalline silicon

solar cells, by the decoration of crystallographic defects [91], [214]. They are of particular interest to solar cell producers as potential contaminants, due to their high diffusivity and solubility in silicon enabling the potential for significant in-diffusion at very low temperatures, indeed even room temperature.

Nickel is easily introduced from contamination of the wafer surface at elevated temperatures [215]. Since Ni diffuses interstitially and is neutral at any position of the Fermi level in the band gap [215], its diffusivity has been the subject of much debate. The most commonly used diffusivity is $D_{Ni}(T) = 2.3 \times 10^{-3} \exp(-0.47\ eV/k_BT)\ cm^2/s$, as determined from neutron activation analysis (NAA) [216]. However, this value has been the subject of significant scrutiny of late due to the activation energy, 0.47 eV, differing by more than a factor of two compared to the value of 0.21eV calculated by the nudged elastic band (NEB) method [217]. Further, a more recent study, using an Al-Si sink layer to immobilise Ni during and after cooling, produced a new description of diffusivity with $D_{Ni}(T) = 1.69 \times 10^{-4} \exp(-0.15\ eV/k_BT)\ cm^2/s$ which is applicable over the temperature range 665 – 885 °C [215].

Correspondingly, the high diffusivity of copper allows it to be easily introduced by contamination of the wafer surface at elevated temperatures [218]. Unlike most other 3d transition metals, Cu diffuses in silicon in the Cu^+ charge state [219]. The first direct experimental measurements of the diffusivity of copper at ambient temperatures (240 - 380 K range), were performed by Istratov et al. using the transient ion drift technique in low boron-doped float zone silicon [220]. An expression for the interstitial Cu

intrinsic diffusion coefficient was given as $D_{Cu}(T) = (3.0 \times 10^{-4}) \exp(-0.18\ eV/k_BT)\ cm^2/s$.

Nickel and copper have the highest solubilities of the 3d transition metals in silicon. The solubility for Ni and Cu are given as the equilibrium concentration in silicon as a function of temperature $[Ni] = \exp(3.2 - (1.68\ eV/k_BT))\ cm^{-3}$ and $[Cu] = \exp(2.4 - (1.49\ eV/k_BT))\ cm^{-3}$ [221]. Although these expressions were determined at much greater temperatures, it is possible by extrapolation, to estimate the room temperature solubility concentrations. These are much lower than the levels determined by Coletti to cause significant amounts of bulk recombination in silicon [7].

The low energy barrier to diffusion and high diffusivity even at low temperatures, make Cu and Ni prime candidates for room temperature contamination. Indeed, evidence for room temperature diffusion of copper was found historically by Prigge et al. [210] and Wagner et al. [211], who confirmed that Cu can be introduced via colloidal silica polishing, and increase the recombination activity of the wafer. Room temperature diffusion of Ni was also found by Yarykin and Weber [222], investigating wet chemical etching in contaminated alkaline solutions. By identifying the deep-level response from the electrically active NiVO defect, a lower limit for the diffusivity at 35 °C was determined as $10^{-9}\ cm^2/s$.

Since both copper and nickel have been found at grain boundaries in APT [155], [158], it is important that methods are developed that can identify unintentional contamination being introduced during sample preparation prior to analysis. In this

chapter, a correlative EBIC, EBSD and APT method is demonstrated in order to understand the effect of colloidal silica polishing on the electrical properties of defects in multicrystalline silicon and to show that both copper and nickel decoration of crystallographic defects can be produced by colloidal silica polishing at room temperature.

4.2 Results and Analysis

4.2.1 Electron Beam Induced Current

In order to investigate the effect of colloidal silica polishing on the electrical properties, EBIC measurements were made on the same wafer before and after a 12 hour colloidal silica polish. EBIC images are shown in Figure 4.1, with the numerical value of contrast of selected grain boundaries and dislocations indicated in the higher magnification images c and d. It is clear that the grain boundaries become significantly more electrically active after colloidal silica polishing. Interestingly, not all grain boundaries respond equally to the polishing process, with some grain boundaries becoming significantly more recombination active than others. In addition, intragrain dislocations (Figure 4.1e), which are not observed in the EBIC image before polishing, become active and visible after colloidal silica polishing. This is a clear indication that impurities have been introduced by the polishing process and have segregated to crystallographic defects, introducing recombination active levels into the band gap.

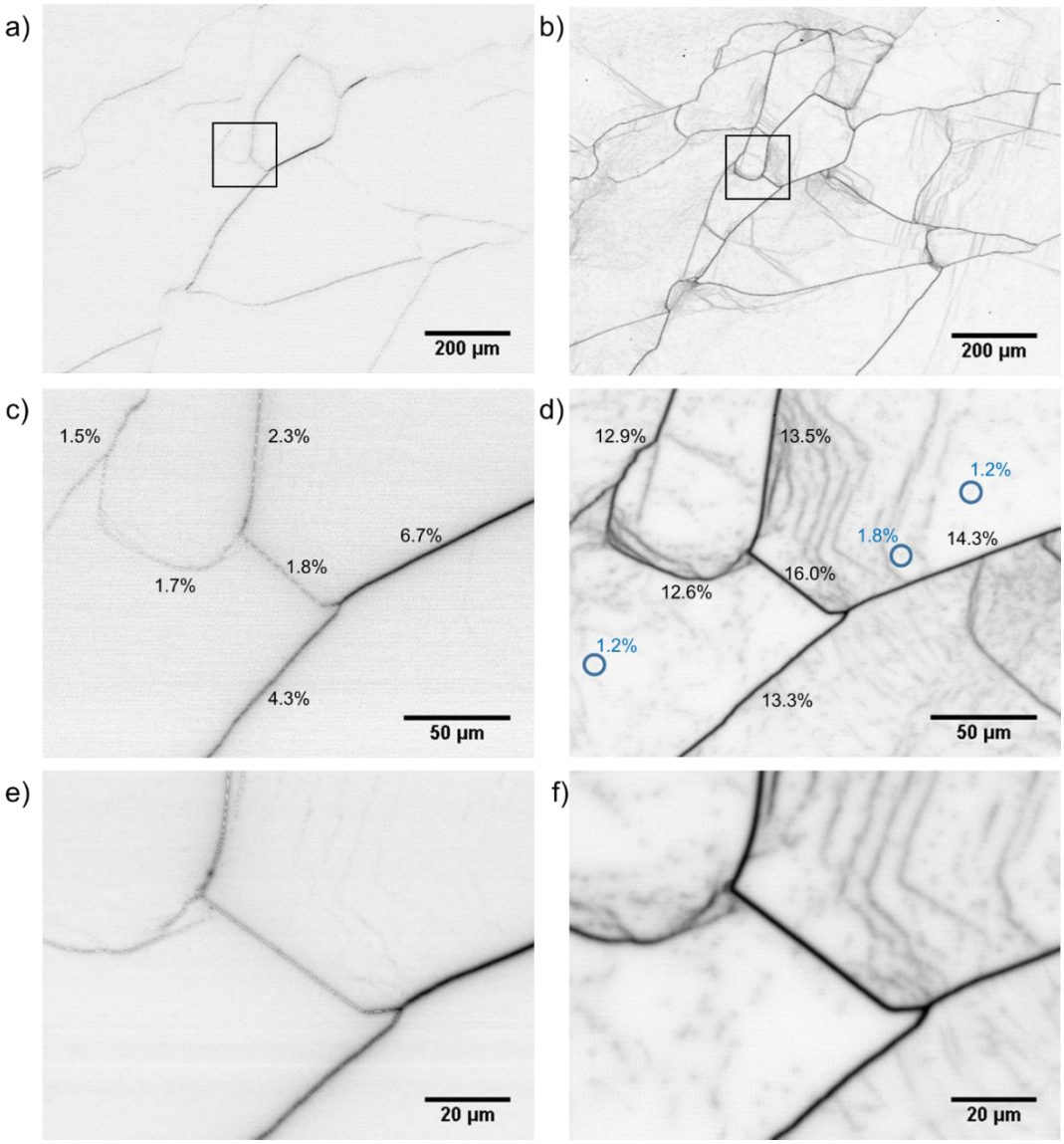


Figure 4.1. Electron beam induced current images of the same p-type wafer (1.3 Ω) before and after colloidal silica polishing, with a) being prior to colloidal silica and b) subsequent to colloidal silica polishing. c) and d) are magnified EBIC images of a) and b) respectively, from the region of interest marked. In c) and d) the EBIC contrast of the grain boundaries before and after colloidal silica polishing, and for three dislocations not previously observed before polishing, are displayed. e) and f) show higher magnification EBIC images before and after colloidal silica polishing respectively.

The EBIC analysis shown in Figure 4.1, was performed on sister wafers which had been exposed to an extensive 12 hour polishing process. However, in the literature, colloidal silica polishing is often performed for much shorter times. To investigate whether measurable contamination can occur in these times, a 30 minute colloidal silica polish was performed on a separate wafer, with EBIC measurements made before and after (Figure 4.2). From the figure, it is again clear that polishing significantly increases the contrast of all grain boundaries measured. Additionally, previously unmeasurable intragranular dislocations become electrically active after colloidal silica polishing. This is an important feature of the polishing process and will be discussed in more detail later.

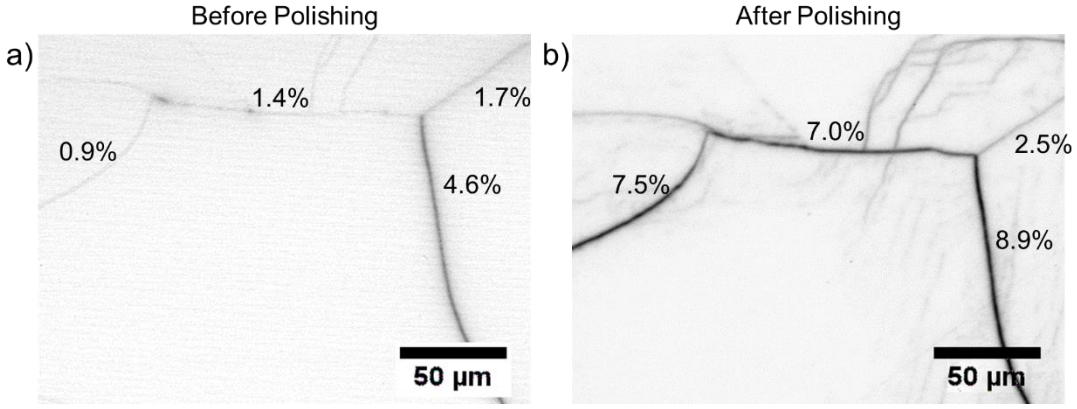


Figure 4.2. Electron beam induced current images of the same wafer before (a) and after (b) a 30 minute colloidal silica polish. EBIC contrasts for a number of grain boundaries are displayed on the figure.

4.2.2 Electron Backscatter Diffraction

The boundaries measured via EBIC in Figure 4.1 were confirmed as small angle grain boundaries using EBSD (Figure 2a). Interestingly, before polishing, the more recombination active grain boundaries were found to have the greatest misorientation

(Figure 2b). This corresponds to a higher dislocation density along the grain boundary and therefore more sites for impurities [223]. After a 12 hour colloidal silica polish this trend becomes less evident, with a notable outlier at a misorientation of 2°, however a general increase in the EBIC contrast for greater grain boundary misorientations was observed.

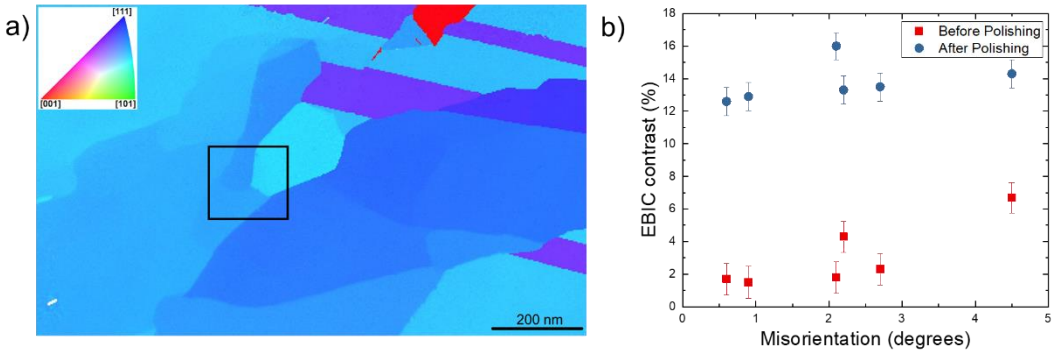


Figure 4.3. a) EBSD inverse pole figure (IPFY) map of sample measured in Figure 4.1, with region selected for EBIC at greater magnification marked. b) EBIC contrast for grain boundaries marked in Figure 4.1 c and d plotted against grain boundary misorientation before and after a 12 hour colloidal silica polish.

Similarly to Figure 4.3, the grain boundaries analysed after a 30 minute colloidal silica polish were found to be small angle grain boundaries (Figure 4.4). After 30 minutes of colloidal silica polishing, all grain boundaries increase in EBIC contrast. By comparing EBSD and EBIC, the increase in recombination activity with greater misorientation, observed in Figure 4.3, is less clear in Figure 4.4, with the lowest EBIC contrast after polishing observed at the greatest misorientation.

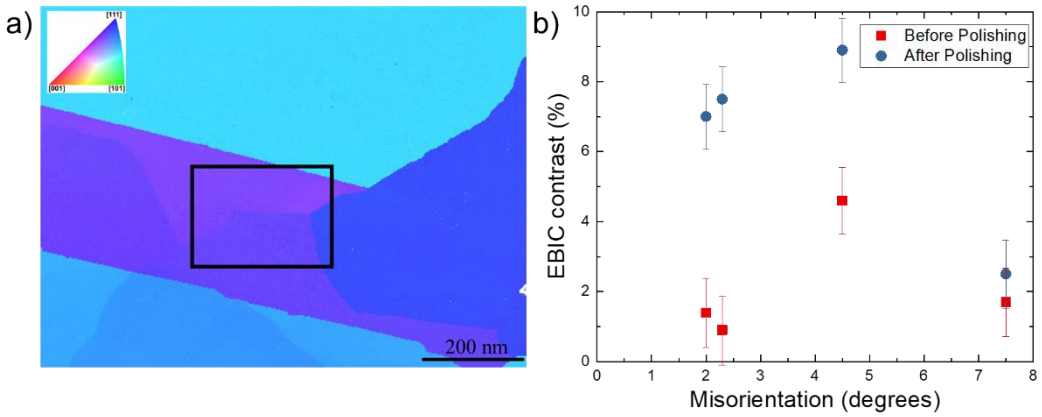


Figure 4.4. a) EBSD inverse pole figure (IPFY) map, with the region measured using EBIC in Figure 4.2 marked. b) EBIC contrast for grain boundaries marked in Figure 4.2 plotted against grain boundary misorientation before and after a 30 minute colloidal silica polish.

4.2.3 Atom Probe Tomography

In order to determine which impurities are introduced from the colloidal silica polishing process and the extent of this contamination, APT of an identical grain boundary in sister wafers with and without a 12 hour colloidal silica polish was performed. This analysis was performed on different wafers than that analysed via EBIC and EBSD. Figure 4.5 shows APT datasets for the unpolished specimen, containing a grain boundary enriched in oxygen, carbon and nitrogen. These light elements have been found to decorate grain boundaries in the literature [214] and their effect on recombination activity was discussed extensively in Section 2.1.2.1. In addition, two regions of interest (60 nm x 20 nm x 150 nm) are marked on the figures. The region shown in red contains the matrix, while the blue region encompasses the grain boundary. The regions are placed next to each other in the dataset, in order to

reduce the effect of the evolution of background throughout the APT analysis [185], so as to enable a direct comparison between the sampled sub-volumes.

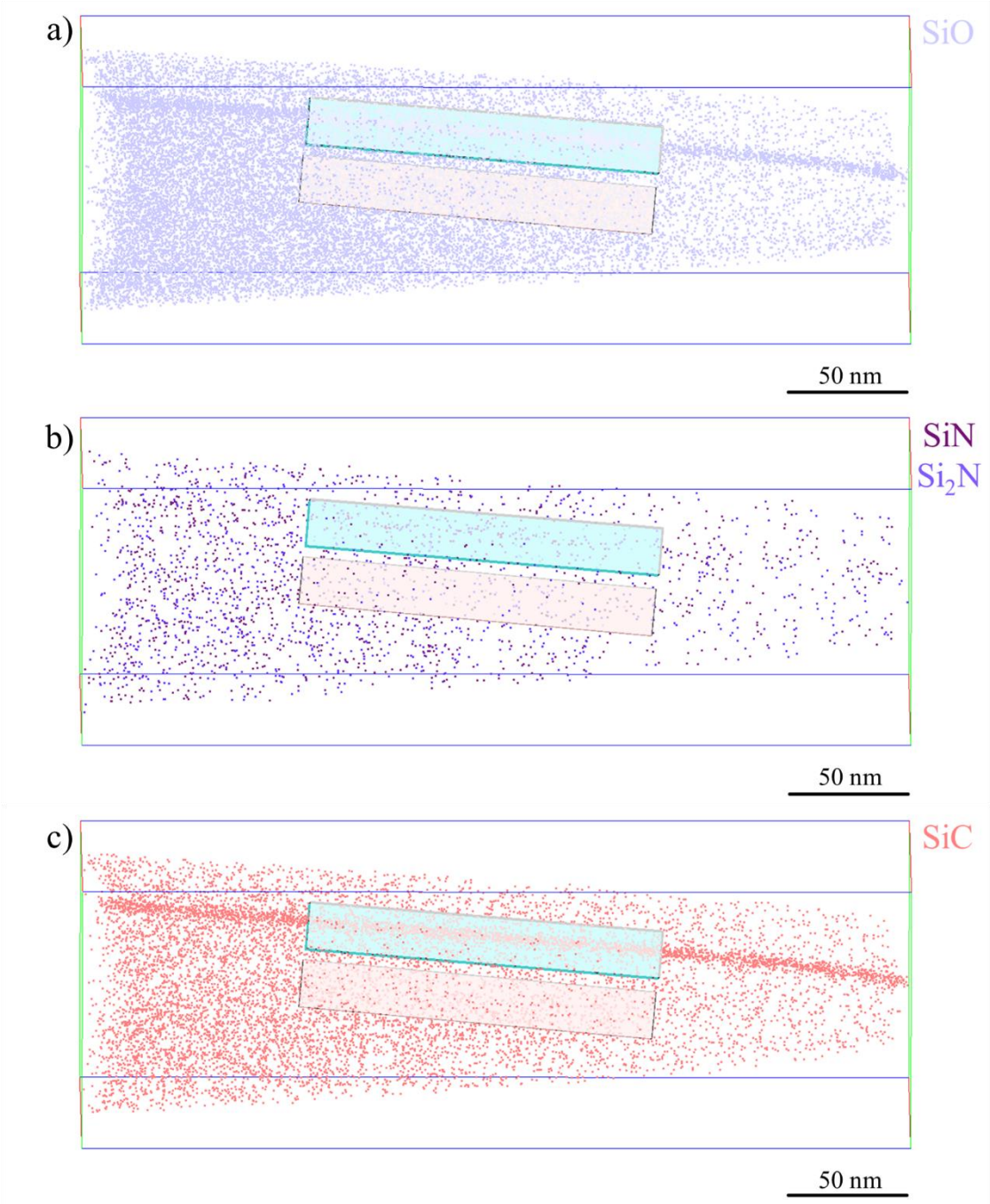


Figure 4.5. APT analysis of the sample which was not exposed to colloidal silica polishing, showing decoration of the grain boundary by a) oxygen, b) nitrogen and c) carbon. Boxes outlining regions of interests containing the matrix (red) and the grain boundary (blue) are marked.

As previously stated, nickel and copper are known impurities in multicrystalline silicon and possible candidates for room temperature contamination. Figure 4.6 shows the distribution of nickel and copper in the unpolished specimen. The distribution of these elements are shown as background noise, with no detectable signal of nickel or copper at the boundary (see Figure 4.9).

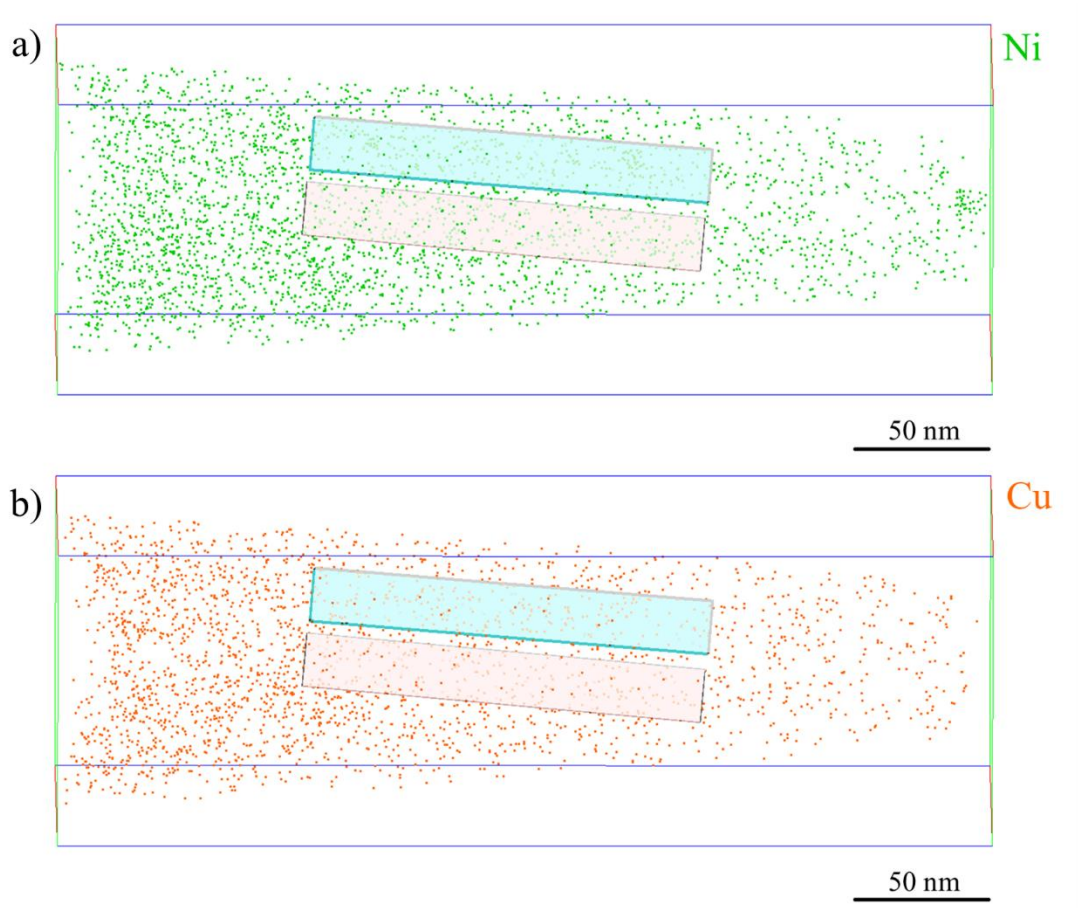


Figure 4.6. APT analysis of the sample which was not exposed to colloidal silica polishing, showing background noise in a) nickel and b) copper. Boxes outlining regions of interests containing the matrix (red) and the grain boundary (blue) are marked.

Similarly, to the unpolished specimen, the polished grain boundary was found enriched in carbon, oxygen and nitrogen (Figure 4.7). As previously described, regions of

interest (60 nm x 20 nm x 150 nm) are shown enclosing the matrix and grain boundary. Since these light elements were found in both the unpolished and polished specimens, we do not believe they are the cause of the significant increase in recombination activity after polishing.

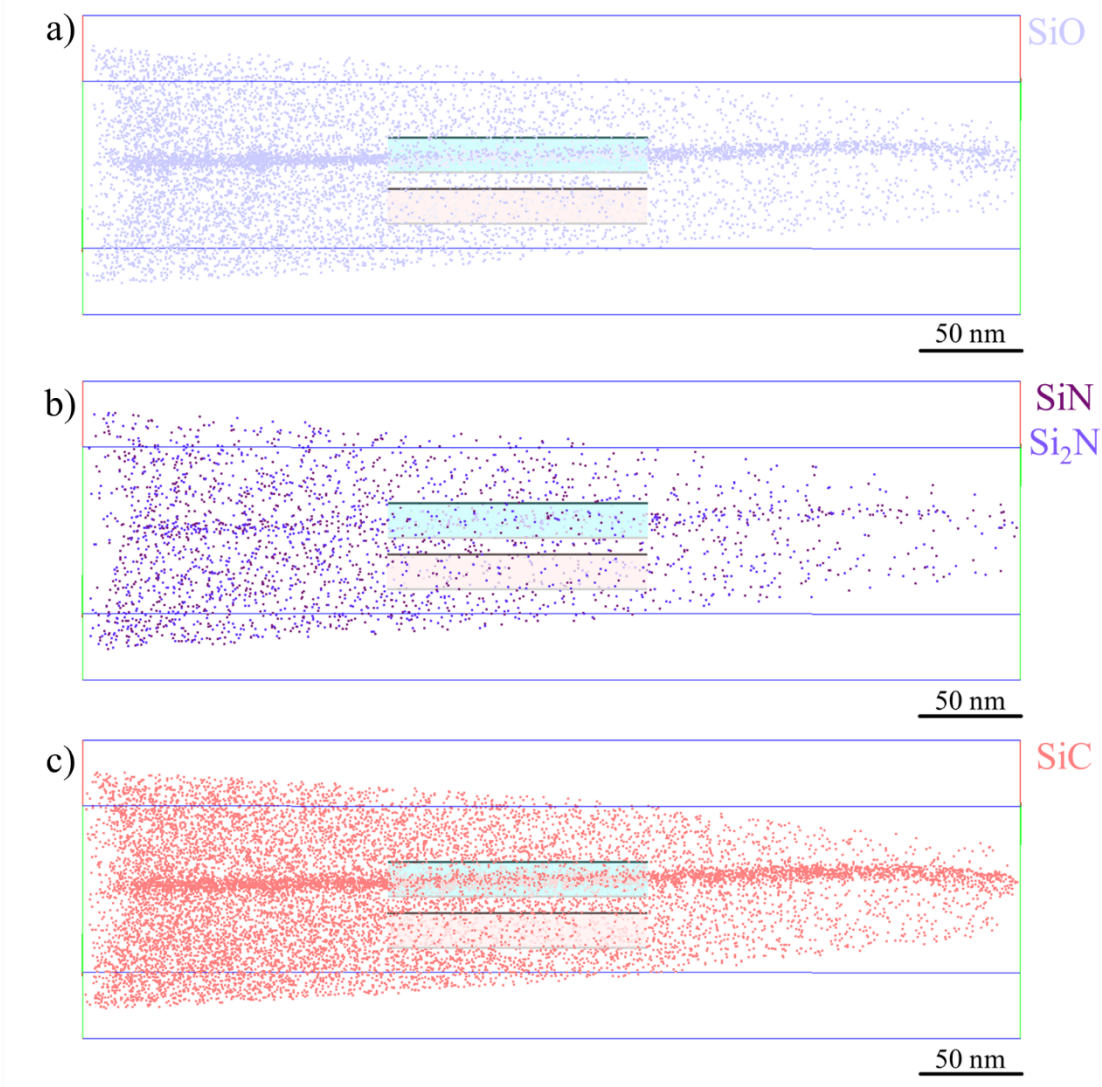


Figure 4.7. APT analysis of the sample exposed to a 12 hour colloidal silica polish, showing decoration of the grain boundary by a) oxygen, b) nitrogen and c) carbon. Boxes outlining regions of interests containing the matrix (red) and the grain boundary (blue) are marked.

In contrast to the unpolished specimen, the grain boundary in the colloidal silica polished specimen is significantly enriched in nickel and copper (Figure 4.8). These transition metals were introduced by the polishing process and are found in substantial quantities decorating the grain boundary.

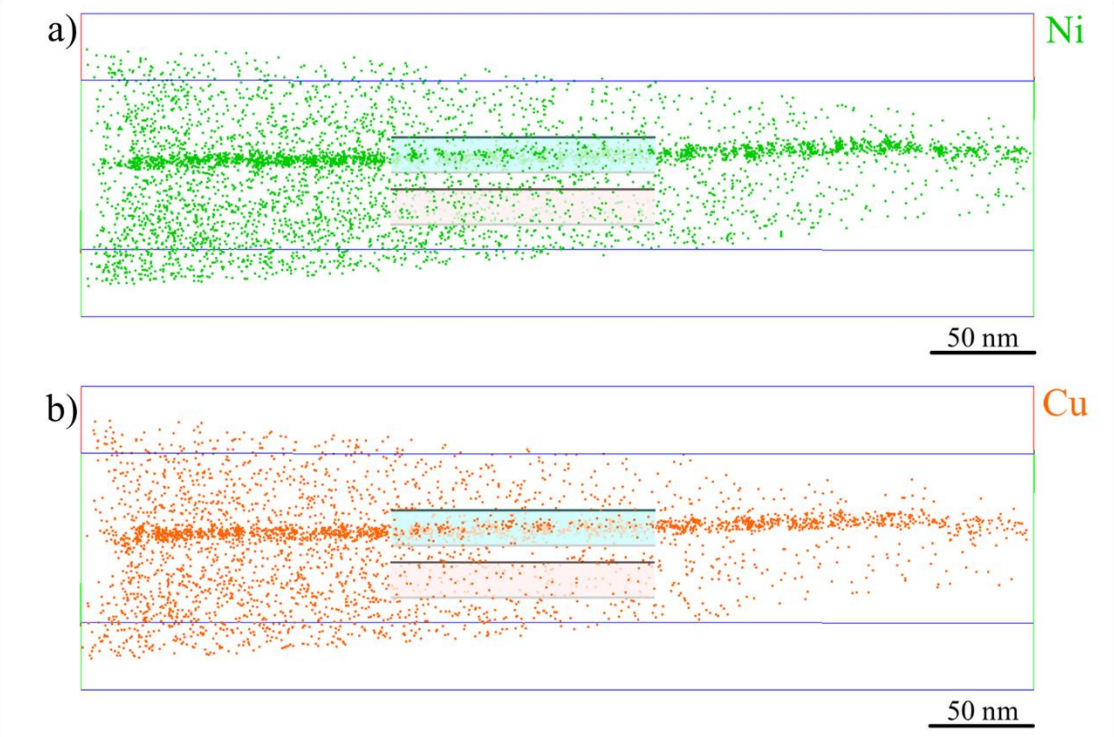


Figure 4.8. APT analysis of the sample exposed to a 12 hour colloidal silica polish, showing decoration of the grain boundary by a) nickel and b) copper. Boxes outlining regions of interests containing the matrix (red) and the grain boundary (blue) are marked.

Further evidence for the introduction of copper and nickel to the grain boundary after colloidal silica polishing is shown in Figure 4.9. This figure displays the mass spectra for the regions of interest containing the matrix and grain boundary of the polished and unpolished specimen. For the unpolished grain boundary (Figure 4.9b), a small peak is observed at 60 Da, which corresponds to the presence of SiO_2^+. No other peaks were observed in the mass-to-charge-state region containing Ni and Cu.

In contrast, the colloidal silica polished grain boundary mass spectra contains large peaks of the naturally occurring isotopic ratios corresponding to Ni and Cu. Notably, no Ni or Cu was detected above background noise in the matrix (Figure 4.9c), indicating that the transition metals are strongly bound to grain boundaries and are depleted in the matrix.

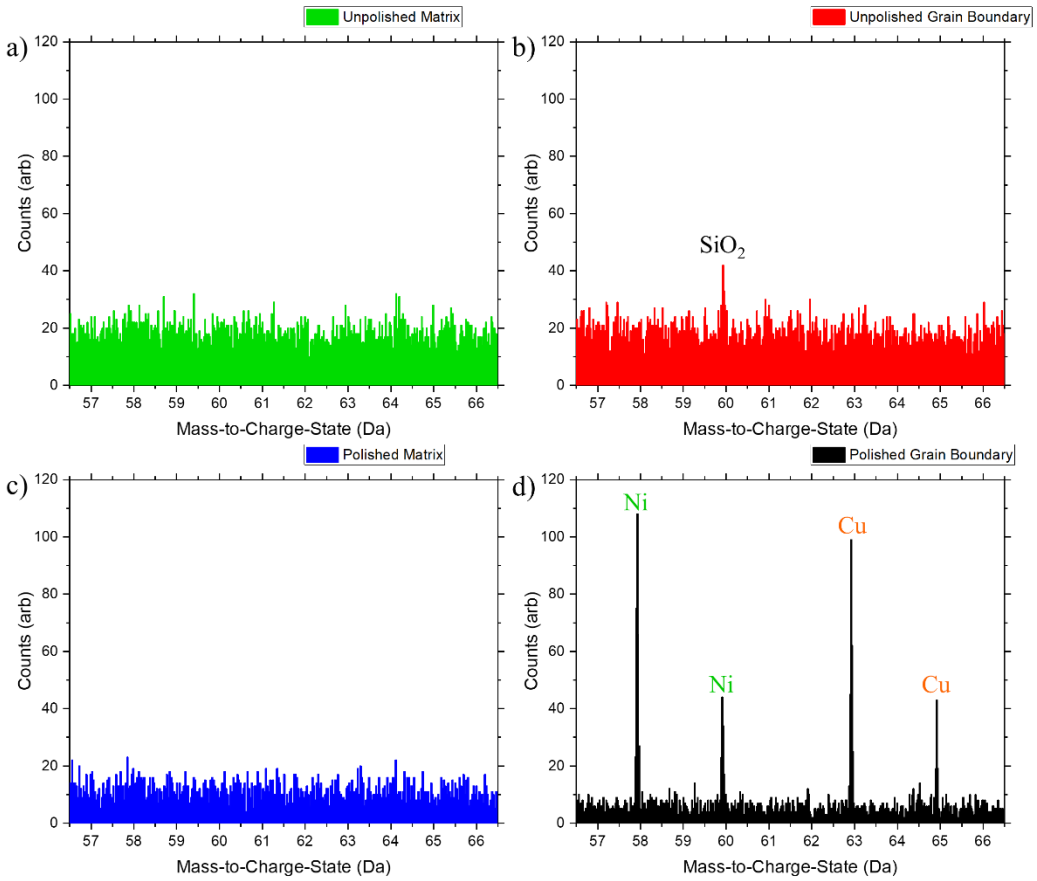


Figure 4.9. Mass spectra of two regions of interest containing the matrix and grain boundary for both the unpolished and 12 hour colloidal silica polished samples.

4.3 Discussion

Unintentional incorporation of metallic impurities during the various processing stages of the silicon wafer is a significant issue in the silicon photovoltaics community, since such small levels of impurities can be extremely detrimental to device performance and high diffusivity of some transition metals in Si. Nickel and copper have both been identified as potential contaminants, which significantly hinder the efficiency of solar cells [7].

Here, the effect of colloidal silica polishing, to produce a flat surface prior to microscopical analysis, has been investigated. The effect of colloidal silica, a widely used process to create flat surfaces prior to microscopy, on the electrical properties was examined using EBIC mapping (Figure 4.1). After polishing for 12 hours, all of the measured grain boundaries became much more electrically active. In addition, intragrain dislocations appear recombination active after polishing. This trend was replicated, even when polishing for the much shorter duration of 30 minutes, with significant increases in defect recombination activity (Figure 4.2).

Since it is known that clean dislocations are essentially electrically inactive [77], the activation after polishing indicates decoration by impurities in the polishing solution. This phenomenon was previously noticed by Kittler and Seifert [76], who commented on the ‘peculiar’ influence of polishing on (EBIC) contrast. They noted that dislocations, which were previously inactive became electrically active at room temperature. However, no reference to contamination was given, since no direct evidence of contamination at defects was achievable at that time.

The source of this contamination during the colloidal silica polishing process is unknown, although it is well known that such polishing can contain and introduce significant levels of impurities [224], [225]. An additional source of contamination, is from the distilled water used to clean the samples and also the polishing pad itself. A notable factor, which may contribute significantly to the levels of contamination observed, is the high pH of the polishing solution. In general, basic solutions are used to remove organic contaminants and acidic solutions are more effective at removing heavy metallic contamination [226]. It is for this reason, in the solar cell community, chemomechanical polishing slurry chemistries have been optimised to limit contamination [207]. However, we still believe that many Universities still make EBIC specimens without recourse to carefully controlled clean room environments and thus the findings of this research, that colloidal silica polishing can introduce electrically active impurities at room temperature, are relevant to much other EBIC work in the literature.

The grain boundaries analysed by EBSD were found to be primarily small angle grain boundaries (Figure 4.3, Figure 4.4). These boundaries are often found to be considerably recombination active, and so appreciably reduce the efficiency of multicrystalline silicon solar cells [227]. In the work of Wang et al. [223], small angle grain boundaries can be well described by a collection of Lomer dislocations, with increasing dislocation densities at greater misorientations. The increased dislocation density at greater misorientations results in a larger number of sites to accommodate impurities and hence increased grain boundary recombination [31]. A notable outlier to this trend is seen in Figure 4.3b, where the grain boundary with the greatest

misorientation also had the lowest EBIC contrast after polishing. This replicates the work by Sameshima et al. [89], who found that misorientation was not the sole indicator of recombination activity.

In order to determine the cause of the resultant activation of defects, APT of a grain boundary before and after polishing, in sister wafers was performed. This technique provides both compositional and spatial information of impurities at individual crystallographic defects. The light elements carbon, nitrogen and oxygen were found to decorate the grain boundaries in the unpolished (Figure 4.5) and polished (Figure 4.7) datasets. Since substantial levels of these impurities are found at the boundary before and after colloidal silica polishing, they are not thought to be the cause for the significant increase in defect recombination activity. More details on the decoration of defects via light elements are presented in Chapter 5.

The major difference between the unpolished and colloidal silica polished grain boundaries, is the significant quantity of Cu and Ni found to segregate to the boundary after polishing (Figure 4.8). This is further evidenced by comparing the APT mass spectra of the grain boundary before and after colloidal silica polishing (Figure 4.9). The segregation of these transition metals to crystallographic defects is believed to be the cause of their electrical activation after polishing [228].

Since this study analysed HPMC-Si, which has a relatively high density of grain boundaries, it is interesting to note the effect of such defects. It is well known that impurities segregate to crystallographic defects, regions of local disorder, in order to

relieve strain caused by lattice mismatch [213]. Since the EBIC contrast of grain boundaries and intragranular dislocations becomes much greater after polishing, it is evident that Cu and Ni diffuse to and segregate at these defects at room temperature. However, since Cu and Ni are found co-located at the grain boundary, it is not possible to distinguish how much of a role each impurity plays in the increase grain boundary recombination activity.

Cu and Ni have a well-known affinity to grain boundaries in silicon, with previous work by Rizk et al., using transmission electron microscopy, clearly confirming the preferential formation of nanosize Cu and Ni precipitates at the grain boundary [229]. Additional work by Ohno et al., using APT, co-segregated Ni and Cu precipitates were observed at specific grain boundary sites [155]. In this study, both Cu and Ni were observed to decorate the grain boundary, but no evidence of large precipitates was seen.

From EBIC measurements, it is clear that not all grain boundaries respond equally to colloidal silica polishing. Indeed, certain grain boundaries that had very low recombination activity prior to polishing become significantly more recombination active. We speculate this relates to the presence of large concentrations of grain boundary precipitation sites, which are not previously occupied. This is analogous to the internal gettering and activation of previously undecorated random angle grain boundaries during phosphorus diffusion gettering [90].

Although APT analysis was performed on wafers exposed to a 12 hour colloidal silica polishing process, results in Figure 4.2, clearly show that polishing for just 30 minutes resulted in a significant increase in defect recombination activity. The average increase in EBIC contrast of 4 times for the 30 minute colloidal silica polished sample compares to an average increase of 6 times for the 12 hour polished sample, shown in Figure 4.1. Considering that this sample was polished in colloidal silica for over 24 times longer, we can presume two possibilities. First, impurities reach the defects much more quickly to begin with and then the concentration starts to plateau at the defects. The second possibility is that the electrical activity does not respond linearly to the impurity concentration. Indeed the work by Fell et al. [15] concludes that the recombination activity responds linearly to the impurity concentration up to the point at which the Fermi level becomes pinned to the defect states. Atom probe tomography is a powerful tool that, in correlation with EBIC, could answer this question.

4.4 Conclusions

In this chapter, the effect of colloidal silica polishing, under standard laboratory conditions, on high performance multicrystalline silicon was determined. From the use of EBIC on the same wafer, before and after colloidal silica polishing, a large increase in recombination activity at both grain boundaries and previously inactive intragranular dislocations was revealed. It was therefore concluded that using colloidal silica polishing on silicon, to create a flat surface, can introduce copper and nickel that decorate crystallographic defects, even at room temperature. Such polishing should be avoided if meaningful conclusions are to be drawn regarding the electrical activity of

different defects in silicon. Instead, satisfactory specimens may be produced by a combination of diamond polishing followed by wet chemical etching.

5 The Effect of Gettering and Conventional Hydrogen Passivation on High Performance Multicrystalline Silicon

5.1 Introduction

Phosphorus diffusion gettering and hydrogen passivation are two of the most essential and industrially relevant techniques used in the photovoltaics community, as described in Section 2.4 and Section 2.5. Although widespread, understanding of the mechanisms underpinning these techniques has been limited by the complexity of studying the individual atomic level defects, affected by the application of these processes [32], [230]. There is currently an incomplete understanding of which impurities and at which particular locations are especially hazardous to solar cell efficiencies. Additionally, it is still unknown why some crystallographic defects remain electrically active after processing, while some become electrically inactive.

In this chapter, the effect of phosphorus diffusion gettering (PDG) and hydrogen passivation are studied on numerous length scales. As discussed in Section 3.3 p-type high performance multicrystalline silicon (HPMC-Si) is a commonly used material for modern solar cells and hence was chosen for this study. The effect of processing was studied using four directly adjacent sister wafers (as described in Section 3.3) from the ingot. Details of the processing steps performed are given in experimental methods, in Section 3.2. One of the wafers was analysed subsequent only to saw damage removal and texturing, termed As-Cast. The second wafer underwent a hydrogenation step via the deposition and firing of a surface nitride (H Passivated), the third underwent a PDG

process (Gettered) and the final wafer had both a PDG process and a hydrogenation step (Gettered + H).

In contrast to previous studies, which were limited in the length scale studied from the microscale down to the atomic scale [158], this study is unique in regards to the large variation in length scales studied. This approach was developed to provide a detailed and comprehensive analysis of the material. As previously covered in Section 3.2, the characterisation techniques range from the macroscale of PL, to the microscale of EBIC mapping and EBSD and finally to the nanoscale and even atomic scale with TEM and APT.

5.2 Photoluminescence

Photoluminescence is an extremely effective tool, which allows for large-scale mapping of electrical activity across a 6 inch by 6 inch wafer (Section 3.13). Figure 5.1 displays the PL images of the H passivated, and gettered and hydrogen passivated wafer. Although high efficiency has been achieved in large areas of the wafer, it is apparent that a number of regions remain highly recombination active in both PL images. These consist of clearly visible electrically active grain boundaries and a number of intragrain regions. Note that, also visible on the right PL image is a central large dark vertical line, which is a scratch from the handling process and was therefore discounted in the analysis.

Since PL examines large 6 inch by 6 inch wafers, sectioning into smaller areas for micro-analysis was required. Three regions were selected, labelled A, B and C (Figure

5.1). Region A is a large region of high recombination, which significantly reduces the overall efficiency of the wafer. These low lifetime regions are often assumed to be the result of dislocation clusters and networks [231], [232], however little further characterisation in the literature has been performed. Region B consists of a single recombination active grain boundary, isolated from other boundaries by large grains. Finally, Region C consists of a number of apparent twin boundaries and two recombination active grain boundaries, whose electrical activity appears to terminate within the wafer.

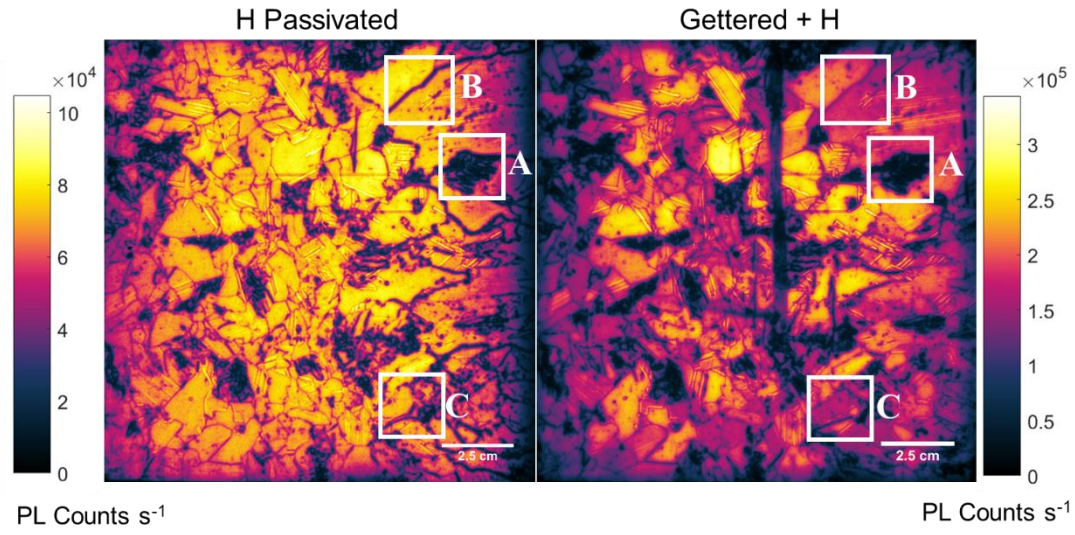


Figure 5.1. Photoluminescence maps of the H Passivated and Gettered + H (passivated) wafers. Marked are three regions (A, B and C), which were selected for further analysis. Note the different PL counts scales for the two PL maps. An exposure of 1 sun for 0.1 s was used for both images. Images were acquired at The University of New South Wales by P. Hamer.

5.3 PL Region A

The region marked as Region A in the PL images (Figure 5.1) is of concern to solar cell manufacturers. This region is extremely recombination active and covers a large

area of the wafer. However, it is very difficult to resolve the structure of defects in this area from PL alone and therefore further microscopical techniques were used.

5.3.1 Electron Backscatter Diffraction

Electron backscatter diffraction, employed on the highly recombination active Region A in the As-Cast sample, is shown in Figure 5.2. This technique provides crystallographic information regarding grain boundary type and misorientation. Apart from the twin Σ3 boundary at the top left corner, the region consists of an extremely high density of low angle grain boundaries.

These low angle grain boundaries were made visible in EBSD by using grain reference orientation deviation (GROD) mapping. This considers the whole region as a single grain and plots the variation in misorientation of individual pixels to the average grain orientation as different colours. As can be seen in the GROD angle histogram, the majority of low angle grain boundaries measured have a misorientation between 0.5° – 3.5°.

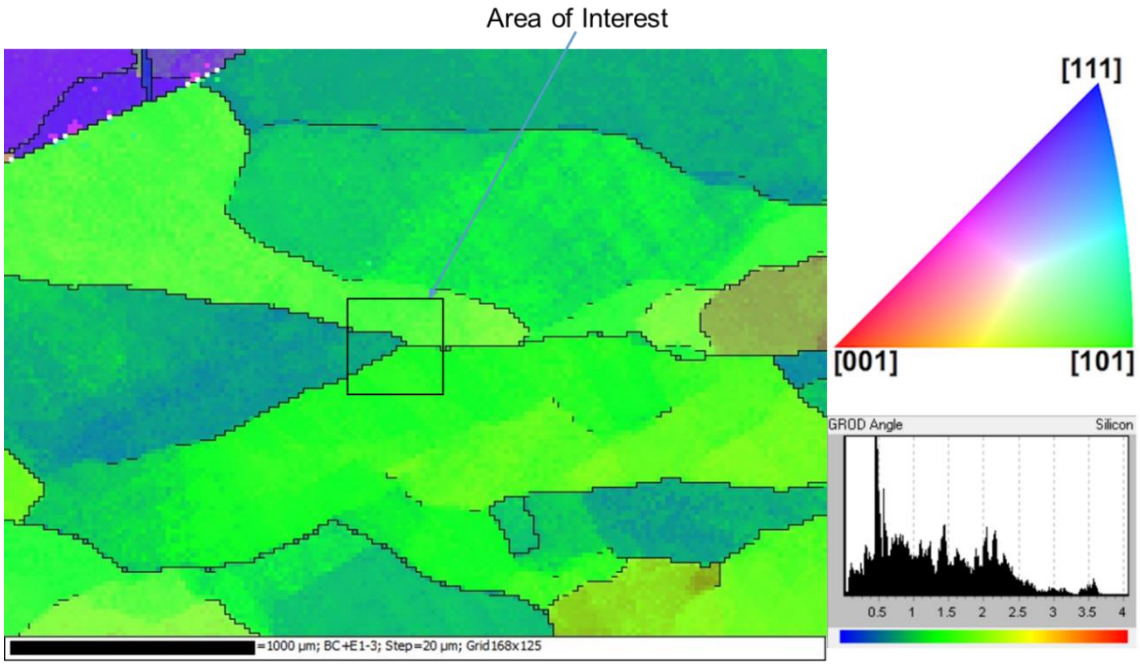


Figure 5.2. Electron backscatter diffraction inverse Y pole figure map (IPFY) of the As-Cast wafer of Region B. The grain reference orientation deviation (GROD) map is also shown overlaid on top.

5.3.2 Electron Beam Induced Current

The electrical activity of Region A, taken at a much greater resolution than in PL, was acquired using electron beam induced current (EBIC) mapping. The significant and detrimental effect due to the presence of large densities of low angle grain boundaries, is clearly seen in Figure 5.3. After gettering, the grain boundaries become significantly more recombination active. Since PL averages over a large area, the entire region appears electrically active, with insufficient resolution to determine the individual boundaries. Interestingly, this result casts doubt on whether any large recombination active intragrain regions seen in PL can be ascribed to large dislocation clusters without further analysis, as they are commonly attributed [231], [232].

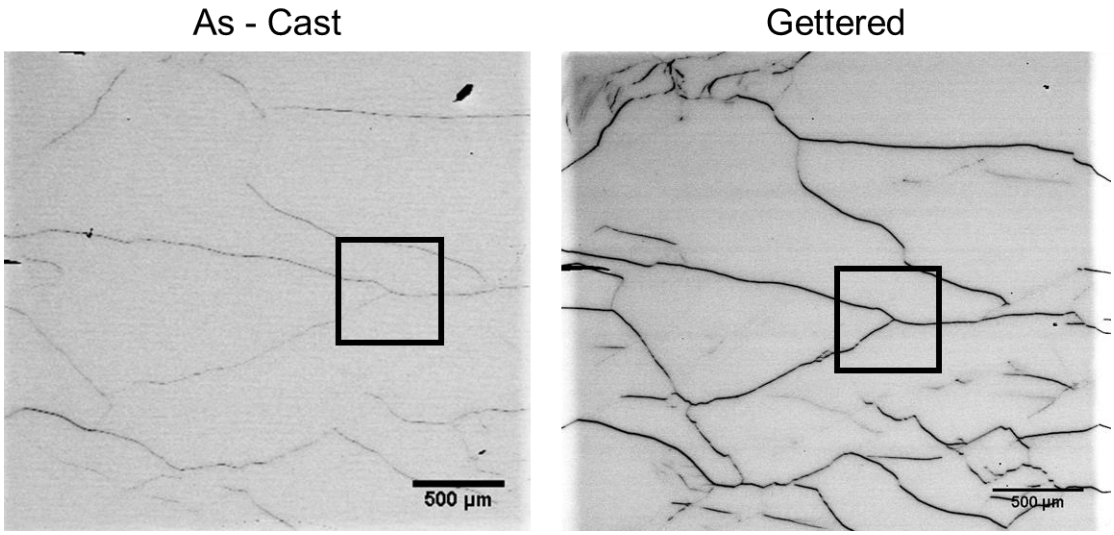


Figure 5.3. Electron beam induced current mapping of Region A for the As-Cast and Gettered wafers. The region selected for higher magnification and quantitative EBIC mapping in all three sister is marked.

A quantitative EBIC contrast comparison of the triple points marked in Figure 5.3, for the four processing conditions analysed, is shown in Figure 5.4. Since the wafers were sisters, i.e. taken from directly adjacent regions in the ingot, they are not precisely identical. However, assuming the distribution of impurities at the grain boundaries over such a short distance is negligible; they can be viewed as near identical grain boundaries in the different samples.

The recombination activity of the grain boundaries increased significantly after phosphorus diffusion gettering. This is thought to be caused by impurity redistribution during the high temperature and fast cool of during the gettering. The grain boundary recombination activity does however decrease with the application of hydrogen passivation. This supports the hypothesis that hydrogen bonds to impurities at

crystallographic defects, thereby eliminating dangling bonds and removing deep levels in the band gap [132]. The grain boundary recombination activity in the gettered and hydrogen passivated sample is, however, still greater than in the As-Cast state, suggesting that hydrogenation is not completely effective in passivating all the impurities gettered to the grain boundary during the PDG process. The lowest grain boundary EBIC contrast was observed in the hydrogen passivated sample. In this case, the lack of the high temperature PDG process limits the potential for significant internal gettering, while hydrogen was able to passivate impurities that were present initially at the grain boundary. Also shown on the EBIC micrographs (Figure 5.4) are the regions of grain boundary that were selected for further analysis via TEM and APT.

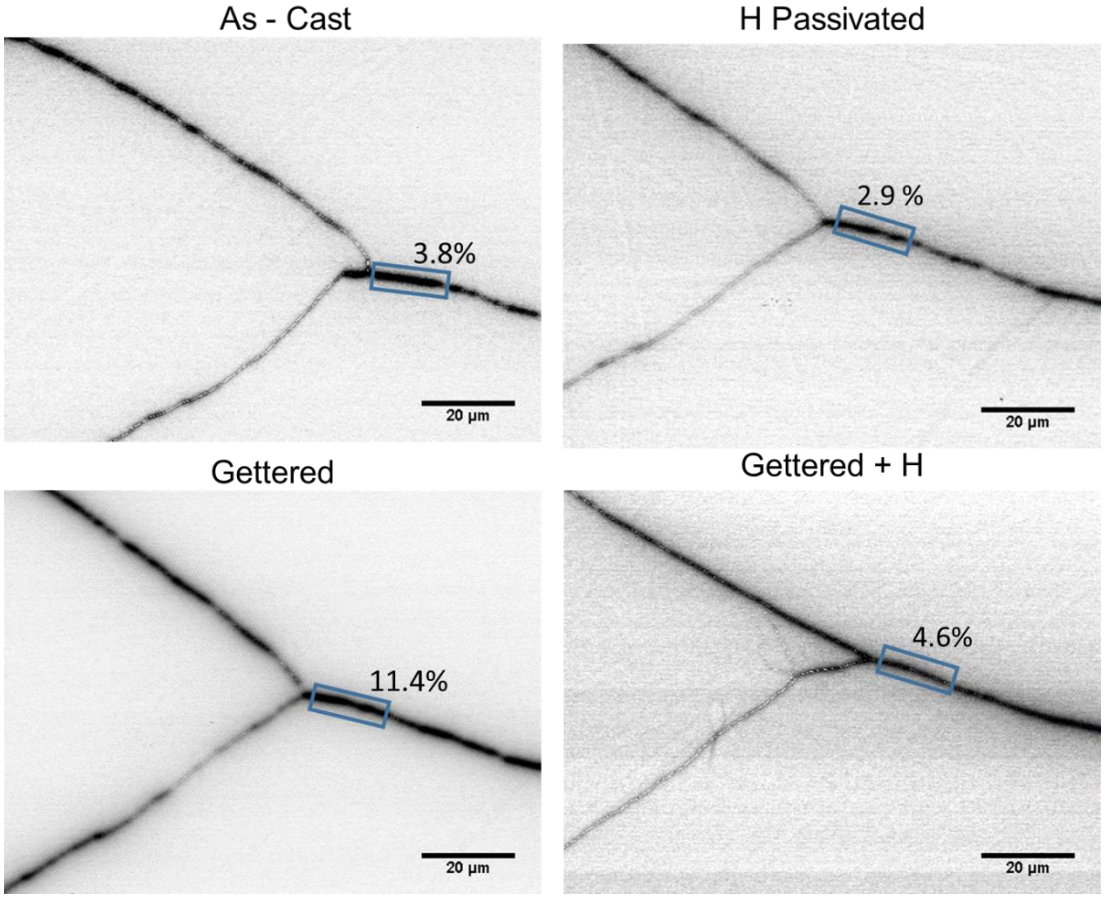


Figure 5.4. Quantitative EBIC of the triple point marked in Figure 5.3 for the As-Cast, H Passivated Gettered and Gettered + H (hydrogen passivation) sister wafers. The EBIC contrast for the regions marked are shown on the figure. Additionally, the marked regions indicate the section of the grain boundaries, which were further analysed using TEM and APT.

5.3.3 Transmission Electron Microscopy

Transmission electron microscopy (TEM) was used extensively in this study, as an effective pre-screening technique for specimens prior to atom probe. The use of this technique to ensure the grain boundary is at the apex of the needle, was found to vastly increase the number of successful analyses incorporating a grain boundary.

TEM images of the grain boundaries from sister wafers, measured by EBIC and EBSD are shown in Figure 5.5. The low angle grain boundaries in each of the samples consisted of a series of dislocations in a line, which compensate for the observed misorientation. Since the TEM was performed on APT needles using the custom single tilt holder, determining the exact type of dislocations and grain boundary type was difficult. The boundaries are, however, thought to be pure tilt boundaries due to the similarity in appearance to previous studies and the abundance of such boundaries in HPMC-Si [31], [89]. Pure tilt boundaries are edge dislocations above one another, with the misorientation of the boundary determining the dislocation spacing.

In addition to the presence of dislocations, grain boundary faceting was also observed in both the Gettered and Gettered + H samples, and to a much greater degree the H Passivated sample. Since faceting can occur over large distances, the As-Cast grain boundary will also likely contain faceting but outside the analysis volume. These facets are important as they are often found to contain highly electrically active impurities [159].

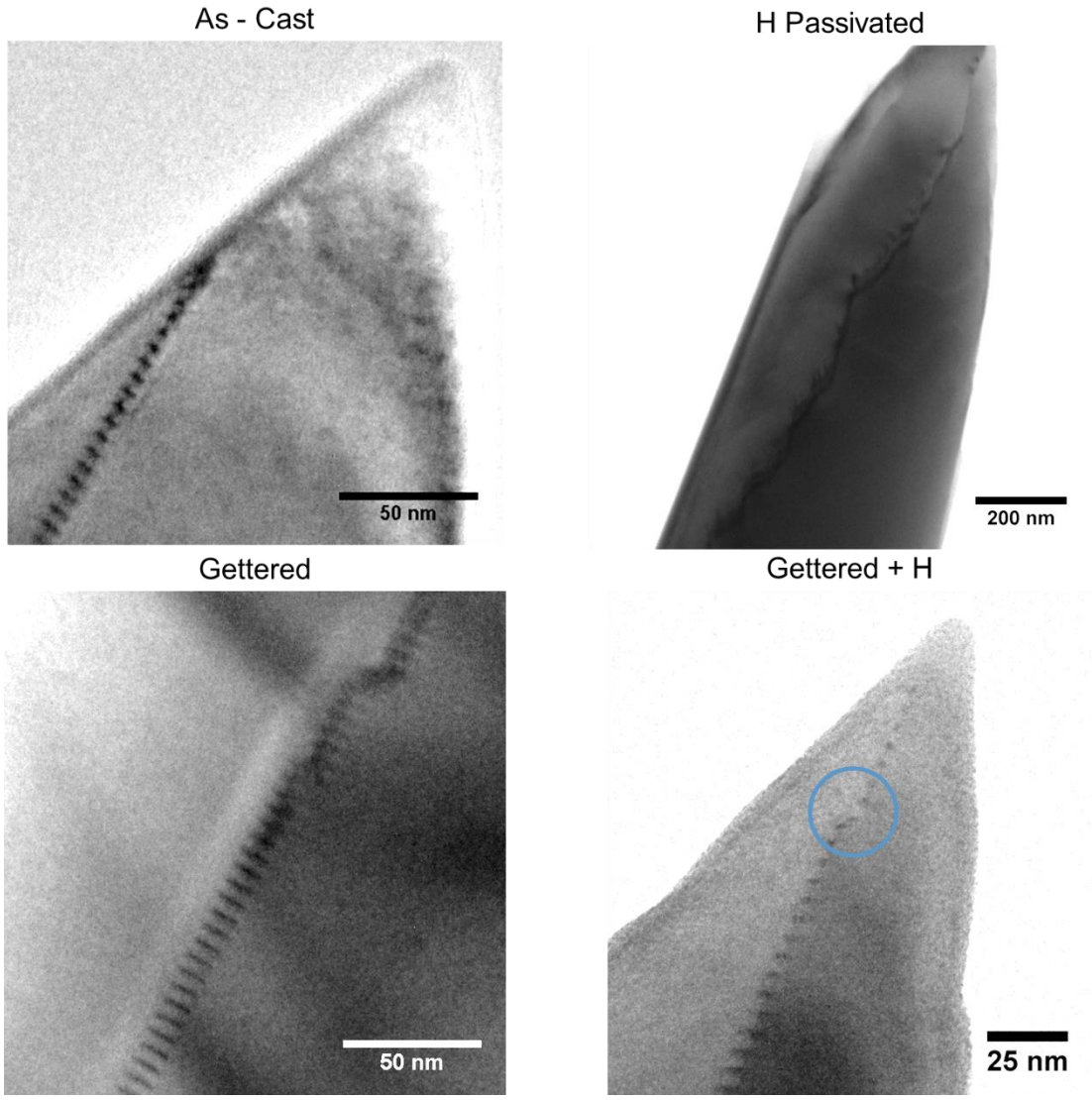


Figure 5.5. Bright field transmission electron microscopy images of APT needles prior to atom probe analysis. All of these needles contain the low angle grain boundaries marked in Figure 5.4. All of the grain boundaries consist of a series of dislocations, on top of one another. Facets in the boundaries are present in the 'H Passivated', 'Gettered' and 'Gettered + H' samples.

5.3.4 Atom Probe Tomography

The atom probe analysis of the As-Cast specimen is shown in Figure 5.6. A clear excess of carbon was observed decorating the individual dislocations, which comprise

the grain boundary. The carbon was detected as the complex molecular ion, SiC^+. The detection of molecular ions is a common phenomenon in APT, in which certain elements are more easily field evaporated as complex molecules. No other impurities were observed segregated to the grain boundary. This includes nitrogen, a commonly observed impurity at silicon grain boundaries [44], [46], which has been previously reported at 35 Da.

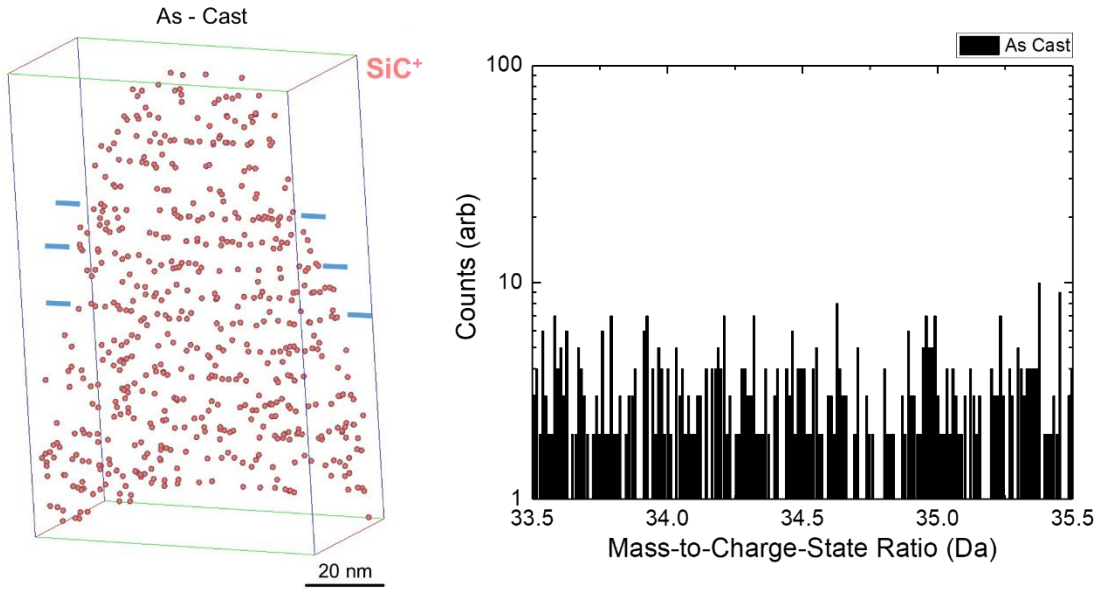


Figure 5.6. Atom probe analysis of the As-Cast low angle grain boundary. An excess of SiC^+ clearly marks the grain boundary running through the needle. The SiC^+ is found to line the individual dislocations, of which a few are marked for clarity. No other impurities are observed above background noise to decorate the grain boundary, with the mass spectra of the grain boundary on the right showing no peak at 35 Da.

With the much greater amounts of faceting observed in the H passivated grain boundary, observed via TEM in Figure 5.5, observing individual dislocations enriched in SiC^+ is much more difficult. Similarly, to the As-Cast sample, no other impurities

were observed at the grain boundary, with only background noise and no discernible peak at 35 Da in the mass spectrum.

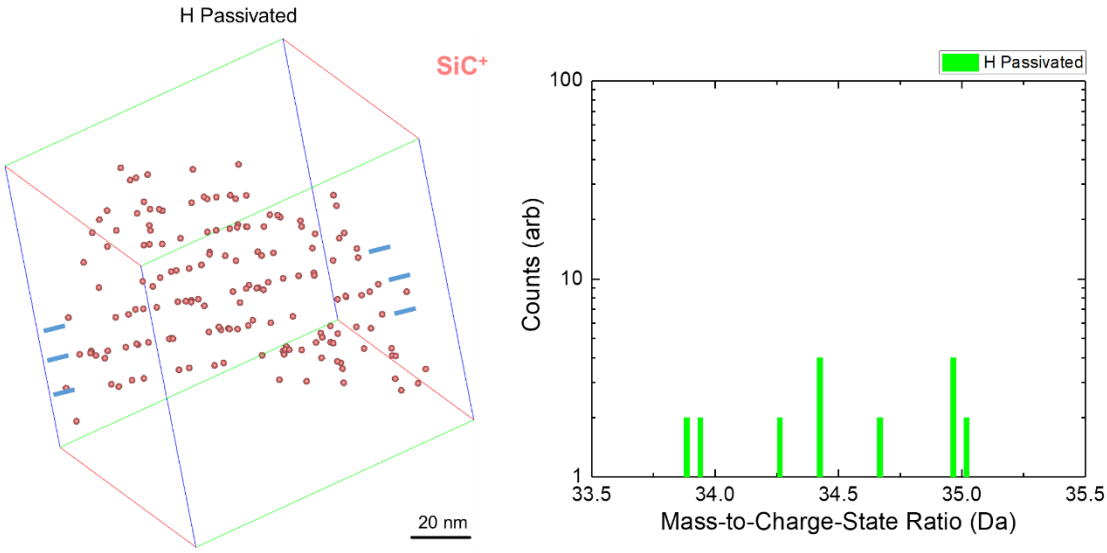


Figure 5.7. Atom probe analysis of the H Passivated low angle grain boundary. An excess of SiC^+ clearly marks the grain boundary running through the needle. The SiC^+ is found to line the individual dislocations, of which a few are marked for clarity. No other impurities are observed above background noise to decorate the grain boundary, with the mass spectra of the grain boundary on the right showing no peak at 35 Da, with just background noise seen.

Figure 5.8 shows the APT analysis of the Gettered sample. As in the As-Cast and hydrogen passivated samples, the small angle grain boundary was seen decorated, with SiC^+ lining each individual dislocation in the boundary. However, in contrast to the As-Cast sample analysis, in this case the presence of nitrogen was observed at the boundary. The nitrogen was detected primarily in the form of Si_2N^{2+} at 35 Da. It also appears distributed heterogeneously throughout the boundary, decorating a number of dislocations at the top of the dataset. Additionally, a peak at 35 Da was found in lower

concentrations at apparent high energy sites [158], [233] throughout the boundary. No other impurities, such as the transition metals copper, nickel or iron, were observed at the boundary.

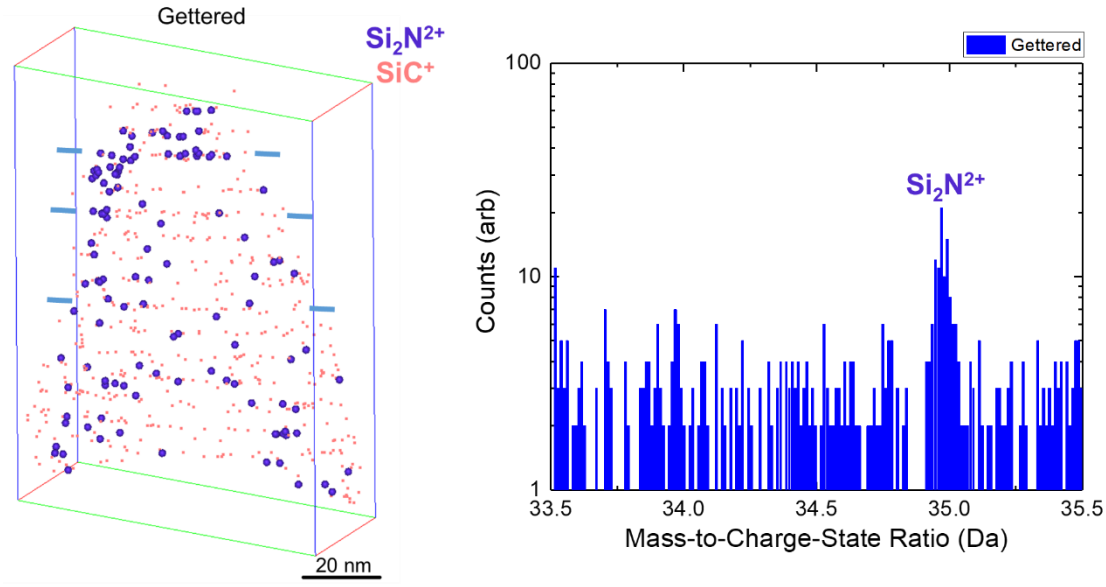


Figure 5.8. Atom probe analysis of the Gettered low angle grain boundary. An excess of SiC^+ clearly marks the grain boundary running through the needle, found to decorate individual dislocations, of which a few are marked for clarity. In addition to the excess of carbon at the boundary, nitrogen was also observed present at the boundary. The nitrogen was observed via the detection of the complex molecule Si_2N^{2+} at 35 Da, with a peak clearly observed in the mass spectra of the grain boundary on the right.

Atom probe analysis of the gettered and hydrogen passivated sample is shown in Figure 5.9. The boundary, as in the case of the other three sister wafers, consisted of grain boundary dislocations decorated by SiC^+. Si_2N^{2+} decorated two dislocations towards the top of the dataset. This correlates strongly to a facet in the boundary, shown in more detail in Figure 5.18. Additional Si_2N^{2+} forms small clusters at various sites throughout the boundary.

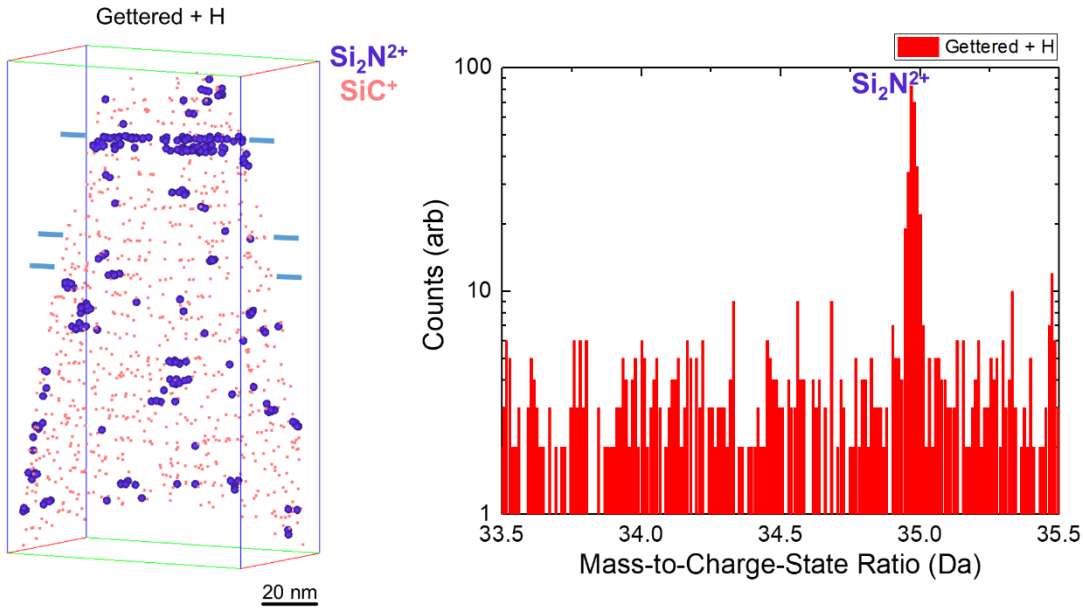


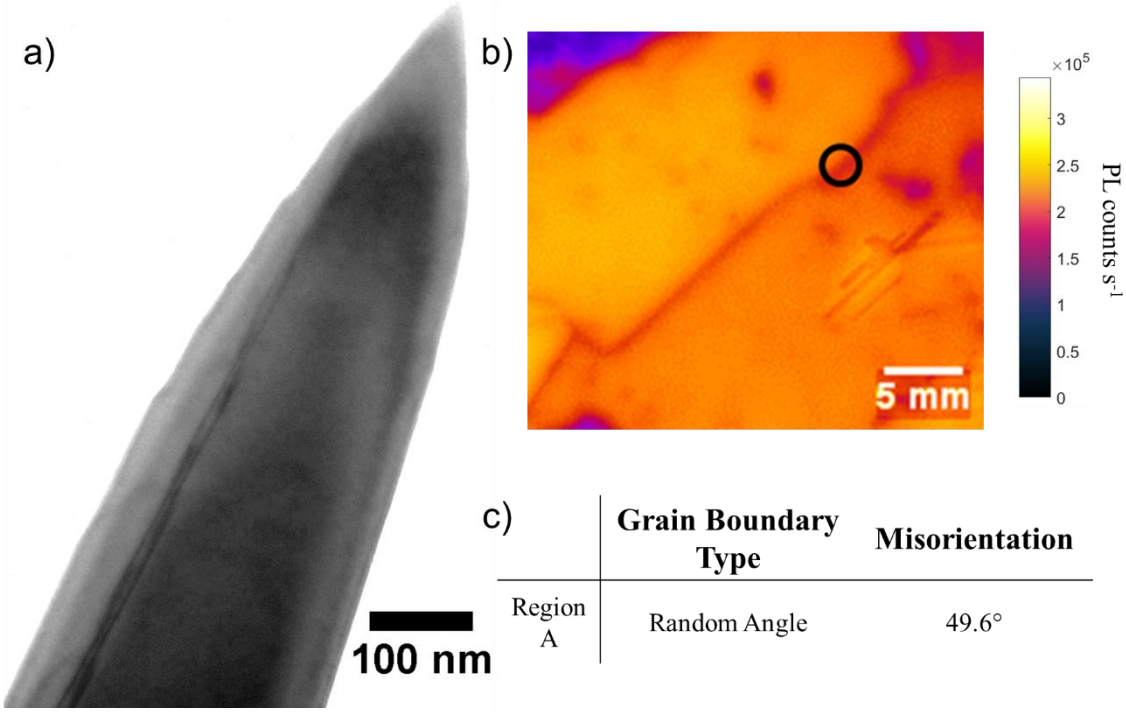
Figure 5.9. Atom probe analysis of the Gettered + H (hydrogen passivation) low angle grain boundary. An excess of SiC^+ clearly marks the grain boundary running through the needle, found to decorate individual dislocations, of which a few are marked for clarity. In addition to the excess of carbon at the boundary, nitrogen is also observed decorating some dislocations and also other seemingly heterogeneous sites through the grain boundary. The nitrogen is observed via the detection of the complex molecule Si_2N^{2+} at 35 Da, with a peak clearly observed in the mass spectra of the grain boundary shown on the right.

5.4 PL Region B

In order to provide a contrast to Region A, in which a high density of grain boundaries are present, a single isolated grain boundary was analysed in Region B (see Figure 5.1). This grain boundary was separated from other boundaries by large grains and is significantly electrically active after gettering and hydrogen passivation, as shown in PL in Figure 5.10b. The grain boundary studied in this investigation was taken from

the gettered sister wafer. These are known to have the greatest amount of recombination, thought to be as a result of increased concentrations of impurities caused by internal gettering to the defects [91].

Figure 5.10a shows TEM of the grain boundary containing APT specimen. Unfortunately, no EBIC was performed on this wafer prior to APT analysis, due to experimental difficulties. The boundary was, however, confirmed using EBSD, as a random angle grain boundary with a misorientation of 49.6° (Figure 5.10c).



c)

	Grain Boundary Type	Misorientation
Region A	Random Angle	49.6°

Figure 5.10. a) Transmission electron microscope image of the APT specimen from the gettered wafer in Region B. b) Photoluminescence of the gettered and hydrogenated wafer, with the region of grain boundary analysed in the gettered sample marked. c) Table showing grain boundary type and misorientation, acquired via EBSD, for the gettered grain boundary analysed.

Atom probe analysis of the grain boundary in Region B, for the Gettered sample is shown in Figure 5.11. The random angle grain boundary was observed to be decorated in a number of impurities including the light elements oxygen, carbon and nitrogen. Additionally, Cu was detected at the grain boundary. Since the grain boundary is separated from other grain boundaries by large grains, it is thought that gettering allows for sufficient amounts of copper to diffuse to the boundary and hence be detected in APT.

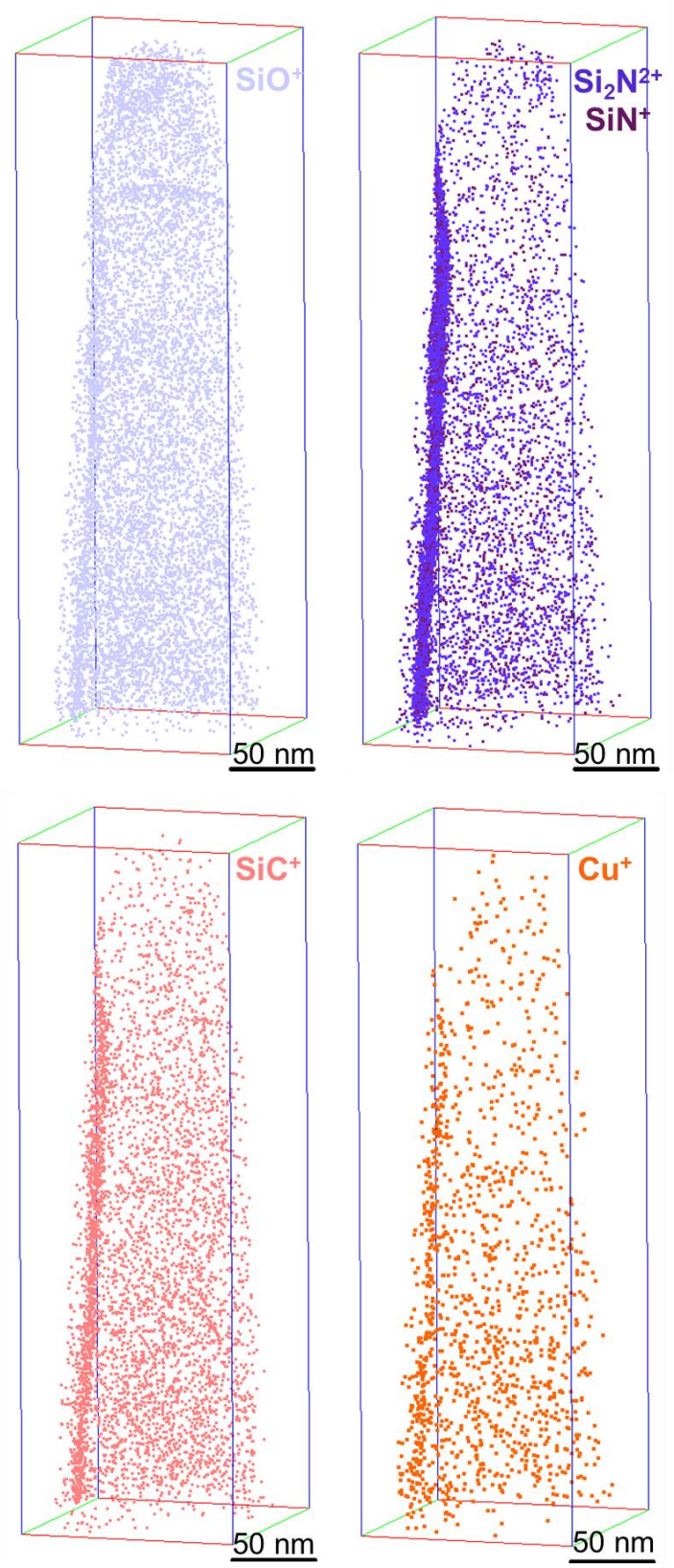


Figure 5.11. Atom probe analysis of the grain boundary from Region B from the gettered wafer. Grain boundary is decorated with an excess in carbon, oxygen, nitrogen and copper.

5.5 PL Region C

The final region studied in this chapter was Region C (Figure 5.1), which contains a significant concentration of both recombination active and inactive grain boundaries. In order to understand the difference between grain boundary type and recombination activity, and provide the most industrially relevant results, the material studied was subject to both phosphorus diffusion gettering and hydrogen passivation prior to analysis. This most closely replicates the finished material in a high performance multicrystalline solar cell.

5.5.1 Electron Backscatter Diffraction

An electron backscatter diffraction map of Region C is shown in Figure 5.12. This region contains a number of Σ3 twin boundaries, marked by thick white lines. These are not usually of concern to a solar cell, as a perfectly coherent Σ3 (111) boundary is recombination inactive and have previously been found to not be decorated by any impurities [30]. The region of interest selected for EBIC and further analysis is marked on the figure.

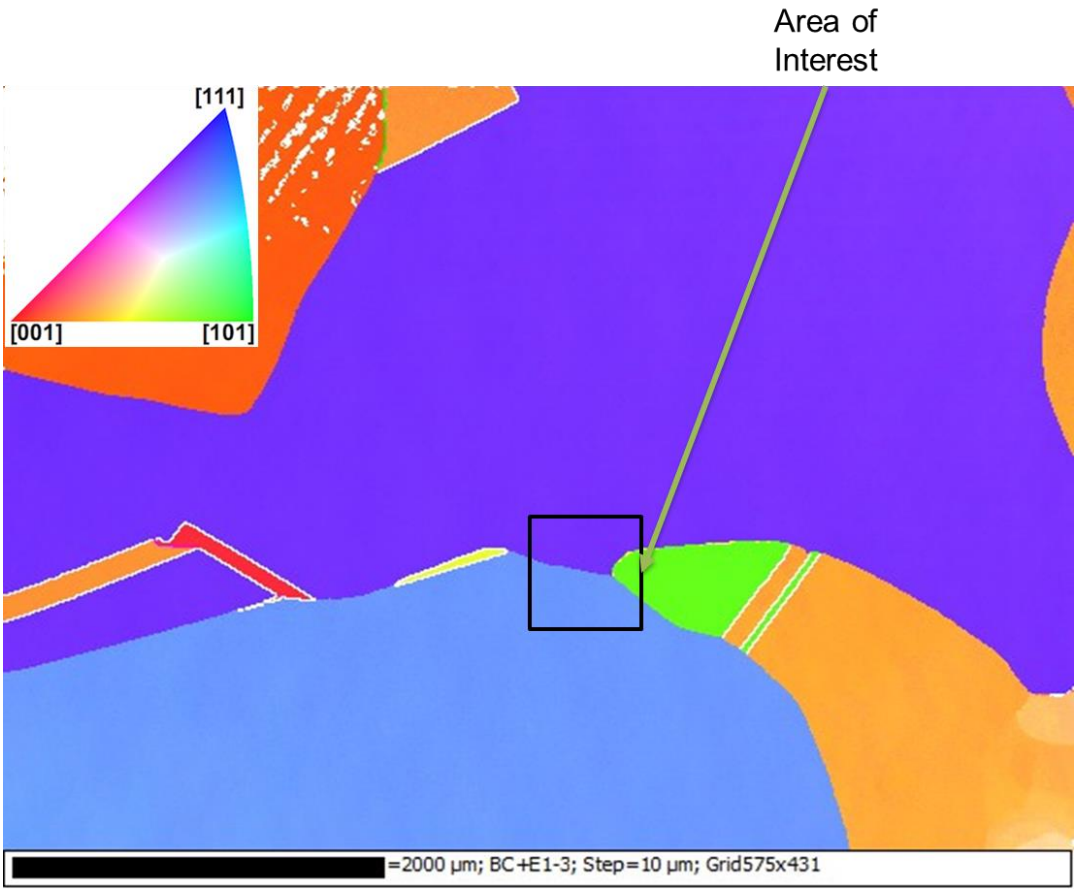


Figure 5.12. EBSD inverse pole figure (IPFY) map of Region C, in the gettered and hydrogen passivated sample. The region selected for further analysis using EBIC and APT is marked.

5.5.2 Electron Beam Induced Current Mapping

Electron beam induced current mapping of Region C, is shown in Figure 5.13, from the gettered and hydrogen passivated sample. Three grain boundaries are observed, with two having no apparent recombination activity and one boundary possessing a strong EBIC contrast of 10.9 %, similar in contrast to the gettered low angle grain boundary in Figure 5.4. The two inactive grain boundaries were only observed by bright lines, caused by surface etch pits from the Secco etching process. In these

regions, greater generation of electron hole pairs occurred due to secondary electron interactions, resulting in greater measured currents.

The inactive grain boundaries, measured after gettering and hydrogen passivation, were both found to be random angle grain boundaries with a misorientation of >40°. These types of grain boundaries are often observed to be strongly recombination active after gettering, but become electrically inactive following hydrogen passivation [91]. In contrast to the inactive grain boundaries, the active grain boundary displayed in Figure 5.13 is a small angle grain boundary with a misorientation of 7.6°. Small angle grain boundaries usually respond much less favourably to hydrogen passivation, which may be the cause of the difference in EBIC contrasts [31].

In an attempt to provide further information into the cause of this vast difference in recombination activity, APT analysis of the active and inactive grain boundaries was undertaken. The regions from which the grain boundary liftout originated are marked in Figure 5.13.

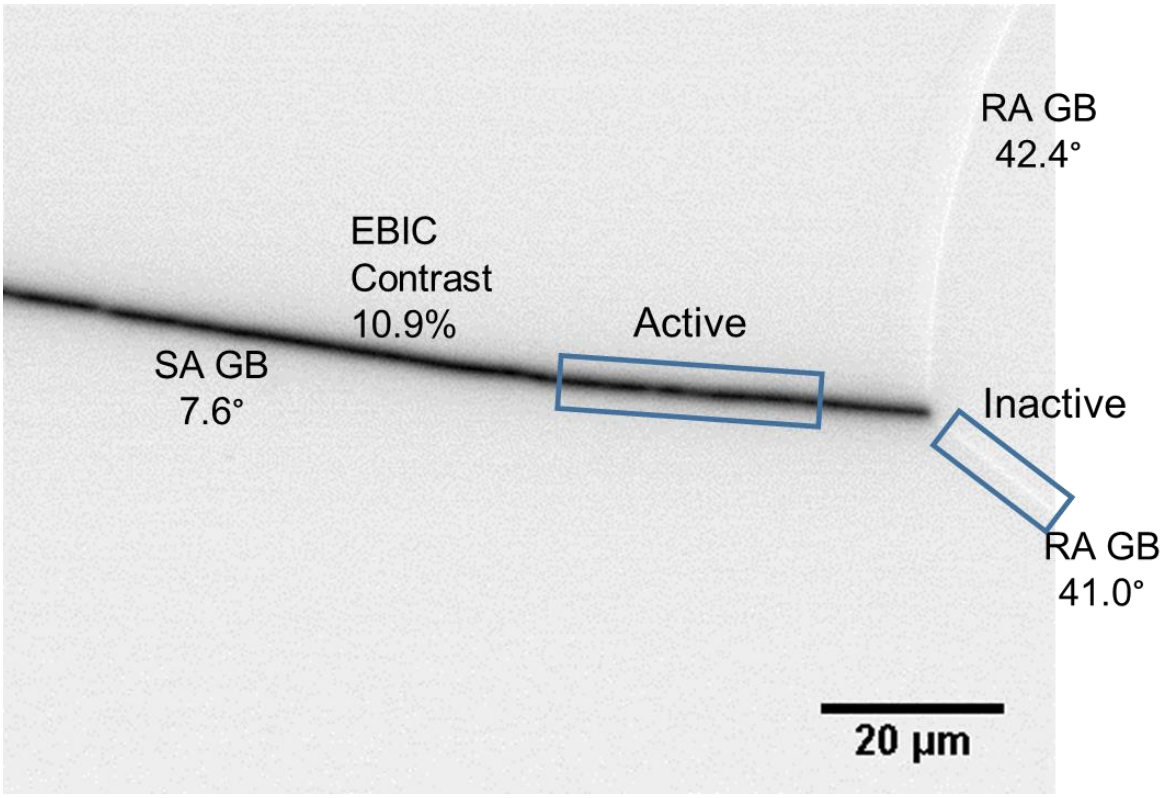


Figure 5.13. Electron beam induced current map of the area marked in Figure 5.12. The active and inactive grain boundaries selected for APT are marked, in addition to the boundary type and misorientation information measured via EBSD, where RA and SA are random angle and small angle grain boundaries respectively.

5.5.3 Atom Probe Tomography

APT analysis of the active and inactive grain boundaries are shown in Figure 5.14 and Figure 5.15 respectively. Both grain boundaries contain the light elements nitrogen, carbon and oxygen. These are found at the majority of grain boundaries, and usually correlate with increased recombination activity. This is particularly the case for Si_2N^{2+} at 35 Da, which has been identified as a potential contaminant and cause of significant recombination [158], [233].

Unlike in Section 5.3.4, individual dislocations are not resolvable in the small angle grain boundary. This is due to the much greater misorientation of around 7.6°, which relates to a much smaller dislocation spacing than in Region A. Using Equation 5.1, it is possible to calculate a spacing of 2.9 nm assuming <011> Lomer dislocations [68]. Although APT is theoretically able to resolve atoms at these spacings, in this case resolving individual dislocations was made impossible by the significant quantity of impurities at the boundary and APT aberrations during the experiment [189], [193].

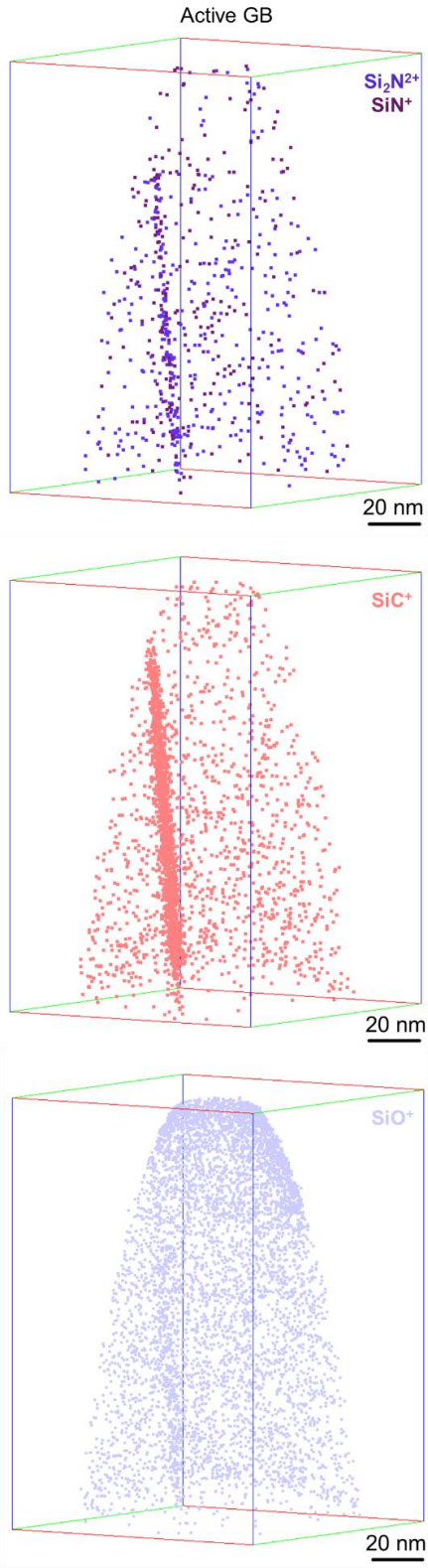


Figure 5.14. APT analysis of the active grain boundary from Region C, in the gettered and hydrogen passivated sample. Boundary clearly observed with excesses in nitrogen, carbon and oxygen.

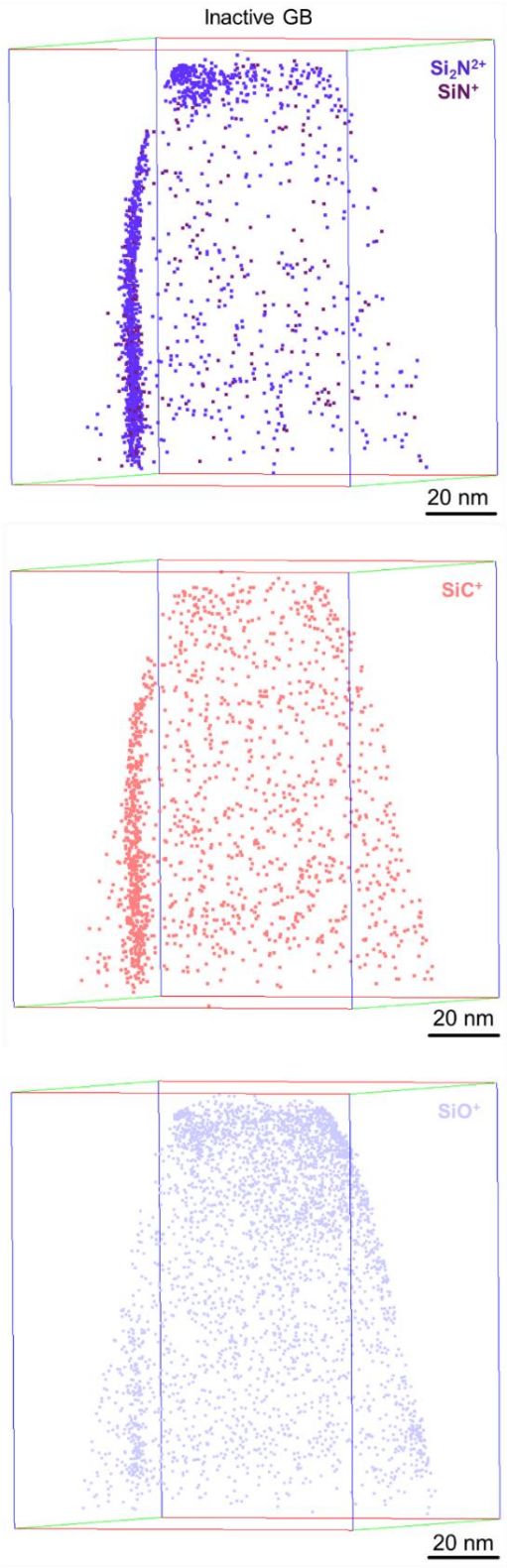


Figure 5.15. APT analysis of the inactive grain boundary from Region C, in the gettered and hydrogen passivated sample. Boundary clearly observed with excesses in nitrogen, carbon and oxygen.

The Gibbsian excess values (described in Section 3.12.5) for the active and inactive grain boundaries are shown in Figure 5.16. In the case of the inactive grain boundary, significantly greater levels of nitrogen are observed at the boundary than for the active boundary. It is however worth noting, that the EBIC and APT analysis was performed after gettering and hydrogen passivation. Hydrogen passivation could therefore be seen as effective at passivating the large quantities of nitrogen present. However, it is still unknown why the treatment was not effective on the small angle grain boundary.

Additionally, only a slight increase in carbon was observed at the electrically active grain boundary. It is therefore unlikely that this increase was responsible for the vast increase in recombination activity. Furthermore, the oxygen levels for the inactive grain boundary contained a significant degree of error, preventing the drawing of conclusions regarding oxygen. This error was caused by the presence of surface oxide, which forms during exposure to air between FIB sample preparation and APT analysis.

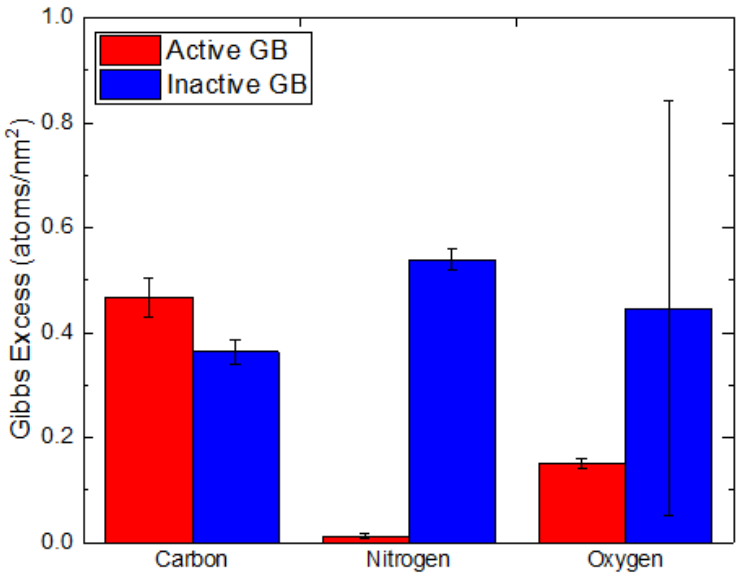


Figure 5.16. Gibbsian excess values for carbon, nitrogen and oxygen for both the active and inactive grain boundaries marked in Figure 5.13.

5.6 Discussion

In this chapter, a number of grain boundaries, taken from high performance multicrystalline silicon sister wafers, were analysed over various length scales. The effect of processing was investigated by the use of four sister wafers, exposed to different industrially relevant processing methods, namely As-Cast, hydrogen passivation, phosphorus diffusion gettering, and phosphorus diffusion gettering followed by hydrogen passivation. The correlation of electrical activity and local chemistry over various length scales allowed for a novel characterisation of the deleterious crystallographic defects seen in multicrystalline silicon.

The high resolution EBIC images of Region A (identified in Figure 5.1), shown in Figure 5.3, revealed a high density of recombination active grain boundaries. These boundaries were confirmed as small angle grain boundaries, consisting of a series of dislocations to accommodate for the misorientation between grains [234]. A number of studies have noted the deleterious properties of small angle grain boundaries [50], [134], [213], [235]. These boundaries are thought to contain greater levels of metallic impurities than other silicon grain boundaries [31] and also respond much less effectively to hydrogen passivation [91]. Quantitative EBIC of a small angle grain boundary in sister wafers exposed to differing treatments is shown in Figure 5.4.

Interestingly, following phosphorus diffusion gettering, the EBIC contrast vastly increased from the As-Cast sample. This phenomenon was ascribed to internal gettering of impurities to the grain boundaries during the process [236]. At the high temperatures of gettering, larger precipitates dissolve creating a solid solution in the

material. Then under the much faster cooling of gettering, impurities have insufficient time to form large precipitates and segregate to grain boundaries [237]. Hydrogen passivation following gettering was effective at reducing the recombination activity of the boundary. However, the boundary was still electrically active at room temperature and remains at a greater level than in the As-Cast wafer.

The lowest EBIC contrast was observed in the H passivated sample. This is thought to be due to the absence of internal gettering from not undertaking prior PDG. In the rapid firing of the H passivation process, there was insufficient time for diffusion of impurities to grain boundaries. In addition, grain boundary contrast was further reduced by the positive passivating effects of atomic hydrogen, which bonds to dangling bonds and other deep levels in the band gap [132].

Prior to APT analysis, TEM was performed on each of the needles, as shown in Figure 5.5. Bright field TEM images confirmed the small angle grain boundary as a series of dislocations, with a number of facets irregularly distributed throughout the grain boundary. Assuming the grain boundary is a pure tilt boundary, it is possible to estimate the spacing between the dislocations from the misorientation using the following equation:

$$2D = \frac{|\underline{b}|}{\sin(\frac{\theta}{2})} \qquad (5.1)$$

where D is the dislocation spacing, $\underline{b}$ is the Burgers vector of the dislocations, and θ is the misorientation between the two grains. In the case of the small angle grain

boundary measured in Figure 5.5 with a misorientation of 3.8°, and also assuming the dislocations are <110> Lomer edge dislocations, commonly seen at grain boundaries [68], the calculated dislocation spacing is 5.8 nm.

The dislocation spacing of ≈ 6 nm, as predicted by Equation 5.1, was observed in TEM. This is displayed in Figure 5.17, shown in greyscale pixel values from a line scan along the grain boundary. APT of the small angle grain boundaries from Region A displays carbon, in the form of SiC^+, lining the individual dislocations along the grain boundary. The reconstruction parameters for the APT analysis were calibrated to match the dislocation spacing measured by TEM, with the SiC^+ concentration profile marking the individual dislocations (Figure 5.17). It should be stated that the exact dislocations measured in TEM and APT are not identical and therefore the dislocation spacing in TEM was used only as a potential tool to improve the APT reconstruction.

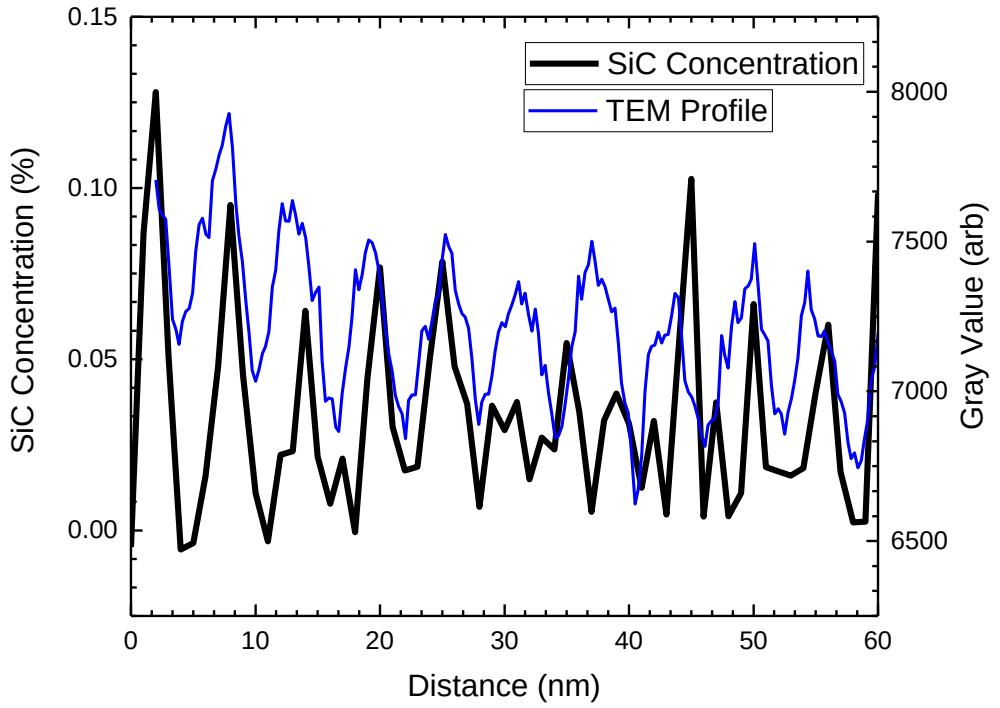


Figure 5.17. Concentration line profile (shown in black) of SiC^+ along the grain boundary in the gettered sample shown in Figure 5.8. Plotted in blue, the greyscale line profile through the various dislocations in the TEM image shown in Figure 5.5, taken prior to APT. This was used to improve the accuracy of the reconstruction process.

Carbon is observed to decorate the dislocations in all four datasets. Carbon is a commonly found impurity in multicrystalline silicon, arising from both the feedstock and in-diffusion from the crucible [238]. It is often found in the ingot as large SiC particles, which instead of being recombination active themselves, accumulate impurities that cause the detrimental effects observed [44], [239]. Carbon is also found at dislocations, with Pizzini et al. [42], showing that the density and electrical activity of dislocations in an mc-Si ingot is strongly dependent on the carbon concentration.

In this study, carbon was found at all of the small angle grain boundaries measured by APT. This includes the very low recombination activities seen in the As-Cast and hydrogen passivated grain boundaries. It is therefore possible to conclude that carbon is relatively benign concerning the recombination activity of the defect. Indeed, carbon can be ruled out as the impurity responsible for the significant increase in recombination activity after gettering. This agrees with literature findings, which find significant quantities of carbon in silicon are tolerable providing transition metals are not present [240].

In contrast to carbon, a peak at 35 Da was seen following gettering, which correlated strongly to the increase in recombination activity. Throughout this chapter I have referred to this peak as $^{28}Si_2{}^{14}N^{2+}$. However, this peak has previously been observed at recombination active facets in APT and been tentatively ascribed as $^{56}FeN^{2+}$ [159], [241]. In order to determine the chemical nature of this peak, a region of interest containing the 35 Da peak decorated facet was isolated, vastly increasing the signal-to-noise ratio for the peak in the resulting mass spectrum (Figure 5.18). Making use of the region of interest drawn encompassing the facet, it is possible to observe the side peaks corresponding at 35.5 Da and 36 Da. These are of the approximate correct isotopic abundances for $^{29}Si^{14}N_2{}^{2+}$ and $^{30}Si^{14}N_2{}^{2+}$, marked by blue horizontal lines on the figure. If, as stated in the literature [159], [241], the peak at 35 Da was $^{56}Fe^{14}N^{2+}$, a peak at 34 Da corresponding to $^{54}Fe^{14}N^{2+}$, should be present above the noise (green horizontal lines), albeit this only corresponds to the detection of two or three counts. This still however provides strong evidence that in this case, the peak observed at

35 Da is in fact $^{28}Si_2{}^{14}N^{2+}$, further supported by the co-location of $^{28}Si^{14}N^{+}$ to this region (Figure 5.18).

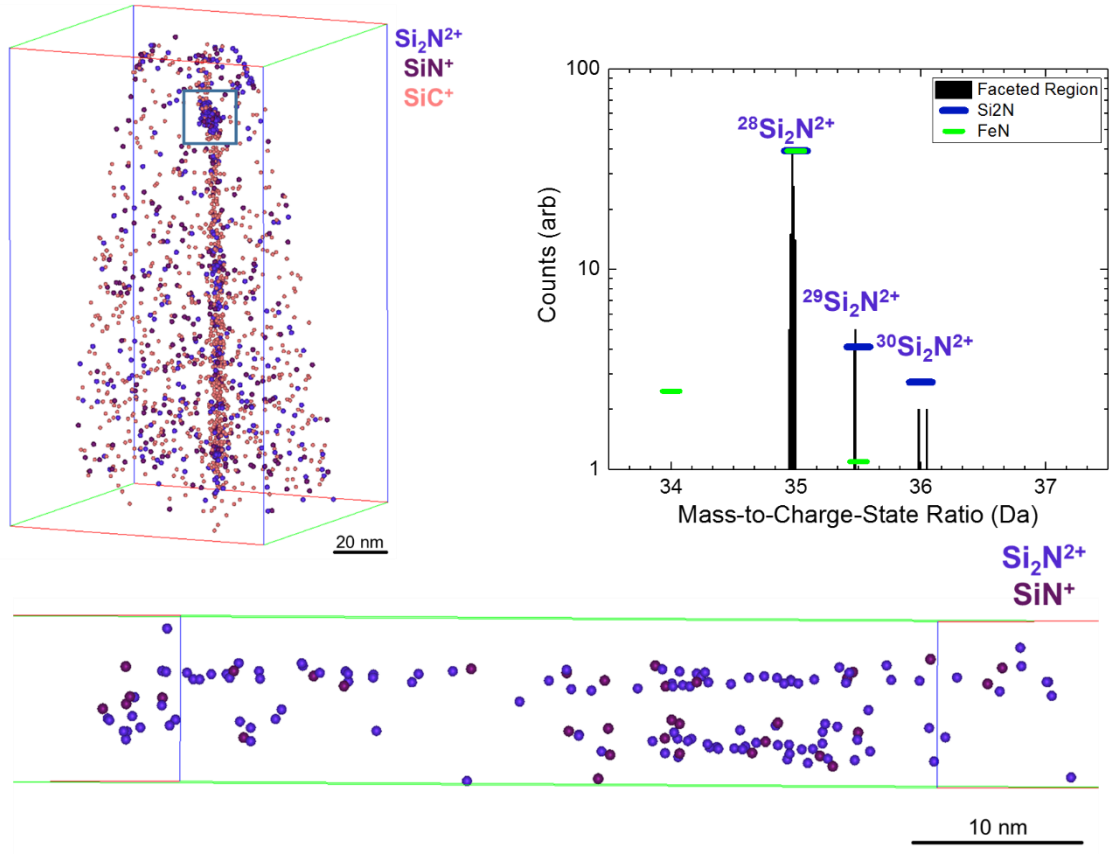


Figure 5.18. Atom probe analysis of the 'Gettered + H (hydrogen passivation)' sample, looking parallel to the grain boundary. Nitrogen in the form of SiN^+ and Si_2N^{2+} is found to preferentially segregate to the kink in the grain boundary. A region of interest just containing the nitrogen rich kinked section of the boundary, as marked in the left atom map, is shown in the bottom figure. The mass spectra for this region is shown on the right with the expected abundancies for Si_2N^{2+} and FeN^{2+} displayed on the figure in blue and green respectively.

With the strong correlation between the presence of Si_2N^{2+} and an increase in recombination activity, it is necessary to consider the possibility of nitrogen as a harmful impurity in silicon solar cells. Nitrogen is introduced in significant quantities

during the silicon ingot casting process, via ingress from the silicon nitride crucible [242]. Although N is a well-known impurity in silicon, very few studies have published work regarding the effect of nitrogen and other light elements, which primarily focus on large SiN particle inclusions present within the ingot [44]. Previous work has found that nitrogen can bond strongly to dislocations, introducing shallow donor levels, and can also increase the density of defect states at grain boundaries [46], [82], [131], [243].

However, the majority of papers find that nitrogen, especially when present as a split-interstitial dimer (N2), is electrically inactive [244]. In addition, nitrogen oxygen complexes, are also recombination inactive at room temperatures [42]. Indeed, significant quantities of nitrogen and oxygen were found present at the electrically inactive grain boundary in this study (Figure 5.15). A second explanation for the increase in recombination activity after gettering could be the redistribution of small concentrations of metallic impurities to grain boundaries. If these impurities are below the detection limit of APT, they will not be observed above background noise but may still increase recombination (Section 5.6.1). The significant quantities of nitrogen at 35 Da after gettering may represent the high energy sites present at grain boundaries in which impurities segregate to during the PDG process.

Region B displays a lone grain boundary, isolated by large grains. This grain boundary is initially recombination active and remains so after gettering and H passivation, as seen in PL (Figure 5.1). Using EBSD, this grain boundary was confirmed as a random angle grain boundary with a misorientation of 49.6°. Random angle grain boundaries

are known sinks for impurities in silicon, as a result of the large lattice mismatch and dangling bonds present [213]. This often results in a denuded zone around the boundaries, in which intragrain impurities segregate to the grain boundaries, leaving a high lifetime region in the vicinity [134].

APT was used to determine the local chemistry of the isolated grain boundary in Region B, for the gettered wafer (shown in Figure 5.11). Phosphorus diffusion gettering is known to significantly increase the recombination activity of random angle grain boundaries [91], [236]. This grain boundary was found to contain an excess in the light elements carbon, oxygen and nitrogen and also the transition metal copper.

As previously described in Section 2.4.2.1, the increase in recombination at grain boundaries is caused by internal gettering during the relatively fast cool of PDG. In contrast to Region A, few other defects are present in Region B, making the isolated grain boundary one of the sole defects for which impurities to segregate to in this region (Figure 5.1). This is likely the underlying reason that copper is seen for the first time above noise in APT at a grain boundary, in HPMC-Si without intentional contamination [90], [155], [158], [214].

The presence of copper at this grain boundary and the notable absence of other transition impurities is especially interesting to solar cell manufacturers, albeit APT sensitivity of transition metals must be considered and is discussed in detail later (See Section 5.6.1). Copper is a known impurity in silicon and can be easily introduced from the production environment and also from the feedstock. Although copper has

been linked to light induced degradation [245], Cu and its complexes have long been considered relatively benign in p-type silicon, compared to other transition metal impurities [7], [74], [220]. However, in the presence of existing lattice defects, its recombination activity becomes much more significant. Indeed, in the Ph.D. work completed by Stoffers using APT, only the most recombination active grain boundary contained Cu [246]. Correlating to the work completed in this study, no other transition metals were observed.

Region C, shown in Figure 5.13 contains both inactive and active grain boundaries, as measured by EBIC. From EBSD measurements, shown in Figure 5.12, the active boundary was measured as a small angle grain boundary, whereas the inactive grain boundaries were large random angle grain boundaries. This finding correlates with a number of studies, in which random angle grain boundaries become passivated after hydrogenation, unlike small angle grain boundaries, which remain electrically active [91], [134], [145].

Performing APT on these two grain boundaries provides a significant and surprising insight into the grain boundary chemistry, following processing. The active, small angle grain boundary is distinctly different to the boundaries studied in Region A. First individual dislocations are not resolvable, due to the much greater misorientation of 7.6° in contrast to 3.8°. Using Equation 5.1, an approximate dislocation spacing of 2.9 nm was calculated. This is much more difficult to resolve using APT.

Although individual dislocations could not be resolved in Figure 5.14, the grain boundary was found decorated in carbon and in nitrogen as Si_2N^{2+} and SiN^{+}. From Region A, an excess in Si_2N^{2+} at grain boundaries was only seen after gettering and correlated with an increase in recombination. Since the active grain boundary in Region C was subject to gettering, one can postulate that the redistribution of nitrogen and subsequent ineffectiveness of hydrogen passivation is the cause of the significant recombination. No transition metals are observed at the grain boundary in APT, but it is possible that small but unmeasurable levels are also responsible for the recombination. Please see Section 5.6.1 for more information.

APT of the inactive random angle grain boundary yields a surprising result. In addition to decoration by oxygen and carbon, nitrogen at 35 Da (Si_2N^{2+}) was found in extremely high levels at the boundary (Figure 5.15). Unlike the random angle grain boundary, no copper or any other transition metals were found at the grain boundary. In the work by Pizzini [42], grain boundaries were found to passivate in the presence of significant levels carbon, nitrogen and oxygen. This seems to contradict the conclusions that nitrogen is especially hazardous to grain boundaries. However, the levels of nitrogen in the study by Pizzini [42] are much greater than the wafers analysed in this study and passivation only occurs with an equiconcentration of carbon and oxygen. Unfortunately, APT does not provide insight into the precise cause of recombination, and therefore determining the exact element(s) responsible for recombination activity is difficult.

Random angle grain boundaries often respond strongly to hydrogen passivation, evolving from extremely recombination active to completely inactive [91]. It is therefore reasonable to postulate that the inactivity at the measured grain boundary was caused by the effectiveness of hydrogen passivation to bond to nitrogen and other elements found at the grain boundary. However, the characterisation approach presented above does not allow for the direct observation of hydrogen passivation. This would potentially allow for the question of why hydrogen is able to passivate random angle grain boundaries, while small angle grain boundaries remain electrically active. The development of a new approach to investigate this issue will be discussed in Chapter 6.

5.6.1 APT Sensitivity

In order to make definitive conclusions regarding the chemical identity of the impurities, which cause recombination at individual defects, it is necessary to determine the sensitivity of APT for this application. In this study, there are two main aspects of the APT technique that limit the sensitivity of APT for specific impurities, primarily transition metals. The first is mass-to-charge-state overlap of ions measured and the second is the random background noise in the mass spectra.

Mass-to-charge-state-ratio peak overlaps are a common and adverse aspect of many mass spectra techniques. In the case of silicon, there are a number of major overlaps that restrict the detection of transition metals, which are often seen as the major deleterious impurities [86]. The large quantity of overlaps in this system are shown in Figure 5.19, in which Fe, Ni and Cr all are seen to overlap with silicon-containing

molecules. Perhaps the most severe is the direct overlap at 28 Da of $^{56}Fe^{2+}$ and $^{28}Si^{+}$, which are both major isotopes. The expected low levels of Fe at the individual defects makes deconvolution to determine relative contributions of the overlapping peak using minor isotopes extremely difficult. Additional overlaps are seen between transition metals, such as Cr and molecules of silicon and lighter elements, which are found in abundance at grain boundaries (see Figure 5.15).

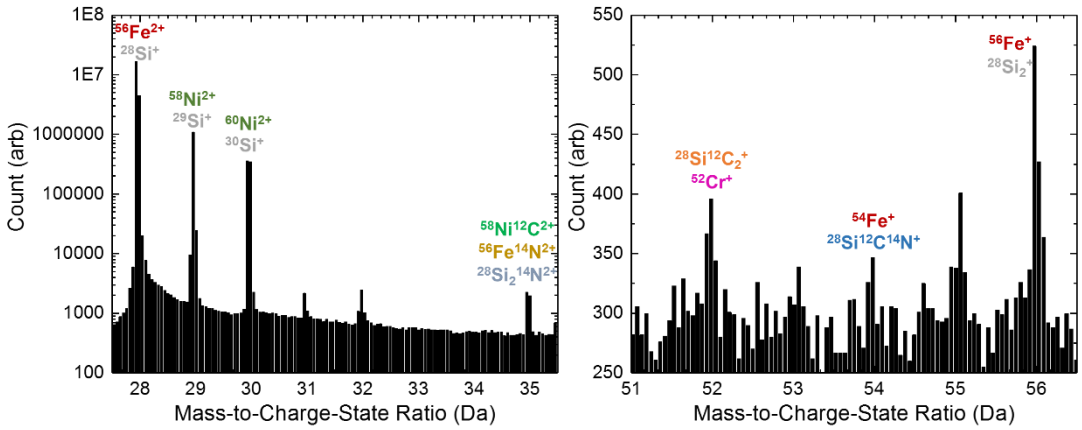


Figure 5.19. Mass spectra of a multicrystalline silicon dataset, showing a number of major overlaps.

In addition to mass-to-charge-state ratio overlaps, the second and key aspect regarding this study, is whether APT has the sensitivity to detect impurities which cause recombination above background noise. In order to examine this an individual dislocation is selected, with the use of a region of interest and the mass spectra is extracted (Figure 5.20). From the work of Wilshaw [70] and Kittler [247], it is known that significant and measurable EBIC contrast is achievable from the presence of 200 deep centres per micron. The length of the region of interest containing the dislocation is 60 nm in length, corresponding to 12 electrically active impurity atoms required for

measurable recombination. The detection efficiency of the LEAP 5000 XR instrument used in this study is 52%, meaning that only approximately a half of evaporated ions are detected. Therefore, only 6 electrically active impurity atoms would be observed.

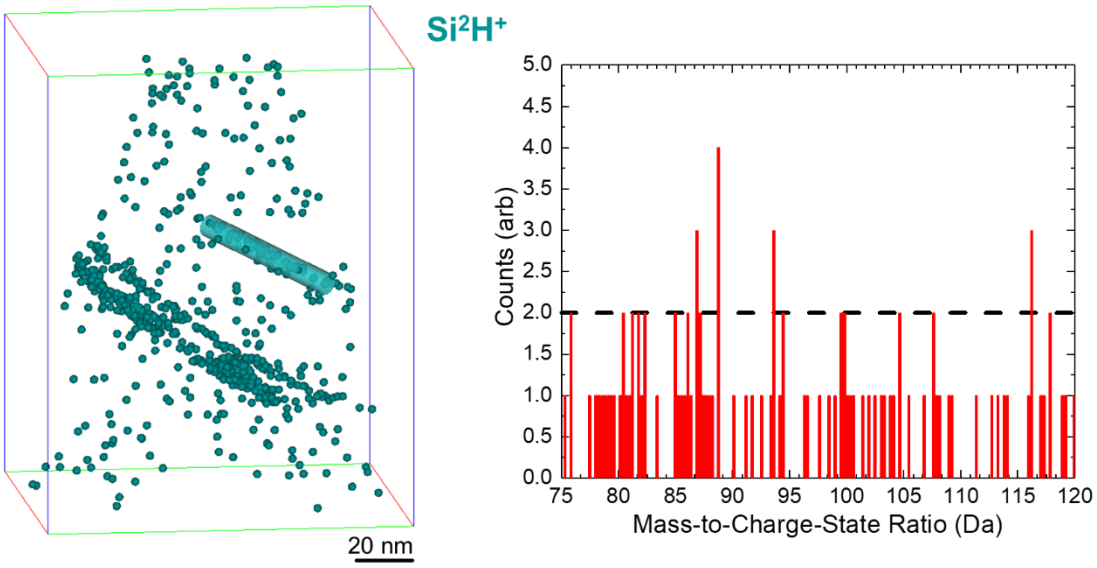


Figure 5.20. APT dataset showing three dislocations shown decorated in Si^2H^+. A region of interest of 60 nm in length was taken containing one of the dislocations and its mass spectra is shown on the right for a region containing just the background. The black dotted line signifies the calculated background for this region of 2 counts per Da.

An estimate of whether it would be possible to observe this many ions confidently, can be made by assuming the background follows a Poisson distribution (as described in [185]). This background, from the region of interest containing the dislocation, is shown in Figure 5.20. A mean of 2.2 counts per Da was calculated, approximated to a λ of 2. Plotting a Poisson distribution with mean of two counts per Da, the observation of a background peak of 6 counts or more has a probability of 0.45%, using the equation:

$$P(x \geq 6, \lambda) = \sum_{6}^{\infty} e^{-\lambda} \frac{\lambda^x}{x!} \qquad (5.2)$$

for a cumulative Poisson distribution P(x), where λ is the mean and x the number of counts observed.

It is therefore extremely likely that a peak of 6 ions can be observed above background noise in the mass spectra. However, isotopic abundances reduce the number of counts in the major isotopic peak. For example, the primary isotope of Ni at 58 Da only has a natural abundance of 68%. To put this in context, assuming that Ni is the cause of the dislocation recombination, and 12 ions are evaporated at the dislocation, only approximately 4 ions would be observed at 58 Da. In this case, there is a much larger probability (5%) of observing a peak of this height in the background noise. This can however be negated by sampling longer lengths of dislocation or analysing a greater number of dislocations and summing the mass spectra.

Further to this calculation, an approximation for the initial concentration of transition metals such as Fe, Cu and Ni, can be made. This approximation requires a number of assumptions, regarding the material grain size and impurity location. First, the material is assumed to contain cubic grains with a length of 1 mm, in which all impurities are distributed evenly at the grain boundaries. Next, an APT dataset containing a 100 nm x 20 nm section of the grain boundary is analysed. In order to observe an impurity, an assumed peak of 20 counts is required. For Fe, as a result of the direct overlap at 56 Da ($^{56}Fe^{+}/^{28}Si_2^{+}$), the peak at 54 Da should be used. By taking into account isotopic

abundancies, the detector efficiency of the APT (52%) and the sharing of grain boundaries between grains, a rough estimation of detection limits for individual elements can be determined.

Table 5.1. Estimation of APT detection limits for Fe, Ni and Cu.

	APT Detection Limit
Fe	1×10^{15} cm^{-3}
Ni	8×10^{13} cm^{-3}
Cu	8×10^{13} cm^{-3}

To summarise, the primary issue in this study regarding the detection of small levels of impurities at crystallographic defects in APT, relates to the large number overlaps between transition metals and silicon containing molecular ions. These overlaps increase the detection limit of APT to levels greater than the expected concentration of these impurities (see Figure 2.3). Although the issue of detection limit can be partially negated by sampling large lengths of defects, mass overlaps still significantly hinder the ability of APT to detect transition metals.

5.7 Conclusions

In this chapter, a number of grain boundaries from a HPMC-Si ingot were studied after various stages of processing. A high density of low angle grain boundaries, as found

in Region A, were found by PL to be very deleterious to the efficiency of the wafer. The recombination activity of these boundaries were found to increase after gettering, which coincided with the decoration of ions at 35 Da, as measured by APT, later confirmed as Si_2N^{2+}. No transition metals were observed to decorate these low angle grain boundaries, above an APT detection limit of 10^{15} cm^{-3} for Fe.

In contrast, a high angle grain boundary was found decorated in Cu after gettering, in addition to the light elements O, C and N. This grain boundary was isolated from other boundaries by large grains. This was thought to be the cause of grain boundary Cu concentrations being above the detection limit for APT.

Finally, two grain boundaries of vastly different recombination activities were analysed. In contrast to the low angle grain boundaries measured, the recombination inactive grain boundary actually contained much higher levels of nitrogen than the active boundary. Since APT cannot directly observe the cause of recombination, it is difficult to determine which elements are responsible. This boundary had however been exposed to hydrogen passivation, which may be the cause of the reduced recombination activity.

6 Direct Observation of Hydrogen at Defects in Passivated Multicrystalline Silicon

6.1 Introduction

As discussed in Section 2.5, the introduction of atomic hydrogen, from dielectric layers during high temperature steps in the processing of silicon has been shown to result in increases in bulk carrier lifetime by almost an order of magnitude [248], and the complete electrical deactivation of certain grain boundaries [134], [143], [145], [249].

Although hydrogen passivation is the most effective current commercial process in reducing this recombination, there remain a number of significant unanswered questions about the process [33], [145]. In particular, it is not understood why hydrogen passivation is effective on some defects but not others [250]. For example, Bertoni et al. [145], recently showed that while a random angle grain boundary clearly responds to hydrogen passivation, a Σ27 boundary subject to the same process remains electrically active. Also unresolved are the mechanisms by which charge carrier injection (by light or biased junctions), hydrogen and defect charge states and/or prior gettering steps act to change the effectiveness of hydrogen passivation [237], [251], [252].

The primary reason so little is known about the hydrogen passivation process is that the bulk hydrogen concentrations (10^{14}-10^{16} cm^{-3}) involved in these processes are well below the detection limits of most available techniques [253]–[255]. Indeed, the characterisation of hydrogen in material microstructure remains a formidable

challenge even for modern high-resolution microscopes. This inability to directly image hydrogen, particularly at the atomic-scale, has limited the understanding of its role in affecting the performance of a wide range of materials.

APT is a 3D nanoscale microscopy technique that provides both chemical identity and precise spatial location of individual atoms within a material microstructure (see Section 3.12). Since APT provides both spatial and compositional information at the atomic-scale it has obvious potential to bring new insights to the mechanisms behind the hydrogen passivation of defects in silicon. However, a major drawback in the design of current atom probes is the significant amount of ambient hydrogen that is present in the analysis chamber during operation. This hydrogen adsorbs onto the specimen and is then evaporated from its surface just like the constituent atoms [256]. Hence, it is not possible to distinguish hydrogen present in the analysis chamber from hydrogen introduced during passivation. This issue however, can be mitigated by passivating with ^{2}H (deuterium), which has a low natural abundance of 0.015% and can therefore be distinguished from the environmental hydrogen, which is overwhelmingly ^{1}H.

Although APT has not previously been used to detect ^{2}H in passivated mc-Si, a number of authors have used this approach with other materials. Takahashi et al. [257] and Chen et al. [258], directly observed the presence of hydrogen trapped at nanoscale carbides in steels, while the first APT observation of ^{2}H segregation to the grain boundary was presented by Sundell et al. [256] in a zirconium alloy. However, in that study, ^{2}H was detected at 18 Da in the mass-to-charge-state spectrum in the form of

$^{2}H\,^{16}O^{+}$ ions. This peak overlaps with $^{1}H_{2}{}^{16}O^{+}$, a molecule also routinely detected in APT experiments. Therefore, despite persuasive evidence provided by the authors, it was not possible to definitively confirm the presence of ^{2}H at this oxide grain boundary.

In this chapter by combining hydrogen passivation, underpinned by isotopic substitution from an atomic source, with the 3D atomic-scale characterisation technique atom probe tomography (APT) and crystallographic information by transmission Kikuchi diffraction (TKD), I present a novel experimental protocol for the direct and unambiguous imaging of individual hydrogen atoms at defects within multicrystalline silicon. This was performed on p-type HPMC-Si (Section 3.3) using remote plasma hydrogenation with isotopically pure ^{2}H (Section 3.4.4).

Prior to analysis, it was important to consider the APT operating conditions (Section 3.12.3). Voltage pulsing mode has previously been utilised in the APT analysis of metal alloys to reduce the effects of mass spectrum overlaps caused by complex ions and thereby simplify the quantification of ^{2}H. However, this must be balanced with specimen viability, which is of increasing consequence when combining APT with correlative analyses on the same tip. The silicon materials analysed in this work have been found to be significantly less viable to APT analysis under such experimental conditions, and hence laser pulsing was implemented instead. Furthermore, it is shown in this chapter that the use of laser pulsing to examine these silicon samples did not prevent isolation of the ^{2}H signal.

6.2 Results

Figure 6.1 shows the correlative analytical applied to a random angle grain boundary isolated within the hydrogenated silicon. This type of grain boundary is known to be electrically active but also susceptible to hydrogen passivation [134]. Figure 6.1a presents an SEM image of the silicon wafer surface, with the etch pits formed during Secco etching marking the grain boundaries clearly visible (see Section 3.5.3). The grain boundary was then lifted out using FIB methods described in Section 3.10, to produce the sharp needle-shaped geometry required for APT (Figure 6.1b). Figure 6.1c shows a TKD image of the needle, used to ensure the alignment of the grain boundary along the axis of the needle and to characterise the misorientation and rotation axis of the boundary. In Figure 6.1d, an APT map showing hydrogen, unambiguously detected in the form of $^{2}H_{2}^{+}$ ions at 4 Da in the APT mass spectrum, can be observed to segregate at the grain boundary.

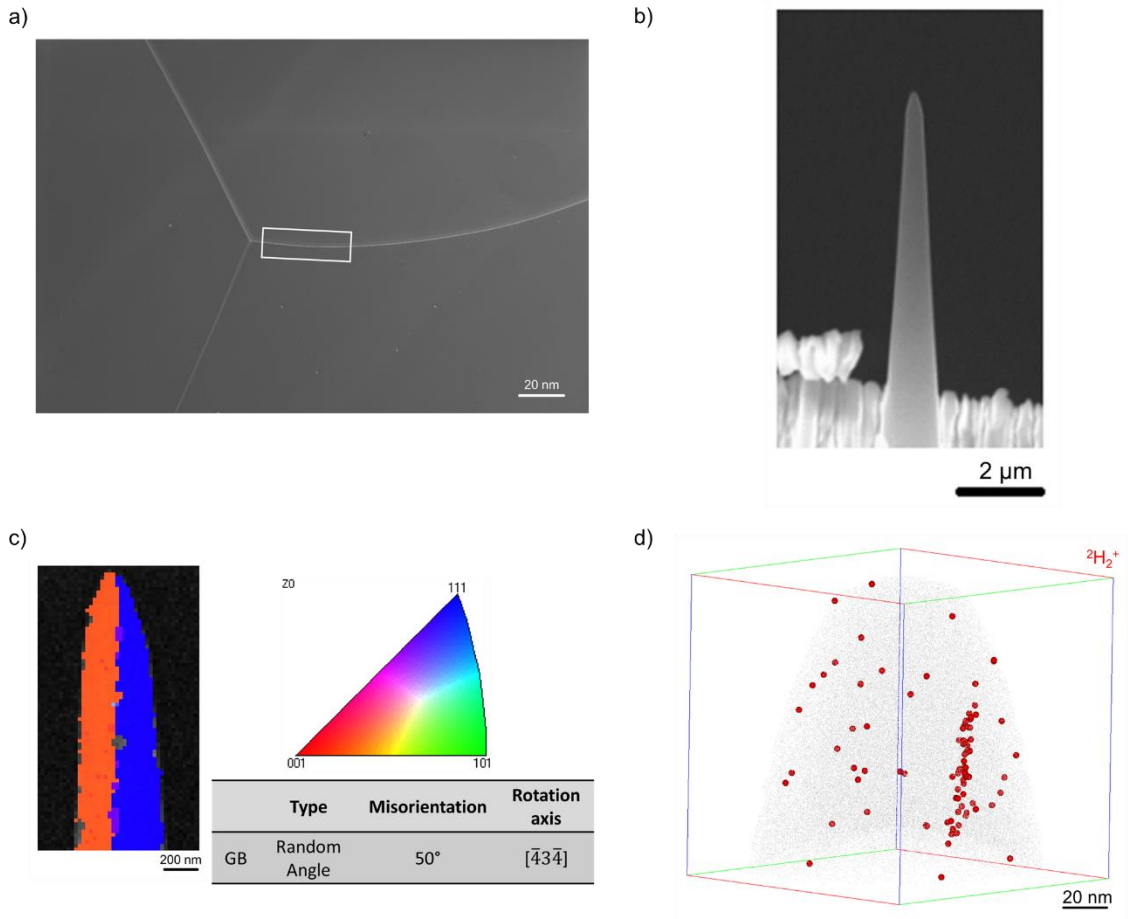


Figure 6.1. a) Scanning electron micrograph of the Secco etched silicon sample, with the random angle grain boundary selected for analysis marked. b) Scanning electron micrograph of the grain boundary atom probe needle. c) Inverse pole figure (IPF-Z) of the specimen, subsequent to APT analysis with a table displaying the grain's misorientation and rotation axis. d) APT dataset showing the enrichment of $^2H_2^+$ at the grain boundary, with a small fraction of Si atoms (grey) shown for reference.

Although ^2H can be detected unambiguously in the form of $^2H_2^+$ at 4 Da, the majority is detected in the molecular ion Si^2H^+. This is shown in Figure 6.2, in which the random angle grain boundary shown in Figure 6.1, is displayed decorated in both $^2H_2^+$ and $^{29}Si^2H^+$.

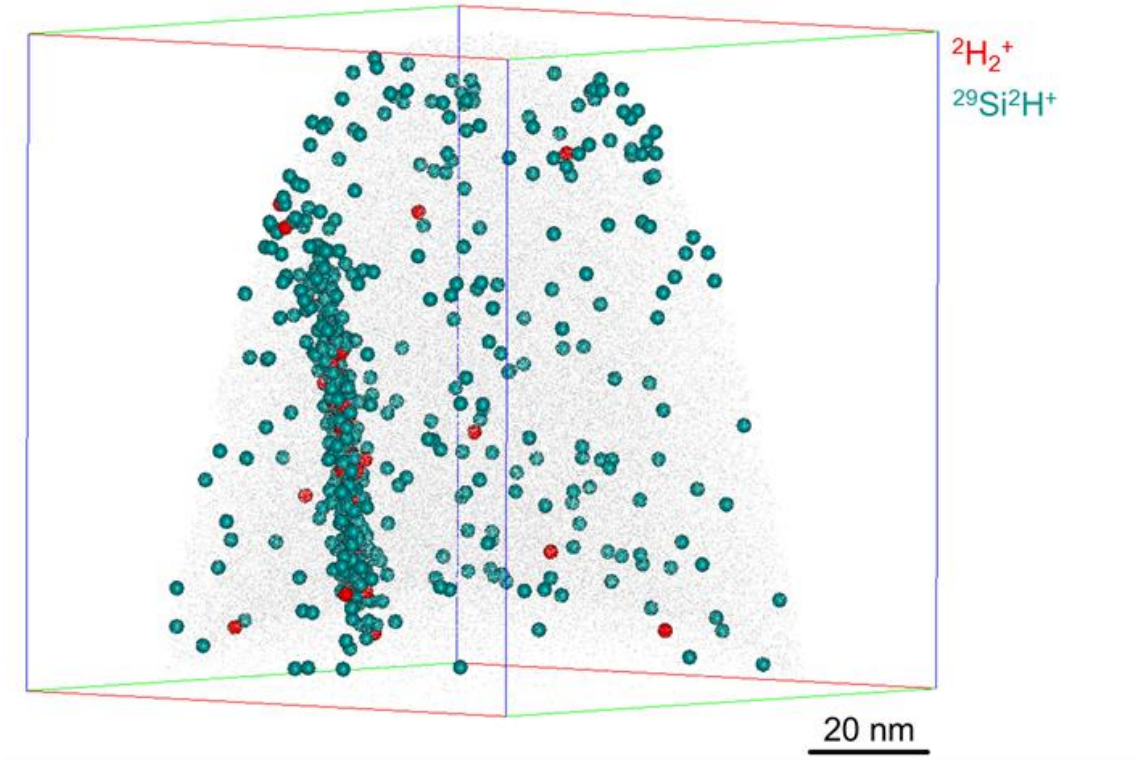


Figure 6.2. APT analysis of the random angle grain boundary shown in Figure 6.1, displaying an enrichment of $^{2}H_{2}^{+}$ and $^{29}Si^{2}H^{+}$ at the grain boundary, with a small fraction of Si atoms (grey) shown for reference.

Within the same ^{2}H charged silicon sample, hydrogen was also found at three dislocations close to a twin boundary, as presented in Figure 6.3. These are observable both perpendicular (Figure 6.3a) and parallel (Figure 6.3b) to the dislocation line direction. A clear enrichment of $^{2}H_{2}^{+}$ is observed at the dislocations, but a much greater quantity of hydrogen is detected in the form of $Si^{2}H^{+}$ ions. This is most apparent in the mass spectra of dislocation III compared to the matrix. At the dislocation mass spectra, a clear and unequivocal peak at 4 Da is observed, corresponding to $^{2}H_{2}^{+}$. Additionally, the peak at 30 Da is significantly larger, due to large amounts of $^{28}Si^{2}H^{+}$. The results in Figure 6.3 unambiguously demonstrate hydrogen segregating to dislocations in mc-

Si and correlate well with the reduction in recombination activity of dislocations observed after hydrogen passivation [251], [259].

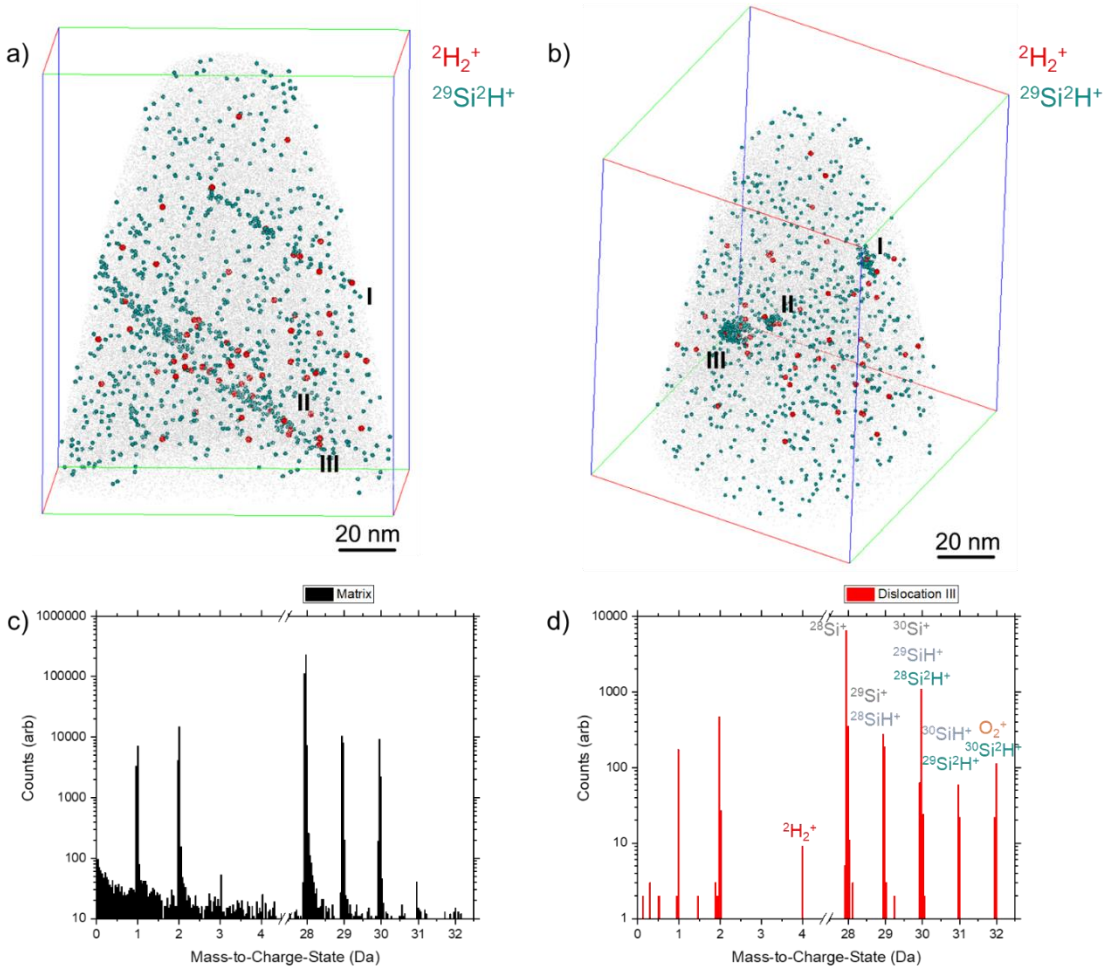


Figure 6.3. APT datasets showing the enrichment of $^{2}H_2^+$ and $^{29}Si^{2}H^+$ at three individual dislocations, with a small fraction of Si atoms (grey) shown for reference. a) Viewing perpendicular to the dislocation. b) Viewing along the length of the dislocations. c) Mass spectra of the matrix of the APT specimen shown in a). d) Mass spectra of dislocation III, showing clear enrichment in ^{2}H at 4 Da, 31 Da and 32 Da.

In contrast to dislocations, perfectly coherent Σ3 twin boundaries are known to be electrically inactive in mc-Si [260]. However, it is not known whether hydrogen

segregates to these boundaries during passivation. Figure 6.4 displays a forward scattered image showing the dislocation free Σ3 twin boundary, extracted from a ^{2}H charged mc-Si wafer, and corresponding dataset. This boundary was characterised via TKD (Figure 6.4d), which was essential in confirming the presence of the grain boundary in the dataset and also the boundary type. No enrichment of $^{2}H_{2}^{+}$ or indeed any other impurities, such as carbon, oxygen or transition elements, are observed at this boundary.

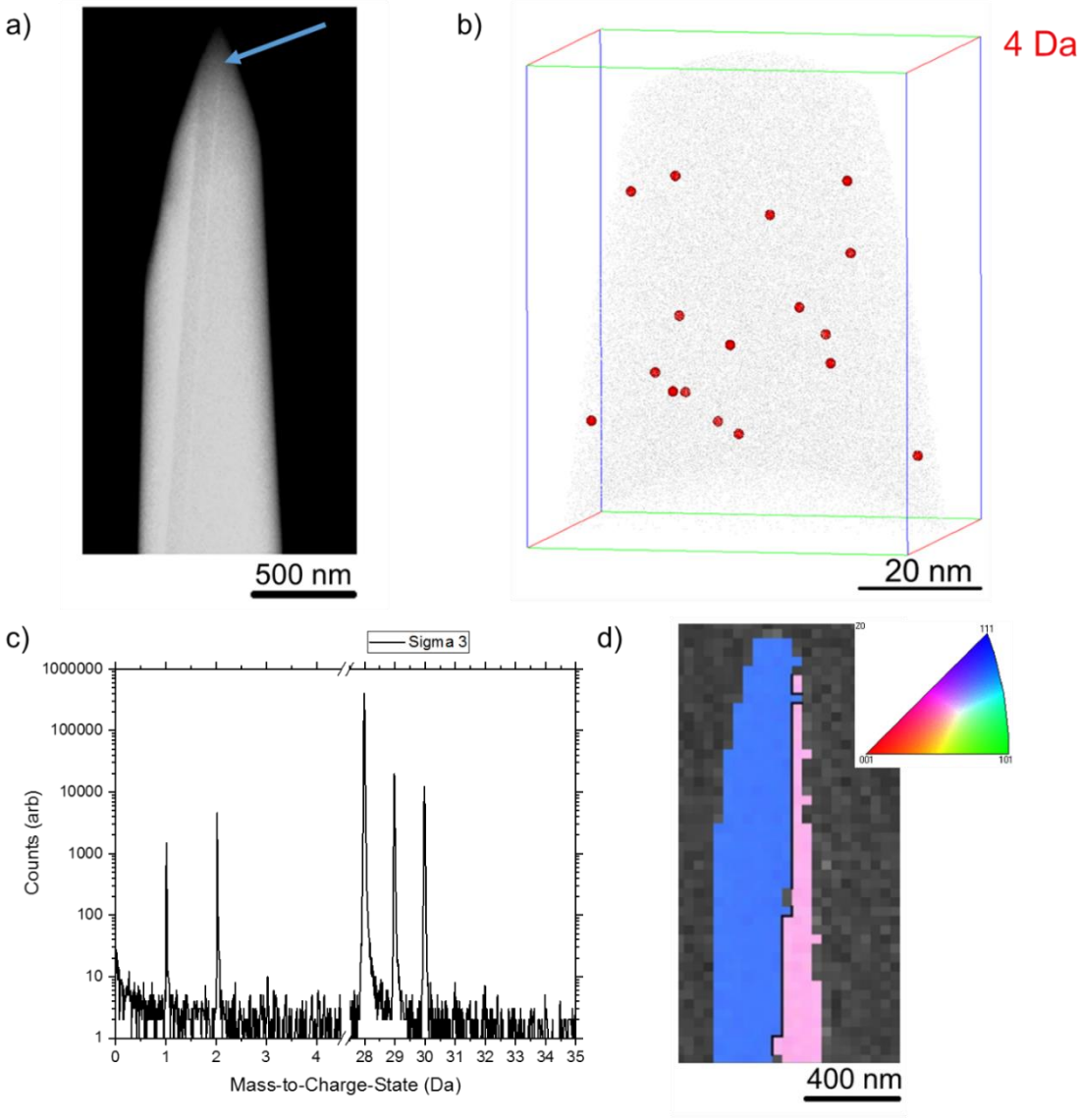


Figure 6.4. a) Forward scatter image of a needle prior to APT analysis, with the grain boundary marked. b) APT dataset of the needle analysed containing a Σ3 grain boundary, with the signal of ^{2}H shown to be background noise (with a small fraction of Si in grey shown for reference). c) Mass spectra of the Σ3 grain boundary containing dataset. d) TKD of the needle prior to APT analysis. The needle was polished to ensure the grain boundary was at the apex of the needle.

6.3 Discussion and Analysis

By extracting regions of interest and their corresponding mass spectra, it is possible to produce a quantitative estimation for the total amount of ^{2}H present at individual grain boundaries and dislocations. This can then be used in future studies to determine if there is a correlation between the quantity of hydrogen at different crystallographic defects and electrical activities before and after hydrogen passivation.

Figure 6.5 presents the mass spectra for a deuterated and non-deuterated random angle grain boundary. These datasets were acquired using the same experimental conditions (Section 3.12.3). Using the $[Si^{+}]$ to $[Si^{2+}]$ ratios for both datasets, the electric field at the needle apex for both specimens, can be approximated to 19 Vnm^{-1} (see Kingham [261]). In addition to the presence of the unambiguous $^{2}H_{2}$ peak at 4 Da, it can be seen that the deuterated sample also exhibits significantly higher peaks at 30, 31 and 32 Da relative to the $^{28}Si^{+}$ and $^{29}Si^{+}$ peaks. While the peak at 4 Da is unambiguously due to $^{2}H_{2}^{+}$ ions, this only represents a fraction of the total ^{2}H detected in the APT experiment. The majority of ^{2}H is detected as $Si^{2}H^{+}$ ions, contributing to the peaks at 30, 31 and 32 Da. However, these overlap with the detection of other ions e.g. $^{28}Si^{2}H^{+}$ and $^{30}Si^{+}$ at 30 Da, therefore, a deconvolution analysis must be applied to estimate the contribution of the ^{2}H containing ions to each of these peaks.

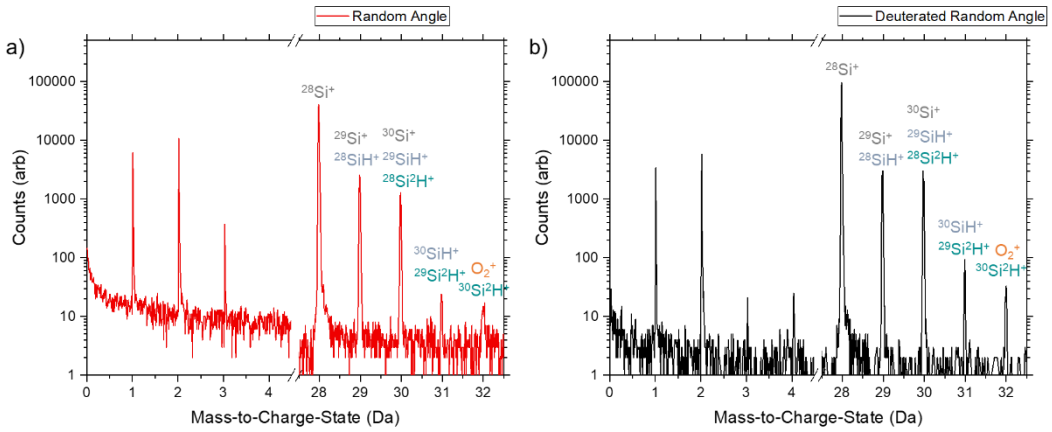


Figure 6.5. a) Mass spectra of a random angle grain boundary from a sample, which has not received any hydrogen treatment. b) Mass spectra of the random angle grain boundary shown in Figure 6.2, from a sample which has been passivated by ^{2}H.

By assuming that the isotopes of silicon are observed in their natural relative abundances [262], and the fact that the $^{28}Si^{+}$ peak has no significant overlaps in this system, it is possible to determine the relative contributions to these peaks. This deconvolution was performed by extracting a region of interest from the dataset containing an area of the grain boundary or along the length of a dislocation. Then using the open source programme AtomProbeLab (https://sourceforge.net/projects/atomprobelab/), which uses the maximum likelihood method, the quantity of ^{2}H present was determined within confidence intervals (95% in this study), as described in [263]. Since the detector has an efficiency of only 52%, a calculation of dividing the number of counts by 0.52 was required to determine the total number of $^{2}H^{+}$ ions present. This deconvolution of the peaks maximised the likelihood of composition, based on the atomic abundance of silicon and the counts in the ranges (28-32 Da). From performing the deconvolution, it was determined that the

vast majority of ^{2}H was evaporated as $Si^{2}H^{+}$, with less than 1% of ^{2}H present in the 4 Da peak. Therefore the values for ^{2}H present at individual defects were given only with regards to ^{2}H detected as $Si^{2}H^{+}$, and do not take into account ^{2}H present at 2, 3 and 4 Da. Hence, the values given for ^{2}H present should be viewed as lower estimates for the quantity present.

Table 6.1 shows the calculated Gibbsian interfacial excess quantities of ^{2}H present, at the random angle grain boundary and along each of the three dislocations as described in [196]. Dislocation **III** is clearly shown to have the largest quantity of ^{2}H along the length sampled, as might be expected from the dataset presented in Figure 6.3. Although this study does not allow for the determination of the cause of the variation between dislocations, it clearly shows the ability of the deconvolution method to allow for quantitative comparisons regarding the magnitude of the hydrogen present to be made. To give a rough estimation of number of ^{2}H per atomic site along the dislocations, the Burgers vector of a standard [110] dislocation was used. This dislocation type was chosen, representing an undissociated Lomer dislocation, since they are well known and extremely deleterious to silicon solar cells [68]. In this case dislocation **I** and **II** have ≈ 5 ^{2}H ions per atomic site and dislocation **III** has ≈ 8 ^{2}H ions per atomic site. Since this is a rough estimation, with the types of dislocations not measured, these values can only be given as reference and must be studied further.

Table 6.1. Quantity of ^{2}H calculated as a Gibbsian interfacial excess for the random angle grain boundary shown in Figure 6.2, for the three dislocations shown in Figure 6.3 and for the Σ3 grain boundary shown in Figure 6.4. Upper and lower bounds are determined, within 95% confidence intervals.

	RA	Σ3	I	II	III
^{2}H Quantified	$1.4 \pm 0.15 \times 10^{14}$ counts cm^{-2}	Below detection limit ≈2×10^{12} counts cm^{-2}	14 ± 1.5 counts nm^{-1}	13 ± 2 counts nm^{-1}	22 ± 1.5 counts nm^{-1}

In this study, a high yield of APT specimens successfully analysed containing ^{2}H enriched grain boundaries was achieved. Although previous studies investigating the distribution of ^{2}H in steels have utilised cryogenic transport to increase the quantity of ^{2}H measured at crystallographic defects [258], we believe this unnecessary since ^{2}H has to be chemically bound at the defect for passivation to occur. However, statistical certainty for the quantity of ^{2}H present can be improved via the sampling of large lengths of grain boundaries, using the method discussed in [157].

6.4 Conclusions

The ability to quantify the amount of hydrogen present at a grain boundary or dislocation is an important breakthrough for the characterisation of hydrogenation in multicrystalline silicon for solar cell applications. With regards to electrically active grain boundaries that are less susceptible to hydrogen passivation, it will allow determination of whether this is due to a lesser affinity of hydrogen to segregate at these features or if there are other causes such as the presence of specific impurities

which are not passivated. The technique is also applicable to the crystallographic defects that limit the performance of cast monocrystalline solar cells.

This information is invaluable for informing the further development of casting methods for crystalline silicon growth, in order to avoid the formation of defects than cannot be passivated [32], [34]. It can also be observed how specific processing conditions, such as temperature and carrier injection [252], [264], can either increase or decrease the amount of hydrogen present at crystallographic defects. A better understanding of these effects is critical for optimising such processes and continuing to improve the performance of solar cells based on these materials.

7 Alternative Solar Cell Materials: Wide-scale Application of Atom Probe Tomography

7.1 Introduction

With the rapidly advancing and widespread use of photovoltaic module production, the development of new materials and processes has become a major research focus. In this chapter, two promising new materials and the effect of two unique processes are investigated. The effect of saw damage gettering and boron diffusion gettering were investigated on Red Zone p-type HPMC-Si silicon and n-type HPMC-Si respectively. The effects of these processes were examined using a multiscale approach, ranging from the macroscale to the microscale and finally to the nanoscale using APT analysis.

As discussed in Section 3.3, the Red Zone HPMC-Si wafers examined in this study are taken from the bottom of a high performance multicrystalline ingot. This is material which would usually be discarded from the ingot, due to the high levels of impurities caused by in-diffusion from the crucible [20]. A potentially cheap and industrially viable process, able to reduce the quantity of impurities to a tolerable level, is saw damage gettering (SDG). This technique utilises the surface damage layer caused by diamond wire sawing of wafers, via the preferential precipitation of impurities in the saw damage region, in combination with a specific thermal treatment to reduce metallic impurity concentrations [265]. The use of this process, as a precursor to standard solar cell processing, may allow for the reduction of scrap waste from the ingot, increasing the yield from the casting process.

In contrast to the much lower efficiencies of Red Zone p-type HPMC-Si, the other material studied in this chapter is n-type HPMC-Si. This material, developed by Fraunhofer ISE, has recently achieved record conversion efficiencies of 22.3% [266]. The superior material performance of n-type silicon is caused primarily by its relative tolerance of common impurities such as Fe. This results in much greater minority carrier diffusion lengths compared to p-type substrates with similar impurity concentrations [267]. In order to produce the p-type emitter, a boron diffusion is required. This process often coincides with an increase in grain boundary recombination activity [268]. The approach developed in this thesis is well-suited to investigate the cause of this phenomenon and investigate which impurities are particularly hazardous in n-type silicon.

7.2 Saw Damage Gettering of Red Zone Multicrystalline Silicon

In this section, the effect of SDG on Red Zone HPMC-Si is investigated via macroscale measurements and then to the near atomic-scale using APT. Depth and lateral spatial resolutions of ~ 0.2 and ~ 0.4 nm respectively are achievable for this technique [269], in combination with local impurity detection limits down to ppm levels, depending on the spatial segregation of impurities, potential mass spectra overlaps and the signal to background ratio [183]. This technique therefore, in association with crystallographic information from TKD, allows for a detailed characterisation of an individual grain boundary.

7.2.1 Macroscale Analysis

The application of SDG on p-type Red Zone HPMC-Si greatly improved the minority carrier lifetime, as shown in Figure 7.1a. When comparing the lifetime of the SDG groups to the As-Cast group, or the No-SDG group (heat treatment applied but without saw damage), it is shown that the combination of saw-damage and the thermal treatment is necessary to provide improvement in lifetime. The interstitial iron concentration, which is readily observed via lifetime spectroscopy, was also reduced for the SDG groups.

Although using minority carrier lifetime spectroscopy cannot determine which impurities are the dominant sources of recombination, the results presented in Figure 7.1c does allow some conclusions to be drawn. When samples were removed above 700 °C the lifetime after gettering was reduced, indicating that the lifetime limiting impurities are highly mobile in silicon at temperatures below 700 °C. This suggests that faster diffusing elements, such as Cu and Ni are important for recombination, in contrast to slower diffusing elements such as Fe and Cr [221].

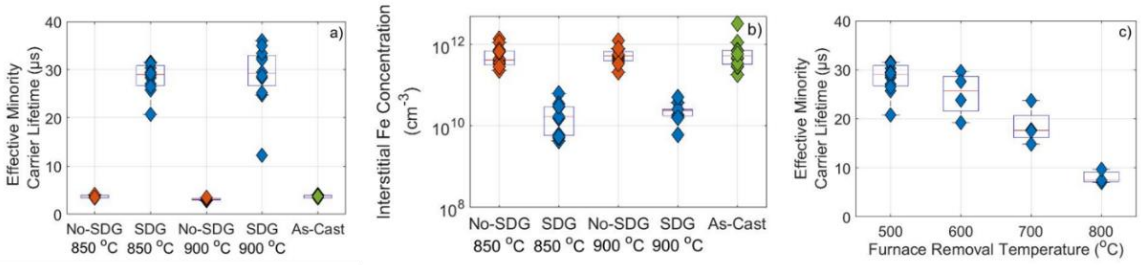


Figure 7.1. a) Lifetime for different SDG processing routes, b) Interstitial Fe concentration for different SDG processing routes, and c) Lifetime for specimens removed at a range of temperatures compared to the standard 500 °C. Produced in collaboration with E. Shaw.

In order to investigate the distribution of lifetime before and after gettering, photoluminescence was used, as shown in Figure 7.2. Prior to gettering, the lifetime of both the bulk and at grain boundaries is extremely low. Following SDG, intragrain lifetimes are significantly improved. However, most grain boundaries remain significantly recombination active, with some much more electrically active than others. The two grain boundaries of varying recombination activities (high activity (1) and low activity (2)), which were selected for further analysis are marked in Figure 7.2.

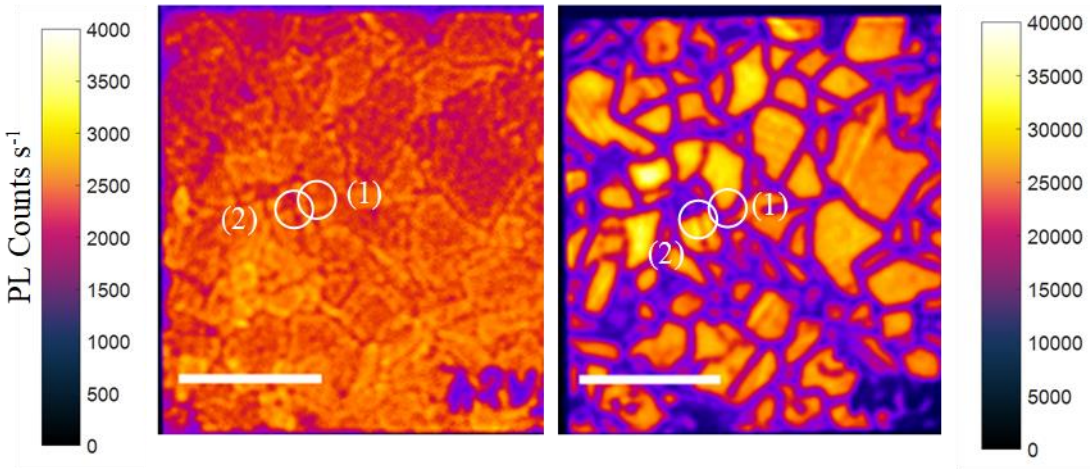
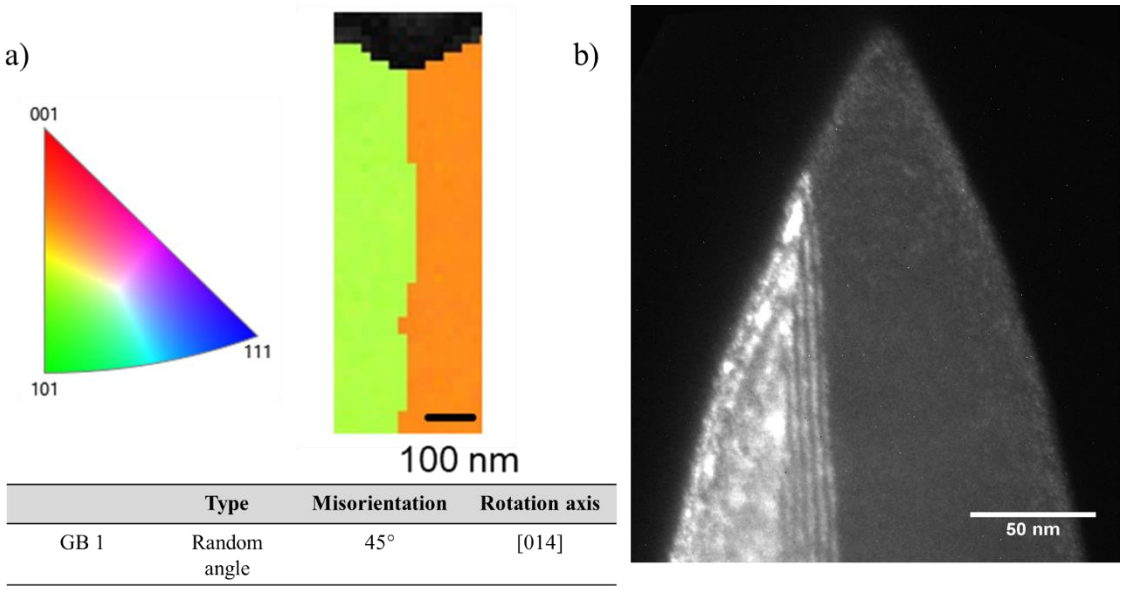


Figure 7.2. Photoluminescence images of Red Zone HPMC-Si sister wafers before (left) and after (right) saw damage gettering. The grain boundaries selected for further analysis are marked. Scale bars 10 mm. An exposure of 1 sun for a duration of 1 s was used for both images. Surface passivated by SiN_x. Images were acquired by P. Hamer at the University of Warwick.

7.2.2 Nanoscale Analysis

Following macroscale analysis of both lifetime and composition, two grain boundaries with varying recombination activities were selected for analysis. As seen in Figure 7.2, the recombination activity of the first grain boundary is much greater after SDG

compared to that of second grain boundary. Using TKD of a lamella containing the high activity grain boundary, this was confirmed as a large random angled grain boundary, with a misorientation of 45° (Figure 7.3a). This lamella was then made into an APT specimen using FIB methods (as discussed in Section 3.10), with TEM used to confirm the grain boundary's presence at the tip apex prior to APT analysis (Figure 7.3b for the pre-gettered wafer).



	Type	Misorientation	Rotation axis
GB 1	Random angle	45°	[014]

Figure 7.3. a) Inverse pole figure (IPFY) of a lamella containing the high activity grain boundary and table indicating the misorientation and rotation axis of the boundary. b) Dark field TEM image of APT specimen from the pre-gettered wafer containing high activity grain boundary prior to APT analysis.

APT analysis for the high activity grain boundary of the pre-gettered wafer is shown in Figure 7.4. From the figure, the clear enrichment of the light elements oxygen, carbon and nitrogen at the grain boundary can be observed. Additionally, the transition

metal copper is also seen at the boundary. These elements appear to be distributed near homogenously throughout the boundary, with no evidence of clustering or the formation of precipitates.

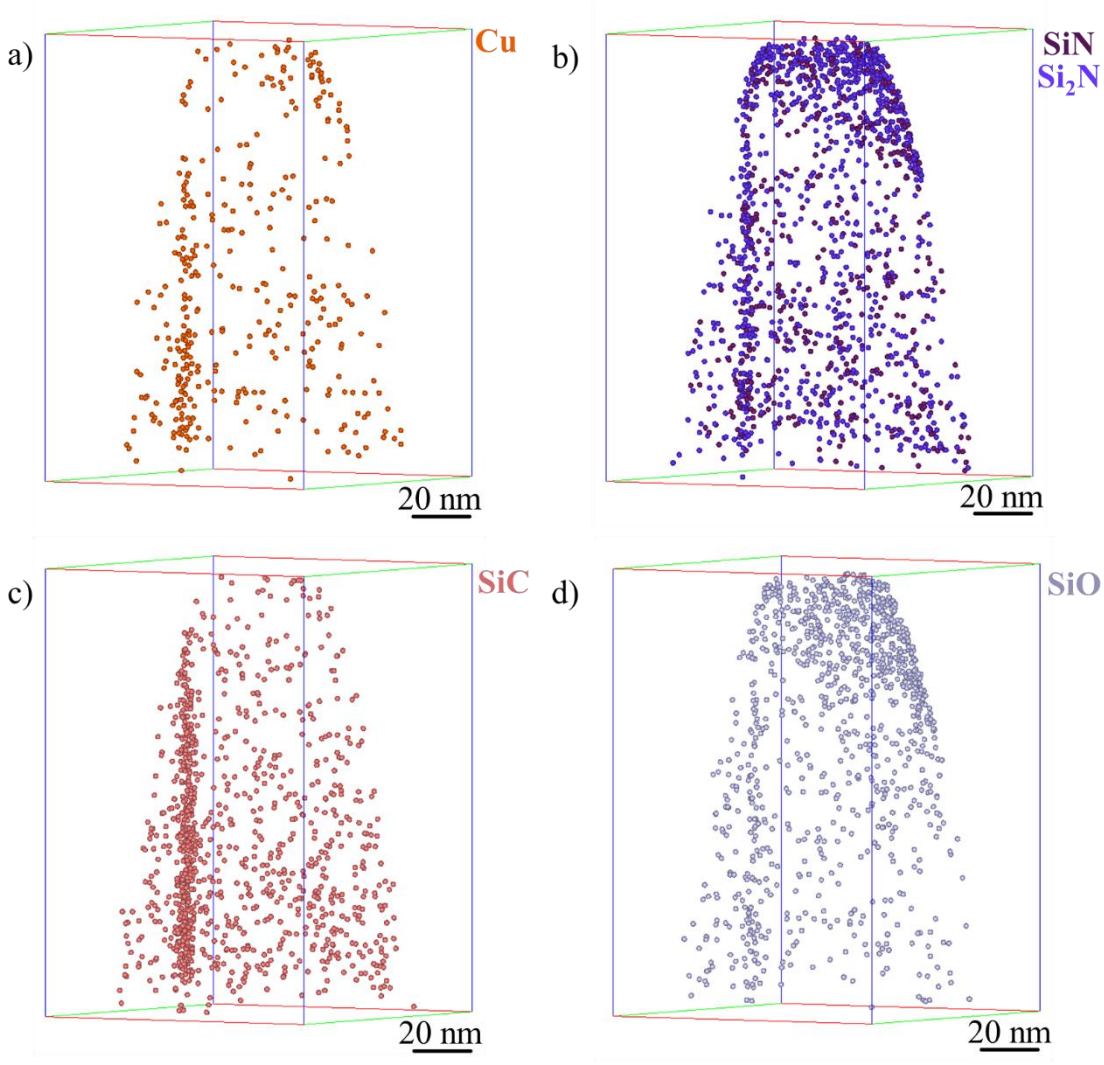


Figure 7.4. APT analysis of the high activity grain boundary prior to SDG. The grain boundary is shown enriched in a) Cu, b) SiN and Si_2N, c) SiC and d) SiO.

In order to determine the effect of SDG on the local chemistry of the high activity grain boundary, Gibbsian interfacial excess measurements (see Section 3.12.5 for

details) were made on APT datasets before and after SDG. The results of the excess calculations are given in Table 7.1. As previously observed in Figure 7.4, the high activity grain boundary prior to SDG is enriched in C, N, O and Cu. The greatest enrichment is observed in oxygen and carbon. After SDG, significant reductions in the impurities present at the boundary occur. Only carbon remains at similar levels before and after SDG. The level of copper is seen to decrease dramatically after gettering, indicating that SDG is successful at removing this element. This is also true for oxygen, which reduces in concentration significantly following SDG.

Table 7.1. Gibbsian excess values for Cu, N, C and O of the high activity grain boundary before and after SDG.

	Cu	N	C	O
Before SDG	0.02 $\pm$ 0.003 counts nm^{-2}	0.03 $\pm$ 0.004 counts nm^{-2}	0.15 $\pm$ 0.004 counts nm^{-2}	0.29 $\pm$ 0.05 counts nm^{-2}
After SDG	0.00 $\pm$ 0.007 counts nm^{-2}	0.00 $\pm$ 0.02 counts nm^{-2}	0.16 $\pm$ 0.05 counts nm^{-2}	0.05 $\pm$ 0.12 counts nm^{-2}

The second grain boundary analysed showed very little recombination activity in the photoluminescence images. It was therefore expected that less decoration would be observed on this grain boundary. Figure 7.5 presents TKD and atom probe images of this grain boundary with no gettering. From the Y inverse pole figure map, it was possible to determine the boundary as a $\Sigma 3$ {111} twin boundary and to ensure the grain boundary is in the APT sample prior to analysis. This boundary has been widely reported [29], [90], [270] to be less recombination active and to be a weak gettering site for impurities. This is borne out by the atom probe results, which observed no significant decoration of the grain boundary by metallic impurities, carbon or nitrogen.

Indeed, the only means of clearly observing the grain boundary in the atom probe reconstruction was through elevated levels of oxygen. Since it is known that perfectly coherent Σ3 {111} are impurity free [30], oxygen is instead thought to decorate facets as observed by Liebscher et al. [241].

For the sample after SDG, the grain boundary was extremely difficult to detect in the APT reconstruction, presumably due to a reduction in oxygen concentration similar to that observed for the high activity grain boundary. While this makes it difficult to be certain where the grain boundary was located in the atom probe needle, there was no evidence of any gettering of copper or other light elements to low activity grain boundary in the SDG sample. TKD does however provide evidence that the grain boundary was in the needle prior to analysis.

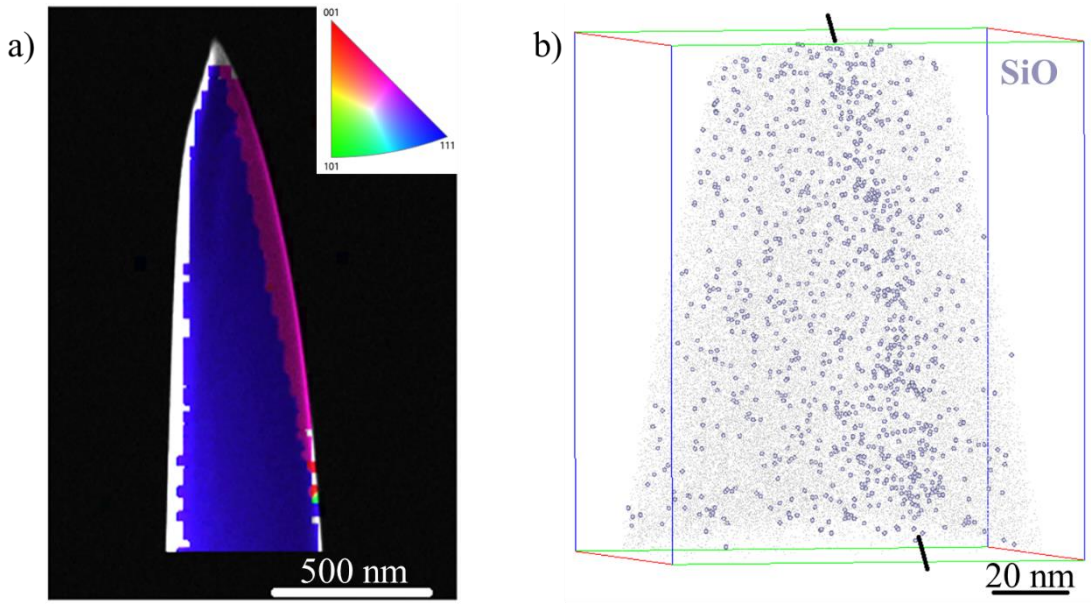


Figure 7.5. a) Inverse pole figure (IPFY) of the low activity grain boundary in the pre-gettered specimen prior to APT, showing a Σ3 twin grain boundary. b) Atom probe 3D reconstruction of GB 2 in the pre-gettered wafer showing a slight enrichment in SiO at the boundary. A small fraction of silicon atoms (grey) are shown for reference.

7.2.3 Discussion

Bulk lifetime measurements, shown in Figure 7.1, clearly demonstrate the effectiveness of SDG as a gettering technique. However, this improvement is largely in the intra-grain regions, leaving the grain boundaries as the primary sources of recombination in the gettered wafer. The recombination activity of grain boundaries in multicrystalline silicon is known to depend strongly upon the orientation of the boundary and decoration with metallic impurities. In light of previous results in the literature [29], [90], [270], it is unsurprising that the high activity grain boundary was determined to be random angle, while the almost inactive grain boundary was a Σ3 twin.

It was also expected that the high activity grain boundary would show high concentrations of a large number of metallic impurities. However, only Cu was observed decorating the grain boundary. Surprisingly no Fe or Ni was observed, although they are known impurities in multicrystalline silicon, often seen in large quantities [27]. The lack of detected Fe at grain boundaries may be caused by the presence of large intragranular Fe clusters, as seen by Istratov et al. [49], which are termed efficient gettering sites and can in fact improve diffusion lengths. In contrast, the distribution of Cu along the boundary was found to be homogenous with no direct evidence of clustering or precipitation. This is in contrast to results by Buonassisi et al. [27], who observed a number of nanoprecipitates elongated along the grain boundary direction. Although it is not possible to exclude the presence of such precipitates given the small volumes sampled by the APT analyses, it is interesting to

note that a homogenous distribution was observed. This is thought to have a much greater effect on the recombination activity of the defect, compared to a small number of large, widely distributed precipitates [50].

Since the second analysed grain boundary was found to be a Σ3 grain boundary and was almost electrically inactive, it was expected to have very low levels of metallic impurities. This is as a result of coherent Σ3 grain boundaries having lower levels of strain and much fewer nucleation sites for the precipitation of impurities [91]. In this study, prior to gettering, the grain boundary is only observed by a small increase in oxygen content at the grain boundary. This is the only time oxygen is found decorating Σ3 grain boundaries and may be caused by facets along the boundary, as seen by Liebscher et al. [233]. Following SDG, which is found to reduce oxygen concentrations at grain boundaries (Figure 4a), determining whether a grain boundary is present becomes difficult, with no evidence of transition metal impurities or light impurities present.

The main drawback of the TKD and APT analysis process is the time required to prepare and characterise a sample. This means that it is prohibitively difficult to analyse comparatively large sections of a grain boundary. While the technique used in this work, described in detail in [157], allows for larger areas of grain boundary to be analysed in a single sample, it is still not possible to establish statistical certainty as to the decoration of the entire grain boundary. Nonetheless, in combination with microscopic recombination characterisation using photoconductance and photoluminescence, it is possible to draw some tentative conclusions as to the critical

impurities responsible for recombination in Red Zone HPMC-Si samples before and after SDG.

Copper is a known fast diffuser in silicon [221], and is present in large quantities in red zone material. Although recombination as an interstitial atom is known to be weak, copper is found to decorate defects [271] and increase their recombination activity. Since Cu is highly soluble in silicon, a longer cool is likely important for effective gettering. Although SDG has significantly reduced the quantities of copper at the grain boundary, its presence after PDG is still likely to be responsible for at least part of the recombination activity.

The reduction in copper after SDG for the high activity grain boundary and the lifetime results (Figure 1c), in which a slow cool is required for high lifetimes, supports the hypothesis that copper is a primary element responsible for the increased lifetimes observed. As a result of industry time and cost pressures, phosphorus diffusion gettering (PDG) does not usually involve any form of slow cool [62]. It is therefore possible that the strong activation of grain boundaries after PDG, found by Sio et al. [35], is due to insufficient driving force for copper to be efficiently gettered to the phosphorus region.

7.3 Boron Diffusion of n-type High Performance Multicrystalline Silicon

As previously discussed, n-type silicon solar cells require a boron diffusion in order to produce the p-type surface emitter. Although boron diffusions have been found to

getter impurities, they have similar issues to PDG regarding the activation of defects [268].

The multiscale approach developed in this thesis was applied to investigate a number of grain boundaries before and after boron diffusion. The electrical activity was first measured across the entire sample using micro-PL. Following electrical measurements, the grain boundary types and misorientations were determined by EBSD. Finally, the defect compositions were analysed on the atomic scale using APT.

7.3.1 Photoluminescence

As discussed in Section 3.13, micro-PL provides high resolution mapping of recombination activity. Figure 7.6 shows micro-PL of two n-type high performance multicrystalline silicon wafers, before and after a boron diffusion. After the boron diffusion, intragrain regions are seen to increase significantly in lifetime, represented by the higher counts measured in PL. Grain boundaries however, become significantly more recombination active after boron diffusion, possibly indicating internal gettering of impurities to defects during the high temperature treatment. The three grain boundaries that were selected for further analysis are marked on Figure 7.6. Grain boundary 1 (GB1) becomes less recombination active after boron diffusion, whereas grain boundary 2 (GB2) and 3 (GB3) become significantly more recombination active. GB1 after boron diffusion also contains a highly recombination active area, right at the triple point, found to be a precipitate.

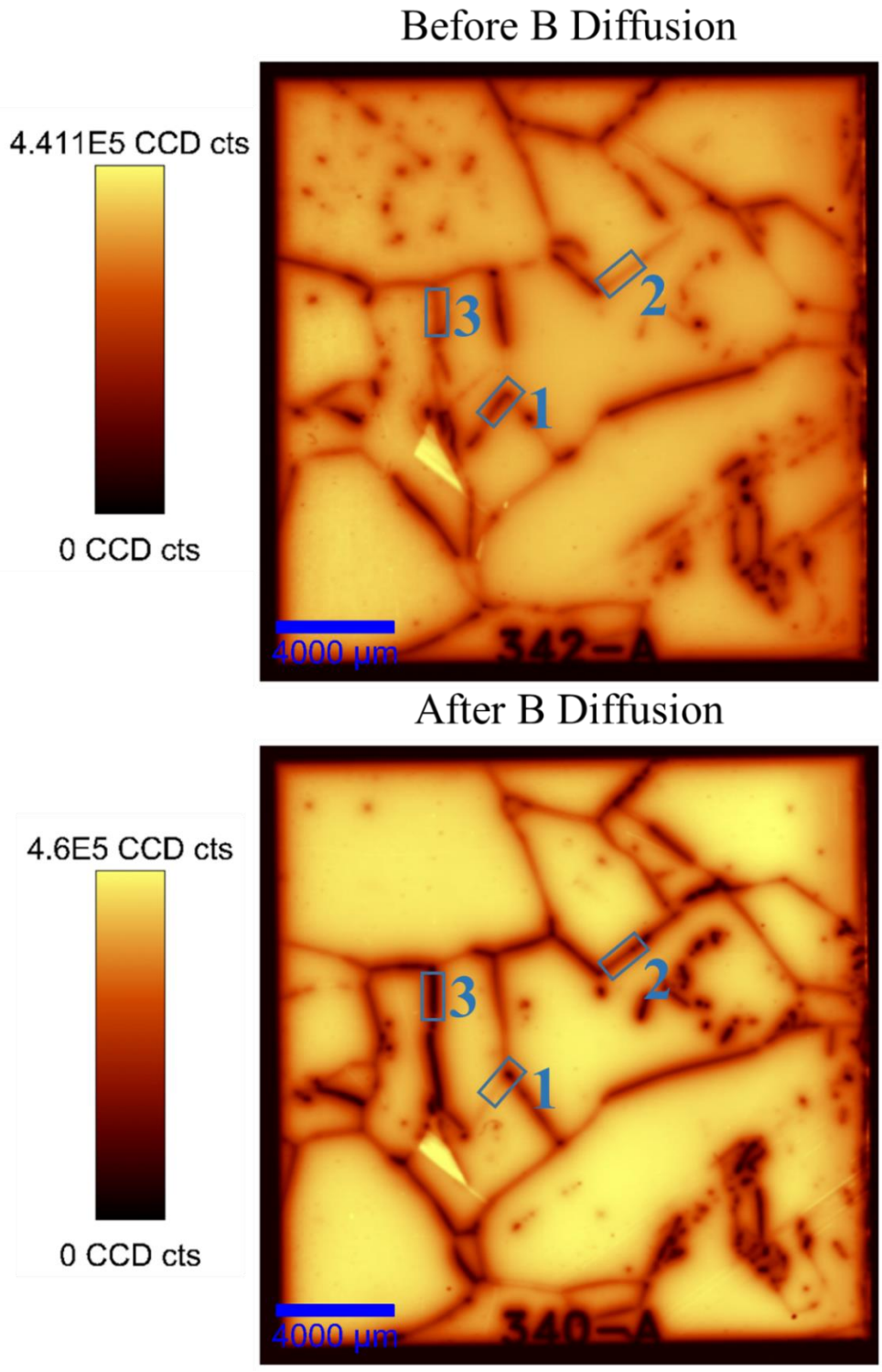


Figure 7.6. Micro-PL of two n-type HPMC-Si wafers before and after boron diffusion. Grain boundaries selected for further analysis are labelled. Images were acquired at the Fraunhofer Institute by F. Heinz. A light intensity of 1 sun was used, with the exposure time adjusted to a reasonable image.

7.3.2 Grain Boundary 1

From micro-PL (Figure 7.6) grain boundary 1 was found to decrease in recombination activity after boron diffusion, in contrast to the vast majority of grain boundaries. Using EBSD, this grain boundary was identified as a random angle grain boundary with a misorientation of 35.7° and a rotation axis of [-210].

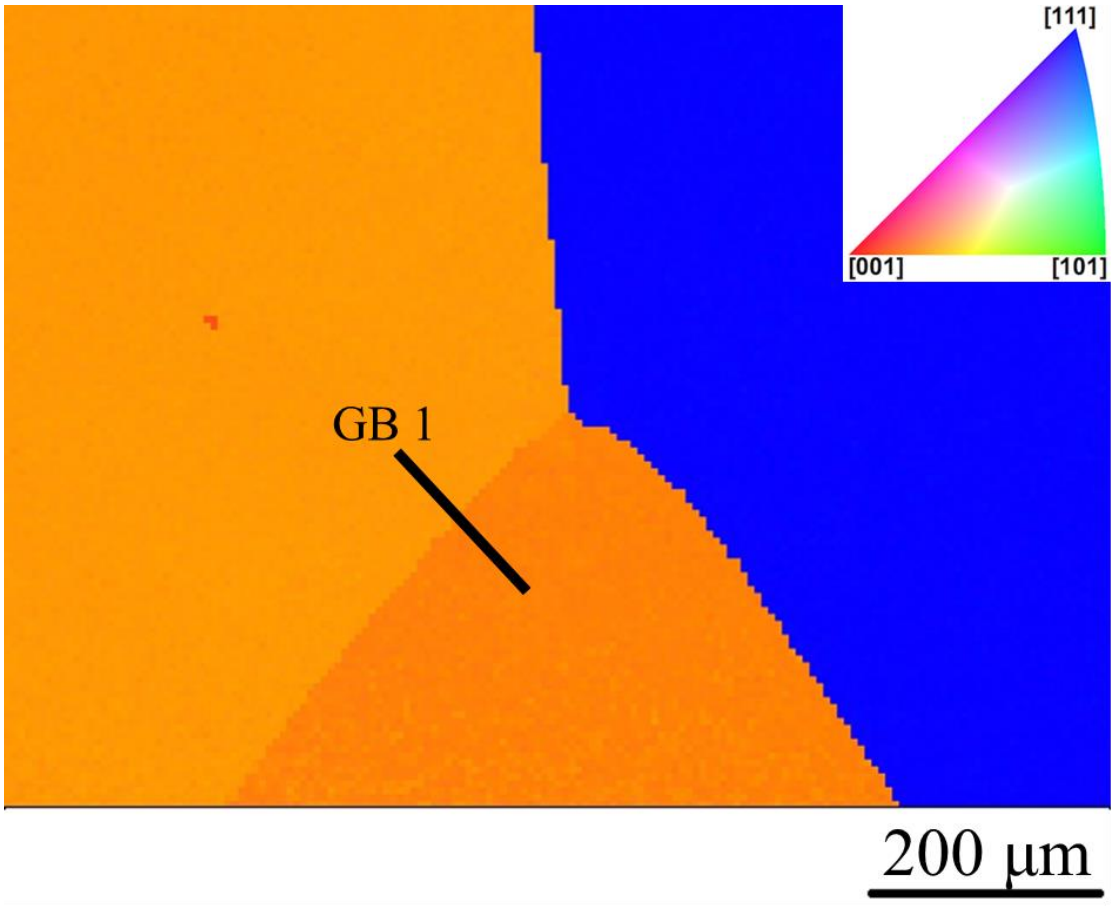


Figure 7.7. Electron backscatter diffraction inverse pole figure (IPFY) map of grain boundary 1.

In order to draw comparisons between the electrical activity of grain boundary composition, APT was performed on GB1 before and after boron diffusion. TKD or TEM were used prior to analysis, in order to confirm the grain boundary is at the apex

of the needle. Figure 7.8 shows a TKD map overlaid on top of a SEM image, showing GB1, from the sample prior to boron diffusion, running through the centre of the needle prior to APT analysis.

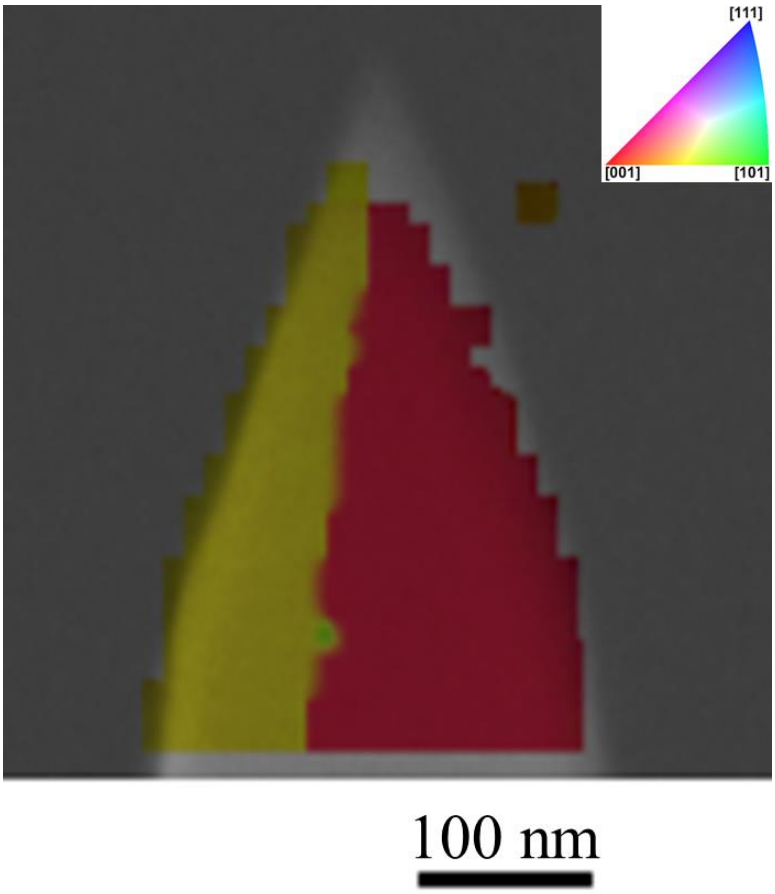


Figure 7.8. Transmission Kikuchi diffraction inverse pole figure (IPFZ) map of GB1, from the Si wafer before boron diffusion, prior to APT analysis.

APT analysis of GB1 from the Si wafer prior to boron diffusion is shown in Figure 7.9. From the figure, a significant excess of carbon and nitrogen can be seen decorating the grain boundary, observed as the molecular ions SiC, SiN and Si_2N. In addition, oxygen is observed at the boundary, in the form of SiO, and on the surface of the needle due to oxidation prior to analysis.

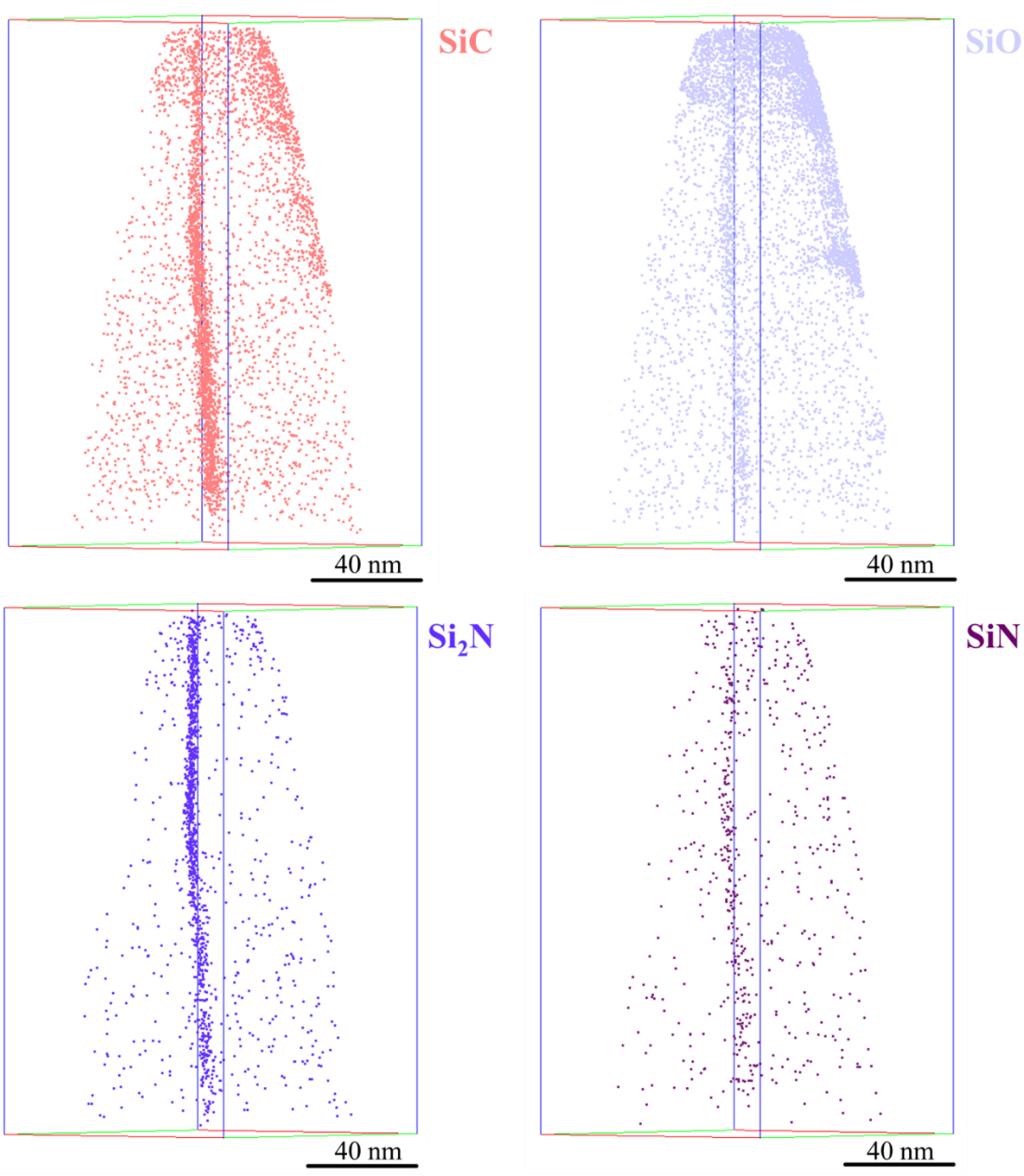


Figure 7.9. APT analysis of GB1 from the Si wafer prior to boron diffusion, showing an excess in carbon, oxygen and nitrogen decorating the boundary.

Following boron diffusion, TEM and APT analysis of GB1 (running parallel to the length of the needle) is shown in Figure 7.10. In this dataset, the triple point at which three grain boundaries meet is captured. At this triple point resides a precipitate that

contains significant levels of oxygen, carbon and nitrogen. GB1 is shown running at the bottom of the dataset, running parallel to the length of the needle. Here a significant excess of carbon, detected via APT in the form of the molecular SiC ions, is found. Much less evident is the additional decoration of the grain boundary by nitrogen and oxygen. Interestingly, much greater quantities of nitrogen are observed at the recombination active grain boundary (Top GB), connected to the top right of GB1 (see Figure 7.6).

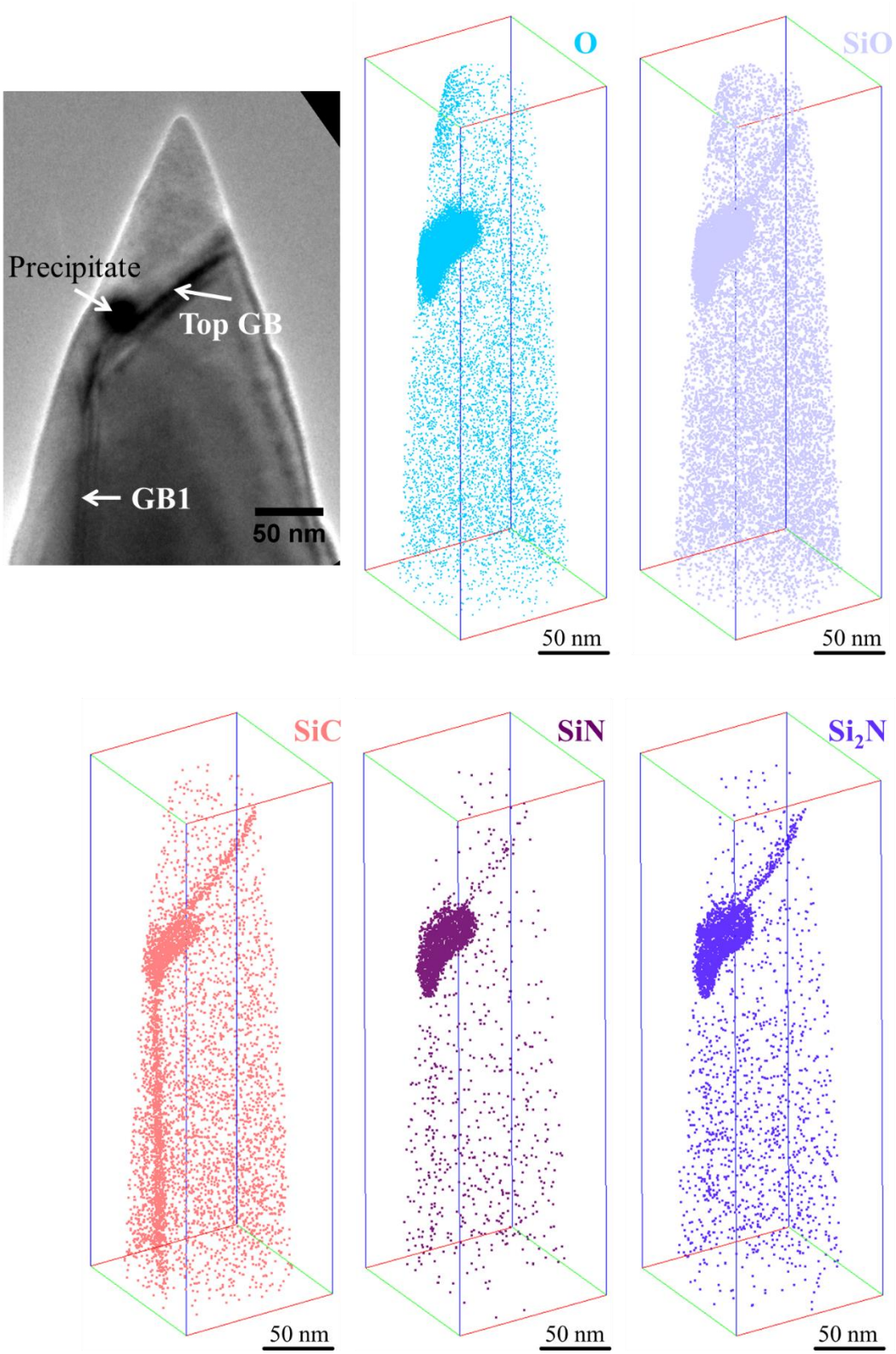


Figure 7.10. APT analysis of GB1 (lower boundary) from the Si wafer after boron diffusion, showing an excess carbon, oxygen and nitrogen decorating the boundary. An additional grain boundary (Top GB) and precipitate are shown at the top of the dataset.

The Gibbsian excess values for the light elements nitrogen, carbon and oxygen, found in GB1 before and after boron diffusion, and also to the top grain boundary seen in Figure 7.10, are shown in Table 7.2. From this table, the less recombination active grain boundary (after boron diffusion) is seen to contain significantly lower levels of nitrogen and carbon. Indeed the nitrogen level is reduced to almost zero, indicating only a weak segregation of N to the boundary. In contrast, greater levels of oxygen are found at the inactive grain boundary, albeit with greater error due to sample surface oxidation, indicating that the quantity of grain boundary oxygen is not dominant in determining recombination activity.

In addition, a direct comparison for the after boron diffusion dataset (Figure 7.10) between the recombination inactive GB1 and the recombination active top GB is made. Although the excess of carbon is lower than GB1, the top GB contains a notably higher level of nitrogen. This again replicates the difference between GB1 before and after boron diffusion, in which the more recombination active grain boundary contains higher quantities of nitrogen. The measurement of excess oxygen contains significantly more error due to sample surface oxidation.

Table 7.2. Gibbsian excess values for GB1 before and after boron diffusion.

	N	C	O
GB1 Before B Diffusion	0.14 ± 0.015 counts nm^{-2}	0.34 ± 0.047 counts nm^{-2}	0.00 ± 0.035 counts nm^{-2}
GB1 After B Diffusion	0.03 ± 0.005 counts nm^{-2}	0.27 ± 0.009 counts nm^{-2}	0.19 ± 0.015 counts nm^{-2}
Top GB After B Diffusion	0.07 ± 0.008 counts nm^{-2}	0.09 ± 0.001 counts nm^{-2}	-0.07 ± 0.117 counts nm^{-2}

APT analysis of the precipitate shown in Figure 7.10 from the sample after boron diffusion is shown in Figure 7.11. From the figure, a clear excess in carbon, oxygen and nitrogen is observed to decorate the grain boundary. These are observed as the molecular ions SiC, SiO, SiN and Si_2N. Since the precipitate is found on the edge of the dataset, determining its exact shape is challenging, although it appears non-spherical as was suggested by TEM in Figure 7.10. Instead, the precipitate is curved, with the top intersecting with the top GB and curving down to intersect with the GB1. Additionally, although oxygen and carbon are distributed homogeneously through the precipitate, nitrogen is found to encapsulate the grain boundary and is highest in concentration at the top GB intersection.

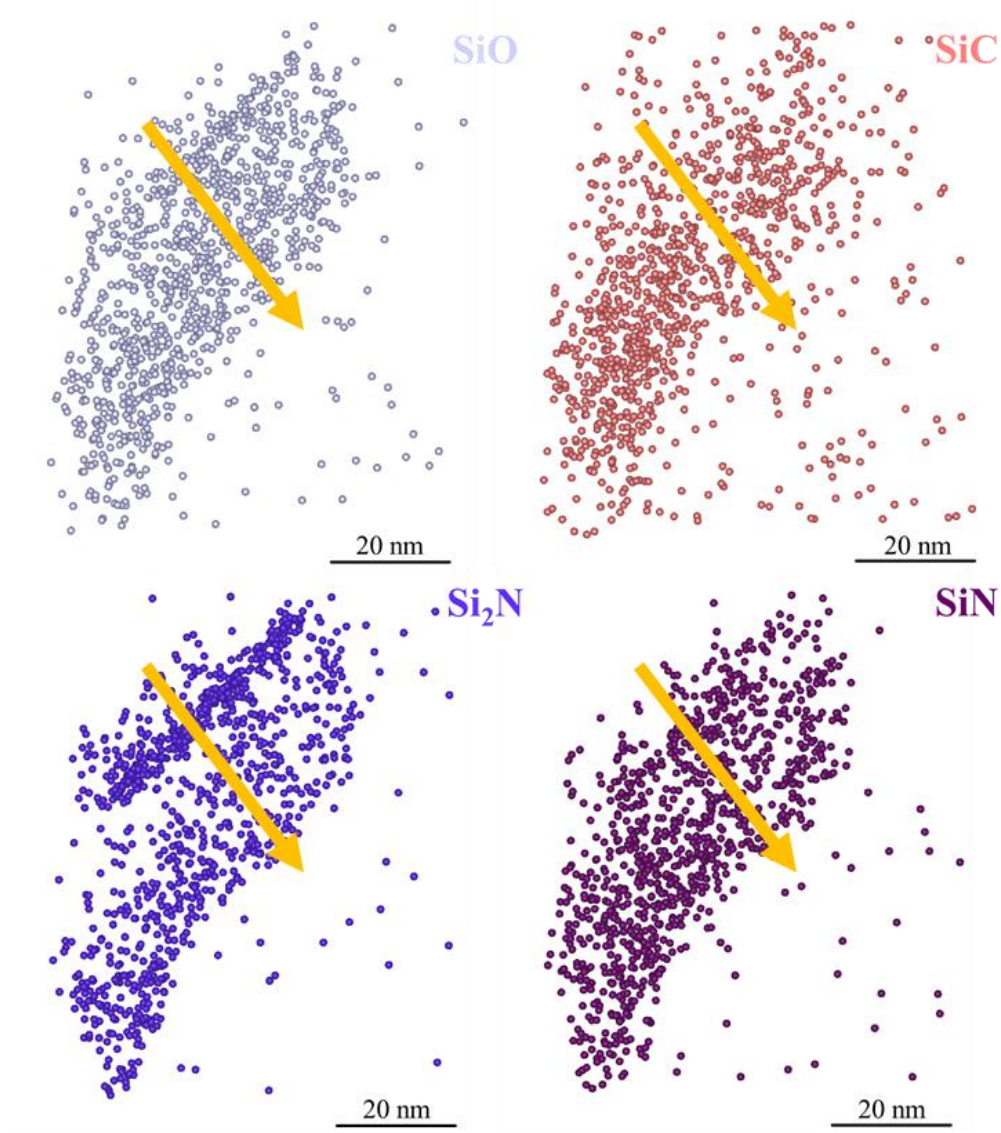


Figure 7.11. APT analysis of the precipitate found in Figure 7.10, showing an enrichment in oxygen, carbon and nitrogen. An arrow indicates the direction of analysis of a 1D concentration profile shown in Figure 7.12.

The 1D concentration profile through the precipitate in Figure 7.11 is plotted in Figure 7.12, showing the distribution of oxygen, carbon and nitrogen. Oxygen is found in the greatest quantities, with concentrations up to 15 at%. This is still much less than the atomic percentage present in a SiO_2 precipitate, with the majority element in this

precipitate still being silicon. Carbon and nitrogen are both found in concentrations up to a maximum of 2.5 at%. Interestingly, nitrogen is observed primarily at the precipitate interface, whereas carbon and oxygen are found in the precipitate bulk.

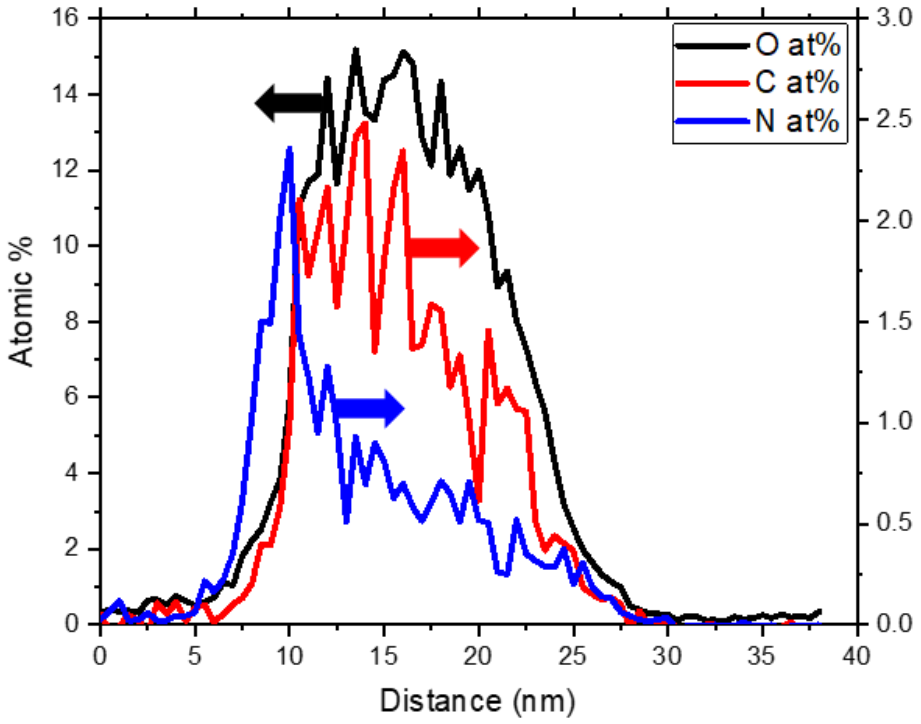


Figure 7.12. 1D concentration profile of the total atomic percentage of oxygen, nitrogen and carbon through the precipitate shown in Figure 7.11. The atomic percentage of oxygen is plotted on the left y-axis, while carbon and nitrogen are plotted with respect to the right y-axis.

7.3.3 Grain Boundary 2

As shown in the micro-PL images in Figure 7.6, grain boundary 2 is seen to increase in recombination activity after boron diffusion, transforming from relatively low recombination activity to significantly recombination active. From EBSD (Figure

7.13) this boundary was determined as a random angle grain boundary, with a misorientation of 45.6° around a rotation axis of [130].

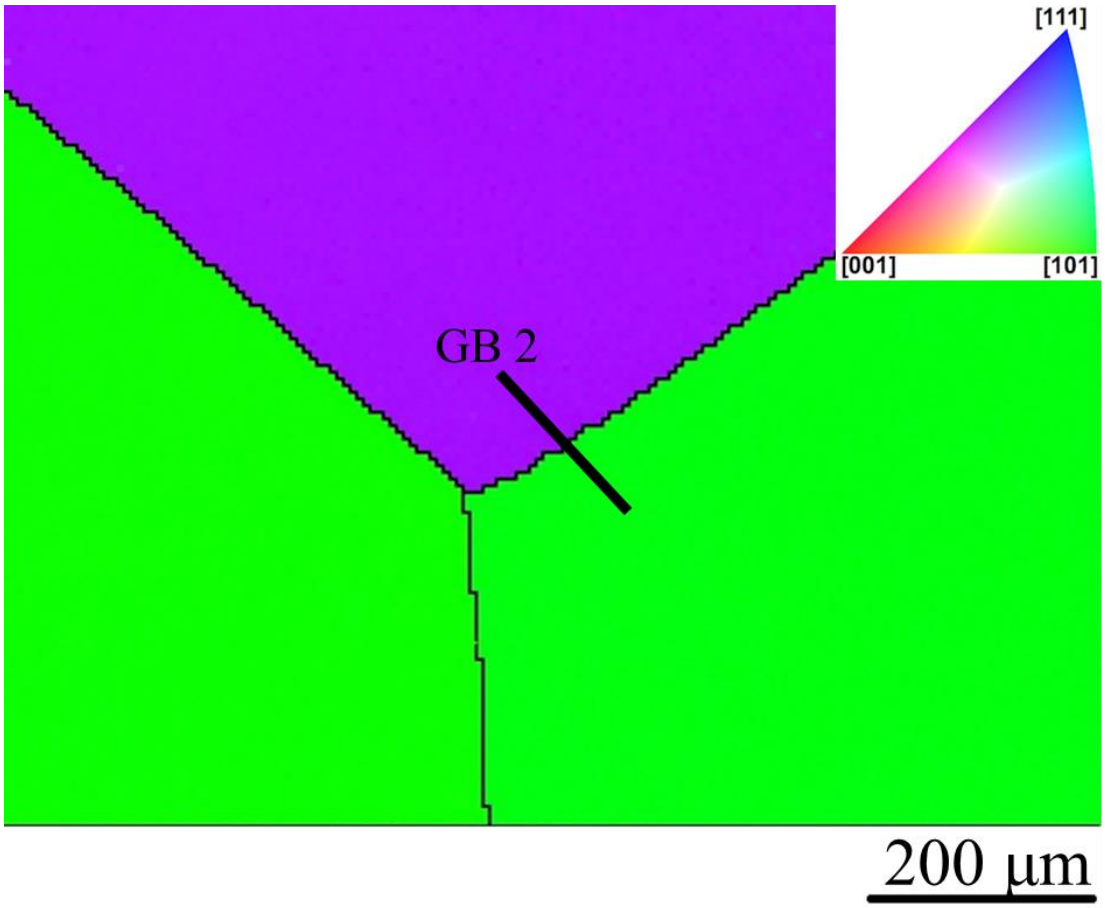


Figure 7.13. Electron backscatter diffraction inverse pole figure (IPFY) map with GB2 marked.

APT analysis of GB2, prior to B diffusion, is shown in Figure 7.14. The grain boundary contains a significant excess of carbon, oxygen and nitrogen. Additionally, the boundary is not straight throughout the dataset, but contains a distinct kink, at which an oxygen cluster is observed.

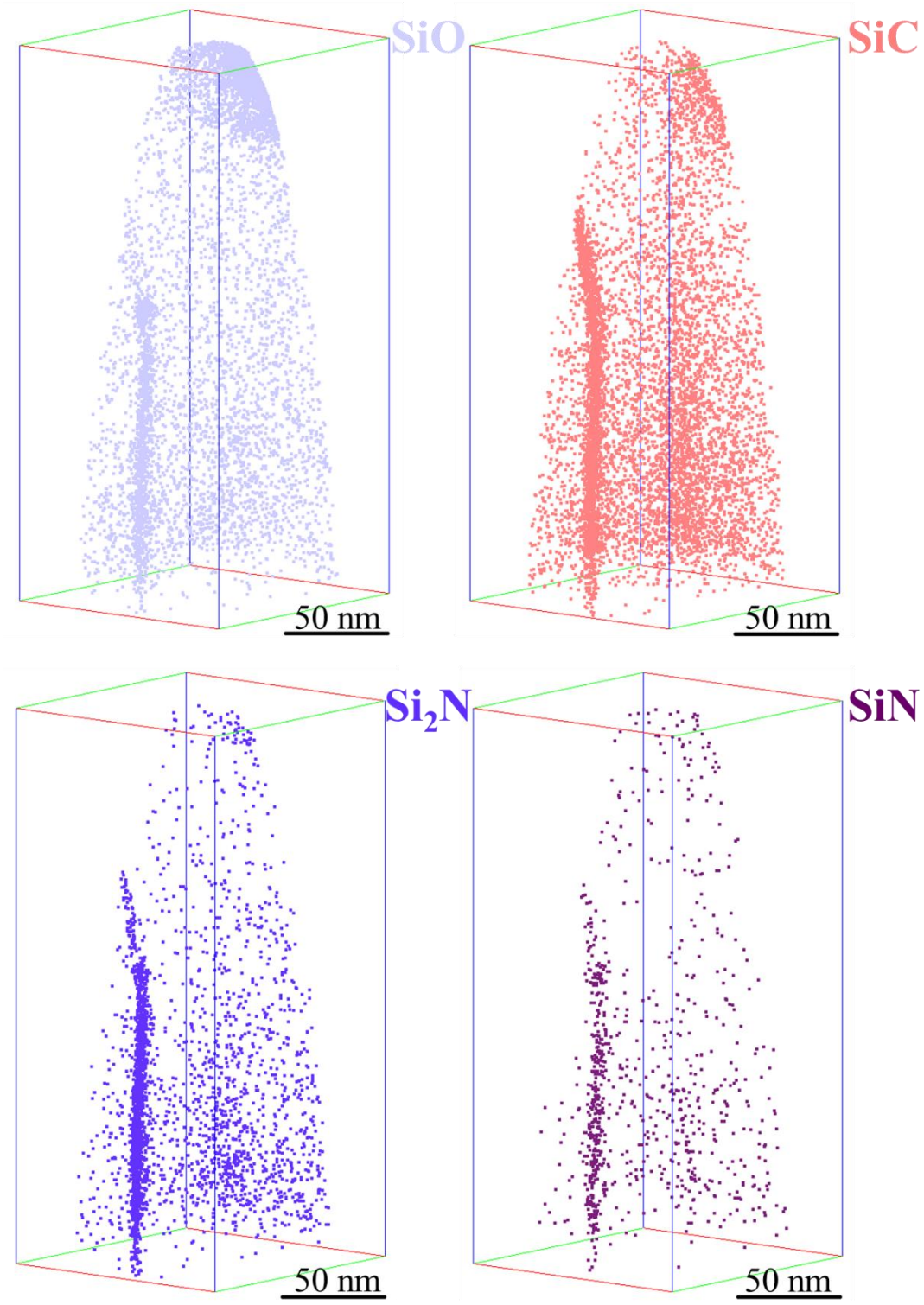


Figure 7.14. APT analysis of GB2 from an n-type HPMC-Si wafer prior to B diffusion, showing an excess in oxygen, carbon and nitrogen decorating the grain boundary.

APT analysis of GB2, extracted from a wafer following to B diffusion, is shown in Figure 7.15. Again, as for other grain boundaries analysed in this study, the boundary was found decorated in an excess of carbon, oxygen and nitrogen. This dataset is notably smaller than the others in this study, however the grain boundary was still captured and Gibbs excess measurements can still be made.

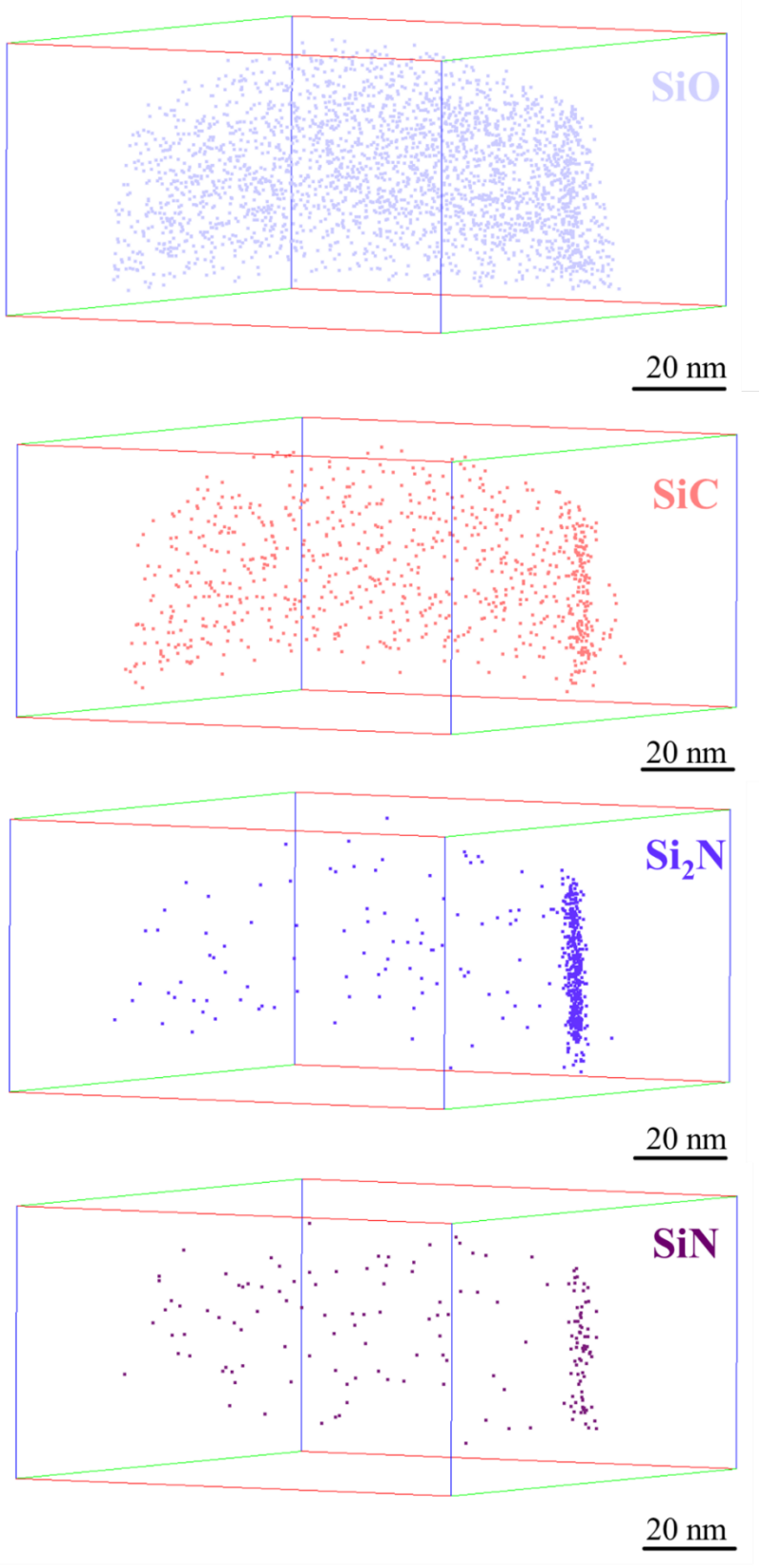


Figure 7.15. APT analysis of GB2 from an n-type multicrystalline silicon wafer after B diffusion, showing an excess in oxygen, carbon and nitrogen decorating the grain boundary.

Gibbsian interfacial excess values for GB2 before and after boron diffusion are shown in Table 7.3. From the micro-PL measurements, displayed in Figure 7.6, GB2 is observed to become significantly more recombination active after boron diffusion. This coincides with an increase in nitrogen and oxygen found at the boundary, as measured by APT. In contrast, carbon remains at a similar excess level before and after B diffusion, indicating that it was unaffected by the thermal treatment.

Table 7.3. Gibbsian excess values for GB2 before and after boron diffusion.

	N	C	O
GB2 Before B Diffusion	0.25 ± 0.014 counts nm^{-2}	0.20 ± 0.009 counts nm^{-2}	0.22 ± 0.027 counts nm^{-2}
GB2 After B Diffusion	0.52 ± 0.001 counts nm^{-2}	0.20 ± 0.017 counts nm^{-2}	1.05 ± 0.009 counts nm^{-2}

7.3.4 Grain Boundary 3

Micro-PL in Figure 7.6 shows that grain boundary 3 became significantly more recombination active after a boron diffusion. EBSD of the region containing GB3 is shown in Figure 7.16, with Σ3 (111) grain boundaries of misorientation 60° are shown marked via a red line. Although GB3 is recombination active before and after B diffusion, other Σ3 (111) grain boundaries marked on the left are inactive throughout processing.

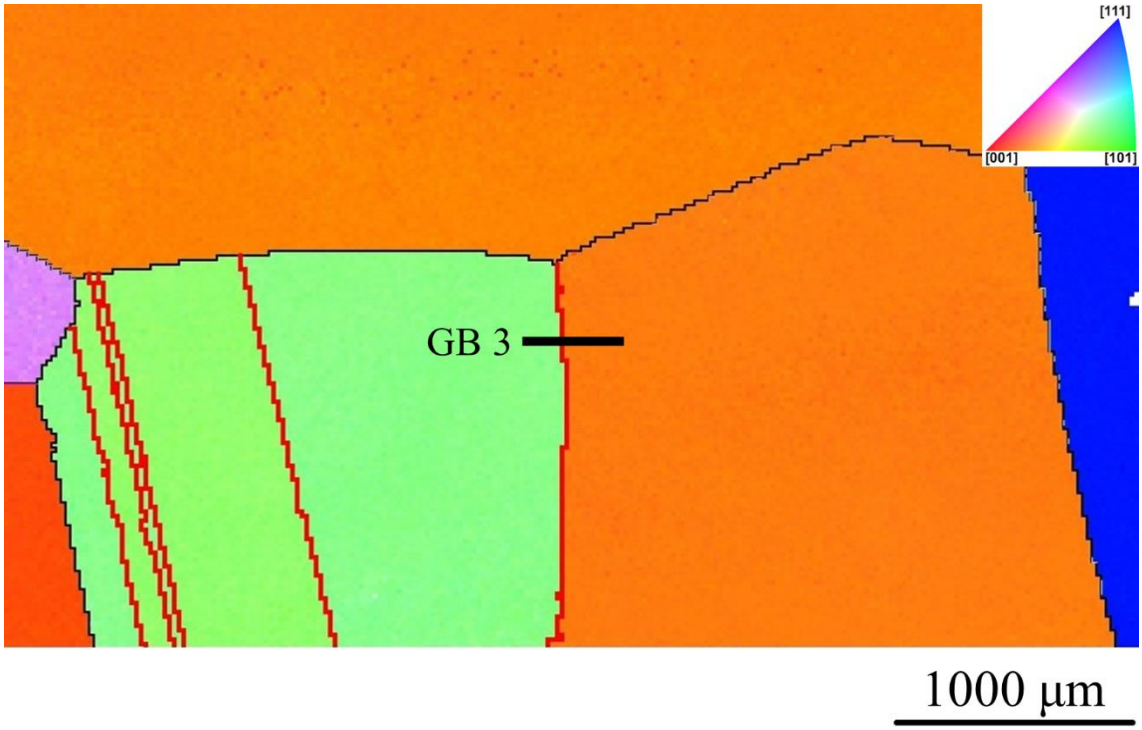


Figure 7.16. Electron backscatter diffraction inverse pole figure (IPFY) map, with GB3 marked. Σ3 {111) grain boundaries are marked by red lines.

A TEM bright field image of GB3, from the Si wafer prior to B diffusion, is shown in Figure 7.17. In this figure the interfaces between the bottom and top surfaces with the grain boundary plane, are marked. From this figure, it is clear that the boundary contains a large number of facets. Although the grain boundary is on the macro scale defined as a Σ3 (111) grain boundaries, which are known to be recombination inactive in silicon [30], on the micro and atomic scales a large degree of incoherence is present. Unfortunately, although a number of attempts were made to capture this boundary in an APT dataset, each needle fractured rapidly during analysis. This may be caused by localised stresses at the facetted grain boundary within in the needle, which likely enhances the probability of fracture.

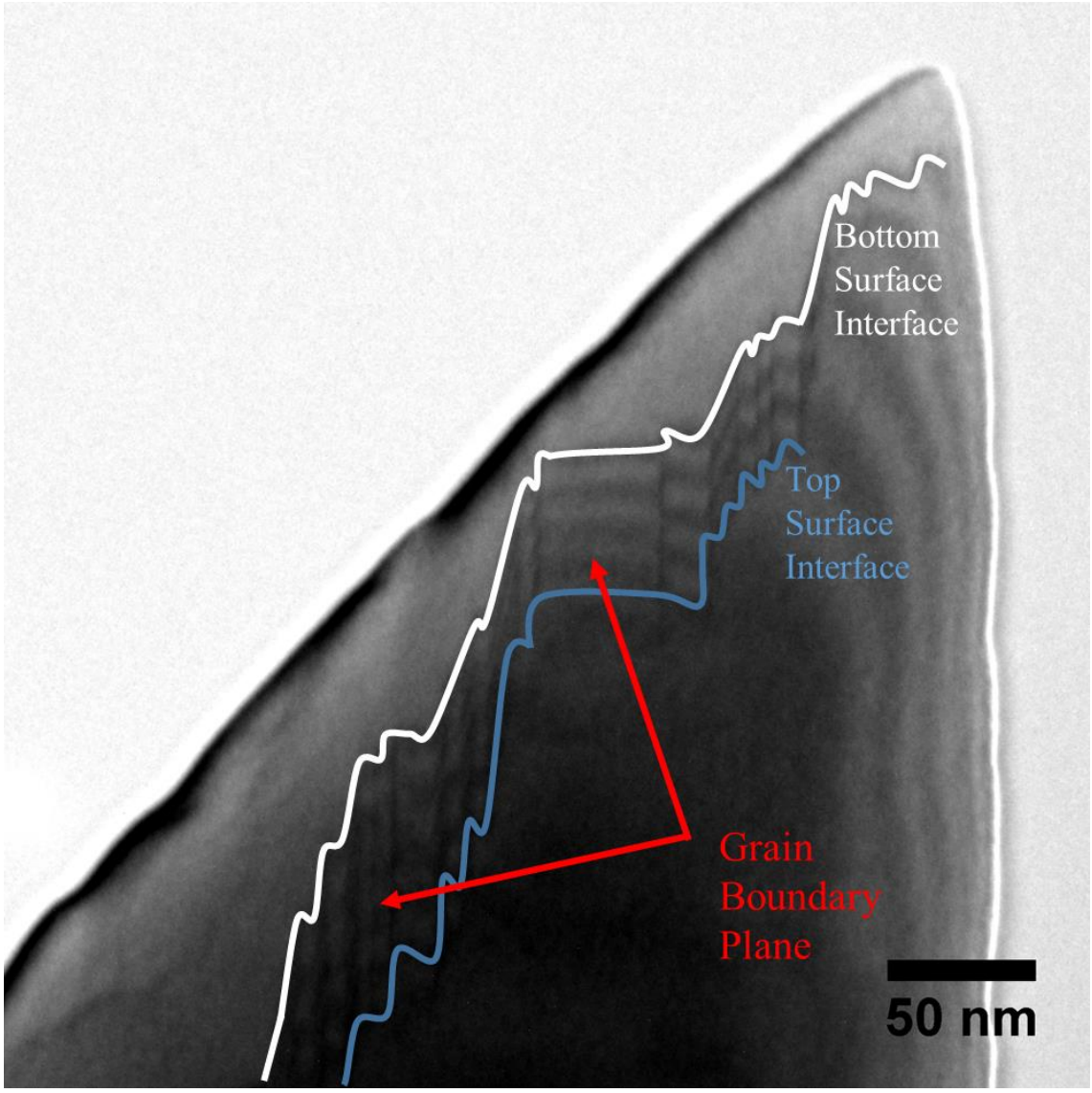


Figure 7.17. TEM bright field image of GB3, with the bottom surface and top surface interfaces with the grain boundary marked. The grain boundary plane is showed, containing significant faceting.

7.3.5 Discussion

In this section, a number of grain boundaries were studied before and after boron diffusion, correlating electrical activity, grain boundary type, and grain boundary composition. Figure 7.6 shows micro-PL of two n-type sister wafers in the As-cast

state and subsequent to boron diffusion. As previously discussed by Schindler et al. [126], boron diffusions result in a decrease in average lifetime, due to the strongly increased recombination at most structural defects, such as dislocations and grain boundaries. In contrast, intra-grain regions improve, due to the redistribution of impurities to grain boundaries during the B diffusion process [127]. In order to understand this effect further, three individual grain boundaries were studied before and after B diffusion.

GB1 (as marked in Figure 7.6), in contrast to the majority of grain boundaries, decreases dramatically after B diffusion becoming almost electrically inactive. APT analysis of grain boundary 1 is shown before (Figure 7.9) and after B diffusion (Figure 7.10). In both datasets the light elements carbon, nitrogen and oxygen are observed to decorate the boundary (as quantified in Table 7.2). Comparing before and after boron diffusion, oxygen was observed to increase significantly after boron diffusion. In contrast, nitrogen significantly reduces in grain boundary excess, while carbon maintains a similar excess before and after B diffusion.

The random angle GB2 was observed to increase in recombination activity following B diffusion (Figure 7.6). The Gibbsian excess values are shown in Table 7.3. Oxygen and nitrogen were both observed to increase in excess at the grain boundary after B diffusion, while carbon contained a similar excess before and after processing.

Since n-type multicrystalline silicon has not been examined using APT previously, APT analysis can only be compared to p-type silicon. The light elements observed to

decorate GB1 and GB2 have previously been detected in p-type using APT by Ohno et al. [156], Stoffers et al. [158] and also in Chapter 5. This is unsurprising, since ingot casting and subsequent B diffusions are performed at high temperatures at which the material will act in an intrinsic manner and is unaffected by the doping.

By comparing the APT analysis of GB1 and GB2, a notable feature is the lack of transition metals detected at both grain boundaries. The detection of such impurities in atom probe is limited by the technique's sensitivity and mass-to-charge-state overlaps. It is therefore not possible to conclude no transition metals decorate these boundaries. This is discussed in detail in Section 5.6.1.

In contrast, carbon is present at both GB1 and GB2 before and after B diffusion. Carbon is a known impurity in silicon, found at both grain boundaries [41] and dislocations [157]. Indeed, density functional calculations by Zhao et al. [272], [273] predict the strong gettering of carbon to grain boundaries, with the segregation of C to regions with compressed Si-Si bond lengths being energetically favourable. The excess in carbon remains at a similar level before and after B diffusion, for both grain boundaries. This strongly suggests that carbon does not play a significant role in the increase/decrease in recombination activity in this material. Additionally, since carbon was detected at the low recombination activity GB1 after B diffusion, its effect on GB recombination activity is thought to be limited. This supports the findings of Moeller et al. [274], in which carbon is described as forming defects that are of low electrical activity.

Quantifying the excess of grain boundary oxygen is much more difficult, due to the oxidation of the needle surface prior to APT analysis. Oxygen was however observed to increase in excess for both GB1 and GB2 after boron diffusion. Often found precipitated at grain boundaries and co-located with carbon [274], [275], oxygen is a well-known impurity in multicrystalline silicon. The excess of oxygen to grain boundaries after boron diffusion indicates internal gettering during the thermal treatment, in which oxygen present in large precipitates, as observed by Moeller et al. [276], segregate to grain boundaries during cooling. The increase in oxygen for GB1 does not correlate to the decrease in electrical activity following B diffusion, suggesting that the grain boundary oxygen excess does not play a dominant role in causing grain boundary recombination.

The light element nitrogen is the only observed impurity where the GB excess directly relates to the recombination activity in GB1 and GB2. Moreover, the recombination active top grain boundary (Figure 7.10) contains significantly more nitrogen than the electrically inactive GB1 after B diffusion observed in the same dataset. The nitrogen observed at these boundaries are detected via APT in the form of the molecular ions SiN^{+} and predominantly Si_2N^{2+}. The detection of Si_2N^{2+} at 35 Da is controversial, with Liebscher et al. [233] and Stoffers et al. [159] interpreting and reporting this peak to be due to the detection of FeN^{2+}. For an in-depth discussion regarding the peak at 35 Da, see Section 5.6.

The influence of nitrogen on the recombination activity of crystallographic defects has been the subject of debate, with Pizzini [42] found preliminary evidence that nitrogen

could contribute to grain boundary passivation. More recently however, in float zone material, Mullins et al. [277] found that nitrogen could introduce deep levels in the band gap which can increase recombination activity. APT does not provide information regarding which impurities are electrically active. However, the strong correlation with nitrogen and recombination activity in our samples and additional evidence from Stoffers et al. [159] of 35 Da observed at recombination active facets, makes a case that nitrogen may contribute to grain boundary recombination activity. Nevertheless, this conclusion should be treated tentatively, since nitrogen may instead be acting as a marker that behaves in a similar manner as a transition metal impurity below the detection limit (Section 5.6).

A precipitate was observed at the triple point of GB1 after boron diffusion (Figure 7.10). This precipitate is thought to be the cause of the significant recombination activity of the triple point, as observed by micro-PL (Figure 7.6). APT analysis of the precipitate, shown in Figure 7.11, displays the presence of the light elements oxygen, carbon and nitrogen. A number of different precipitates are known to exist in silicon. These include undissolved SiC particles incorporated from the melt [28], [42] and SiO_2 precipitates [42]. These precipitates are often observed at crystallographic defects, such as dislocations and grain boundaries, with SiO_2 precipitates acting as internal gettering sinks and showing strong recombination activity [278].

In this study, the precipitate contains approximately 16 at% oxygen and up to 2.5 at% carbon and nitrogen. The precipitate is therefore not a SiO_2 precipitate and has to the author's knowledge not been observed in silicon previously. From the 1D

concentration profile through the precipitate (Figure 7.12), nitrogen is seen to reside primarily at the interface. This phenomenon has been reported by Karoui and Rozgonyi [48], in which nitrogen segregates to oxide precipitate interfaces forming an oxynitride shell, both from the out-diffusion of nitrogen from the precipitate and vacancies at the precipitate interface acting as a sink for nitrogen. A strong argument for the reduction of nitrogen from GB1 (Table 7.1) and hence reduction in recombination activity after boron diffusion (Figure 7.6) is thought to be caused by nitrogen gettering to the oxide precipitate interface.

Grain boundary 3 is a Σ3 twin boundary (Figure 7.16) that becomes significantly more recombination active following boron diffusion (Figure 7.6). This is in stark contrast to other twin boundaries observed to the left of GB3 (Figure 7.16) which are electrically inactive before and after B diffusion. Although all of these grain boundaries are measured in EBSD as Σ3 {111} grain boundaries, TEM of GB3 (Figure 7.17) confirms that the boundary is in fact heavily faceted.

Although high resolution TEM was not used in this study, these facets strongly resemble the 'zig-zag' Σ3 {111} and Σ3 {112} facets observed by Chen et al. [260]. Using annular dark field TEM imaging, Chen et al. found the irregular parts of the 'zig-zag' to be extremely effective gettering sites for Fe and become recombination active. These faceted Σ3 grain boundaries have also been observed by Liebscher et al. [233]. At these facets, carbon, nitrogen and iron (found as FeN^{2+} at 35 Da, see Section 5.6) are found via APT analysis, which are thought to be the cause of the recombination activity. This is in contrast to straight, coherent Σ3 {111} grain

boundaries that are electrically inactive and are clean from impurities [30]. In this study, the facets present on GB3 provide efficient gettering sites for impurities, released from large precipitates during the high temperature boron diffusion process. This significantly increases the recombination activity of the grain boundary. Unfortunately, APT analysis of this boundary was not obtained, with specimens fracturing rapidly during analysis, potentially due to localised stresses at the grain boundary facets within the needle.

7.4 Conclusions

In this chapter a multiscale characterisation approach was applied to a variety of grain boundaries in two distinct material systems after two different processing techniques. These are the effect of saw damage gettering on Red Zone HPMC-Si and the effect of boron diffusion on n-type HPMC-Si.

The recombination active Red Zone HPMC-Si grain boundary was found to contain an excess of copper and the light elements oxygen, carbon and nitrogen. SDG, which reduced the recombination activity of the grain boundary, was seen to be effective at decreasing the amount of copper and also oxygen and nitrogen decorating the boundary. In contrast, the amount of carbon remains similar before and after SDG.

The Σ3 {111} grain boundary had a much lower recombination activity, likely due to the lack of metallic impurities observed at the boundary. Prior to gettering, the boundary was observed in APT via increased levels of oxygen, which are known to

getter via SDG. It is therefore difficult to ascertain whether the grain boundary was analysed from the gettered wafer, although no metallic impurities were observed.

For n-type HPMC-Si, the key conclusion regards the direct correlation of nitrogen grain boundary excess to the recombination activity in both GB1 and GB2. In contrast to the lower efficiency Red Zone HPMC-Si, no transition metals were observed to decorate the grain boundaries in n-type HPMC-Si. Carbon, as observed in the Red Zone grain boundaries, maintained a similar excess before and after processing. Finally, a recombination active precipitate was found at the triple point of GB1 following B diffusion, containing oxygen, carbon and encased in nitrogen.

8 Summary and Conclusions

During the course of this work, a novel approach was developed enabling a combined correlative microscopical approach of EBIC, TKD, TEM and APT to study crystallographic defects in multicrystalline silicon. By investigating the electrical activity, crystallographic orientation and composition of individual defects, a significant number of conclusions can be made:

a) **Contamination via colloidal silica polishing (Chapter 4)**

   Colloidal silica polishing, a standard laboratory preparation technique, was found to introduce contamination at room temperature. EBIC on the same wafer before and after colloidal silica polishing showed a large increase in the recombination activity of grain boundaries and dislocations. This coincided with the introduction of copper and nickel, which were observed to decorate grain boundaries using APT. This finding has significant implications for the wider scientific community, outlining the importance of preparing samples without unintentional contamination and the potential issues of using commercially available colloidal silica.

b) **Effect of phosphorus diffusion gettering and hydrogenation on grain boundaries in p-type HPMC-Si (Chapter 5)**

   Using the experimental approach developed in this thesis, seven grain boundaries were studied after various stages of processing. A high density of low angle grain boundaries were found to be extremely deleterious to wafer efficiency. Carbon was found to decorate all the grain boundaries, lining

individual dislocations. The largest EBIC contrast was observed after gettering, coinciding with the decoration of Si_2N^{2+}. No transition metals were observed at the low angle grain boundaries; albeit above a calculated detection limit of 1 x 10^{15} cm^{-3} for Fe. Although nitrogen strongly correlated to recombination activity, the cause of the increase of recombination is not known, with nitrogen potentially acting as a marker for other elements below the detection limit of APT.

In contrast, copper was observed at an isolated high angle grain boundary after gettering. This indicates internal gettering to grain boundaries during PDG. Additional light elements, carbon, oxygen, and nitrogen were also observed to decorate the grain boundary.

Finally, two grain boundaries of vastly different recombination activities were observed. In contrast to the low angle grain boundaries, the recombination inactive grain boundary contained significantly more nitrogen than the active boundary. Since APT cannot directly observe the cause of recombination, it is difficult to determine which elements are responsible. This boundary had however been exposed to hydrogen passivation, which may be the cause of the reduced recombination activity.

The quantity of the light elements carbon, oxygen and nitrogen found to decorate grain boundaries in this study, should outline the importance of investigating the effects of such impurities. This is potentially surprising for

solar cell manufacturers, who often focus primarily on the elimination of metallic impurities.

c) Direct observation of hydrogen at crystallographic defects (Chapter 6)

This thesis presents an important breakthrough for the characterisation of hydrogenation in multicrystalline silicon for solar cell applications. Using the microscopical approach developed in this thesis, in correlation with isotopic doping of ^{2}H, hydrogen can be directly observed to decorate crystallographic defects. An important aspect of this process is the ability to directly quantify the amount of hydrogen present at the defects. This information is invaluable and has the potential to directly answer why some grain boundaries respond to hydrogenation, whereas others do not.

d) Alternative solar cell materials (Chapter 7)

Two alternative solar cell materials were also examined in this thesis, namely p-type Red Zone HPMC-Si and n-type HPMC-Si. For Red Zone, SDG was found to be effective at reducing the amount of copper, nitrogen and oxygen decorating a grain boundary. In contrast, carbon remains similar before and after SDG.

An in-depth study on the effect of boron diffusion on n-type HPMC-Si was also presented. Notably, the defect recombination activity, as measured by micro-PL, was found to directly correlate with the nitrogen excess at the grain boundaries. This finding suggests that nitrogen may play a role in increasing

the recombination activity of grain boundaries in n-type HPMC-Si. Similar to Red Zone HPMC-Si, the carbon excess remained at a similar level before and after boron diffusion. Additionally, a significantly recombination active precipitate at a triple point was found to contain oxygen, carbon, and nitrogen, but no transition metals above the APT detection limit. This again highlights the potential for increased recombination due to the presence of light elements in silicon.

9 Future Work

During the course of this work the power of a combined correlative microscopical approach of EBIC, TKD, TEM and APT to study crystallographic defects in multicrystalline silicon, has been demonstrated. The continued application and further improvement of these techniques offers a wide range of potential new studies, which can enhance our understanding of defects in silicon solar cells. Based on the work conducted in this thesis, the following topics are proposed as potential future areas of study:

a) Quantification of hydrogen at crystallographic defects

The unique approach developed during the course of this thesis, which allows for the direct observation and quantification of hydrogen at individual defects, opens up a wide field of study for the analysis of hydrogen passivation in silicon. By using deuterated nitrides $SiN:^{2}H_{x}$, industrial hydrogenation methods could be accurately replicated. The electrical activity of defects at various stages of processing could then be measured using PL and EBIC. This could then be correlated with the crystallography of the grain boundaries using EBSD and TKD. Finally, the quantity of deuterium can be accurately measured using APT. This study has the potential to directly answer the question why some grain boundaries respond to hydrogenation, whereas others do not [145]. However, in order to make definitive conclusions, a large number of samples are required. This is extremely time consuming and difficult, when considering the large number of processing steps required prior to APT. This is in addition to the difficulty in producing grain boundary containing needles for APT.

b) Isotopic doping of silicon

A common and reoccurring theme of this work, was the inability to accurately determine whether transition metals were present at crystallographic defects, due to mass-to-charge-state overlaps. This is especially prevalent for Fe, which has a direct overlap with silicon. Using isotopically pure ^{54}Fe as an intentional contaminant in the silicon melt, the distribution of Fe can be accurately measured using APT and correlated to electrical activity. Additionally, the question of FeN or Si_2N at 35 Da can be addressed. It is important however, that the introduction of isotopically pure ^{54}Fe, does not also introduce other contaminants which could affect the electrical activity of defects.

c) Oxygen precipitation in Czochralski silicon

The formation of oxygen rings are known to cause increased recombination in single crystal silicon. It is thought that silicon oxide precipitates form under annealing, significantly enhancing recombination. This is especially prevalent when samples are annealed in a nitrogen ambient [279]. Using the correlative EBIC, TEM and APT approach developed in this thesis, the size, composition and structure of these precipitates can be determined and correlated to electrical activity.

d) Alternative and future solar cell materials

In the field of solar cells, a number of new materials are being developed with the aim of replacing conventional p-type multicrystalline silicon. One possible

material is cast monocrystalline silicon, which consists of large grains and regions of high densities of low angle grain boundaries. Using the well-developed and established method from this thesis of characterising grain boundaries using EBIC, EBSD and APT, the defects of this material can be assessed. Defects after various stages of processing can be compared, with the aim of understanding and optimising processing conditions. This method can also be applied to crystallographic defects in silicon wafers produced via direct wafer technologies and alternative semiconductors, such as GaAs where there is a renewed interest in the influence of light elements. These studies would however be extremely time-consuming, requiring multiple samples and correlative analysis using a large number of different analytical techniques.

10 References

[1] F. Fallahi, M. Karimi, and M. C. Voia, "Persistence in world energy consumption: Evidence from subsampling confidence intervals," *Energy Economics*, vol. 57, pp. 175–183, 2016.

[2] K.-Y. Dong, R.-J. Sun, H. Li, and H.-D. Jiang, "A review of China's energy consumption structure and outlook based on a long-range energy alternatives modeling tool," *Petroleum Science*, vol. 14, no. 1, pp. 214–227, 2017.

[3] J. Szlufcik, S. Sivoththaman, J. F. Nijs, R. P. Mertens, and R. Van Overstraeten, "Low cost industrial technologies of crystalline silicon solar cells," *Proceedings of the IEEE*, vol. 85, no. 5, pp. 711–730, 1997.

[4] F. Barbir and H. J. Plass Jr, "Environmental damage due to fossil fuels use," *International Journal of Hydrogen Energy*, vol. 15, no. 10, pp. 739–749, 1990.

[5] Fraunhofer ISE, "Photovoltaics report," 2016.

[6] D. K. Schroder and D. L. Meier, "Solar cell contact resistance - A review," *IEEE Transactions on Electron Devices*, vol. ED-31, no. 5, pp. 637–647, 1984.

[7] G. Coletti, "Sensitivity of state-of-the-art and high efficiency crystalline silicon solar cells to metal impurities," *Progress in Photovoltaics: Research and Applications*, vol. 21, pp. 1163–1170, 2013.

[8] D. Macdonald, H. Mäckel, and A. Cuevas, "Effect of gettered iron on recombination in diffused regions of crystalline silicon wafers," *Applied Physics Letters*, vol. 88, no. 9, pp. 86–89, 2006.

[9] A. Cuevas, M. J. Kerr, C. Samundsett, F. Ferrazza, and G. Coletti, "Millisecond minority carrier lifetimes in n-type multicrystalline silicon," *Applied Physics Letters*, vol. 81, no. 26, pp. 4952–4954, 2002.

[10] M. A. Green, *Silicon Solar Cells*, Print. Sydney: Centre for Photovoltaic Engineering, University of New South Wales, Sydney NSW 2052, Australia, 1995.

[11] M. A. Green, *Solar Cells Operating Principles, Technology and System Applications*. Kensington: Prentice-Hall, Inc, 1998.

[12] W. Shockley and W. T. Read, "Statistics of the Recombination of Holes and Electrons," *Physical Review*, vol. 87, no. 46, pp. 835–842, 1952.

[13] R. N. Hall, "Recombination processes in semiconductors," *Proceedings of the IEE - Part B: Electronic and Communication Engineering*, vol. 106, no. 17, pp. 923–931, May 1959.

[14] A. G. Aberle, *Crystalline Silicon Solar Cells Advanced Surface Passivation and Analysis*, Print. Sydney: Centre for Photovoltaic Engineering, University of New South Wales, Sydney NSW 2052, Australia, 1999.

[15] T. S. Fell, P. R. Wilshaw, and M. D. De Coteau, "EBIC investigations of dislocations and their interactions with impurities in silicon," *Physica Status Solidi (a)*, vol. 138, no. 2, pp. 695–704, 1993.

[16] D. Macdonald and A. Cuevas, "Trapping of minority carriers in multicrystalline silicon," *Applied Physics Letters*, vol. 74, no. 12, pp. 1710–1712, 1999.

[17] A. Cuevas, M. Stocks, D. Macdonald, M. Kerr, and C. Samundsett, "Recombination and trapping in multicrystalline silicon," *IEEE Transactions on Electron Devices*, vol. 46, no. 10, pp. 2026–2034, 1999.

[18] D. Macdonald, L. J. Geerligs, and A. Azzizi, "Iron detection in crystalline silicon by carrier lifetime measurements for arbitrary injection and doping," *Journal of Applied Physics*, vol. 95, no. 3, pp. 1021–1028, 2004.

[19] R. Kvande, L. Arnberg, and C. Martin, “Influence of crucible and coating quality on the properties of multicrystalline silicon for solar cells,” *Journal of Crystal Growth*, vol. 311, no. 3, pp. 765–768, 2009.

[20] R. Kvande, L. J. Geerligs, G. Coletti, L. Arnberg, M. Di Sabatino, E. J. Øvrelid, and C. C. Swanson, “Distribution of iron in multicrystalline silicon ingots,” *Journal of Applied Physics*, vol. 104, p. 064905, 2008.

[21] E. G. Seebauer and K. W. Noh, “Trends in semiconductor defect engineering at the nanoscale,” *Materials Science and Engineering R: Reports*, vol. 70, no. 3–6, pp. 151–168, 2010.

[22] V. Kveder, W. Schröter, A. Sattler, and M. Seibt, “Simulation of Al and phosphorus diffusion gettering in Si,” *Materials Science and Engineering B: Solid-State Materials for Advanced Technology*, vol. 71, pp. 175–181, 2000.

[23] A. A. Istratov, H. Hieslmair, and E. R. Weber, “Iron contamination in silicon technology,” *Applied Physics A: Materials Science and Processing*, vol. 70, no. 5, pp. 489–534, 2000.

[24] V. Raineri, R. J. Schreutelkamp, F. W. Saris, K. T. F. Janssen, and R. E. Kaim, “Reduction of boron diffusion in silicon by 1 MeV 29Si + irradiation,” *Applied Physics Letters*, vol. 58, no. 9, pp. 922–924, 1991.

[25] K. I. Kurobe, M. Miura, K. Hirano, and H. Matsunami, “Spatial distribution of minority-carrier lifetime and local concentration of impurities in multicrystalline silicon solar cells,” *Solar Energy Materials and Solar Cells*, vol. 74, pp. 183–193, 2002.

[26] K. Arafune, T. Sasaki, F. Wakabayashi, Y. Terada, Y. Ohshita, and M. Yamaguchi, “Study on defects and impurities in cast-grown polycrystalline

silicon substrates for solar cells," *Physica B: Condensed Matter*, vol. 376–377, no. 1, pp. 236–239, 2006.

[27] T. Buonassisi, A. A. Istratov, M. D. Pickett, M. Heuer, J. P. Kalejs, G. Hahn, M. A. Marcus, B. Lai, Z. Cai, S. Heald, T. F. Ciszek, R. F. Clark, D. W. Cunningham, A. M. Gabor, R. Jonczyk, S. Narayanan, E. Sauar, and E. R. Weber, "Chemical natures and distributions of metal impurities in multicrystalline silicon materials," *Progress in Photovoltaics: Research and Applications*, vol. 14, no. 6, pp. 512–531, 2006.

[28] X. Tang, L. A. Francis, L. Gong, F. Wang, J.-P. Raskin, D. Flandre, S. Zhang, D. You, L. Wu, and B. Dai, "Solar Energy Materials & Solar Cells Characterization of high-efficiency multi-crystalline silicon in industrial production," *Solar Energy Materials and Solar Cells*, vol. 117, pp. 225–230, 2013.

[29] J. Chen, D. Yang, Z. Xi, and T. Sekiguchi, "Recombination activity of sigma 3 boundaries in boron-doped multicrystalline silicon: Influence of iron contamination," *Journal of Applied Physics*, vol. 97, p. 033701, 2005.

[30] Y. Ohno, K. Inoue, Y. Tokumoto, K. Kutsukake, I. Yonenaga, N. Ebisawa, H. Takamizawa, Y. Shimizu, K. Inoue, Y. Nagai, H. Yoshida, and S. Takeda, "Three-dimensional evaluation of gettering ability of sigma 3 {111} grain boundaries in silicon by atom probe tomography combined with transmission electron microscopy," *Applied Physics Letters*, vol. 103, no. 10, pp. 12–16, 2013.

[31] J. Chen and T. Sekiguchi, "Carrier recombination activity and structural properties of small-angle grain boundaries in multicrystalline silicon,"

Japanese Journal of Applied Physics, Part 1: Regular Papers and Short Notes and Review Papers, vol. 46, no. 10 A, pp. 6489–6497, 2007.

[32] S. Castellanos, K. E. Ekstrøm, A. Autruffe, M. A. Jensen, A. E. Morishige, J. Hofstetter, P. Yen, B. Lai, G. Stokkan, C. del Canizo, and T. Buonassisi, "High-Performance and Traditional Multicrystalline Silicon: Comparing Gettering Responses and Lifetime-Limiting Defects," *IEEE Journal of Photovoltaics*, vol. 6, no. 3, pp. 1–19, 2016.

[33] G. Stokkan, D. S. Marisa, R. Søndenå, M. Juel, A. Autruffe, K. Adamczyk, H. V. Skarstad, K. E. Ekstrøm, M. S. Wiig, C. C. You, H. Haug, and M. M'Hamdi, "Impurity control in high performance multicrystalline silicon," *Physica Status Solidi (A) Applications and Materials Science*, vol. 214, no. 7, p. 1700319, 2017.

[34] G. Stokkan, Y. Hu, O. Mjøs, and M. Juel, "Study of evolution of dislocation clusters in high performance multicrystalline silicon," *Solar Energy Materials and Solar Cells*, vol. 130, pp. 679–685, 2014.

[35] H. C. Sio, S. P. Phang, P. Zheng, Q. Wang, W. Chen, H. Jin, and D. Macdonald, "Recombination sources in p-type high performance multicrystalline silicon," *Japanese Journal of Applied Physics*, vol. 56, p. 08MB16, Aug. 2017.

[36] J. Haunschild, I. E. Reis, J. Geilker, and S. Rein, "Detecting efficiency-limiting defects in Czochralski-grown silicon wafers in solar cell production using photoluminescence imaging," *Physica Status Solidi - Rapid Research Letters*, vol. 5, no. 5–6, pp. 199–201, 2011.

[37] J. D. Murphy, R. E. McGuire, K. Bothe, V. V. Voronkov, and R. J. Falster, "Minority carrier lifetime in silicon photovoltaics: The effect of oxygen

precipitation," *Solar Energy Materials and Solar Cells*, vol. 120, pp. 402–411, 2014.

[38] V. Lang, J. D. Murphy, R. J. Falster, and J. J. L. Morton, "Spin-dependent recombination in Czochralski silicon containing oxide precipitates," *Journal of Applied Physics*, vol. 111, p. 013710, 2012.

[39] C. Cabanel and J. Y. Laval, "Localization of the electrical activity of structural defects in polycrystalline silicon," *Journal of Applied Physics*, vol. 67, no. 3, pp. 1425–1432, 1990.

[40] S. Pizzini, M. Acciarri, and S. Binetti, "From electronic grade to solar grade silicon: Chances and challenges in photovoltaics," *Physica Status Solidi (A) Applications and Materials Science*, vol. 202, no. 15, pp. 2928–2942, 2005.

[41] A. Stoffers, O. Cojocaru-Miredin, O. Breitenstein, W. Seifert, S. Zaefferer, and D. Raabe, "Grain boundary characterization in multicrystalline silicon using joint EBSD, EBIC, and atom probe tomography," in *2014 IEEE 40th Photovoltaic Specialist Conference (PVSC)*, 2014, pp. 0042–0046.

[42] S. Pizzini, "Influence of Extended Defects and Native Impurities on the Electrical Properties of Directionally Solidified Polycrystalline Silicon," *Journal of The Electrochemical Society*, vol. 135, no. 1, pp. 155–165, 1988.

[43] S. Pizzini, "Bulk solar grade silicon: How chemistry and physics play to get a benevolent microstructured material," *Applied Physics A: Materials Science and Processing*, vol. 96, no. 1, pp. 171–188, 2009.

[44] A. K. Søiland, E. J. Øvrelid, T. A. Engh, O. Lohne, J. K. Tuset, and Gjerstad, "SiC and Si3N4 inclusions in multicrystalline silicon ingots," *Materials Science in Semiconductor Processing*, vol. 7, pp. 39–43, 2004.

[45] J. Lu, M. Wagener, G. Rozgonyi, J. Rand, and R. Jonczyk, “Effects of grain boundary on impurity gettering and oxygen precipitation in polycrystalline sheet silicon,” *Journal of Applied Physics*, vol. 94, no. 1, pp. 140–144, 2003.

[46] M. Suezawa, K. Sumino, H. Harada, and T. Abe, “Nitrogen-Oxygen Complexes as Shallow Donors in Silicon Crystals,” *Japanese Journal of Applied Physics*, vol. 25, no. 10, pp. L859–L861, 1986.

[47] S. Woo, M. Bertoni, K. Choi, S. Nam, S. Castellanos, D. M. Powell, T. Buonassisi, and H. Choi, “An insight into dislocation density reduction in multicrystalline silicon,” *Solar Energy Materials and Solar Cells*, vol. 155, pp. 88–100, 2016.

[48] A. Karoui and G. A. Rozgonyi, “Oxygen precipitation in nitrogen doped Czochralski silicon wafers. II. Effects of nitrogen and oxygen coupling,” *Journal of Applied Physics*, vol. 96, no. 6, pp. 3264–3271, 2004.

[49] A. A. Istratov, T. Buonassisi, R. J. McDonald, A. R. Smith, R. Schindler, J. A. Rand, J. P. Kalejs, and E. R. Weber, “Metal content of multicrystalline silicon for solar cells and its impact on minority carrier diffusion length,” *Journal of Applied Physics*, vol. 94, no. 10, pp. 6552–6559, 2003.

[50] T. Buonassisi, A. A. Istratov, M. Heuer, M. A. Marcus, R. Jonczyk, J. Isenberg, B. Lai, Z. Cai, S. Heald, W. Warta, R. Schindler, G. Willeke, and E. R. Weber, “Synchrotron-based investigations of the nature and impact of iron contamination in multicrystalline silicon solar cells,” *Journal of Applied Physics*, vol. 97, p. 074901, 2005.

[51] S. Riepe, I. E. Reis, W. Kwapil, M. A. Falkenberg, J. Schön, H. Behnken, J. Bauer, D. Kreßner-Kiel, W. Seifert, and W. Koch, “Research on efficiency

limiting defects and defect engineering in silicon solar cells - results of the German research cluster SolarFocus," *Physica Status Solidi (C) Current Topics in Solid State Physics*, vol. 8, no. 3, pp. 733–738, 2011.

[52] K. Graff, *Metal Impurities in Silicon-Device Fabrication*, 2nd Ed. Springer, 1999.

[53] D. Macdonald, A. Cuevas, A. Kinomura, Y. Nakano, and L. J. Geerligs, "Transition-metal profiles in a multicrystalline silicon ingot," *Journal of Applied Physics*, vol. 97, p. 033523, 2005.

[54] J. Schön, A. Haarahiltunen, H. Savin, D. P. Fenning, T. Buonassisi, W. Warta, and M. C. Schubert, "Analyses of the evolution of iron-silicide precipitates in multicrystalline silicon during solar cell processing," *IEEE Journal of Photovoltaics*, vol. 3, no. 1, pp. 131–137, 2013.

[55] J. Bailey and E. R. Weber, "Precipitation of Iron in Polycrystalline Silicon," *Physica Status Solidi (a)*, vol. 137, no. 2, pp. 515–523, 1993.

[56] G. Zoth and W. Bergholz, "A fast, preparation-free method to detect iron in silicon," *Journal of Applied Physics*, vol. 67, no. 11, pp. 6764–6771, 1990.

[57] M. E. Rodríguez, A. Mandelis, G. Pan, J. A. García, V. Gorodokin, and Y. Raskin, "Minority carrier lifetime and iron concentration measurements on p-Si wafers by infrared photothermal radiometry and microwave photoconductance decay," *Journal of Applied Physics*, vol. 87, no. 11, pp. 8113–8121, Jun. 2000.

[58] A. Liu, Y.-C. Fan, and D. Macdonald, "Interstitial iron concentrations across multicrystalline silicon wafers via photoluminescence imaging," *Progress in Photovoltaics: Research and Applications*, vol. 19, no. 6, pp. 649–657, Sep.

2011.

[59] J. R. Davis, a. Rohatgi, R. H. Hopkins, P. D. Blais, P. Rai-Choudhury, J. R. McCormick, and H. C. Mollenkopf, "Impurities in silicon solar cells," *IEEE Transactions on Electron Devices*, vol. 27, no. 4, pp. 677–687, 1980.

[60] M. Seibt, R. Khalil, V. Kveder, and W. Schröter, "Electronic states at dislocations and metal silicide precipitates in crystalline silicon and their role in solar cell materials," *Applied Physics A: Materials Science and Processing*, vol. 96, pp. 235–253, 2009.

[61] C. Rudolf, P. Saring, L. Stolze, and M. Seibt, "Co-precipitation of copper and nickel in crystalline silicon," *Materials Science and Engineering B: Solid-State Materials for Advanced Technology*, vol. 159–160, pp. 365–368, 2009.

[62] D. P. Fenning, A. S. Zuschlag, M. I. Bertoni, B. Lai, G. Hahn, and T. Buonassisi, "Improved iron gettering of contaminated multicrystalline silicon by high-temperature phosphorus diffusion," *Journal of Applied Physics*, vol. 113, p. 214504, 2013.

[63] K. Hoummada, D. Mangelinck, B. Gault, and M. Cabié, "Nickel segregation on dislocation loops in implanted silicon," *Scripta Materialia*, vol. 64, no. 5, pp. 378–381, 2011.

[64] A. Bentzen and A. Holt, "Gettering of transition metal impurities during phosphorus emitter diffusion in multicrystalline silicon solar cell processing," *Journal of Applied Physics*, vol. 99, no. 2027, pp. 1–6, 2006.

[65] W. C. Dash, "Copper precipitation on dislocations in silicon," *Journal of Applied Physics*, vol. 27, no. 10, pp. 1193–1195, 1956.

[66] Y. Ohno, T. Shirakawa, T. Taishi, and I. Yonenaga, "Interaction of phosphorus

with dislocations in heavily phosphorus doped silicon," *Applied Physics Letters*, vol. 95, no. 9, pp. 1–4, 2009.

[67] B. Shen, T. Sekiguchi, R. Zhang, Y. Shi, H. Shi, K. Yang, Y. Zheng, and K. Sumino, "Precipitation of Cu and Fe in Dislocated Floating-Zone-Grown Silicon," *Japanese Journal of Applied Physics*, vol. 35, no. 6A, pp. 3301–3305, Jun. 1996.

[68] J. Bauer, A. Hahnel, P. Werner, N. Zakharov, H. Blumtritt, A. Zuschlag, and O. Breitenstein, "Recombination at lomer dislocations in multicrystalline silicon for solar cells," *IEEE Journal of Photovoltaics*, vol. 6, no. 1, pp. 100–110, 2016.

[69] L. Pasemann, H. Blumtritt, and R. Gleichmann, "Interpretation of the EBIC contrast of dislocations in silicon," *Physica Status Solidi (a)*, vol. 70, no. 1, pp. 197–209, 1982.

[70] P. R. Wilshaw, "An SEM EBIC Study of the Electronic Properties of Dislocations in Silicon," University of Oxford, 1984.

[71] W. Seifert, G. Morgenstern, and M. Kittler, "Influence of dislocation density on recombination at grain boundaries in multicrystalline silicon," *Semiconductor Science and Technology*, vol. 8, no. 9, pp. 1687–1691, 1993.

[72] M. Kittler, W. Seifert, and V. Higgs, "Recombination Activity of Misfit Dislocations in Silicon," *Phys. Stat. Sol. (a)*, vol. 137, pp. 327–335, Jun. 1993.

[73] Z. J. Radzimski, T. Q. Zhou, A. Buczkowski, G. A. Rozgonyi, D. Finn, L. G. Hellwig, and J. A. Ross, "Recombination at clean and decorated misfit dislocations," *Applied Physics Letters*, vol. 60, pp. 1096–1098, 1992.

[74] P. R. Wilshaw and T. S. Fell, "Electron Beam Induced Current Investigations of Transition Metal Impurities at Extended Defects in Silicon," *Journal of The*

Electrochemical Society, vol. 142, no. 12, pp. 4298–4304, 1995.

[75] P. R. Wilshaw, T. S. Fell, and M. D. Coteau, "EBIC Contrast of Defects in Semiconductors," *Le Journal de Physique IV*, vol. 01, pp. C6-3-C6-14, 1991.

[76] M. Kittler and W. Seifert, "On the Origin of EBIC Defect Contrast in Silicon," *Physica Status Solidi (A)*, vol. 138, pp. 687–693, 1993.

[77] V. Kveder, M. Kittler, and W. Schröter, "Recombination activity of contaminated dislocations in silicon: A model describing electron-beam-induced current contrast behavior," *Physical Review B*, vol. 63, p. 115208, 2001.

[78] J. S. Kang and D. K. Schroder, "Gettering in silicon," *Journal of Applied Physics*, vol. 65, no. 8, pp. 2974–2985, 1989.

[79] S. A. McHugo, A. C. Thompson, I. Périchaud, and S. Martinuzzi, "Direct correlation of transition metal impurities and minority carrier recombination in multicrystalline silicon," *Applied Physics Letters*, vol. 72, no. 26, pp. 3482–3484, Jun. 1998.

[80] S. A. McHugo, "Release of metal impurities from structural defects in polycrystalline silicon," *Applied Physics Letters*, vol. 71, no. 14, pp. 1984–1986, 1997.

[81] A. Giannattasio, S. Senkader, R. J. Falster, and P. R. Wilshaw, "The role of prismatic dislocation loops in the generation of glide dislocations in Cz-silicon," *Computational Materials Science*, vol. 30, no. 1-2 SPEC ISS., pp. 131–136, 2004.

[82] C. R. Alpass, J. D. Murphy, R. J. Falster, and P. R. Wilshaw, "Nitrogen diffusion and interaction with dislocations in single-crystal silicon," *Journal of*

Applied Physics, vol. 105, no. 1, 2009.

[83] J. D. Murphy, S. Senkader, R. J. Falster, and P. R. Wilshaw, "Oxygen transport in Czochralski silicon investigated by dislocation locking experiments," *Materials Science and Engineering B: Solid-State Materials for Advanced Technology*, vol. 134, no. 2-3 SPEC. ISS., pp. 176–184, 2006.

[84] J. R. Patel and L. R. Testardi, "Electronic effects on dislocation velocities in heavily doped germanium," *Applied Physics Letters*, vol. 30, no. 1, pp. 3–5, 1977.

[85] M. Seibt, D. Abdelbarey, V. Kveder, C. Rudolf, P. Saring, L. Stolze, and O. Voß, "Interaction of metal impurities with extended defects in crystalline silicon and its implications for gettering techniques used in photovoltaics," *Materials Science and Engineering B: Solid-State Materials for Advanced Technology*, vol. 159–160, pp. 264–268, 2009.

[86] J. P. Joly, "Metallic contamination assessment of Silicon wafers," *Microelectronic Engineering*, vol. 40, pp. 285–294, 1998.

[87] L. Priester, *Grain Boundaries*. Springer, 2013.

[88] J. Chen, T. Sekiguchi, R. Xie, P. Ahmet, T. Chikyo, D. Yang, S. Ito, and F. Yin, "Electron-beam-induced current study of small-angle grain boundaries in multicrystalline silicon," *Scripta Materialia*, vol. 52, pp. 1211–1215, 2005.

[89] T. Sameshima, N. Miyazaki, Y. Tsuchiya, H. Hashiguchi, T. Tachibana, T. Kojima, Y. Ohshita, K. Arafune, and A. Ogura, "Interaction between metal impurities and small-angle grain boundaries on recombination properties in multicrystalline silicon for solar cells," *Applied Physics Express*, vol. 5, no. 4, 2012.

[90] M. S. Wiig, K. Adamczyk, H. Haug, K. E. Ekstrøm, and R. Søndenå, “The Effect of Phosphorus Diffusion Gettering on Recombination at Grain Boundaries in HPMC-Silicon Wafers,” *Energy Procedia*, vol. 92, no. 1876, pp. 886–895, 2016.

[91] K. Adamczyk, R. Søndenå, G. Stokkan, E. Looney, M. Jensen, B. Lai, M. Rinio, and M. Di Sabatino, “Recombination activity of grain boundaries in high-performance multicrystalline Si during solar cell processing,” *Journal of Applied Physics*, vol. 123, p. 055705, 2018.

[92] A. Stoffers, B. Ziebarth, J. Barthel, O. Cojocaru-Mirédin, C. Elsässer, and D. Raabe, “Complex Nanotwin Substructure of an Asymmetric Σ9 Tilt Grain Boundary in a Silicon Polycrystal,” *Physical Review Letters*, vol. 115, no. 23, pp. 1–5, 2015.

[93] G. Stokkan, A. Song, and B. Ryningen, “Investigation of the Grain Boundary Character and Dislocation Density of Different Types of High Performance Multicrystalline Silicon,” *Crystals*, vol. 8, p. 341, Aug. 2018.

[94] S. P. Phang and D. MacDonald, “Direct comparison of boron, phosphorus, and aluminum gettering of iron in crystalline silicon,” *J. Appl. Phys*, vol. 109, p. 73521, 2011.

[95] A. Ourmazd and W. Schröter, “Phosphorus gettering and intrinsic gettering of nickel in silicon,” *Applied Physics Letters*, vol. 45, no. 7, pp. 781–783, 1984.

[96] R. Krain, S. Herlufsen, and J. Schmidt, “Internal gettering of iron in multicrystalline silicon at low temperature,” *Applied Physics Letters*, vol. 93, no. 15, pp. 17–19, 2008.

[97] M. Al-Amin and J. D. Murphy, “Combining Low-Temperature Gettering with

Phosphorus Diffusion Gettering for Improved Multicrystalline Silicon," *IEEE Journal of Photovoltaics*, vol. 7, no. 6, pp. 1519–1527, 2017.

[98] G. Coletti, R. Kvande, V. D. Mihailetchi, L. J. Geerligs, L. Arnberg, and E. J. Ovrelid, "Effect of iron in silicon feedstock on p- and n-type multicrystalline silicon solar cells," *Journal of Applied Physics*, vol. 104, p. 104913, 2008.

[99] W. B. Henley and D. A. Ramappa, "Iron precipitation in float zone grown silicon," *Journal of Applied Physics*, vol. 82, no. 2, pp. 589–594, 1997.

[100] S. W. Jones, "Diffusion in silicon," in *Silicon Integrated Circuit Process Technology*, IC Knowledge LLC, 2000, pp. 1–68.

[101] D. Macdonald, A. Cuevas, A. Kinomura, and Y. Nakano, "Phosphorus gettering in multicrystalline silicon studied by neutron activation analysis," *Conference Record of the Twenty-Ninth IEEE Photovoltaic Specialists Conference, 2002.*, pp. 285–288, 2002.

[102] D. Lotfi and E. Hatem, "Phosphorus diffusion gettering process of multicrystalline silicon using a sacrificial porous silicon layer.," *Nanoscale research letters*, vol. 7, no. 338, pp. 1–7, 2012.

[103] A. Haarahiltunen, H. Savin, M. Yli-Koski, H. Talvitie, and J. Sinkkonen, "Modeling phosphorus diffusion gettering of iron in single crystal silicon," *Journal of Applied Physics*, vol. 105, p. 023510, 2009.

[104] H. Talvitie, V. Vähänissi, A. Haarahiltunen, M. Yli-Koski, and H. Savin, "Phosphorus and boron diffusion gettering of iron in monocrystalline silicon," *Journal of Applied Physics*, vol. 109, no. 9, pp. 1–5, 2011.

[105] M. Syre, S. Karazhanov, B. R. Olaisen, A. Holt, and B. G. Svensson, "Evaluation of possible mechanisms behind P gettering of iron," *Journal of*

Applied Physics, vol. 110, p. 024912, 2011.

[106] A. Haarahiltunen, H. Savin, M. Yli-Koski, H. Talvitie, M. I. Asghar, and J. Sinkkonen, "As-grown iron precipitates and gettering in multicrystalline silicon," *Materials Science and Engineering B: Solid-State Materials for Advanced Technology*, vol. 159–160, pp. 248–252, 2009.

[107] M. L. Polignano, G. F. Cerofolini, H. Bender, and C. Claeys, "Gettering mechanisms in silicon," *Journal of Applied Physics*, vol. 62, no. 2, pp. 869–876, 1988.

[108] V. Osinniy, A. Nylandsted Larsen, E. Hvidsten Dahl, E. Enebakk, A. K. Søiland, R. Tronstad, and Y. Safir, "Gettering improvements of minority-carrier lifetimes in solar grade silicon," *Solar Energy Materials and Solar Cells*, vol. 101, pp. 123–130, 2012.

[109] R. J. Falster, D. N. Modlin, W. A. Tiller, and J. F. Gibbons, "Effective gettering of gold in silicon at 900 °C by low-current corona discharge," *Journal of Applied Physics*, vol. 57, no. 2, pp. 554–558, 1985.

[110] D. A. Pietila and D. B. Masson, "Evaluation of Intrinsic Gettering of Gold by Oxide Precipitation in Czochralski Silicon," *Journal of The Electrochemical Society*, vol. 135, no. 3, pp. 686–690, 1988.

[111] S. Dubois, O. Palais, P. J. Ribeyron, N. Enjalbert, M. Pasquinelli, and S. Martinuzzi, "Effect of intentional bulk contamination with iron on multicrystalline silicon solar cell properties," *Journal of Applied Physics*, vol. 102, p. 083525, 2007.

[112] S. Peters, J. Y. Lee, C. Ballif, D. Borchert, S. W. Glunz, W. Warta, and G. Willeke, "Rapid thermal processing: a comprehensive classification of silicon

materials," in *Proceedings of the 29th IEEE PVSC*, 2002, pp. 214–217.

[113] D. Macdonald and A. Cuevas, "The trade-off between phosphorus gettering and thermal degradation in multicrystalline silicon," *European Photovoltaic Solar Energy Conference Proceedings*, pp. 1–6, 2000.

[114] P. S. Plekhanov, R. Gafiteanu, U. M. Gösele, and T. Y. Tan, "Modeling of gettering of precipitated impurities from Si for carrier lifetime improvement in solar cell applications," *Journal of Applied Physics*, vol. 86, no. 5, pp. 2453–2458, 1999.

[115] K. D. Shetty, M. B. Boreland, V. Shanmugam, J. Cunnusamy, C. K. Wu, S. Iggo, and H. Antoniadis, "Lightly doped emitters for high efficiency silicon wafer solar cells," *Energy Procedia*, vol. 33, pp. 70–75, 2013.

[116] M. J. Kerr, J. Schmidt, A. Cuevas, and J. H. Bultman, "Surface recombination velocity of phosphorus-diffused silicon solar cell emitters passivated with plasma enhanced chemical vapor deposited silicon nitride and thermal silicon oxide," *Journal of Applied Physics*, vol. 89, no. 7, pp. 3821–3826, 2001.

[117] A. Cuevas, M. Stocks, S. Armand, M. Stuckings, A. Blakers, and F. Ferrazza, "High minority carrier lifetime in phosphorus-gettered multicrystalline silicon," *Applied Physics Letters*, vol. 70, p. 1017, 1997.

[118] J. Mandelkorn and J. H. Lamneck, "A new electric field effect in silicon solar cells," *Journal of Applied Physics*, vol. 44, no. 10, pp. 4785–4787, 1973.

[119] O. Schultz, S. W. Glunz, and G. P. Willeke, "Multicrystalline silicon solar cells exceeding 20% efficiency," *Progress in Photovoltaics: Research and Applications*, vol. 12, no. 7, pp. 553–558, 2004.

[120] O. Porre, M. Stemmer, and M. Pasquinelli, "LBIC and diffusion length mapping

applied to the investigation of gettering by aluminium diffusion in multicrystalline silicon," *Materials Science and Engineering: B*, vol. 24, no. 1–3, pp. 188–191, 1994.

[121] P. Sana, A. Rohatgi, J. P. Kalejs, and R. O. Bell, "Gettering and hydrogen passivation of edge-defined film-fed grown multicrystalline silicon solar cells by Al diffusion and forming gas anneal," *Applied Physics Letters*, vol. 64, no. 1, pp. 97–99, 1994.

[122] R. D. Thompson and K. N. Tu, "Low temperature gettering of Cu, Ag, and Au across a wafer of Si by Al," *Applied Physics Letters*, vol. 41, no. 5, pp. 440–442, 1982.

[123] M. C. Schubert, W. Kwapil, J. Schoen, H. Habenicht, M. Kasemann, P. Gundel, M. Blazek, and W. Warta, "Analysis of performance limiting material properties of multicrystalline silicon," *Solar Energy Materials and Solar Cells*, vol. 94, no. 9, pp. 1451–1456, 2010.

[124] M. A. Green, "The Passivated Emitter and Rear Cell (PERC): From conception to mass production," *Solar Energy Materials and Solar Cells*, vol. 143, pp. 190–197, 2015.

[125] Z. Wang, P. Han, H. Lu, H. Qian, L. Chen, Q. Meng, N. Tang, F. Gao, Y. Jiang, J. Wu, W. Wu, H. Zhu, J. Ji, Z. Shi, A. Sugianto, L. Mai, B. Hallam, and S. Wenham, "Advanced PERC and PERL production cells with 20.3% record efficiency for standard commercial p-type silicon wafers," *Progress in Photovoltaics: Research and Applications*, vol. 20, no. 3, pp. 260–268, 2012.

[126] F. Schindler, B. Michl, P. Krenckel, S. Riepe, J. Benick, R. Müller, A. Richter, S. W. Glunz, and M. C. Schubert, "Optimized multicrystalline silicon for solar

cells enabling conversion efficiencies of 22%," *Solar Energy Materials and Solar Cells*, vol. 171, pp. 180–186, 2017.

[127] F. Schindler, J. Schön, B. Michl, S. Riepe, P. Krenckel, J. Benick, F. Feldmann, M. Hermle, S. W. Glunz, W. Warta, and M. C. Schubert, "High-Efficiency Multicrystalline Silicon Solar Cells: Potential of n-Type Doping," *IEEE Journal of Photovoltaics*, vol. 5, no. 6, pp. 1571–1579, 2015.

[128] S. Solmi, F. Baruffaldi, and R. Canteri, "Diffusion of boron in silicon during post-implantation annealing," *Journal of Applied Physics*, vol. 69, no. 4, pp. 2135–2142, 1991.

[129] A. Haarahiltunen, H. Talvitie, H. Savin, M. Yli-Koski, M. I. Asghar, and J. Sinkkonen, "Modeling boron diffusion gettering of iron in silicon solar cells," *Applied Physics Letters*, vol. 92, p. 021902, Jan. 2008.

[130] J. Schön, M. C. Schubert, W. Warta, H. Savin, and A. Haarahiltunen, "Analysis of simultaneous boron and phosphorus diffusion gettering in silicon," *Physica Status Solidi (A) Applications and Materials Science*, vol. 207, no. 11, pp. 2589–2592, 2010.

[131] C. H. Seager and D. S. Ginley, "Passivation of grain boundaries in polycrystalline silicon," *Applied Physics Letters*, vol. 34, no. 5, pp. 337–340, 1979.

[132] C. E. Dubé and J. I. Hanoka, "Hydrogen Passivation of Multicrystalline Silicon," *IEEE Photovoltaic Specialist Conference*, pp. 883–888, 2005.

[133] S. K. Estreicher, M. Sanati, and N. Gonzalez Szwacki, "Iron in silicon: Interactions with radiation defects, carbon, and oxygen," *Physical Review B - Condensed Matter and Materials Physics*, vol. 77, no. 12, pp. 1–9, 2008.

[134] J. Chen, D. Yang, Z. Xi, and T. Sekiguchi, “Electron-beam-induced current study of hydrogen passivation on grain boundaries in multicrystalline silicon: Influence of GB character and impurity contamination,” *Physica B: Condensed Matter*, vol. 364, no. 1–4, pp. 162–169, 2005.

[135] O. F. Vyvenko, O. Krüger, and M. Kittler, “Cross-sectional electron-beam-induced current analysis of the passivation of extended defects in cast multicrystalline silicon by remote hydrogen plasma treatment,” *Applied Physics Letters*, vol. 76, no. 6, pp. 697–699, 2000.

[136] M. D. Pickett and T. Buonassisi, “Iron point defect reduction in multicrystalline silicon solar cells,” *Applied Physics Letters*, vol. 92, p. 122103, 2008.

[137] B. Gorka, “Hydrogen Passivation of Polycrystalline Si Thin Film Solar Cells,” Von der Fakultät IV - Elektrotechnik und Informatik der Technischen Universität Berlin, 2010.

[138] A. Saha, Haifeng Zhang, Wen-Cheng Sun, and Meng Tao, “A new method for bulk passivation in multicrystalline-Si by sulfur,” in *2015 IEEE 42nd Photovoltaic Specialist Conference (PVSC)*, 2015, pp. 1–5.

[139] B. L. Sopori, K. Jones, and X. J. Deng, “Observation of enhanced hydrogen diffusion in solar cell silicon,” *Applied Physics Letters*, vol. 61, no. 21, pp. 2560–2562, 1992.

[140] C. Dubé and J. I. Hanoka, “Hydrogen passivation of dislocations in silicon,” *Applied Physics Letters*, vol. 45, no. 10, pp. 1135–1137, 1984.

[141] W. B. Jackson, N. M. Johnson, C. C. Tsai, I. -W. Wu, A. Chiang, and D. Smith, “Hydrogen diffusion in polycrystalline silicon thin films,” *Applied Physics Letters*, vol. 61, no. 14, pp. 1670–1672, 1992.

[142] N. M. Johnson, D. K. Biegelsen, and M. D. Moyer, “Deuterium passivation of grain-boundary dangling bonds in silicon thin films,” *Applied Physics Letters*, vol. 40, no. 10, pp. 882–884, 1982.

[143] S. Martinuzzi, I. Périchaud, and F. Warchol, “Hydrogen passivation of defects in multicrystalline silicon solar cells,” *Solar Energy Materials and Solar Cells*, vol. 80, no. 3, pp. 343–353, 2003.

[144] M. Ogawa, S. Kamiya, H. Izumi, and Y. Tokuda, “Effect of hydrogen at room temperature on electronic and mechanical properties of dislocations in silicon,” *Materials Letters*, vol. 120, pp. 236–238, 2014.

[145] M. I. Bertoni, S. Hudelson, B. K. Newman, D. P. Fenning, H. F. W. Dekkers, E. Cornagliotti, A. Zuschlag, G. Micard, G. Hahn, G. Coletti, B. Lai, and T. Buonassisi, “Influence of defect type on hydrogen passivation efficacy in multicrystalline silicon solar cells,” *Progress in Photovoltaics: Research and Applications*, vol. 19, no. 2, pp. 187–191, 2011.

[146] M. Nacke, M. Allardt, P. Chekhonin, E. Hieckmann, W. Skrotzki, and J. Weber, “Investigations on residual strains and the cathodoluminescence and electron beam induced current signal of grain boundaries in silicon,” *Journal of Applied Physics*, vol. 115, p. 163511, 2014.

[147] J. Palm, “Local investigation of recombination at grain boundaries in silicon by grain boundary-electron beam induced current,” *Journal of Applied Physics*, vol. 74, no. 2, pp. 1169–1178, 1993.

[148] P. R. Wilshaw and G. R. Booker, “New results and an interpretation for SEM EBIC contrast arising from individual dislocations in silicon,” in *Microscopy of Semiconducting Materials*, 1985, pp. 329–336.

[149] O. Breitenstein, J. Bauer, M. Kittler, T. Arguirov, and W. Seifert, “EBIC and luminescence studies of defects in solar cells,” *Scanning*, vol. 30, no. 4, pp. 331–338, 2008.

[150] M. Kittler, C. Ulhaq-Bouillet, and V. Higgs, “Influence of copper contamination on recombination activity of misfit dislocations in SiGe/Si epilayers: Temperature dependence of activity as a marker characterizing the contamination level,” *Journal of Applied Physics*, vol. 78, no. 7, pp. 4573–4583, 1995.

[151] C. Donolato, “An analytical model of SEM and STEM charge collection images of dislocations in thin semiconductor layers. II. EBIC images of dislocations,” *Physica Status Solidi (a)*, vol. 66, no. 2, pp. 445–454, 1981.

[152] L. Pasemann, “A contribution to the theory of the EBIC contrast of lattice defects in semiconductors,” *Ultramicroscopy*, vol. 6, no. 1, pp. 237–250, 1981.

[153] P. C. Phua and V. K. S. Ong, “Determining the location of localized defect in the perpendicular junction configuration with the use of electron beam induced current,” *IEEE Transactions on Electron Devices*, vol. 49, no. 11, pp. 2036–2046, 2002.

[154] B. P. Gorman, H. L. Guthrey, and M. M. Al-Jassim, “Quantification of atomic scale defects in poly Si PV devices using atom probe tomography,” *Conference Record of the IEEE Photovoltaic Specialists Conference*, pp. 1498–1500, 2012.

[155] Y. Ohno, K. Kutsukake, M. Deura, I. Yonenaga, Y. Shimizu, N. Ebisawa, K. Inoue, Y. Nagai, H. Yoshida, and S. Takeda, “Recombination activity of nickel, copper, and oxygen atoms segregating at grain boundaries in mono-like silicon crystals,” *Applied Physics Letters*, vol. 109, p. 142105, 2016.

[156] Y. Ohno, K. Inoue, K. Fujiwara, K. Kutsukake, M. Deura, I. Yonenaga, N. Ebisawa, Y. Shimizu, K. Inoue, Y. Nagai, H. Yoshida, S. Takeda, S. Tanaka, and M. Kohyama, "Impact of local atomic stress on oxygen segregation at tilt boundaries in silicon," *Applied Physics Letters*, vol. 110, p. 062105, 2017.

[157] C. Lotharukpong, D. Tweddle, T. L. Martin, M. Wu, C. R. M. Grovenor, M. P. Moody, and P. R. R. Wilshaw, "Specimen preparation methods for elemental characterisation of grain boundaries and isolated dislocations in multicrystalline silicon using atom probe tomography," *Materials Characterization*, vol. 131, pp. 472–479, 2017.

[158] A. Stoffers, O. Cojocaru-Mirédin, W. Seifert, S. Zaefferer, S. Riepe, and D. Raabe, "Grain boundary segregation in multicrystalline silicon: correlative characterization by EBSD, EBIC, and atom probe tomography," *Progress in Photovoltaics: Research and Applications*, vol. 23, no. 12, pp. 1742–1753, 2015.

[159] A. Stoffers, J. Barthel, C. H. Liebscher, B. Gault, O. Cojocaru-Mirédin, C. Scheu, and D. Raabe, "Correlating Atom Probe Tomography with Atomic-Resolved Scanning Transmission Electron Microscopy: Example of Segregation at Silicon Grain Boundaries," *Microscopy and Microanalysis*, vol. 23, no. 2, pp. 291–299, Apr. 2017.

[160] P. P. Altermatt *et al.*, "High-performance p-type multicrystalline silicon (mc-Si): Its characterization and projected performance in PERC solar cells," *Solar Energy*, vol. 175, no. In Press, pp. 68–74, Nov. 2018.

[161] F. Cao, K. Chen, J. Zhang, X. Ye, J. Li, S. Zou, and X. Su, "Next-generation multi-crystalline silicon solar cells: Diamond-wire sawing, nano-texture and

high efficiency," *Solar Energy Materials and Solar Cells*, vol. 141, pp. 132–138, 2015.

[162] G. Bourret-Sicotte, P. G. Hamer, D. Tweddle, R. S. Bonilla, and P. R. Wilshaw, "Hydrogen Related Defects in Float Zone Silicon Investigated Using a Shielded Hydrogen Plasma," in *2018 IEEE 7th World Conference on Photovoltaic Energy Conversion (WCPEC) (A Joint Conference of 45th IEEE PVSC, 28th PVSEC & 34th EU PVSEC)*, 2018, pp. 0298–0302.

[163] N. A. Aziz, B. Bais, A. A. Hamzah, and B. Y. Majlis, "Characterization of HNA etchant for silicon microneedles array fabrication," *IEEE International Conference on Semiconductor Electronics, Proceedings, ICSE*, pp. 203–206, 2008.

[164] M. Steinert, J. Acker, S. Oswald, and K. Wetzig, "Study on the mechanism of silicon etching in HNO3-rich HF/HNO3 mixtures inf," *Journal of Physical Chemistry C*, vol. 111, no. 5, pp. 2133–2140, 2007.

[165] F. Secco d' Aragona, "Dislocation Etch for (100) Planes in Silicon," *Journal of The Electrochemical Society*, vol. 119, no. 7, pp. 948–951, 1972.

[166] C. Lotharukpong, "Defect characterisation of multicrystalline silicon," University of Oxford, 2015.

[167] J. Chen, T. Sekiguchi, S. Nara, and D. Yang, "The characterization of high quality multicrystalline silicon by the electron beam induced current method," *Journal of Physics: Condensed Matter*, vol. 16, pp. S211–S216, 2004.

[168] S. I. Maximenko, J. A. Freitas, K. Lew, B. L. Vanmil, C. R. Eddy, D. K. Gaskill, T. S. Sudarshan, S. I. Maximenko, J. A. Freitas, K. Lew, and B. L. Vanmil, "Effect of threading screw and edge dislocations on transport properties of 4H

– SiC homoepitaxial layers Effect of threading screw and edge dislocations on transport properties of 4H – SiC homoepitaxial layers," *Journal of Applied Physics*, vol. 108, p. 013708, 2010.

[169] D. B. Holt and E. Napchan, "Quantitation of SEM EBIC and CL signals using Monte Carlo electron-trajectory simulations," *Scanning*, vol. 16, no. 2, pp. 78–86, 1994.

[170] T. E. Everhart and P. H. Hoff, "Determination of kilovolt electron energy dissipation vs penetration distance in solid materials," *Journal of Applied Physics*, vol. 42, no. 13, pp. 5837–5846, 1971.

[171] H. B. Michaelson, "The work function of the elements and its periodicity," *Journal of Applied Physics*, vol. 48, no. 11, pp. 4729–4733, 1977.

[172] S. Sze and K. Ng, *Physics of Semiconductor Devices*, 3rd ed. Hoboken, NJ: John Wiley & Sons, 1981.

[173] A. J. Wilkinson and T. Ben Britton, "Strains, planes, and EBSD in materials science," *Materials Today*, vol. 15, no. 9, pp. 366–376, 2012.

[174] G. C. Sneddon, P. W. Trimby, and J. M. Cairney, "Transmission Kikuchi diffraction in a scanning electron microscope: A review," *Materials Science and Engineering R: Reports*, vol. 110, pp. 1–12, 2016.

[175] K. Babinsky, W. Knabl, A. Lorich, R. De Kloe, H. Clemens, and S. Primig, "Grain boundary study of technically pure molybdenum by combining APT and TKD," *Ultramicroscopy*, vol. 159. pp. 445–451, 2015.

[176] K. P. Rice, Y. Chen, T. J. Prosa, and D. J. Larson, "Implementing Transmission Electron Backscatter Diffraction for Atom Probe Tomography," *Microscopy and Microanalysis*, vol. 22, no. 3, pp. 583–588, 2016.

[177] J. I. Goldstein, D. E. Newbury, J. R. Michael, N. W. M. Ritchie, J. H. J. Scott, and D. C. Joy, *Scanning Electron Microscopy and X-Ray Microanalysis*. New York, NY: Springer New York, 2018.

[178] L. Reimer, "Scanning Electron Microscopy: Physics of Image Formation and Microanalysis, Second Edition," *Measurement Science and Technology*, vol. 11, no. 12, pp. 1826–1826, Dec. 2000.

[179] A. J. Kubis, G. J. Shiflet, R. Hull, and D. N. Dunn, "Focused ion-beam tomography," *Metallurgical and Materials Transactions A*, vol. 35, no. 7, pp. 1935–1943, Jul. 2004.

[180] D. Larson, D. Foord, A. Petford-Long, H. Liew, M. Blamire, A. Cerezo, and G. Smith, "Field-ion specimen preparation using focused ion-beam milling," *Ultramicroscopy*, vol. 79, no. 1–4, pp. 287–293, Sep. 1999.

[181] D. B. Williams and C. B. Carter, *Transmission electron microscopy: A textbook for materials science*, 2nd Ed. Springer, 2009.

[182] E. A. Marquis, M. Bachhav, Y. Chen, Y. Dong, L. M. Gordon, and A. McFarland, "On the current role of atom probe tomography in materials characterization and materials science," *Current Opinion in Solid State and Materials Science*, vol. 17, no. 5, pp. 217–223, 2013.

[183] B. Gault, M. P. Moody, J. M. Cairney, and S. P. Ringer, *Atom Probe Microscopy*. Springer, 2012.

[184] D. N. Seidman and K. Stiller, "An Atom-Probe Tomography Primer," *MRS Bulletin*, vol. 34, no. 10, pp. 717–724, 2009.

[185] D. J. Larson, T. J. Prosa, R. M. Ulfig, B. P. Geiser, and T. F. Kelly, *Local Electrode Atom Probe Tomography*. New York, NY: Springer New York, 2013.

[186] G. L. Kellogg and T. T. Tsong, "Pulsed-laser atom-probe field-ion microscopy," *Journal of Applied Physics*, vol. 51, no. 2, pp. 1184–1193, 1980.

[187] M. P. Moody, A. Vella, S. S. A. Gerstl, and P. A. J. Bagot, "Advances in atom probe tomography instrumentation: Implications for materials research," *MRS Bulletin*, vol. 41, no. 01, pp. 40–45, 2016.

[188] B. Gault, D. Haley, F. de Geuser, M. P. Moody, E. A. Marquis, D. J. Larson, and B. P. Geiser, "Advances in the reconstruction of atom probe tomography data," *Ultramicroscopy*, vol. 111, no. 6, pp. 448–457, 2011.

[189] B. Gault, M. P. Moody, F. De Geuser, A. La Fontaine, L. T. Stephenson, D. Haley, and S. P. Ringer, "Spatial Resolution in Atom Probe Tomography," *Microscopy and Microanalysis*, vol. 16, no. 01, pp. 99–110, 2010.

[190] J. O. Douglas, P. A. J. Bagot, B. C. Johnson, D. N. Jamieson, and M. P. Moody, "Optimisation of sample preparation and analysis conditions for atom probe tomography characterisation of low concentration surface species," *Semiconductor Science and Technology*, vol. 31, p. 084004, 2016.

[191] M. K. Miller, K. F. Russell, K. Thompson, R. Alvis, and D. J. Larson, "Review of atom probe FIB-based specimen preparation methods," *Microscopy and microanalysis : the official journal of Microscopy Society of America, Microbeam Analysis Society, Microscopical Society of Canada*, vol. 13, no. 6, pp. 428–436, 2007.

[192] T. F. Kelly and M. K. Miller, "Invited review article: Atom probe tomography," *Review of Scientific Instruments*, vol. 78, no. 3, pp. 1–20, 2007.

[193] B. Gault, F. Danoix, K. Hoummada, D. Mangelinck, and H. Leitner, "Impact of directional walk on atom probe microanalysis," *Ultramicroscopy*, vol. 113, pp.

182–191, 2012.

[194] D. J. Larson, B. P. Geiser, T. J. Prosa, and T. F. Kelly, “Atom Probe Tomography Spatial Reconstruction : Current Status and Future Directions,” *Current Opinion in Solid State and Materials Science*, vol. 39, pp. 740–741, 2012.

[195] T. F. Kelly and D. J. Larson, “Atom Probe Tomography 2012,” *Annual Review of Materials Research*, vol. 42, pp. 1–31, 2012.

[196] M. K. Miller and G. D. W. Smith, “Atom probe analysis of interfacial segregation,” *Applied Surface Science*, vol. 87–88, no. 94, pp. 243–250, 1995.

[197] M. Kittler, W. Seifert, T. Arguirov, I. Tarasov, and S. Ostapenko, “Room-temperature luminescence and electron-beam-induced current (EBIC) recombination behaviour of crystal defects in multicrystalline silicon,” *Solar Energy Materials and Solar Cells*, vol. 72, pp. 465–472, 2002.

[198] T. Trupke, R. Bardos, M. Schubert, and W. Warta, “Photoluminescence imaging of silicon wafers,” *Applied Physics Letters*, vol. 89, p. 044107, 2006.

[199] J. Haunschild, M. Glatthaar, M. Demant, J. Nievendick, M. Motzko, S. Rein, and E. R. Weber, “Quality control of as-cut multicrystalline silicon wafers using photoluminescence imaging for solar cell production,” *Solar Energy Materials and Solar Cells*, vol. 94, no. 12, pp. 2007–2012, 2010.

[200] S. Ostapenko, I. Tarasov, J. P. Kalejs, C. Haessler, and E. Reisner, “Defect monitoring using scanning photoluminescence spectroscopy in multycristalline silicon solar cell,” *Conference Record of the IEEE Photovoltaic Specialists Conference*, vol. 15, pp. 840–848, 2000.

[201] H. Sugimoto, K. Araki, and M. Tajima, “Photoluminescence analysis of

intragrain defects in multicrystalline silicon wafers for solar cells," *Journal of Applied Physics*, vol. 102, p. 054506, 2007.

[202] J. Bullock, D. Kiriya, N. Grant, A. Azcatl, M. Hettick, T. Kho, P. Phang, H. C. Sio, D. Yan, D. Macdonald, M. A. Quevedo-Lopez, R. M. Wallace, A. Cuevas, and A. Javey, "Superacid Passivation of Crystalline Silicon Surfaces," *ACS Applied Materials and Interfaces*, vol. 8, no. 36, pp. 24205–24211, 2016.

[203] F. D. Heinz, W. Warta, and M. C. Schubert, "Optimizing micro Raman and PL spectroscopy for solar cell technological assessment," *Energy Procedia*, vol. 27, pp. 208–213, 2012.

[204] T. Grossmann, T. Wienhold, U. Bog, T. Beck, C. Friedmann, H. Kalt, and T. Mappes, "Polymeric photonic molecule super-mode lasers on silicon," *Light: Science & Applications*, vol. 2, p. e82, May 2013.

[205] H. Nagel, C. Berge, and A. G. Aberle, "Generalized analysis of quasi-steady-state and quasi-transient measurements of carrier lifetimes in semiconductors," *Journal of Applied Physics*, vol. 86, no. 11, pp. 6218–6221, 1999.

[206] B. AlMangour and J. M. Yang, "Improving the surface quality and mechanical properties by shot-peening of 17-4 stainless steel fabricated by additive manufacturing," *Materials and Design*, vol. 110, pp. 914–924, 2016.

[207] G. Fisher, M. R. Seacrist, and R. W. Standley, "Silicon Crystal Growth and Wafer Technologies," *Proceedings of the IEEE*, vol. 100, pp. 1454–1474, May 2012.

[208] H. Aida, H. Takeda, K. Koyama, H. Katakura, K. Sunakawa, and T. Doi, "Chemical Mechanical Polishing of Gallium Nitride with Colloidal Silica," *Journal of The Electrochemical Society*, vol. 158, no. 12, pp. H1206–H1212,

2011.

[209] Y. Ahn, J. Y. Yoon, C. W. Baek, and Y. K. Kim, “Chemical mechanical polishing by colloidal silica-based slurry for micro-scratch reduction,” *Wear*, vol. 257, no. 7–8, pp. 785–789, 2004.

[210] H. Prigge, P. Gerlach, P. O. Hahn, A. Schnegg, and H. Jacob, “Acceptor Compensation in Silicon Induced by Chemomechanical Polishing,” *Electrochemical Society*, vol. 138, no. 5, pp. 1385–1389, 1991.

[211] P. Wagner, H. Hage, H. Prigge, T. Prescha, and J. Weber, “Properties of copper-induced complexes in silicon,” in *Proceedings of the Sixth International Symposium on Silicon Materials Science and Technology*, 1990, pp. 675–686.

[212] P. F. Schmidt and C. W. Pearce, “A Neutron Activation Analysis Study of the Sources of Transition Group Metal Contamination in the Silicon Device Manufacturing Process,” *Journal of The Electrochemical Society*, vol. 128, no. 3, pp. 630–637, 1981.

[213] J. Chen, T. Sekiguchi, D. Yang, F. Yin, K. Kido, and S. Tsurekawa, “Electron-beam-induced current study of grain boundaries in multicrystalline silicon,” *Journal of Applied Physics*, vol. 96, no. 10, pp. 5490–5495, 2004.

[214] D. Tweddle, E. C. Shaw, J. O. Douglas, R. S. Bonilla, M. P. Moody, P. Hamer, and P. R. Wilshaw, “Atom probe Tomography of fast-diffusing impurities and the effect of gettering in multicrystalline silicon,” in *AIP Conference Proceedings*, 2018, vol. 1999, p. 130019.

[215] J. Lindroos, D. P. Fenning, D. J. Backlund, E. Verlage, A. Gorgulla, S. K. Estreicher, H. Savin, and T. Buonassisi, “Nickel: A very fast diffuser in silicon,” *Journal of Applied Physics*, vol. 113, no. 20, p. 204906, May 2013.

[216] M. K. Bakhadyrkhanov, S. Zainabidinov, and A. Khamidov, “Some characteristics of diffusion and electrotransport of nickel in silicon,” *Soviet Physics Semiconductors*, vol. 243, no. 14, 1980.

[217] S. K. Estreicher, D. J. Backlund, C. Carbogno, and M. Scheffler, “Activation energies for diffusion of defects in silicon: The role of the exchange-correlation functional,” *Angewandte Chemie - International Edition*, vol. 50, no. 43, pp. 10221–10225, 2011.

[218] M. Hourai, T. Naridomi, Y. Oka, K. Murakami, S. Sumita, N. Fujino, and T. Shiraiwa, “A method of quantitative contamination with metallic impurities of the surface of a silicon wafer,” *Japanese Journal of Applied Physics*, vol. 27, no. 12, pp. L2361–L2363, 1988.

[219] J. Lindroos and H. Savin, “Review of light-induced degradation in crystalline silicon solar cells,” *Solar Energy Materials and Solar Cells*, vol. 147, pp. 115–126, 2016.

[220] A. A. Istratov and E. R. Weber, “Electrical properties and recombination activity of copper, nickel and cobalt in silicon,” *Applied Physics A: Materials Science & Processing*, vol. 66, no. 2, pp. 123–136, 1998.

[221] E. R. Weber, “Transition metals in silicon,” *Applied Physics A Materials Science & Processing*, vol. 30, no. 1, pp. 1–22, 1983.

[222] N. Yarykin and J. Weber, “Evidence for room-temperature in-diffusion of nickel into silicon,” *Applied Physics Letters*, vol. 109, no. 10, pp. 2014–2017, 2016.

[223] L. Wang, W. Yu, and S. Shen, “Revisiting the structures and energies of silicon 〈110〉 symmetric tilt grain boundaries,” *Journal of Materials Research*, vol.

34, pp. 1021–1033, Mar. 2019.

[224] N. Yarykin and J. Weber, “Nickel in silicon: Room-temperature in-diffusion and interaction with radiation defects,” *Physica Status Solidi (C) Current Topics in Solid State Physics*, vol. 14, no. 7, p. 1700005, 2017.

[225] R. L. Meek, T. M. Buck, and C. F. Gibbon, “Silicon Surface Contamination : Polishing and Cleaning,” *ECS Journal of Solid State Science and Technology*, vol. 120, no. 9, pp. 1241–1246, 1974.

[226] L. T. Canham, M. R. Dyball, and K. G. Barraclough, “Surface copper contamination of as-received float-zone silicon wafers,” *Journal of Applied Physics*, vol. 66, no. 2, pp. 920–927, 1989.

[227] T. Buonassisi, A. A. Istratov, M. D. Pickett, M. A. Marcus, T. F. Ciszek, and E. R. Weber, “Metal precipitation at grain boundaries in silicon: Dependence on grain boundary character and dislocation decoration,” *Applied Physics Letters*, vol. 89, no. 4, pp. 1–4, 2006.

[228] Z. Xi, D. Yang, J. Chen, and T. Sekiguchi, “Recombination behavior of nickel in cast multicrystalline silicon,” *Materials Science in Semiconductor Processing*, vol. 9, pp. 304–307, 2006.

[229] R. Rizk, X. Portier, G. Allais, and G. Nouet, “Electrical and structural studies of copper and nickel precipitates in a Σ=25 silicon bicrystal,” *Journal of Applied Physics*, vol. 76, no. 2, pp. 952–958, 1994.

[230] A. Autruffe, M. M’hamdi, F. Schindler, F. D. Heinz, K. E. Ekstrøm, M. C. Schubert, M. Di Sabatino, and G. Stokkan, “High performance multicrystalline silicon: Grain structure and iron precipitation,” *Journal of Applied Physics*, vol. 122, p. 135103, 2017.

[231] M. Kim, P. Hamer, H. Li, D. Payne, S. Wenham, M. D. Abbott, and B. Hallam, "Impact of thermal processes on multi-crystalline silicon," *Frontiers in Energy*, vol. 11, no. 1, pp. 1–10, 2016.

[232] H. J. Choi, M. I. Bertoni, J. Hofstetter, D. P. Fenning, D. M. Powell, S. Castellanos, and T. Buonassisi, "Dislocation Density Reduction During Impurity Gettering in Multicrystalline Silicon," *IEEE Journal of Photovoltaics*, vol. 3, no. 1, pp. 189–198, 2013.

[233] C. H. Liebscher, A. Stoffers, M. Alam, L. Lymperakis, O. Cojocaru-Mirédin, B. Gault, J. Neugebauer, G. Dehm, C. Scheu, and D. Raabe, "Strain-Induced Asymmetric Line Segregation at Faceted Si Grain Boundaries," *Physical Review Letters*, vol. 121, p. 015702, 2018.

[234] P. Lejček and S. Hofmann, "Thermodynamics and structural aspects of grain boundary segregation," *Critical Reviews in Solid State and Materials Sciences*, vol. 20, no. 1, pp. 1–85, 1995.

[235] P. Käshammer and T. Sinno, "A mechanistic study of impurity segregation at silicon grain boundaries," *Journal of Applied Physics*, vol. 118, p. 095301, 2015.

[236] M. S. Wiig, H. Haug, R. Søndenå, and E. S. Marstein, "Modeling of recombination strength at grain boundaries after phosphorus diffusion gettering and the effect of hydrogen passivation," *Energy Procedia*, vol. 124, pp. 215–224, 2017.

[237] S. Gindner, P. Karzel, B. Herzog, and G. Hahn, "Efficacy of phosphorus gettering and hydrogenation in multicrystalline silicon," *IEEE Journal of Photovoltaics*, vol. 4, no. 4, pp. 1063–1070, 2014.

[238] Y. Y. Teng, J. C. Chen, C. W. Lu, and C. Y. Chen, "The carbon distribution in multicrystalline silicon ingots grown using the directional solidification process," *Journal of Crystal Growth*, vol. 312, no. 8, pp. 1282–1290, 2010.

[239] L. Liu, S. Nakano, and K. Kakimoto, "Carbon concentration and particle precipitation during directional solidification of multicrystalline silicon for solar cells," *Journal of Crystal Growth*, vol. 310, no. 7–9, pp. 2192–2197, 2008.

[240] B. O. Kolbesen and A. Mühlbauer, "Carbon in silicon: Properties and impact on devices," *Solid State Electronics*, vol. 25, no. 8, pp. 759–775, 1982.

[241] C. Liebscher, A. Stoffers, O. Cojocaru-Mirédin, B. Gault, C. Scheu, G. Dehm, and D. Raabe, "Topological Impurity Segregation at Faceted Silicon Grain Boundaries Studied by Correlative Atomic-Resolution STEM and APT," *Microscopy and Microanalysis*, vol. 22, no. Suppl 5, pp. 46–47, 2016.

[242] T. Buonassisi, A. A. Istratov, M. D. Pickett, J. P. Rakotoniaina, O. Breitenstein, M. A. Marcus, S. M. Heald, and E. R. Weber, "Transition metals in photovoltaic-grade ingot-cast multicrystalline silicon: Assessing the role of impurities in silicon nitride crucible lining material," *Journal of Crystal Growth*, vol. 287, no. 2, pp. 402–407, 2006.

[243] C. R. Alpass, A. Jain, J. D. Murphy, and P. R. Wilshaw, "Measurements of Dislocation Locking by Near-Surface Ion-Implanted Nitrogen in Czochralski Silicon," *Journal of The Electrochemical Society*, vol. 156, no. 8, pp. H669–H673, 2009.

[244] R. Jones, S. Aberg, F. Berg Rasmussen, and B. Bech Nielsen, "Identification of the dominant nitrogen defect in silicon," *Physical Review Letters*, vol. 72, no. 12, pp. 1882–1885, 1994.

[245] A. Inglese, J. Lindroos, and H. Savin, “Accelerated light-induced degradation for detecting copper contamination in p-type silicon,” *Applied Physics Letters*, vol. 107, p. 052101, 2015.

[246] A. Stoffers, “Grain boundary segregation in multicrystalline silicon studied by correlative microscopy,” Rheinisch-Westfälischen Technischen Hochschule Aachen, 2017.

[247] M. Kittler and W. Seifert, “On the sensitivity of the EBIC technique as applied to defect investigations in silicon,” *Physica Status Solidi (a)*, vol. 66, no. 2, pp. 573–583, 1981.

[248] M. Sheoran, A. Upadhyaya, and A. Rohatgi, “Bulk lifetime and efficiency enhancement due to gettering and hydrogenation of defects during cast multicrystalline silicon solar cell fabrication,” *Solid-State Electronics*, vol. 52, no. 5, pp. 612–617, 2008.

[249] P. Karzel, M. Ackermann, L. Gröner, C. Reimann, M. Zschorsch, S. Meyer, F. Kiessling, S. Riepe, and G. Hahn, “Dependence of phosphorus gettering and hydrogen passivation efficacy on grain boundary type in multicrystalline silicon,” *Journal of Applied Physics*, vol. 114, p. 244902, 2013.

[250] K. Adamczyk, R. Søndenå, C. C. You, G. Stokkan, J. Lindroos, M. Rinio, and M. Di Sabatino, “Recombination Strength of Dislocations in High-Performance Multicrystalline/Quasi-Mono Hybrid Wafers During Solar Cell Processing,” *Physica Status Solidi (a)*, vol. 215, no. 2, pp. 1–8, 2017.

[251] L. J. Geerligs, Y. Komatsu, I. Röver, K. Wambach, I. Yamaga, and T. Saitoh, “Precipitates and hydrogen passivation at crystal defects in n- and p-type multicrystalline silicon,” *Journal of Applied Physics*, vol. 102, p. 093702, 2007.

[252] P. Hamer, B. Hallam, S. Wenham, and M. D. Abbott, “Manipulation of hydrogen charge states for passivation of P-type wafers in photovoltaics,” *IEEE Journal of Photovoltaics*, vol. 4, no. 5, pp. 1252–1260, 2014.

[253] G. Hahn, A. Schönecker, A. Burgers, R. Ginige, K. Cherkaoui, and D. Karg, “Hydrogen kinetics in crystalline silicon–PECVD SiN studies in mc and Cz silicon,” *Proceedings of the 20th European Photovoltaic Solar Energy Conference and Exhibition*, pp. 717–720, 2005.

[254] M. Stavola, S. Kleekajai, L. Wen, C. Peng, V. Yelundur, A. Rohatgi, L. Carnel, and J. Kalejs, “IR characterization of hydrogen in crystalline silicon solar cells,” *Physica B: Condensed Matter*, vol. 404, pp. 5066–5070, 2009.

[255] G. Hahn, D. Sontag, S. Seren, A. Schonecker, A. R. Burgers, R. Ginige, K. Cherkaoui, D. Karg, and H. Charifi, “Detection of hydrogen in multicrystalline silicon,” *14th NREL Workshop Crystalline Silicon Sol. Cells Modules, Mater. Process.*, pp. 129–133, 2004.

[256] G. Sundell, M. Thuvander, A. K. Yatim, H. Nordin, and H. O. Andrén, “Direct observation of hydrogen and deuterium in oxide grain boundaries in corroded Zirconium alloys,” *Corrosion Science*, vol. 90, pp. 1–4, 2015.

[257] J. Takahashi, K. Kawakami, Y. Kobayashi, and T. Tarui, “The first direct observation of hydrogen trapping sites in TiC precipitation-hardening steel through atom probe tomography,” *Scripta Materialia*, vol. 63, no. 3, pp. 261–264, 2010.

[258] Y.-S. Chen, D. Haley, S. S. A. Gerstl, A. J. London, F. Sweeney, R. A. Wepf, W. M. Rainforth, P. A. J. Bagot, and M. P. Moody, “Direct observation of individual hydrogen atoms at trapping sites in a ferritic steel,” *Science*, vol. 355,

no. 6330, pp. 1196–1199, 2017.

[259] F. Duerinckx and J. Szlufcik, “Defect passivation of industrial multicrystalline solar cells based on PECVD silicon nitride,” *Solar Energy Materials and Solar Cells*, vol. 72, no. 1–4, pp. 231–246, 2002.

[260] B. Chen, J. Chen, T. Sekiguchi, M. Saito, and K. Kimoto, “Structural characterization and iron detection at ∑3 grain boundaries in multicrystalline silicon,” *Journal of Applied Physics*, vol. 105, no. 11, pp. 1–6, 2009.

[261] D. R. Kingham, “The post-ionization of field evaporated ions: A theoretical explanation of multiple charge states,” *Surface Science*, vol. 116, no. 2, pp. 273–301, 1982.

[262] P. Biévre, M. Gallet, N. E. Holden, and I. L. Barnes, “Isotopic Abundances and Atomic Weights of the Elements,” *Journal of Physical and Chemical Reference Data*, vol. 13, no. 3, pp. 809–891, 1984.

[263] A. J. London, D. Haley, and M. P. Moody, “Single-Ion Deconvolution of Mass Peak Overlaps for Atom Probe Microscopy,” *Microscopy and Microanalysis*, vol. 23, no. 2, pp. 300–306, 2017.

[264] S. H. Lee, M. F. Bhopal, D. W. Lee, and S. H. Lee, “Review of advanced hydrogen passivation for high efficient crystalline silicon solar cells,” *Materials Science in Semiconductor Processing*, vol. 79, pp. 66–73, 2018.

[265] E. C. Shaw, P. Hamer, K. A. Collett, G. Bourrett-Sicotte, R. S. Bonilla, and P. R. Wilshaw, “Saw Damage Gettering for industrially relevant mc-Si feedstock,” *Physica Status Solidi (A) Applications and Materials Science*, vol. 214, no. 7, p. 170037, 2017.

[266] F. Schindler, A. Fell, R. Müller, J. Benick, A. Richter, F. Feldmann, P.

Krenckel, S. Riepe, M. C. Schubert, and S. W. Glunz, “Towards the efficiency limits of multicrystalline silicon solar cells,” *Solar Energy Materials and Solar Cells*, vol. 185, pp. 198–204, 2018.

[267] J. Benick, A. Richter, R. Müller, H. Hauser, F. Feldmann, P. Krenckel, S. Riepe, F. Schindler, M. C. Schubert, M. Hermle, A. W. Bett, and S. W. Glunz, “High-Efficiency n-Type HP mc Silicon Solar Cells,” *IEEE Journal of Photovoltaics*, vol. 7, no. 5, pp. 1171–1175, 2017.

[268] F. Schindler, B. Michl, A. Kleiber, H. Steinkemper, J. Schön, W. Kwapil, P. Krenckel, S. Riepe, W. Warta, and M. C. Schubert, “Potential gain in multicrystalline silicon solar cell efficiency by n-type doping,” *IEEE Journal of Photovoltaics*, vol. 5, no. 2, pp. 499–506, 2015.

[269] Y. Shimizu, Y. Kawamura, M. Uematsu, K. M. Itoh, M. Tomita, M. Sasaki, H. Uchida, and M. Takahashi, “Atom probe microscopy of three-dimensional distribution of silicon isotopes in Si28/ Si30 isotope superlattices with sub-nanometer spatial resolution,” *Journal of Applied Physics*, vol. 106, p. 076102, 2009.

[270] Y. M. Yang, A. Yu, B. Hsu, W. C. Hsu, A. Yang, and C. W. Lan, “Development of high-performance multicrystalline silicon for photovoltaic industry,” *Progress in Photovoltaics: Research and Applications*, vol. 23, pp. 340–351, 2015.

[271] Y. Ohno, K. Inoue, K. Kutsukake, M. Deura, T. Ohsawa, I. Yonenaga, H. Yoshida, S. Takeda, R. Taniguchi, H. Otubo, S. R. Nishitani, N. Ebisawa, Y. Shimizu, H. Takamizawa, K. Inoue, and Y. Nagai, “Nanoscopic mechanism of Cu precipitation at small-angle tilt boundaries in Si,” *Physical Review B* -

Condensed Matter and Materials Physics, vol. 91, p. 235315, 2015.

[272] D. Zhao and Y. Li, "Carbon segregation at Σ3 {1 1 2} grain boundaries in silicon," *Computational Materials Science*, vol. 143, pp. 80–86, 2018.

[273] D. Zhao and Y. Li, "Lattice distortion induced site dependent carbon gettering at twin boundaries in silicon," *Journal of Alloys and Compounds*, vol. 712, pp. 599–604, 2017.

[274] H. J. Möller, L. Long, M. Werner, and D. Yang, "Oxygen and Carbon Precipitation in Multicrystalline Solar Silicon," *physica status solidi (a)*, vol. 171, no. 1, pp. 175–189, 1999.

[275] S. Pizzini, P. Cagnoni, A. Sandrinelli, M. Anderle, and R. Canteri, "Grain boundary segregation of oxygen and carbon in polycrystalline silicon," *Applied Physics Letters*, vol. 51, no. 9, pp. 676–678, 1987.

[276] H. J. Möller, C. Funke, A. Lawerenz, S. Riedel, and M. Werner, "Oxygen and lattice distortions in multicrystalline silicon," *Solar Energy Materials and Solar Cells*, vol. 72, pp. 403–416, 2002.

[277] J. Mullins, V. P. Markevich, M. Vaqueiro-Contreras, N. E. Grant, L. Jensen, J. Jabłoński, J. D. Murphy, M. P. Halsall, and A. R. Peaker, "Thermally activated defects in float zone silicon: Effect of nitrogen on the introduction of deep level states," *Journal of Applied Physics*, vol. 124, p. 035701, Jul. 2018.

[278] S. Binetti, J. Libal, M. Acciarri, M. Di Sabatino, H. Nordmark, E. J. Øvrelid, J. C. Walmsley, and R. Holmestad, "Study of defects and impurities in multicrystalline silicon grown from metallurgical silicon feedstock," *Materials Science and Engineering B: Solid-State Materials for Advanced Technology*, vol. 159–160, pp. 274–277, 2009.

[279] F. Shimura and R. S. Hockett, “Nitrogen effect on oxygen precipitation in Czochralski silicon,” *Applied Physics Letters*, vol. 48, no. 3, pp. 224–226, 1986.